University of Castilla-La Mancha

Smart Hydrogels based on 1,3,5-triazines for Hydrophobic Drug Delivery Applications

Jorge Leganés Bayón

May 2021

UNIVERSITY OF CASTILLA-LA MANCHA

Faculty of Chemical Science and Technology

Department of Inorganic Chemistry, Organic Chemistry and Biochemistry

JORGE LEGANÉS BAYÓN

Submits this Thesis entitled

"Smart Hydrogels based on 1,3,5-triazines for Hydrophobic Drug Delivery Applications"

For the obtention of the degree of

International Doctorate in Sustainable Chemistry

Ciudad Real, May 2021

La Dra. Sonia Merino Guijarro, Profesora Titular y la Dra. Ana María Sánchez-Migallón Bermejo, Catedrática, ambas del Área de Química Orgánica de la Facultad de Ciencias y Tecnologías Químicas de la Universidad de Castilla-La Mancha

CERTIFICAN:

Que el trabajo de investigación titulado "Smart Hydrogels based on 1,3,5-triazines for Hydrophobic Drug Delivery Applications" constituye la Memoria que presenta D. Jorge Leganés Bayón, Graduado en Química por la Universidad Autónoma de Madrid, para optar al Título Internacional de Doctor en Química Sostenible. Así mismo, que este trabajo ha sido realizado en el Departamento de Química Inorgánica, Orgánica y Bioquímica de la Facultad de Ciencias y Tecnologías Químicas de la Universidad de Castilla-La Mancha, y que cumple con todos los requisitos necesarios para su presentación. Y para que así conste, firman el presente certificado en Ciudad Real a 30 de abril de 2021.

Fdo: Dra. Sonia Merino

Fdo: Dra. Ana M. Sánchez-Migallón

Agradecimientos

Lo primero, me gustaría agradecer a Sonia y a Ana, mis directoras de tesis, por vuestra supervisión y apoyo durante todos estos años, por encauzarme cuando derivo en el laboratorio, por aconsejarme a la hora de redactar (y no enrollarme tanto)...Sonia, gracias por aconsejarme en el mundo de los hidrogeles, por todas las veces que cruzaba a tu despacho a resolverme dudas sin previo aviso, estando siempre liada. Ana, gracias por enseñarme el mundo de las triazinas y resolverme todas las dudas de química. Gracias también por ser mi segunda madre, de preocuparte tanto por mí y de mi tiroides. ¡Muchas gracias a las dos! 😊.

Gracias a Ester Vázquez por darme la oportunidad de trabajar en tu equipo e iniciarme tanto en el mundo del grafeno como en el de los hidrogeles, a los que tanta caña les he dado con el martillo, el cúter, los imanes….gracias también por el valioso conocimiento que me has aportado en nuestras reuniones así como por apoyarme en todos mis momentos de despistes. ¡Muchísimas gracias por todo Ester!

Gracias también a Marian, por resolverme dudas, por enseñarme cosillas del TGA y el BET y ayudarme con las "publis". En general, gracias a todas las jefas del MSOC y la "Facul", ¡sois un equipazo!

Al resto de los profesores de la facultad: Antonio de la Hoz, siempre dispuesto a ayudar cuando me paso por tu despacho con dudas. A Juan y Julián, por resolverme mis "rayadas" de Orgánica. Juan, gracias por despegarme los imanes cuando se juntaban, si no llega a ser por ti no habría habido manera. Ángel, gracias por ser mi mentor del aparato de Microondas, que intimida sólo de mirarlo. A Andrés Moreno por los momentos de cafés, siempre haciéndolos más amenos. A Pilar, Prado, Victoria y Enrique, que también me habéis resuelto dudas más de una vez.

Al departamento de Analítica: a Gregorio, gracias por enseñarme a usar el HPLC y sentarnos a debatir sobre hidrogeles. A Aurelia, por tu ayuda con todas las dudas de analítica y siempre dispuesta a prestarme un ratillo de tu tiempo.

Al equipo técnico del IRICA: agradecer Mónica y *Mari Carmen* por vuestros cursos de TGA y Rayos X que tan útiles me han sido. A Carlos Rivera, por tu ayuda con los aparatos de la tercera planta y tus geniales explicaciones que tanto he disfrutado. A César, por dejarme apurar a los últimos minutos en el IRICA antes de cerrar. Fuera del IRICA, quiero agradecer a Óscar Juan Dura por toda su ayuda y su claridad a la hora de explicarnos todo.

Al equipo técnico de la "Facul": a Rian, por encontrarme enseguida los reactivos nada más pedírselos cuando no los encontraba. A *Txiqui*, por nuestra confianza y sus lecciones de cómo cuidarme más el pelo. A las conserjes de la facultad/IRICA: Ana, Teresa, Cristina, Prado, por atenderme siempre que os preguntaba.

To the people in Saarbrücken: I would like to thank Aranzazu Del Campo for giving me the opportunity of carrying out a doctoral stay in her laboratories at the Institute of New Materials (INM) in Saarbrücken, Germany. I would also like to thank Dra. Julieta Páez for her constant supervision and explanations during my stay there. Finally, I want to thank all the Dynamic Biomaterials group for their welcoming and funny moments in the "coffee and cakes": Mitchel, Shardul, Sam, Zahra, Minye, the spanish crew….and outside the lab, to my *bestie* Tina: wir werden uns bald wieder treffen!

A los bioquímicos de la Facultad de Medicina: A "Fronti", por nuestras conversaciones sobre *Sapiens* y el devenir de la vida. A Inma por las batallas cortando los geles para cultivos y Carlos Alberto, por aguantarnos yendo y viniendo a medir alícuotas y lidiar con nuestros experimentos con las "celulillas".

A los chicos del "Labo" de la facultad: Alberto y *Manu*, por las bromas, confianza y tantas risas que nos hemos "echao", a *Pradito*, siempre tan maja y alegre. A *Rodri*, siempre dispuesto a ayudar. A los chicos de microondas: Iván, Bea, Carlos, también por vuestra ayuda y por los momentos de cafés y a *Jesusete*, por todos los momentos de apoyo. A *Almu* y a *Isa* también, ¡un saludo! Gracias a Alba "churumbela", por nuestros momentos en el laboratorio y lo bien que lo hemos pasado y a *Guille*, por aguantar mis rollos de mecanismos. Gracias también a Beatricce, por los buenos momentos y por acogerme en Trieste.

A mi grupete del "Labo": a los que ya no estáis, Cristina, gracias por todos los momentazos y sobre todo tu ayuda al principio de la tesis. A José Miguel, por todos sus chistes, a Yoli y Míguel, también por todos los buenos momentos. A los más junior, a Alicia, Irene y Carlos por amenizarme los cafés en pandemia. Gracias a *Javi*, por preguntarme siempre qué tal me va y por enseñarme el mundo de la vendimia. A Antonio "químico" por su sabiduría, tanto experimental como manchega, su valiosa ayuda y sus útiles tutoriales. A Antonio "ingeniero", aunque tarde en contestarte a los "wasap" sabes que somos "compis" y somos igual de "rarunos". A *Edu*, el más "ganso" de todos. Anda que no nos amenizas los ratos cuando estás tú. Además, nos dejas usar el SEM si nos portamos bien. A *Josuete*, mi más leal admirador, a la par que majísimo y que me has ayudado mil y una veces. A *Adri*, gracias por tus consejos sabios a la hora de buscar Postdocs. A mis "chatis": *AliN, AliF* y *Vivi*, sabéis que soy el hombre más apuesto que habéis conocido. Mil gracias por todas las bromas telefónicas e

inocentadas que me habéis "colado". *AliN* y *Vivi*, gracias por tantas dudas que me habéis resuelto. *AliF*, gracias por prestarnos el "oro negro" tan valioso cuando no teníamos a mano. A mi "number one", Ana, mil gracias por toda tu ayuda en el "Labo" y por ser mi compi de viajes en tren. *¡Te extraño, guey!* A *todos vosotros* por los todos los momentos que hemos vivido dentro del "Labo" y fuera de él, en viajes, congresos, visita de estancia, veranitos ¡y los viajes que espero que nos queden! Os quisiera agradecer especialmente por haber mostrado *incuestionable* interés en todas mis explicaciones sobre mecanismos de Química Orgánica.

Fuera del "Labo": gracias al comando Alcobendas: Alex, Diego, Lolo, Javi y Alberto, cuyo apoyo ha sido crucial durante la pandemia. Habría pagado todas las multas por quebrantar el toque de queda con tal de seguir en nuestro querido *sótano* más tarde de las 12. Aunque al final por lo visto nunca llegaban. A mis amigas de Madrid, Ali y marta por vuestra compañía y escapadas a la naturaleza…y a l@s chic@s de Oliva por todos nuestros momentos.

Por último, pero no menos importante, a mi familia: gracias a *mis padres* por aguantarme todos los fines de semana, aconsejarme y apoyarme. A mi *hermano*, por estar siempre ahí, por llevarme a conocer mundo, museos, exposiciones…y sobre todo de compras a por ropa nueva. En definitiva, ¡gracias por ser las mejores y más importantes personas para mí! A mi *Tita* y mi primo, por todas las cenas de Navidad. Con vosotros siempre ha sido más fácil, ¡os debo de todo! Besos y abrazos a todos.

Gracias a todossss

Thanks to allllll

Jorge

Index

Abbreviations

^{13}C-NMR	Carbon Nuclear Magnetic Resonance
^{1}H-NMR	Proton Nuclear Magnetic Resonance
3-(NisA)	(3-(Nitrosalicylic Acid))
AA	Acrylic Acid
AAm	Acrylamide
AFM	Atomic Force Microscopy
Alg	Alginate
AMF	Alternating Magnetic Field
ANBP	*p*-dialkylAminoNitroBiPhenyl
BSA	Bovine Serum Albumin
BZ	BenZocaine
CDK	Cyclin-Dependent Kinase
CDs	CycloDextrins
CMC	Critical Micellar Concentration
CNTs	Carbon NanoTubes
CUR	CURcumin
DATs	DiAminoTriazines
DBCO	DiBenzoCyclOctyne
DCM	DiChloroMethane
DEX	DEXtran
DEX-AN	Acrylate-o-Nitrobenzyl-functionalized DEXtran
DFT	Density Functional Theory
DI	DeIonized Water
DIPEA	DiIsoPropylEthylenediAmine

DMP	Dess-Martin Periodinane
DMSO	DiMethyl SulfOxide
DOX	DOXorubicin
DSC	Differential Scanning Calorimetry
DSPEG	Dithiolated Poly(EthyleneGlycol)
ECM	ExtraCellular Matrix
EDX	Energy Dispersive X-ray spectroscopy
EGA	Evolved Gas Analysis
EGDMA	Ethylene Glycol DiMethAcrylate
EMEM	Eagle's Minimum Essential Medium
EMF	External Magnetic Fields
EPI	EPIchlorohydrine
FITC-BSA	Fluorescein IsoThioCyanate-Bovine Serum Albumin
FLG	Few-Layer Graphene
FOSA	2-(N-ethylperFluoroOctaneSulfonamido) ethylAcrylate
FT-IR	Fourier Transform InfraRed spectroscopy
GFP	Green Fluorescent Protein
GI	GastroIntestinal
HA	HydroxyApatite
HK	HonoKiol
HPE	Hyperbranched PolyEster
HPLC	High-Performance Liquid Chromatography
IB	IBuprofen
ILTG	IsoLiquiriTiGenin
IMI	IMIpramine
ISM	Industrial, Scientific and Medical Broadbands

KPS	Potassium PerSulfate
LD	LevoDopa
MBA	N,N'-MethyleneBis(Acrylamide)
MBT	2-(MercaptoBenzoThiazole)
MCR	MultiComponent Reaction
MEO_2MA	2-(2-MethoxyEthoxy)ethyl MethAcrylate
MMA	Methyl MethAcrylate
MNPs	Magnetic NanoParticles
MWs	MicroWaves
mw	Monomer Weight
MWCNTs	Multi-Walled Carbon NanoTubes
MZ	MetronidaZole
NAGA	*N*-AcryloylGlycinAmide
NIR	Near InfraRed
NMO	*N*-Methylmorpholine *N*-Oxide
NMs	NanoMaterials
NPs	NanoParticles
NR	Nile Red
NX	NaproXene
OEGMA	Oligo(EthyleneGlycol)methylether MethAcrylate
o-NB	Ortho-NitroBenzyl
PAA	PolyAcrylic Acid
PAAm	Poly(AcrylAmide)
PAMAM	PolyAMidoAMine
PANI	PolyANIline
PBE	Perdew–Burke–Ernzerhof
PBS	Phosphate Buffered Saline

PCL	Poly(ε-CaproLactone)
PDMS	Poly(DiMethylSiloxane)
pDNA	Plasmid DeoxyriboNucleic Acid
PEDOT	Poly(3,4-EthyleneDiOxyThio-phene)
PEG	Poly(Ethylene Glycol)
PEGDA	PolyEthylene Glycol DiAcrylate
PEGMA	Poly(Ethylene Glycol) MethAcrylate
PHB	Poly[(*r*-3-HydroxyButyrate]
p-HEMA	Poly-2-HydroxyEthyl MethAcrylate
P_{inc}	INCident Power
PLA	Poly(Lactic Acid)
PLGA	Poly(Lactic-*co*-Glycolic Acid)
PMA	Poly(MethAcrylate)
PMNB	*P*-MethoxyNitroBiphenyl
PNIPAAm	Poly(*N*-IsoproPylAcrylAmide)
POLTF	POst-Lens Tear Film
PPO	Poly(Propylene Oxide)
PRGs	Photo-Responsive Groups
PTX	PacliTaXel
PVA	PolyVinyl Alcohol
PVDAT	Poly(VinylDiAminoTriazine)
PVL	Poly (δ-ValeroLactone)
PXRD	Powder X-Ray Diffraction
QDs	Quantum Dots
QTOF	Quadrupole Time Of Flight mass spectrometry
RA	Retinoic Acid
RBPY	Tris(2,2'-BiPYridine)Ruthenium(II)

RHO	RHOdamine 101
SD	Swelling Degree
SDS	Sodium Dodecyl Sulfate
SEM	Scanning Electron Microscopy
SGF	Simulated Gastric Fluid
SIESTA	Spanish Initiative for Electronic Simulations with Thousands of Atoms
S_NAr	Nucleophilic Aromatic Substitution
SPAAC	Strain Promoted Azide–Alkyne Cycloaddition
SPIONs	SuperParamagnetic Iron Oxide Nanoparticles
SQUID	Superconducting QUantum Interference Device
SWCNT	Single-Walled Carbon NanoTubes
TEM	Transmission Electron Microscopy
TGA	ThermoGravimetric Analysis
THF	TetraHydroFuran
t_{ir}	Irradiation Time
TM	TaMoxifen
TPAP	TetraPropylAmmonium Perruthenate
UCNPs	UpConverting NanoParticles
UV	UltraViolet
VDAT	6-Vinyl-2,4-DiAmino-1,3,5-Triazine

Abstract

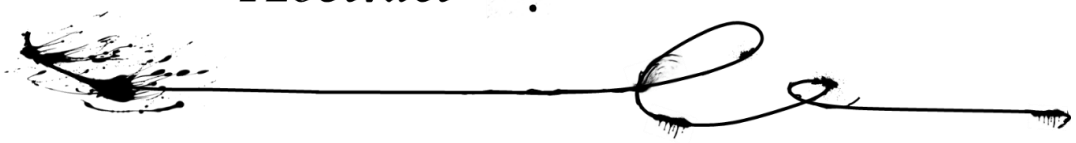

Abstract

Currently, around 40% drugs in the market and 60% in the research and development stage are hydrophobic. In consequence, due to their poor water-solubility, they pose the risk of precipitation in the physiological media, leading to poor tolerance and low absorption in the organism. To overcome these setbacks, these hydrophobic drugs are incorporated within hydrophilic drug reservoirs *prior* to their incorporation inside the organism, which facilitates the dissolution of these drugs in the physiological media and allows their delivery to target tissues.

Hydrogels are suitable materials that may be used as such containers due to their biocompatibility, bioadhesivity and similarity to the extracellular matrix. However, their highly hydrophilic character poses an intrinsic problem: their incapacity to incorporate and release hydrophobic drugs within their polymeric network.

The current research, which is summarized in chapter 1 of this thesis, introduces hydrogels as reservoirs to deliver drugs inside the body in a controlled manner and assesses the strategies that incorporate hydrophobic drugs inside these hydrophilic materials, namely: incorporation of hydrophobic domains within the hydrogel network, introduction of hydrophobic nanoparticles or copolymerization with amphiphilic moieties, such as cyclodextrins. Finally, the biomedical applications of these hydrophobic hydrogels is reviewed.

In this work, we studied diaminotriazines (DATs) as potential hydrophobic building blocks for hydrophobic hydrogels, due to the ability of the former to stablish a variety of hydrophobic intermolecular interactions even in the presence of water.

Thus, chapter 2 deals with the synthesis and characterization of hydrogels based in the 1,3,5-triazine ring. First, the design and optimization of the hydrogels is covered. For this, we investigated the influence on their structure of the monomers and crosslinkers used in the fabrication of these materials. Further, we studied the swelling degree, pore sizes and mechanical properties. Finally, since the heterocycle has basic character, the behavior of the hydrogel towards the environmental pH was also examined.

We have next studied their capacity to incorporate drugs of different hydrophobic nature and their ability to release them to prove their drug delivery performance. In order to check the utility of these hydrogels for tissue engineering applications, we have also studied the release of growth factors, such as retinoic acid.

Finally, we have modelized through theoretical calculations the hydrophobic domains taking place inside the hydrogels, which were in accordance with the obtained experimental results.

Nanomaterials are compounds of growing relevance due to their chemical and physical properties. In chapter 3, graphene and magnetic nanoparticles have been studied for the preparation of hybrid hydrogels. Graphene was prepared following a mechanochemical approach, previously developed in our research group, while the magnetic nanoparticles were prepared in two different manners, namely, the blending method and the *in situ* co-precipitation method. The incorporation of these nanomaterials inside our 1,3,5-triazine-based hydrogels allows us to prepare novel materials responsive to external stimuli.

The hydrophobic drug loading and drug release performance of these novel hydrogels is studied in chapter 4. Graphene hybrid hydrogels were tested for microwave-responsive drug release as a means for the delivery of a hydrophobic drug *via* a remote and innocuous stimulus. We used microwave radiation of 1GHz, exclusive in our laboratory. In addition, the multi-stimuli response towards simultaneous pH and microwave stimuli is tested. Further, magnetite hybrid hydrogels were tested for drug release triggered by a Neodymium magnet (N35). Finally, both graphene and magnetite hybrid hydrogels were investigated for cell viability studies, in order to evaluate them for tissue engineering applications.

In chapter 5, the work performed in the doctoral stay at the Leibniz Institute for New Materials (INM) in Saarbrücken, Germany, is covered. The project focused on the fabrication of cell-friendly light-degradable hydrogels by means of Passerini multicomponent reactions, to reduce the synthetic effort for their fabrication.

Resumen

En la actualidad, alrededor del 40% de los fármacos que se comercializan y el 60% de los compuestos en fase de desarrollo son hidrofóbicos. Su baja solubilidad en agua puede ocasionar su precipitación en medio fisiológico, lo que causa una mala tolerancia y baja absorción en el organismo. Para solventar el problema, estos fármacos hidrofóbicos se incorporan dentro de reservorios hidrofílicos para su ingesta en el organismo, facilitando su transporte a los órganos diana.

Los hidrogeles son materiales blandos idóneos para usarse como reservorios por su biocompatibilidad, bioadhesividad y similitud con la matriz extracelular. Sin embargo, su elevado carácter hidrofílico plantea un problema fundamental: su dificultad para incorporar y liberar fármacos hidrofóbicos de su red polimérica.

Las principales estrategias descritas en la bibliografía en las que se usan hidrogeles como reservorios capaces de incorporar y liberar fármacos hidrofóbicos de manera controlada en el organismo, se recogen en el capítulo 1 de esta tesis. Entre ellas, podemos citar la incorporación de dominios hidrofóbicos, la introducción de nanopartículas hidrofóbicas o la copolimerización con restos anfipáticos (ciclodextrinas). Finalmente, se comentan las aplicaciones biomédicas de estos hidrogeles con capacidad hidrofóbica.

El trabajo desarrollado en esta tesis investiga el valor de las diaminotriazinas como soporte de sustancias hidrofóbicas, dado la gran capacidad que presentan para intervenir en la mayoría de las interacciones intermoleculares que se conocen.

En el capítulo 2 se comenta cómo se preparan y caracterizan hidrogeles basados en el anillo de 1,3,5-triazina. En primer lugar, se pone a punto el método de obtención estudiando la influencia de los monómeros y del agente entrecruzante para conseguir hidrogeles manipulables. A continuación, se estudia su grado de hinchamiento, su tamaño de poro y sus propiedades mecánicas. Por otro lado, aprovechando el carácter básico del anillo heterocíclico, se estudia su comportamiento frente al pH.

Posteriormente, se ha estudiado la utilidad de estos nuevos materiales para incorporar fármacos de naturaleza hidrofóbica creciente y su habilidad para liberar dichas drogas de manera controlada. Estos hidrogeles pueden tener aplicación en el campo de la ingeniería de tejidos dada su capacidad para albergar y liberar un factor de crecimiento como el ácido retinoico.

Finalmente, se ha modelizado con cálculos teóricos los dominios hidrofóbicos que forman las triazinas dentro de la matriz del hidrogel, encontrándose concordancia con los datos experimentales.

Los nanomateriales son compuestos de creciente importancia debido a sus propiedades físicas y químicas que los hace valiosos en múltiples aplicaciones. En este sentido, en el capítulo 3 se utilizan grafeno y nanopartículas magnéticas para preparar hidrogeles híbridos. El grafeno se ha preparado por exfoliación mecanoquímica, mientras que las nanopartículas magnéticas se sintetizaron mediante dos métodos, el método *blending* y el método de coprecipitación *in situ*. La incorporación de estos nanomateriales a nuestros hidrogeles de 1,3,5-triazina nos permite preparar nuevos materiales sensibles a estímulos externos.

La capacidad de carga y liberación de fármacos hidrofóbicos en estos nuevos hidrogeles híbridos se estudia en el capítulo 4. Para los hidrogeles de grafeno se ha utilizado como estímulo remoto e inocuo una radiación microondas de 1 GHz, exclusiva de nuestro laboratorio. Además, se ha analizado la influencia de dicha radiación combinada con la variación de pH. En el caso de los híbridos con propiedades magnéticas, se ha utilizado un imán de Neodimio (N35) para el estudio de la liberación de la carga hidrofóbica. Finalmente, se ha estudiado la viabilidad celular de estos hidrogeles híbridos para su futura aplicación en ingeniería de tejidos.

En el capítulo 5, se detalla el trabajo realizado en la estancia predoctoral en el Instituto de Nuevos Materiales (INM) en Saarbrücken, Alemania. El proyecto se basa en la preparación de hidrogeles biocompatibles y sensibles a la luz, por medio de reacciones multicomponente de Passerini.

Objectives

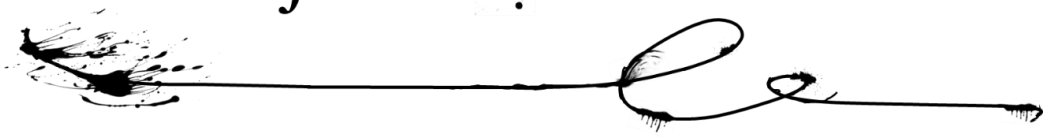

Objectives

The main objective of this work is the preparation of hydrogels that can be used for the efficient loading and subsequent release of hydrophobic drugs in a controlled manner.

To achieve such goal, a series of partial objectives were set:

- Preparation of 1,3,5-triazine derivatives which may be used as monomers for polymeric systems.
- Synthesize new soft manipulable materials from such monomers.
- Study the swelling capacity of these hydrogels in water, their pore sizes and mechanical properties.
- Evaluate their capacity to incorporate hydrophobic drugs.
- Analyze through theoretical calculations the hydrophobic nature of these hydrogels based in the DAT skeleton.
- Prepare and characterize graphene and magnetite nanoparticles in order to incorporate them in the hydrogel structure and confer them with stimuli-responsiveness.
- Characterize these nanocomposite hydrogels and evaluate the influence of these nanomaterials in their structure.
- Study their drug release capacities towards different external stimuli.
- Study their viability in the presence of cells for biomedical applications.

Chapter 1

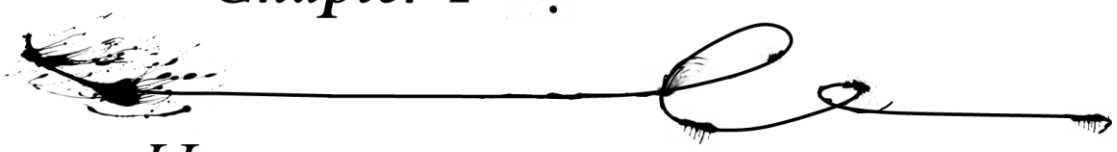

Hydrogels for Hydrophobic Drug Delivery

1.1. Hydrogels as drug delivery reservoirs

Hydrogels are defined as three-dimensional, physically and/or chemically crosslinked polymer networks which can incorporate up to thousands of times their dry weight in water or other fluids. Due to their high water content and their elastic nature, hydrogels mimic the mechanical and physiochemical properties of the native extracellular matrix (ECM) of many tissues, rendering them highly biocompatible with barely no irritation with surrounding tissues.[1]

These characteristics along with their unique porous structure and their capacity to respond to different stimuli, such as pH, temperature or enzymatic activities, have prompted the scientific community to investigate a wide variety of applications for these materials, particularly for medical treatments (Figure 1).[2,3]

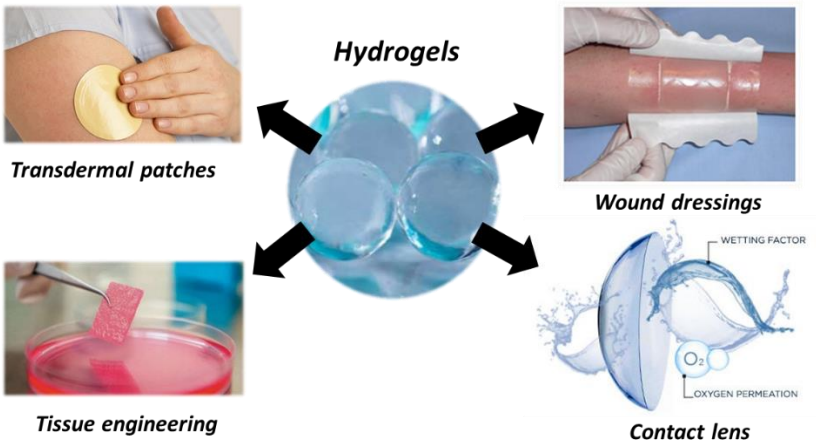

Figure 1. Hydrogels for biomedical applications.

Nowadays, conventional drug administration often requires high dosages or repeated administration to achieve therapeutic effect. As a consequence, this can lower drug efficacy and patient compliance, resulting in side effects and toxicity.[3]

To address these issues, research in the last decades has focused on controlled drug delivery systems. Drug delivery technologies refers to approaches, formulations and systems for transporting a pharmaceutical compound throughout the body in a dose-dependent manner in order to achieve safely the therapeutic effect and avoid drug toxicity (Figure 2).[4]

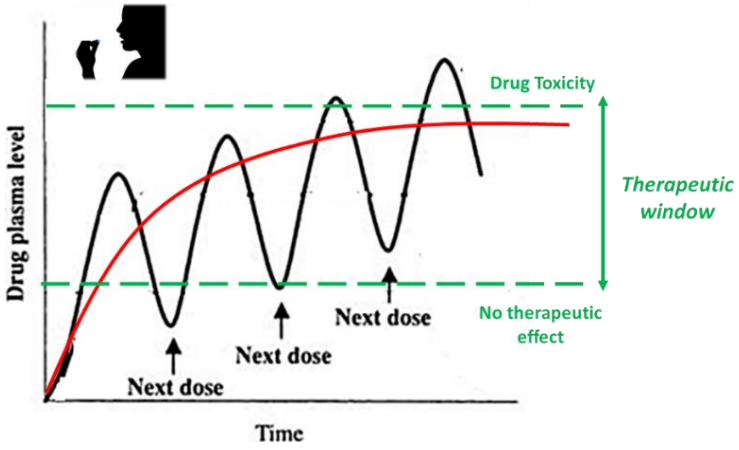

Figure 2. Routes of drug administration. Conventional drug intake with oral pill forms (black) and drug intake with drug delivery containers (red).

In this sense, hydrogels are a particularly appealing type of drug delivery system due to their high-water content and porous nature (Figure 3), which confers them the capability to easily encapsulate and release hydrophilic drugs.[2]

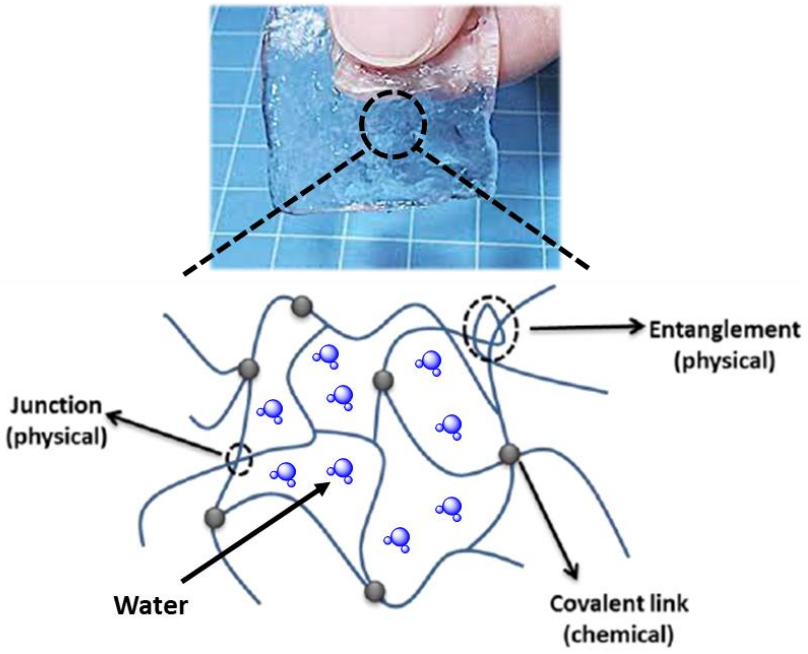

Figure 3. Internal structure of hydrogels.

Hydrogels as delivery systems can be classified into three main categories based on their size: macroscopic hydrogels, microgels and nanogels.

Macroscopic hydrogels usually range from millimetres to centimetres, therefore, they are either implanted surgically into the body or placed in contact with the body for transepitelial drug delivery (Figure 4).[3] Although transepithelial barriers (including skin, intestine and mucosa) are impenetrable to macroscopic hydrogels, they can be permeable to the drugs released from them. When the barriers, however, have low permeability to the drug or when the target site is located deep within the tissue, placement of the hydrogel in the body may be necessary, thus directly bypassing the epithelial barriers and concentrating the drug release at target site.[5] However, surgical implantation is invasive and potentially leads to risks associated with surgery.[6]

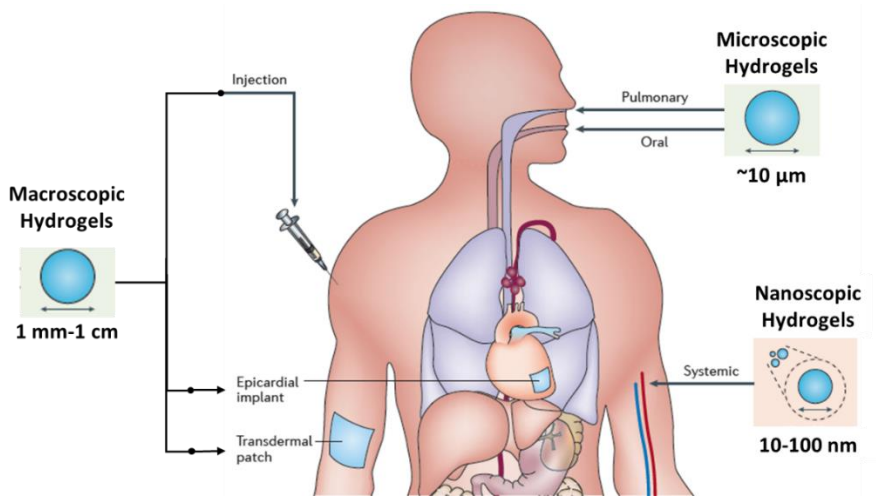

Figure 4. Delivery routes for hydrogel systems. Macroscopic hydrogels may be implanted, patched or injected. Additionally, microgels are suitable for oral and pulmonary delivery and nanogels are suitable for systemic administration.

To address this issue, emphasis has been placed on the development of injectable macroscopic hydrogels (Figure 4), known as *in situ*-gelling hydrogels, which are largely designed on the principles of gelation in the body. These systems can be injected in liquid form and undergo a sol-gel transition inside the human body; because this process occurs so slowly, the solution can be injected before solidification takes place. Once inside the body, the release of drugs from the hydrogel matrix can be tailored to occur at target site under certain stimuli that induce biodegradation of the material and release of the payload.[6]

A parallel solution to these alternatives is to use small hydrogel particles, such as **nanogels and microgels,** which have some advantages over macroscopic analogues. Due to their small size (<1 mm), not only they are

needle-injectable, transepithelial or locally injected, but also enable other routes of delivery, such as oral, pulmonar and systemic drug administration (Figure 4). Depending on their size, they can be cleared by kidney filtration or phagocytized by macrophages.[7] Apart from overall size, the bioadhesive properties are important factors in the selection of delivery routes: biological barriers such as the intestinal epithelium and mucosa are often wet and slippery, limiting the ability of the hydrogels to adhere. Adhesion of the hydrogel to the epithelium can prolong the retention of the system at target site and provide sufficient dose for the desired therapeutic effect.[8] In addition, the mechanical toughness of a hydrogel is key to maintain its structure and avoid fracture, prevent cell escape and associated risks.[9]

The porous structure of hydrogels, which results as a consequence of the crosslinking of polymer networks, is also an essential aspect for their applicability as drug delivery reservoirs. Macropores inside hydrogels range from 10-500 μm, while the spacing between polymers, known as the polymer mesh, ranges from 5-100 nm. At the molecular or atomistic scale, drugs can interact with the polymer in the mesh via a range of mechanisms, such as covalent linkage to a polymer chain (Figure 5).

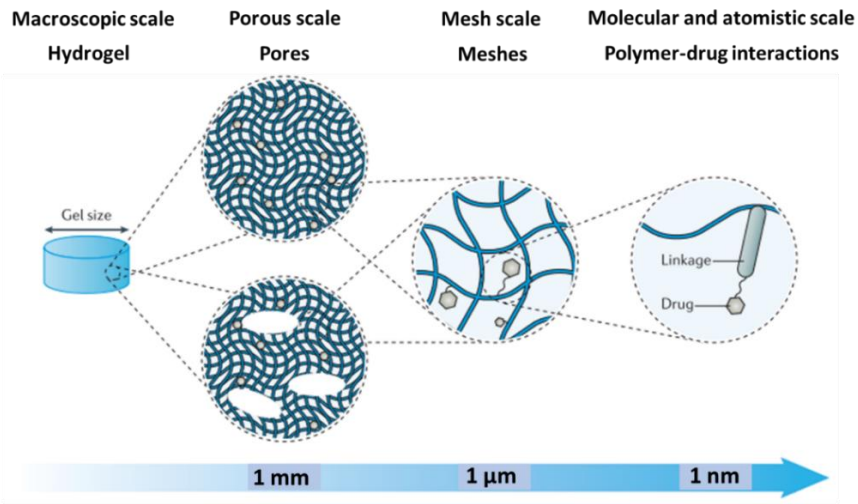

Figure 5. Multiscale scheme of hydrogels.

The mesh size determines how drugs diffuse through the hydrogel, as it controls steric interactions between the drugs and the polymer network, and thus is key to the success of these materials as optimal candidates for the delivery of a drug in a controlled manner. Overall, three possible scenarios are contemplated (Figure 6):

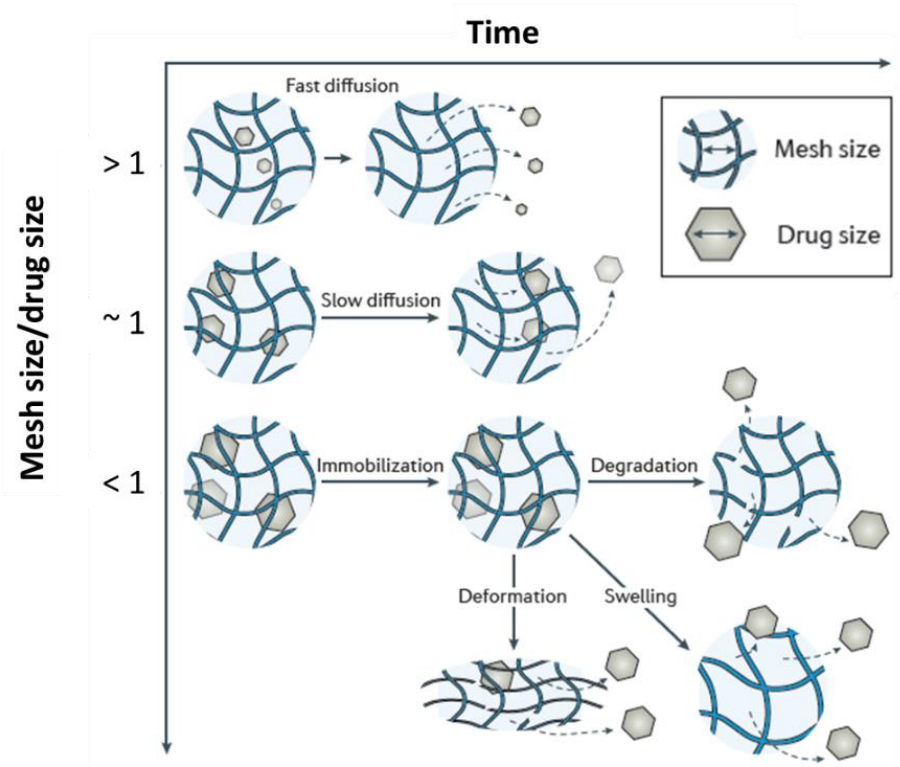

Figure 6. Drug release from hydrogels mediated by mesh size.

– When the **mesh size is larger than the drug**, the drug release process is dominated by diffusion, whereby small drug molecules migrate freely through the network without any influence of the mesh.

– When the **mesh size approaches the drug size**, the effect of steric hindrance on drug diffusion becomes prominent and the overall effect is slow drug diffusion, which allows for slow and extended release.
The mesh size of a hydrogel may be reduced by increasing the concentrations of the polymer content or the crosslinker, which induce significant friction between drugs and polymer chains and the path length for drug transport increases.[10]

– When the **mesh size is smaller than the drug size**, the drugs are immobilized by the strong hindrance exerted by the polymer mesh and drugs remain physically entrapped inside the network; in this scenario, the entrapped drug may be released by several mechanisms.
Through network degradation, for instance, the mesh size increases as the network degrades, allowing drugs to diffuse out of the hydrogel. This

process typically occurs at the crosslinking joints and is mediated by **hydrolysis**[11] or enzyme activity.[12]
Alternatively, entrapped drugs may be released by controlled swelling of the hydrogels; the drug is released after the hydrogel swells and the mesh size increases, a process that is typically triggered by **external stimuli** such as pH[13] or temperature,[14] to name a few.

Finally, through **mechanical deformation** of the network, entrapped molecules may be released from the hydrogel, since this increases the mesh size by changing the network structure and trigger convective flow within the network.[15]

Another approach to control drug release from hydrogels is to design chemical bonds between the drug and the polymer chains. This strategy may even terminate drug diffusion if the drug-polymer interactions are strong enough, and it is particularly useful when small drugs are delivered, since otherwise they would be released in very short periods.

Various chemical and physical interactions may be used, ranging from covalent conjugation to secondary interactions such as electrostatic and hydrophobic interactions (Figure 7).

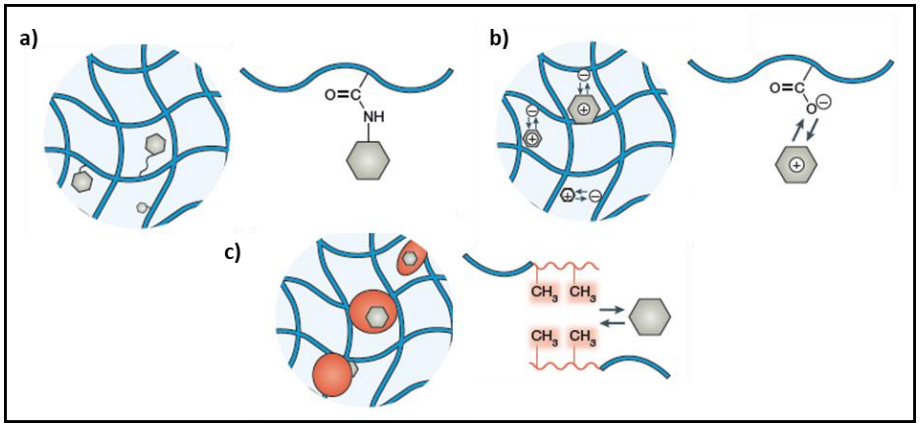

Figure 7. Drug-polymer interactions that mediate drug release a) covalent linkage b) electrostatic interaction c) hydrophobic interaction.

– **Covalent linkages** between the drug and the polymer (Figure 7a) immobilize the drug and can either be highly stable (amide bonds), which retain the drug until the network degrades, or cleavable (ester bonds), which may be programmed, like degradable crosslinkers, to

cleave over time or in response to environmental stimuli, and thus the drugs are released at a rate dictated by the cleavage of these linkers.

- **Electrostatic interactions** are strong bonds that occur between charged drugs and charged polymer chains, which immobilize the charged drugs to the polymer matrix (Figure 7b). The drugs may be released when the hydrogel is degraded or when the electrostatic interaction is screened by mobile ions from the environment. For example, alginate-based hydrogels, which carry carboxylate negative groups, have been used to deliver cationic growth factors.[16]

- Lastly, drugs may be retained inside hydrogels *via* **hydrophobic associations** (Figure 7c). For example, hydrophobic aliphatic chains can be incorporated into hydrogels that self-assemble to form a hydrogel for delivery of anticancer drugs.[17] Inclusion of cyclodextrins is also useful; these oligosaccharides comprise both external hydrophilic character and internal hydrophobic pockets with which hydrophobic drugs can associate.[18]

However, the encapsulation and release of hydrophobic drugs from hydrogels results problematic, since they are generally incompatible with the hydrophilic polymer matrix and limit their effectiveness of drug delivery.[19] This incompatibility is due to the intrinsic hydrophilic nature of hydrogel matrices, which are suitable depots to host water soluble molecules by swelling the hydrogel in aqueous drug solutions.

On the contrary, since hydrophobic substances are sparsely soluble in aqueous solutions, these are poorly incorporated into the hydrogel network.[20] This drawback is the main concern for applicability of hydrogels in the drug delivery field, since over 40% marketed drugs and around 60% therapeutic compounds at the research and development stage account for hydrophobic molecules.[21]

To overcome these setbacks, several strategies to improve the delivery of hydrophobic drugs have been so far attempted, which will be discussed in detail in the following section.

1.2. Hydrogels for hydrophobic drug delivery

Amongst the earliest available methods for improving hydrophobic drug delivery, the most straightforward seems to be modification of the hydrophobic drug to increase their water solubility, rather than modifying the scaffold of the carrier itself. This is readily achieved by converting the drug into their salt forms, which have notably higher solubilities than their corresponding acidic or basic forms.

However, being salts, the potential risk of drug precipitation in the body due to pH changes is considerable, especially for oral administration. For example, the salts of acidic drugs tend to precipitate where pH is low, (gastric fluid, pH = 1.2) or in higher pH environments for basic salts, such as the duodenum (pH = 6.5-7);[22,23] in addition, this methodology is not feasible for neutral compounds. To circumvent this, salt formulation may be optimized by careful selection of counter ions and by minimizing the formation of salts *in vivo*.

To further improve the bioavailability of poorly water-soluble drugs, these may be transported inside drug delivery vehicles. These include, broadly, polymer and hydrogel reservoirs.

The simplest polymeric containers as drug delivery reservoirs mainly represent micelles[24,25] and vesicles,[26] which are formed *via* self-assembly of amphiphilic block copolymers in aqueous solutions. In these systems, the drugs are physically entrapped in the hydrophobic cores of the block copolymers assemblies, which increases substantially their water solubilities and stabilizes the assemblies in aqueous media.

A major inconvenient of self-assembled systems, however, is that they rapidly disassemble below their critical association concentration or under external stimuli,[27,28] which is typically followed by undesirable burst release of drug molecules. As an alternative to block copolymer assembly, unimolecular containers with core-shell structures are more environment-resistant due to the covalent nature of their bonds, such as dendrimers,[29] star polymers[30] and hyperbranched polymers (Figure 8).[31]

These macromolecules are highly branched and multifunctional, with many arms emanating from the core. The interior can be made hydrophobic, where

hydrophobic drugs can be encapsulated, while the periphery may be engineered with different multifunctionalities.

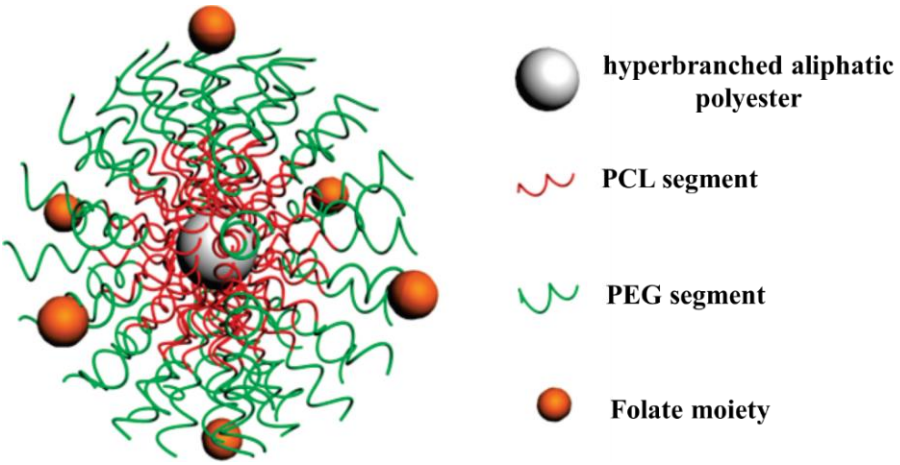

Figure 8. Structure of amphiphilic hyperbranched polymer based on poly(ε-caprolactone) (PCL) and poly(ethylene glycol) (PEG).

These systems, however, show structural rigidity that results in small internal free volume, thus compromising the hydrophobic drug encapsulation efficiency.[32] In addition, these carriers circulate in blood only for a short period of time, thus the plasma half-life is limited, which compromises the sustained release in the long term. This typically requires repeated administration of these nanocarriers, which increases the long term toxicity.[33]

Hydrogels, on the contrary, are bulky, non-circulating and stable carriers throughout the release period that enable to extend the duration of drug action,[34] and thus avoid repeated administration. These advantages grant them particular attention in the field of drug delivery of hydrophobic compounds.

Despite their nature is intrinsically hydrophilic, hydrogels may be easily modified to increase their hydrophobic character *via* a number of ways, such as introducing hydrophobic domains or adding amphiphilic nanoparticles inside the polymer network, which helps enhance their hydrophobic drug delivery performance.[35]

1.2.1. Preparation of hydrophobic hydrogels

The different strategies for preparing hydrogels fitted for delivery of hydrophobic drugs are, broadly:

- Incorporation of hydrophobic domains into the hydrogels
- Addition of nanoparticles
- Incorporation of cyclodextrins

1.2.1.1. Incorporation of hydrophobic domains in hydrogels

One of the most feasible approaches to increase the hydrophobicity of hydrogel systems consists in introducing hydrophobic domains within the polymer network. The presence of these supramolecular structures helps to encapsulate hydrophobic cargos into the hydrogels *via* hydrophobic associations and facilitates their release in a controlled manner by gradual disassembly of the domains.

Additionally, hydrophobic modifications not only provide the hydrogels with hydrophobic depots, but also suppress the hydrogel swelling under physiological conditions to improve their mechanical robustness.[36] As a consequence, the hydrogels are less susceptible to mechanical failure during payload release at the administration sites and thus premature release is avoided.

Several methods are employed for introducing hydrophobic domains into hydrogels, namely, self-assembly of block copolymers, self-aggregation of hydrophobic side chains and covalent crosslinking.

a) Self-assembly of main block polymer chains

Synthetic copolymers with alternate hydrophilic and hydrophobic segments are able to form physically-crosslinked hydrogels in water at sufficient concentrations and under specific conditions, as a consequence of the nano-aggregation of hydrophobic blocks.

In dilute aqueous solution, symmetric ABA (A: hydrophobic, B: hydrophilic) tri-block and AB di-block copolymers self-assemble intro aggregates with a dense core made of end-block A and inter-loops made of mid-block B. Once

the concentration reaches critical percolation concentration, A-blocks of different cores join together bridged in between B-blocks throughout the entire system to create a hydrogel (Figure 9).[37]

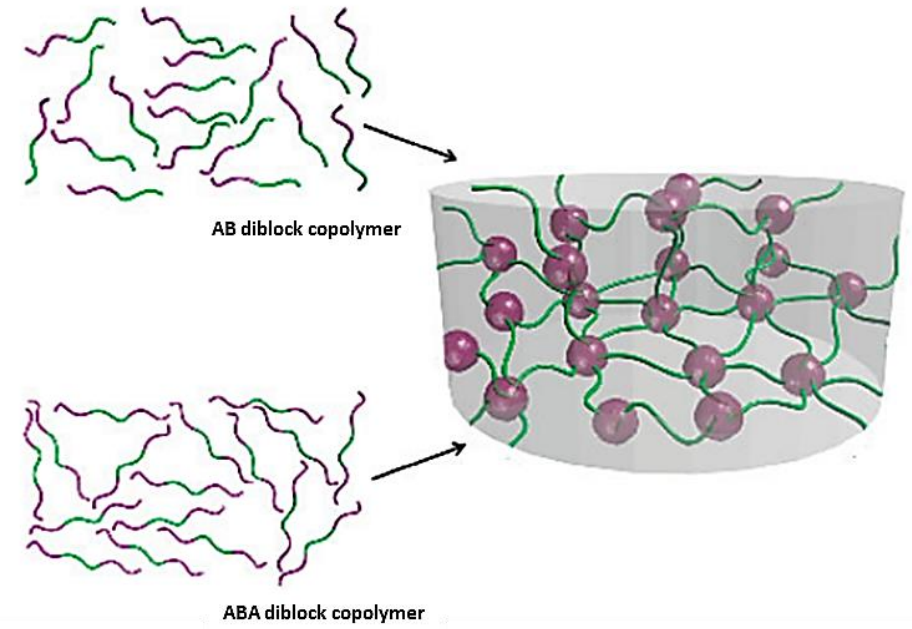

Figure 9. Hydrogel formation via self-assembly of amphiphilic block copolymers: AB di-block and ABA tri-block copolymers (A: hydrophobic, purple, B: hydrophilic, green).

In general, amphiphilic tri-block copolymers form hydrogels easily with respect to di-block counterparts. This is due to the energy that terminal A hydrophobic blocks need to overcome in order to aggregate, which is reduced through relaxation of the interfacial tension by incorporation of hydrophilic segments between hydrophobic blocks.[37] This causes the gelation concentration of di-block copolymers to be much higher than the tri-block ones, which makes the reverse transformation opposite: hydrophilic chains of di-block copolymers are easily un-entangled whereas tri-block ones are more likely to develop into stronger interlocking structures.

Poly(ethylene glycol) (PEG) is a commercially available hydrophilic polymer that possesses high water solubility, biocompatibility and low immunogenicity, which makes it particularly useful as a hydrophilic B block.

The hydrophobic A end-block can be replaced with a thermo-responsive copolymer, which allows the hydrogel to respond to changes in temperature and usually undergo a sol-gel phase transition when the temperature changes

from room to physiological temperatures.[38] These blocks increase the hydrophobicity and drug loading capacity of hydrophobic drugs by micellization.

The common hydrophobic block copolymers are shown in Figure 10. Tri-block copolymers made of PEG (block B) and poly(propylene oxide) (PPO) (block A) are the as PEG most common thermo-responsive polymers. These are typically arranged PEG-PPO-PEG (BAB), known as poloxamers or pluronics, which show exceptional thermogelling behavior.

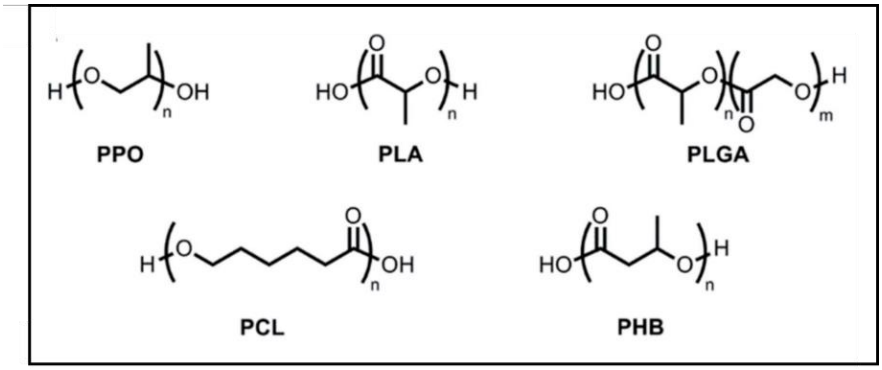

Figure 10. Hydrophobic polymer blocks in thermosensitive tri-block copolymers. PPO Poly(propylene oxide), PLA: Poly(D,L-lactide), PLGA: Poly(D,L-lactide-*co*-glycolide), PCL: Poly(ε-caprolactone), PHB: Poly[(*R)*-3-hydroxybutyrate].

Poloxamer 407 is a viscous liquid at room temperature or below but forms a hydrogel at body temperature (37ºC).[39] With poloxamers, however, high concentration of PPO hydrophobic blocks is required to achieve critical micellar concentration (CMC), the concentration above which micelles are formed. Having a high CMC causes rapid physical dissociation, causing an unwanted burst effect of the payload when the hydrogels are injected into physiological fluid.

An alternative thermogelling tri-block hydrogel is the poly(lactic acid) (PLA) and PEG in the disposition PLA-PEG-PLA (ABA), which has been extensively studied for drug delivery applications due to their biodegradability, biocompatibility and ability of self-assembly in aqueous media.[40] These systems have successfully achieved high encapsulation efficiency and sustained release of hydrophobic drugs such as camptothecin (80% and release rate over 20 days)[41] and naltrexone (60% and sustained release up to 35 days) (Figure 11).[40]

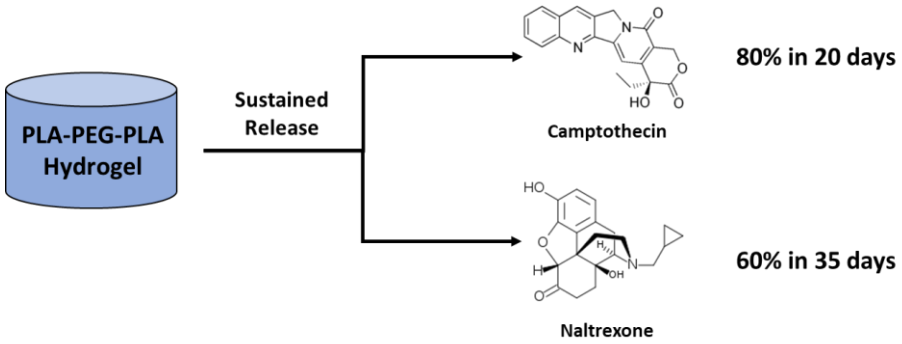

Figure 11. Sustained release of hydrophobic drugs from amphiphilic hydrogels (PLA-PEG-PLA).

Further enhancement of PLA-based tri-block hydrogels has been achieved with a less hydrophobic version of this block, namely, poly(lactic-co-glycolic acid) (PLGA), arranged as PLGA-PEG-PLGA (ABA), which is a free flowing water soluble solution at low temperatures but transitions to gel at body temperature.[42]

Since thermo-responsive hydrogels usually transition to gel at 37ºC, a typical unwanted effect is the rapid gelation of the hydrogel inside the needle during injection, thus blocking the syringe and compromising drug administration.[43] To circumvent this, additional pH-sensitive copolymers are added to the thermo-responsive ones, so that for gelation to occur, not just a temperature increase but also a change in pH values must be met.

Examples of this methodologies are triblock copolymers made of PEG and poly(amidoamine) (PAMAM) as PAA-PEG-PAMAM (ABA) (Figure 12). At low pH values (pH = 3.0) the PAA block is hydrophilic but at higher pHs, such as 7.4, the PAMAM block becomes hydrophobic. The resultant PAA-PEG-PAMAM copolymer was found to undergo a sol-gel transition at pH = 7.4 and at 37ºC.[38]

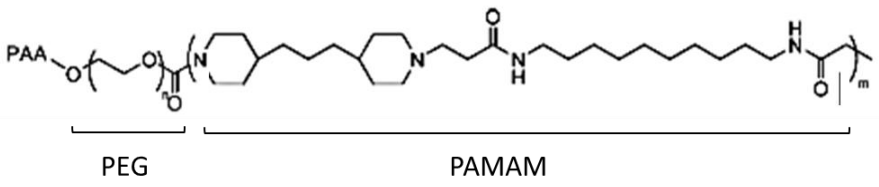

Figure 12. Structure of the PAA-PEG-PAA hydrogel.

b) Self-aggregation of hydrophobic side polymer chains

An alternative to introducing hydrophobic copolymer blocks is to chemically modify the linear hydrophilic chains with hydrophobic end-groups. However, this strategy comes at the expense of compromising the crosslinking sites, since they usually reside in the chain ends of the hydrophilic polymers.

Instead, an alternative approach to hydrophobically modify the hydrogels is to graft hydrophobic side chains on the hydrophilic backbones of the polymers, leaving the crosslinking sites intact. This way, the hydrophobic side chains aggregate into hydrophobic domains between hydrophilic main chains (Figure 13). With this methodology, the pendant hydrophobic groups may be independently modified to tune the hydrophobic affinity of the system without compromising the overall structure.

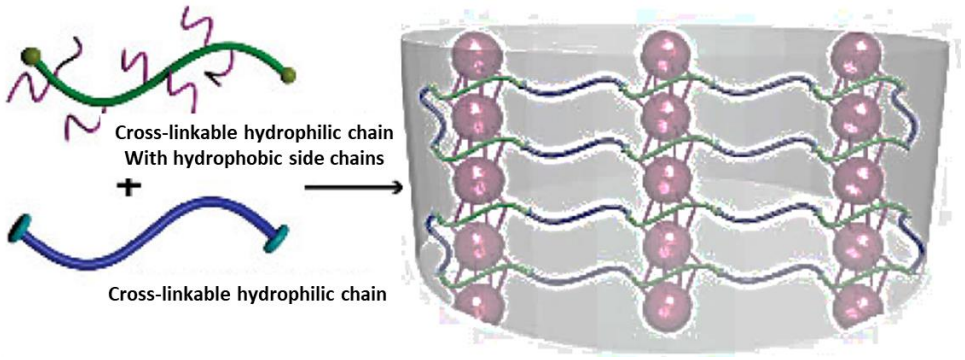

Figure 13. Hydrogel formation via aggregation of hydrophobic side chains grafted from the main polymer backbone.

An additional advantage of this methodology is that the aggregation of the hydrophobic side chains also functions as physical cross-linking joints that dissipate energy, thus enhancing the mechanical properties of the hydrogel.

Among these hydrophobic moieties to graft as side chains are bulky alkyl chains, fluorocarbon-based groups, oligo(ester) and oligo (carbonate) chains. Long alkyl chains, for example, are typical hydrophobic groups attached to the polymer backbones. When grafted to linear polysaccharides, alkyl chains can give rise to physical hydrogels due to intermolecular hydrophobic interactions; examples include alkylating chitosans with C_{12} side chains[44] or C_{16} alkyl chains to hyaluronic acid,[45] which show partially hydrophobic character. Derivatizing with long alkyl chain groups, however, lowers the solubility of the polymers in

water, forcing the synthesis to be carried out in organic solvents, which may pose additional toxicity.

However, this may be circumvented by conducting the polymerization in sodium dodecyl sulfate (SDS) solutions, or by adding salts in order to help micellar growth.[46] In addition to alkyl chains, many other hydrophobes have been studied, such as the strongly hydrophobic monomer 2-(N-ethylperfluorooctane sulfonamido)ethylacrylate (FOSA), in which the fluorocarbon chain produces much stronger hydrophobic associations than hydrocarbon chains inside the hydrogels (Figure 14).[47]

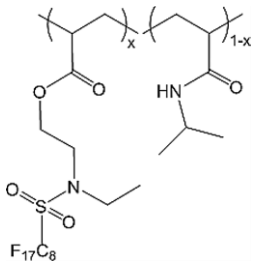

Figure 14. Chemical structure of 2-(*N*-ethylperfluorooctane sulfonamido)ethylacrylate (FOSA)-based hydrophobic hydrogels.

c) Covalent crosslinking of hydrophobic and hydrophilic chains

Hydrophobic domains may also be introduced by crosslinking of hydrophobic chains or monomers with hydrophilic ones or by using hydrophobic crosslinkers (Figure 15). These hydrogels are called amphiphilic hydrogels.

The reactions require organic solvents to dissolve the hydrophobic reagents, however, the final hydrogels may still swell in water. Despite this drawback, the covalent crosslinking method is more reliable than self-assemble, since is far less concentration-dependent and temperature-sensitive.

More importantly, the synthesis of these hydrogels involves a simple chemistry without the needs of initiators, coupling reagents or additives. Free radical polymerization is one of the most employed techniques to develop this type of hydrogels.

The typical example is that of a double network prepared from the amphiphilic poly(methacrylate) (PMA)-based co-network and a second poly(acrylamide) (PAAm) network.

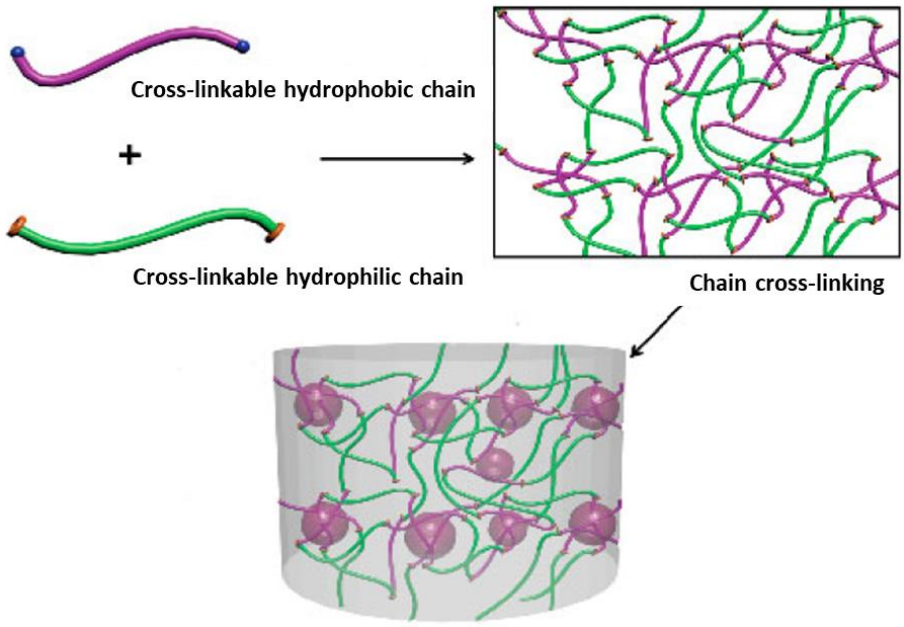

Figure 15. Hydrogel formation via crosslinking of hydrophobic and hydrophilic chains to form amphiphilic hydrogels.

The first step consists in obtaining a hydrogel network made of PMA chains crosslinked with ethylene glycol dimethacrylate (EGDMA). Subsequently, the second network was formed inside the PMA/EGDMA one using photopolymerization of acrylamide (AAm) crosslinked with *N,N'*-methylenebis(acrylamide) (MBA) (Figure 16).[48]

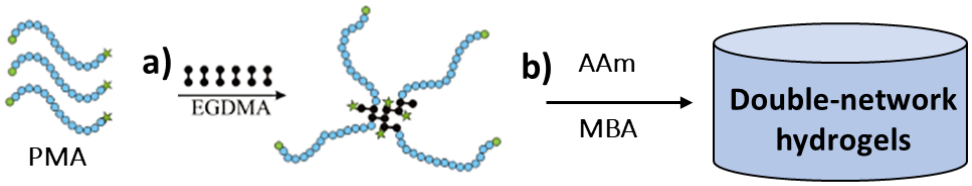

Figure 16. Synthesis of double-network hydrogels.

An alternative to obtain hydrophobic hydrogels with this methodology is using free-radical polymerization of silicon-based monomers, which are widely used for contact lens manufacturing.[49] The polymerization is carried out mixing a silicon-based monomer, a MA-based co-monomer, a crosslinking agent and an amphiphilic macromer, whose role is to prevent macrophase separation during synthesis due to the opposite nature of the monomers.

PEG-based hydrogels have also been widely used to prepare covalently crosslinked hydrogels with hydrophobic domains. PEG may be combined with polydimethylsiloxane (PDMS) using tetrahydrofuran (THF) under UV exposure.[50–52]

Another example of crosslinking hydrophilic and hydrophobic segments uses 4-arm-PEG as the hydrophilic backbone. Taking advantage of the end-hydroxyl groups of the PEG-arms, sebacoyl chloride was used as a hydrophobic crosslinker *via* condensation reaction with the 4-arm PEG. Since the latter and the sebacoyl chloride are bonded *via* ester bonds, the hydrogel resulted biodegradable (Figure 17).[53]

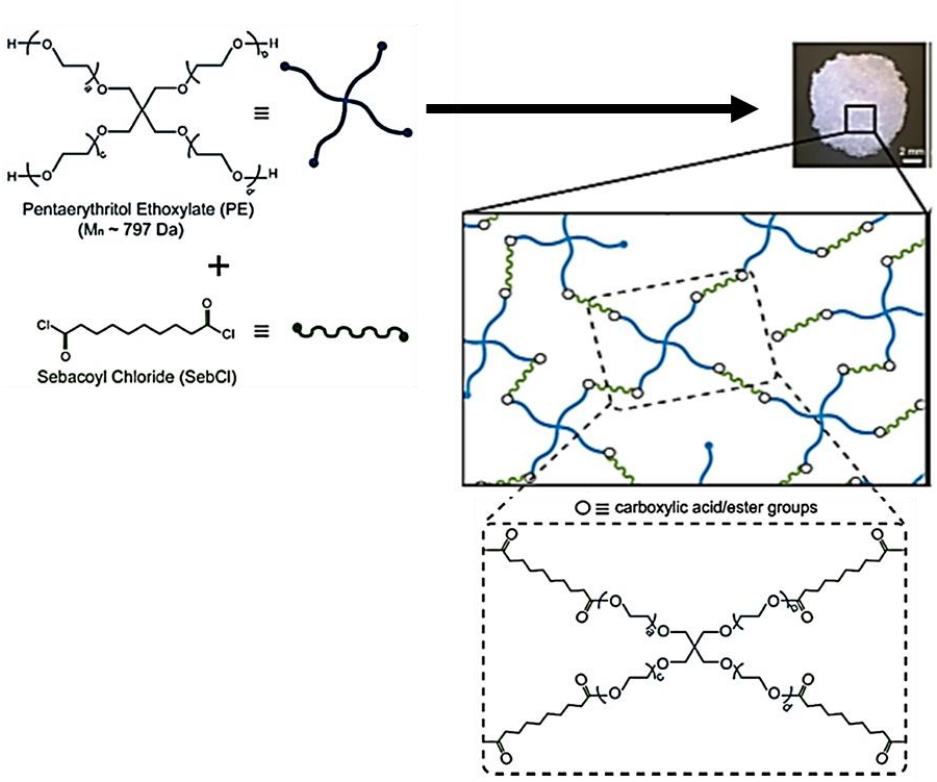

Figure 17. 4 arm-PEG crosslinked with sebacoyl chloride to form amphiphilic hydrogels.

Other approaches used pyromellitic anhydride as hydrophobic functional crosslinker due to the presence of anhydride groups in its structure than easily react with hydroxyl groups of other polymer chains through condensation reactions, thus avoiding initiators, coupling agents or additives that pose additional toxicity.[54]

1.2.1.2. Addition of nanoparticles

Nanoparticles may also be dispersed inside hydrogels to achieve hydrophobic depots in the material. The nanoparticles may interact with the hydrophilic network either physically or through covalent bonds. Typically, nanoparticles are introduced through covalent bonds following a "graft onto" approach, by which the particles are functionalized with polymerizable groups on the surface and then copolymerized with hydrophilic monomers, either acting themselves as crosslinkers or in the presence of external crosslinking agents (Figure 18).This way, the nanoparticles stay inside the hydrogels and avoid leaking outwards.

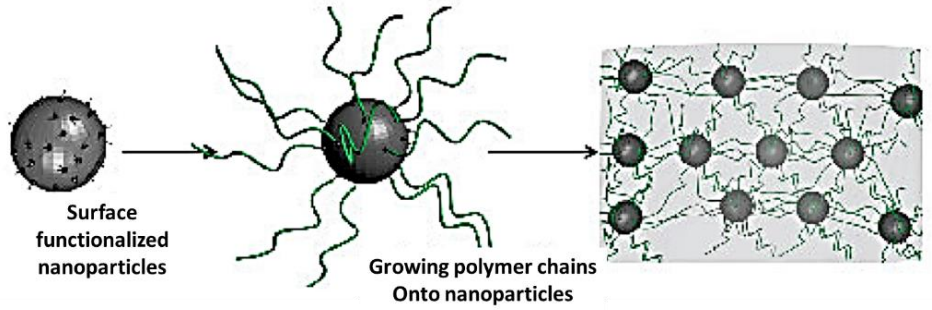

Figure 18. Hydrogel formation via "graft onto" approach by polymerization of surface-functionalized nanoparticles and hydrophilic chains via covalent coupled link.

Examples of covalently bonded nanoparticles to the polymer chains include grafting of acrylic monomers, such as acrylic acid (AA) and octylphenol-oligo(oxyethylene)acrylate on the surface of silicon nanoparticles to build a network of PAA hydrophilic backbone chains with randomly distributed nanoparticles and aggregation of hydrophobic branches (octylphenol) as physical crosslinks.[55]

On the other hand, nanoparticles may also be physically absorbed to the polymer chains in order to form hydrogels, for which several prerequisites need to be met. These include strong affinity between the particles and the polymer chains, the necessity for every polymer chain and nanoparticle to stablish two interactions to achieve percolation of the network and a controlled diameter of the nanoparticle that must be comparable or less than the length of the polymer strands. Following these rules, PLA nanoparticles were incorporated into self-assembled hydrogels *via* the physical interactions.[56]

1.2.1.3. Incorporation of cyclodextrins

Cyclodextrins (CDs) are cyclic oligosaccharides of 6,7 and 8 dextrose units, corresponding to α-CD, β-CD and γ-CDs, respectively. They are bonded through 1-4 carbon bonds and have been extensively used for complexation of hydrophobic molecules.[22] CDs are depicted as cone-shape structures, inside which hydrophobic molecules can be encapsulated reversibly by formation of inclusion complexes, which enhances their bioavailability.

Incorporating CDs into hydrogels increases the hydrophobic drug loading capacities and sustains the release, due to host-guest interactions.[57] CDs may be incorporated covalently, either directly by crosslinking them or copolymerizing them with vinyl/acrylic monomers, or physically, through supramolecular assembly.

For example, CDs have been crosslinked with coupling agents such as epichlorohydrine (EPI), which react with the free hydroxyl groups of the complexes to yield hydrogels (Figure 19).[58]

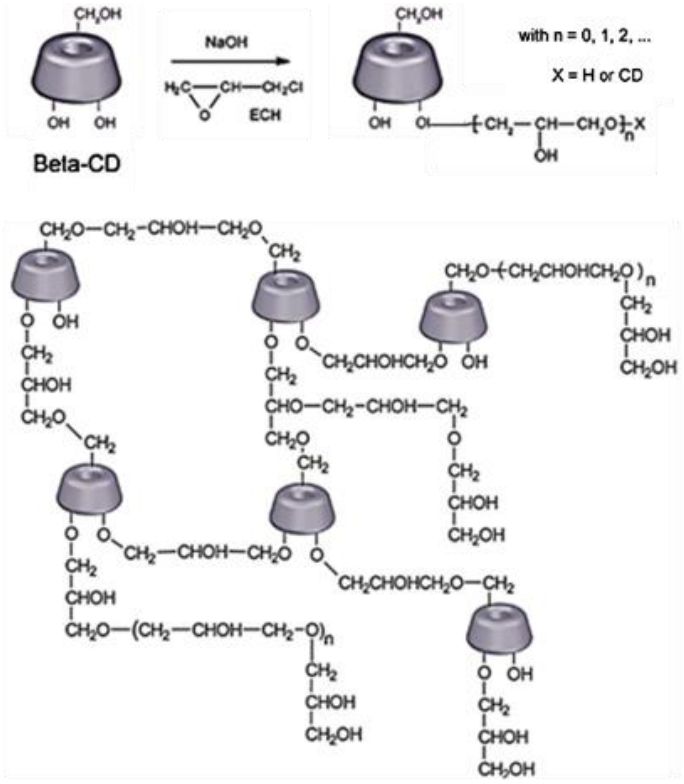

Figure 19. Chemical reaction between β-Cyclodextrin (β-CD) and epichlorohydrin (up) and epichlorohydrin-crosslinked CD-based hydrogel.

CD-based hydrogel systems have been used to load and release bupivacaine for oral sustained delivery,[59] as well as antibiotics[60] and hydrophobic drugs such as anticancer drugs.[61] Acrylated-CDs have also been polymerized into acrylic acid polymers for hydrophobic drug delivery,[62] however, due to toxicity of the synthetic nature of the crosslinkers, greener crosslinkers have been employed, such as citric acid, which was used to crosslink γ-CDs to prepare hydrogel for delivery of hydrophobic drug anthracycline.[63]

1.2.2. Drug delivery applications of hydrophobic hydrogels

The hydrogel formulations discussed so far have been used as potential systems for delivery or hydrophobic drugs, mainly for oral, subcutaneous, transdermal and ocular delivery.

1.2.2.1. Oral drug delivery

Oral drug administration is the preferred route of drug administration due to its simplicity and comfortability; it presents advantages over intravenous administration such as lower price, reduced side effects due to better control over dosage and better patient compliance.[64,65] It has some drawbacks as the harsh conditions of the gastrointestinal (GI) tract can degrade the drugs, while also drugs administered using this route suffer the first-pass effect.

By oral administration of encapsulated drugs inside hydrogels, however, these may be released over controlled periods of time while protecting the drug from the harsh conditions in the stomach.[66] This may be achieved by designing hydrogels with pH-responsive groups that release the cargo in specific parts of the GI.[67] If, in addition, hydrophobic domains are added to these pH-responsive moieties, hydrophobic agents may be released at desirable sites of the GI.

The ideal key building block for oral delivery are hydrogels containing anionic groups, such as polyacrylic acid (PAA) and derivatives. These hydrogels can swell when the pH is above the pKa of the PAA chains (~4.8) due to the deprotonation of the carboxylic acids, which leads to repulsion between negatively charged carboxylate forms, whereas the pores will remain closed when the pH is below the pKa values (Figure 20).[67]

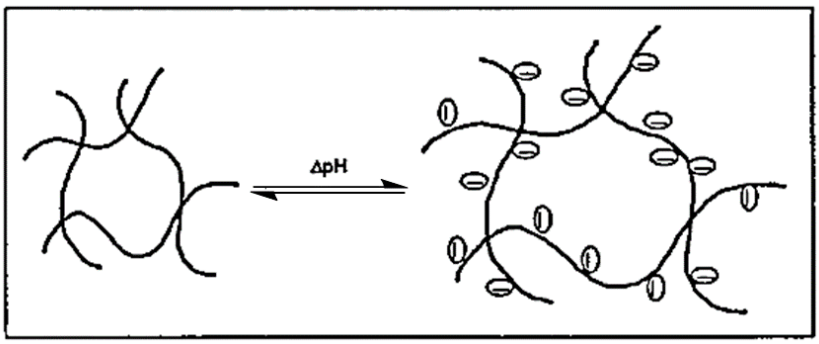

Figure 20. Expansion of environmentally responsive hydrogel due to ionization of pendant groups at alkaline pH values.

This entails that drugs loaded into these systems could be protected from the acidic environment and released in the alkaline conditions of the small intestine or colon. For example, pluronic triblock copolymers were grafted with PAA chains in order to develop pH-sensitive hydrogels that were able to deliver an array of hydrophobic drugs such as campothecins, steroids, doxorubicin (DOX), mitomycin C and mitoxantrone.[68]

Fluorescein, a hydrophobic model low-molecular-weight drug, was also delivered from hydrogels based on the hydrophobic methyl methacrylate (MMA) monomer copolymerized with pH-sensitive AA.[69,70]

Despite the progress of hydrophobic PAA-based hydrogels, due to the non-degradability of the PAA moieties, other biodegradable materials such as polypeptides may be preferred. For example, polypeptide-based hydrogels were crosslinked with poly(2-hexenoic acid), which is a hydrophobic version of the PAA, due to the presence of butyl alkyl chains, and were used for oral delivery of insulin.[71] In another example, drug delivery was not only locally achieved in the colon, but also across the epithelial layer of the GI tract into the blood stream in order to treat breast cancer. This was achieved by copolymerization with itaconic acid, the pH-responsive moiety, and poly(ethylene glycol) methacrylate (PEGMA) to produce a hydrogel.

Further, docetaxel, a hydrophobic anticancer drug, was loaded within PCL-PEG-PCL micelles inside the hydrogel. At low pH, the itaconic acid moieties remained neutral and the pores were closed, whereas at high pH the carboxylates repel themselves and the pore size increased, releasing the hydrophobic cargo at the epithelial layer of the intestine (Figure 21).[72]

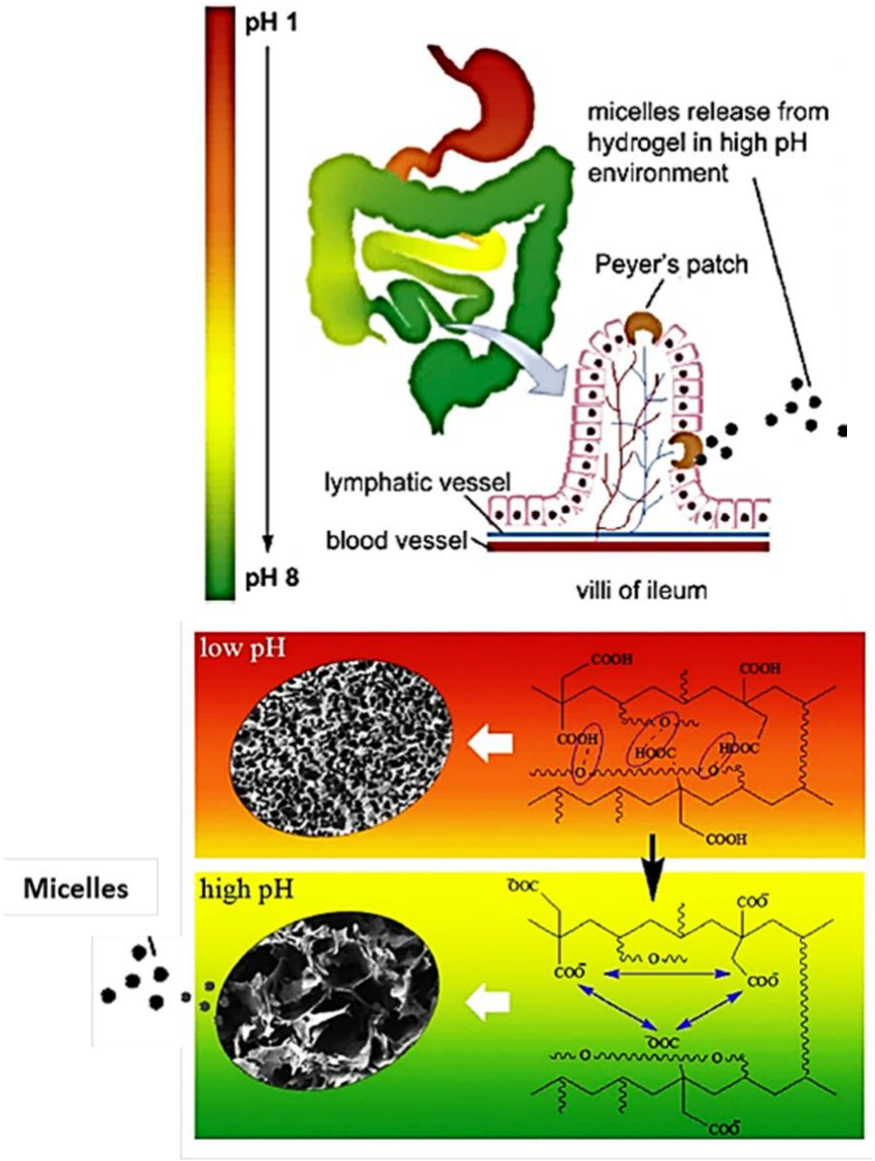

Figure 21. Drug-loaded micelle delivery in gastrointestinal (GI) tract. pH value increases from 1 (in stomach) to 8 (in ileum). The hydrogels shrink in low pH environment, while in a high pH environment, they swell and release the payload.

1.2.2.2. Subcutaneous drug delivery

Subcutaneous delivery consists in administration of the drug carriers directly into the blood stream, for which it is indispensable that the systems are injectable and display suitable sol-gel transitions under physiological conditions.[73] These systems may thus achieve localized treatment without the

need for invasive surgical placement of the drug carriers close to the treatment site, as well as surgical interventions to clear the carriers afterwards.

As commented previously, the majority of *in situ* gelling systems are based on thermo-sensitive block copolymers, which display sol-gel transitions around body temperatures. This allows the hydrogels to undergo transition from free-flowing sol at room temperature to a polymerized gel at physiological temperature (Figure 22), with the insoluble drugs partitioned onto the self-assembled hydrophobic domains.

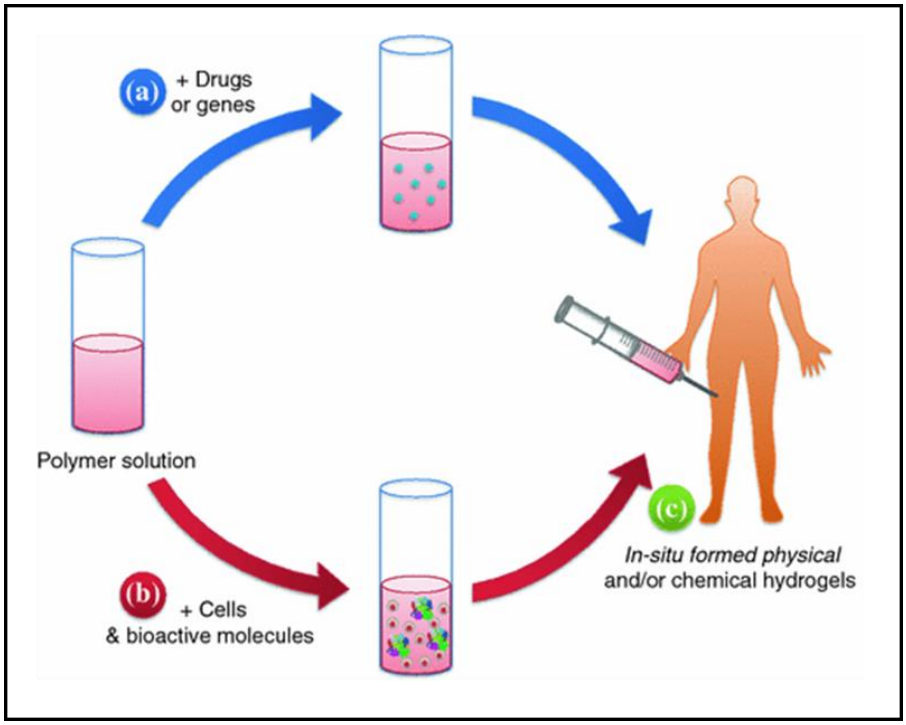

Figure 22. Scheme of subcutaneous drug delivery using injectable hydrogels.

These systems must have low viscosity (free-flowing aqueous solutions) to facilitate subcutaneous injection, fast gelation *in vivo* to minimize initial burst release, long term sustained drug release as well as high biocompatibility and biodegradability.[74]

Most thermosensitive polymers are comprised of block copolymers containing PEG (hydrophilic and biocompatible) and hydrophobic blocks, arranged as ABA or BAB. PCL is a biodegradable hydrophobic block suitable for subcutaneous delivery, and thus early attempts to overcome premature

gelation tried to optimize classic polymers such as PCL-PEG-PCL and pluronic.[73,75]

This way, hydrophobic drugs such as paclitaxel (PTX) were encapsulated inside liposomes and dispersed within a thermosensitive hydrogel, which improved stability and sustainability for the delivery of the hydrophobic drug.[76] Further research showed that diblocks and triblocks of PEG and PCL retained structural integrity during cargo release for extended periods (30 days) when subcutaneously injected into rats, both for bovine serum albumin (BSA)[77] and honokiol (HK), a hydrophobic compound (Figure 23).[78]

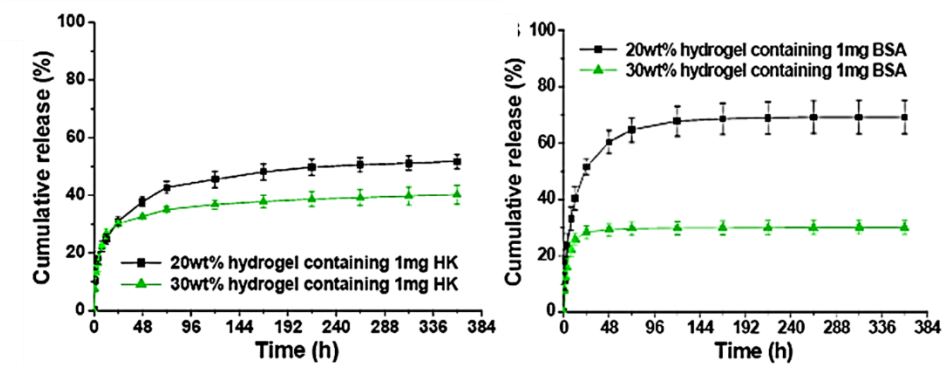

Figure 23. In vitro release behavior of small hydrophobic drug honokiol (HK) (left) and macromolecular protein drug bovine serum albumin (BSA) (right) from PCL-PEG-PCL hydrogels.

PCL-based polymers however, present unwanted low degradation, for which several strategies were employed to chemically increase their degradation rates. This way, modified PCL-PEG-PCL hydrogels were able to release paclitaxel (PTX) for a few months in combination with iodine-131 and doxorubicin (DOX) for chemoradiotherapy treatments, improving antitumor effect and minimizing drug toxicity.[79]

Further examples investigated PLGA-PEG-PLGA triblocks, which was also amongst the first thermosensitive systems used for subcutaneous injection. With this system, spirolactone, a hydrophobic compound, was released over 2 months whereas ketoprofen, more water-soluble, was released within the first 2 weeks by diffusion.[80] Alternatively, the degradation rates of polyester-based thermogelling polymers may be accelerated by substituting PCL blocks with poly (δ-valerolactone) (PVL), which undergo faster ester degradation through

lipases and release low molecular weight by-products that are easily eliminated.[81]

Polypeptide systems have also been investigated since they are suitable depots for delivery of hydrophobic small molecules in the central nervous system to regulate gene expression and other cellular functions. For example, tamoxifen (TM), a hydrophobic anticancer drug, was released from a hydrogel depot injected into forebrain or after spinal cord injury in mice, which altered gene expression.[82]

In addition to synthetic drugs, hydrophobic growth factor antibodies can also be administered subcutaneously using injectable hydrogels that deliver the payload locally. A triblock copolymer of PEG containing a vitamin residue, which increased hydrophobicity, was able to deliver subcutaneously growth factors Herceptin[83] and Avastin[84] *in vivo.*

1.2.2.3. Transdermal drug delivery

The transdermal is a route of administration where active ingredients are delivered across the skin normally through transdermal patches or ointments into the circulation for systemic effect (Figure 24). As an alternative to oral drug delivery, it has proven a painless pathway which may be self-administered and leads to patient higher compliance. In addition, the transdermal route is less demanding for the drug carriers than oral administration, since both the harsh environments of the gastrointestinal (GI) tract and first-pass effect could be circumvented.[85]

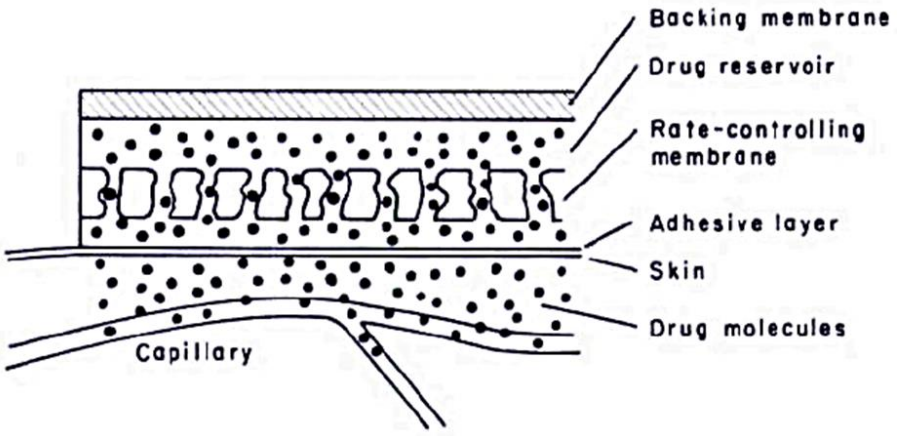

Figure 24. Schematic cross-section of a transdermal therapeutic system.

The main drawback of the transdermal route is that only a few drugs fulfill all the physiochemical requirements to permeate passively through the skin. Since hydrogels absorb the moisture of the skin and resemble the extracellular matrix (ECM) of skin tissues,[86] these could be employed as membranes with loaded hydrophobic drugs in order to improve the percutaneous delivery of poorly water soluble agents to treat skin diseases.

One of the most common skin illness is skin inflammation and acne, which is caused by pH imbalance. Typically, skin pH oscillates between 5-6, whereas skin pH values straying away from this interval may compromise the barrier function of the *stratum corneum*.[87]

To overcome acne growth, a hydrogel made from hyaluronic acid and cellulose was shown to deliver a hydrophobic antimicrobial agent, isoliquiritigenin (ILTG), at specific pH of 7, where bacterial colony formation presents its peak of activity. At this pH, the hydrogel significantly increased swelling and ILTG could be released; due to the hydrogel-assisted swelling of the skin, the antimicrobial could permeate the skin barrier *via* the follicular pathway.[88]

Similar to pH-responsive systems, thermosensitive hydrogels have been also successfully applied for skin treatments. A thermoresponsive hydrogel made from PEG-PCL-PEG was loaded with curcumin, a hydrophobic compound active for wound healing applications, encapsulated into micelles. Once the hydrogel reached skin temperature (32ºC), it transitioned from sol to gel, thus adhering to the wounded skin and released curcumin in a sustained manner (40%) over 14 days.[89]

Other approaches concerning thermo-responsive hydrogels have been carried out for skin sustained release. By using microneedles, affected dermatomed skin was microperforated and a methotrexate-loaded thermoresponsive copolymer based on poloxamer (PEG-PPO-PEG triblock copolymer) was injected through the micropores. Once reached skin temperature, the polymer solution transitioned into gel, achieving the shape of the microneedles and this allowed for the sustained release of the hydrophobic active compound (Figure 25).[90]

Transdermal delivery may not only be limited to outer skin treatment but may be used to bypass the epidermis and dermis to be transported into the blood system through skin, in which case the drug permeation turns to be

crucial. Hydroxypropyl-β-CD is a permeation enhancer for hydrophobic drugs *via* inclusion complex formation; by functionalization of drug-loaded hydroxypropyl-β-CD particles into hydrogels, the percutaneous absorption of various hydrophobic drugs has been increased to successfully treat different diseases *via* transdermal administration, such as in hormone treatments,[91] diabetes[92] or cancer.[93]

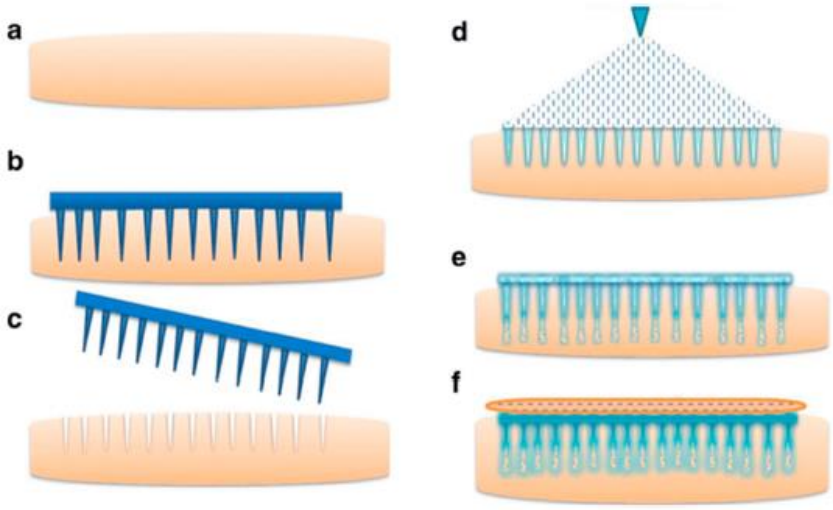

Figure 25. Drug delivery from in situ gelling hydrogel microneedles. a) non-porated skin b) perforated skin with microneedles c) pore formation and removal of microneedles d) application of thermogelling solution e) flow of solution in the sol state through the pores f) gel transition at skin temperature and sustained release of drug.

1.2.2.4. Ocular drug delivery

Topical delivery of drugs by eye-drops comprises 90% of all ophthalmic formulations; this method is very inefficient, since only about 5% of the drug applied as drops penetrates through the cornea to reach intraocular tissue while the rest is lost due to tear drainage, where the drug gets absorbed into the bloodstream and leads to undesired side effects.[94] Furthermore, the application of ophthalmic drugs as drops results in a rapid variation in the drug delivery rates to the cornea, limiting the efficacy of the therapeutic systems.

To overcome these drawbacks, disposable soft contact lenses as new vehicles for ophthalmic drug delivery have been proposed. Herein, the drugs are encapsulated inside nanoparticles and then dispersed in the contact lens

matrix during polymerization. Additionally, the drug-loaded lens will remain transparent if the nanoparticle and drug loadings are sufficiently low.

When the contact lens is placed in the eye, the drug diffuses from the encapsulated nanoparticles out to the polymer matrix and enter the post-lens tear film (POLTF) (Figure 26). The longer residence time of the drug in this film will result in higher flux in the cornea and thus will reduce drug absorption into the bloodstream, minimizing side effects and extending the release.

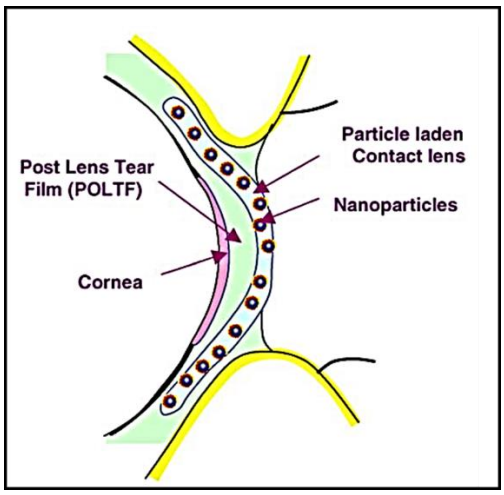

Figure 26. Illustration of the particle-loaded lens inserted in the eye.

Following this methodology, hydrogels based on poly-2-hydroxyethyl methacrylate (p-HEMA) were loaded with lidocaine emulsion and used as contact sustained-release lens, increasing the residence time of the drug up to 8 days.[95]

Ocular hydrophobic drug delivery may also be achieved by grafting CDs to the hydrogels. In this manner, contact lenses based on pHEMA hydrogels with incorporated CD-functionalized crosslinkers were able to deliver diclofenac, a hydrophobic drug, for 25 days in a sustained manner.[96]

1.3. References

[1] J. L. Drury, D. J. Mooney, *Biomaterials* **2003**, *24*, 4337–4351.

[2] J. Li, D. J. Mooney, *Nat. Rev. Mater.* **2016**, *1*, 16071.

[3] T. R. Hoare, D. S. Kohane, *Polymer (Guildf).* **2008**, *49*, 1993–2007.

[4] G. Tiwari, R. Tiwari, S. Bannerjee, L. Bhati, S. Pandey, P. Pandey, B. Sriwastawa, *Int. J. Pharm. Investig.* **2012**, *2*, 2–11.

[5] W. Liu, Æ. M. Griffith, Æ. F. Li, *J. Mater. Sci. Mater. Electron.* **2008**, *19*, 3365–3371.

[6] L. Yu, J. Ding, *Chem. Soc. Rev.* **2008**, *37*, 1473–1481.

[7] F. Alexis, E. Pridgen, L. K. Molnar, O. C. Farokhzad, *Mol. Pharm.* **2008**, *5*, 505–515.

[8] N. A. Peppas, J. J. Sahlin, *Biomaterials* **1996**, *17*, 1553–1561.

[9] E. H. Nafea, A. Marson, P. J. Martens, *J. Control. Release* **2011**, *154*, 110–122.

[10] B. Amsden, *Macromolecules* **1998**, *31*, 8382–8395.

[11] T. Boontheekul, H. Kong, D. J. Mooney, *Biomaterials* **2005**, *26*, 2455–2465.

[12] M. Ishihara, K. Obara, T. Ishizuka, M. Fujita, M. Sato, K. Masuoka, Y. Saito, H. Yura, T. Matsui, H. Hattori, et al., *J. Biomed. Mater. Res. - Part A* **2003**, *64*, 551–559.

[13] A. M. L. S. M. Christopher, *Physiol. Behav.* **2016**, *176*, 100–106.

[14] C. Gong, T. Qi, X. Wei, Y. Qu, Q. Wu, F. Luo, Z. Qian, *Curr. Med. Chem.* **2013**, *20*, 79–94.

[15] N. Huebsch, C. Kearney, X. Zhao, C. Cezar, *Proc. Natl. Acad. Sci.* **2014**, *111*, 9762–9767.

[16] E. A. Silva, D. J. Mooney, *Biomaterials* **2010**, *31*, 1235–1241.

[17] B. E. B. Jensen, I. Dávila, A. N. Zelikin, *J. Phys. Chem. B* **2016**, *120*, 5916–5926.

[18] R. Mateen, T. Hoare, *J. Mater. Chem. B* **2014**, *2*, 5157–5167.

[19] J. J. Pillai, A. K. T. Thulasidasan, R. J. Anto, D. N. Chithralekha, A. Narayanan, G. S. V. Kumar, *J. Nanobiotechnology* **2014**, *12*, 1–9.

[20] S. Garg, A. Garg, R. D. Vishwavidyalaya, *Asian J. Biomater. Res.* **2017**, *2*, 163–170.

[21] W. Xu, P. Ling, T. Zhang, *J. Drug Deliv.* **2013**, *2013*, 1–15.

[22] P. Van Hoogevest, X. Liu, A. Fahr, *Expert Opin. Drug Deliv.* **2011**, *8*, 1481–1500.

[23] M. Tawa, Z. Zhang, P. Ratanabanangkoon, P. Shaw, C. R. Guzma, C. R. Gardner, H. Chen, J. Moreau, *J. Pharm. Sci.* **2007**, *96*, 2686–2702.

[24] S. Gohla, K. Ma, R. H. Mu, *Eur. J. Pharm. Biopharm.* **2000**, *50*, 161–77.

[25] A. Rosler, G. W. M. Vandermeulen, H. Klok, *Adv. Drug Deliv. Rev.* **2001**, *53*, 95–108.

[26] K. Kita-tokarczyk, J. Grumelard, T. Haefele, W. Meier, *Polymer (Guildf).* **2005**, *46*, 3540–3563.

[27] S. Peng, K. Wang, D. Guo, Y. Liu, *Soft Matter* **2015**, *11*, 290–296.

[28] E. G. Bellomo, M. D. Wyrsta, L. Pakstis, D. J. Pochan, T. J. Deming, *Nat. Mater.* **2004**, *3*, 244–248.

[29] F. Wang, T. K. Bronich, A. V. Kabanov, R. D. Rauh, J. Roovers, *Bioconjug. Chem.* **2005**, *16*, 397–405.

[30] J. Liu, H. Duong, M. R. Whittaker, T. P. Davis, C. Boyer, *Macromol. Rapid Commun.* **2012**, *33*, 760–766.

[31] S. Chen, X. Z. Zhang, S. X. Cheng, R. X. Zhuo, Z. W. Gu, *Biomacromolecules* **2008**, *9*, 2578–2585.

[32] K. Knop, G. M. Pavlov, T. Rudolph, K. Martin, D. Pretzel, B. O. Jahn, D. H. Scharf, A. A. Brakhage, H. Schacher, U. S. Schubert, *Soft Matter* **2013**, *9*, 715–726.

[33] K. Nagahama, D. Kawano, N. Oyama, A. Takemoto, T. Kumano, J. Kawakami, *Biomacromolecules* **2015**, *16*, 880–889.

[34] G. W. Ashley, J. Henise, R. Reid, D. V. Santi, *Proc. Natl. Acad. Sci. U. S. A.* **2013**, *110*, 2318–2323.

[35] D. Gu, A. J. O'Connor, G. G.H. Qiao, K. Ladewig, *Expert Opin. Drug Deliv.* **2017**, *14*, 879–895.

[36] X. Zhao, *Soft Matter* **2014**, *10*, 672–687.

[37] G. Beaune, C. Ménager, *J. Colloid Interface Sci.* **2010**, *343*, 396–399.

[38] M. K. Nguyen, D. S. Lee, *Macromol. Biosci.* **2010**, *10*, 563–579.

[39] G. Dumortier, J. L. Grossiord, F. Agnely, J. C. Chaumeil, *Pharm. Res.* **2006**, *23*, 2709–2728.

[40] H. Asadi, K. Rostamizadeh, D. Salari, M. Hamidi, *Int. J. Pharm.* **2011**,

416, 356–364.

[41] W. C. Lee, Y. C. Li, I. M. Chu, *Macromol. Biosci.* 2006, *6*, 846–854.

[42] M. Qiao, D. Chen, X. Ma, Y. Liu, *Int. J. Pharm.* 2005, *294*, 103–112.

[43] W. S. Shim, J. S. Yoo, Y. H. Bae, D. S. Lee, *Biomacromolecules* 2005, *6*, 2930–2934.

[44] M. Rinaudo, R. Auzely, C. Vallin, I. Mullagaliev, *Biomacromolecules* 2005, *6*, 2396–2407.

[45] I. Finelli, E. Chiessi, L. Oddo, D. Galesso, D. Renier, G. Paradossi, *Macromol. Chem. Phys.* 2014, *215*, 140–147.

[46] Y. Osada, A. Matsuda, *Nature* 1995, *376*, 219–220.

[47] C. G. Wiener, R. A. Weiss, B. D. Vogt, *Soft Matter* 2014, *10*, 6705–6712.

[48] M. Rikkou-Kalourkoti, E. N. Kitiri, C. S. Patrickios, E. Leontidis, M. Constantinou, G. Constantinides, X. Zhang, C. M. Papadakis, *Macromolecules* 2016, *49*, 1731–1742.

[49] D. E. Liu, T. J. Dursch, Y. Oh, D. T. Bregante, S. Y. Chan, C. J. Radke, *Acta Biomater.* 2015, *18*, 112–117.

[50] E. M. Saffer, M. A. Lackey, D. M. Griffin, S. Kishore, G. N. Tew, S. R. Bhatia, *Soft Matter* 2014, *10*, 1905–1916.

[51] J. Cui, M. A. Lackey, G. N. Tew, A. J. Crosby, *Macromolecules* 2012, *45*, 6104–6110.

[52] J. Cui, M. A. Lackey, A. E. Madkour, E. M. Saffer, D. M. Griffin, S. R. Bhatia, A. J. Crosby, G. N. Tew, *Biomacromolecules* 2012, *13*, 584–588.

[53] B. Ozcelik, A. Blencowe, J. Palmer, K. Ladewig, G. W. Stevens, K. M. Abberton, W. A. Morrison, G. G. Qiao, *Acta Biomater.* 2014, *10*, 2769–2780.

[54] B. Rossi, V. Venuti, F. D'Amico, A. Gessini, F. Castiglione, A. Mele, C. Punta, L. Melone, V. Crupi, D. Majolino, et al., *Phys. Chem. Chem. Phys.* 2015, *17*, 963–971.

[55] J. Yang, F. K. Shi, C. Gong, X. M. Xie, *J. Colloid Interface Sci.* 2012, *381*, 107–115.

[56] E. A. Appel, M. W. Tibbitt, M. J. Webber, B. A. Mattix, O. Veiseh, R. Langer, *Nat. Commun.* 2015, *6*, 1–8.

[57] S. Salmaso, A. Semenzato, S. Bersani, P. Matricardi, F. Rossi, P. Caliceti, *Int. J. Pharm.* 2007, *345*, 42–50.

[58] R. MacHín, J. R. Isasi, I. Vélaz, *Carbohydr. Polym.* 2012, *87*, 2024–2030.

[59] M. Jug, F. Maestrelli, M. Bragagni, P. Mura, *J. Pharm. Biomed. Anal.* 2010, *52*, 9–18.

[60] Y. Guan, L. Qian, H. Xiao, *Macromol. Rapid Commun.* 2007, *28*, 2244–2248.

[61] I. Shown, W. Baek-Ko, C. N. Murthy, *Polym. Bull.* 2012, *69*, 1–13.

[62] E. S. Gil, L. Wu, L. Xu, T. L. Lowe, *Biomacromolecules* 2012, *13*, 3533–3541.

[63] González-Gaitano;G, J. Isasi, I. Velaz, A. Zornoza, *Curr. Pharm. Des.* 2016, *23*, 411–432.

[64] E. Khafagy, M. Morishita, Y. Onuki, K. Takayama, *Adv. Drug Deliv. Rev.* 2007, *59*, 1521–1546.

[65] J. Blanchette, N. Kavimandan, N. A. Peppas, *Biomed. Pharmacother.* 2004, *58*, 142–151.

[66] A. K. Dash, G. C. C. II, *J. Pharmacol. Toxicol. Methods* 1998, *12*, 1–12.

[67] B. Kim, K. La Flamme, N. A. Peppas, *J. Appl. Polym. Sci.* 2003, *89*, 1606–1613.

[68] L. Bromberg, *Expert Opin. Drug Deliv.* 2005, *2*, 1003–1013.

[69] C. A. Schoener, H. N. Hutson, G. K. Fletcher, N. A. Peppas, *Ind. Eng. Chem. Res.* 2011, *50*, 12556–12561.

[70] M. Caldorera-Moore, K. Maass, R. Hegab, G. Fletcher, N. Peppas, *J. Drug Deliv. Sci. Technol.* 2015, *30*, 352–359.

[71] X. Gao, C. He, C. Xiao, X. Zhuang, X. Chen, *Polymer (Guildf).* 2013, *54*, 1786–1793.

[72] C. A. Schoener, H. N. Hutson, N. A. Peppas, *J. Biomed. Mater. Res. - Part A* 2012, *101A*, 2229–2236.

[73] Z. Lin, W. Gao, H. Hu, K. Ma, B. He, W. Dai, X. Wang, J. Wang, X. Zhang, Q. Zhang, *J. Control. Release* 2014, *174*, 161–170.

[74] N. K. Singh, D. S. Lee, *J. Control. Release* 2014, *193*, 214–227.

[75] D. Cohn, A. Sosnik, R. Malal, R. Zarka, S. Garty, A. Levy, *Polym. Adv. Technol.* 2007, *18*, 731–736.

[76] S. Nie, W. L. W. Hsiao, *Int. J. Nanomedicine* 2011, *6*, 151–166.

[77] H. Hyun, Y. H. Kim, I. B. Song, J. W. Lee, M. S. Kim, G. Khang, K. Park, H. B. Lee, *Biomacromolecules* 2007, *8*, 1093–1100.

[78] C. Gong, S. Shi, L. Wu, M. Gou, Q. Yin, Q. Guo, *Acta Biomater.* 2009,

5, 3358–3370.

[79] P. Huang, Y. Zhang, W. Wang, J. Zhou, Y. Sun, J. Liu, D. Kong, J. Liu, A. Dong, *J. Control. Release* **2015**, *220*, 456–464.

[80] B. Jeong, Y. H. Bae, S. W. Kim, *J. Control. Release* **2000**, *63*, 155–163.

[81] H. Lee, F. Zeng, M. Dunne, C. Allen, *Biomacromolecules* **2005**, *6*, 3119–3128.

[82] S. Zhang, M. A. Anderson, Y. Ao, B. S. Khakh, J. Fan, T. J. Deming, M. V Sofroniew, *Biomaterials* **2014**, *35*, 1989–2000.

[83] A. L. Z. Lee, V. W. L. Ng, S. Gao, J. L. Hedrick, Y. Y. Yang, *Adv. Funct. Mater.* **2014**, *24*, 1538–1550.

[84] A. L. Z. Lee, V. W. L. Ng, S. Gao, J. L. Hedrick, Y. Y. Yang, *Biomacromolecules* **2015**, *16*, 465–475.

[85] O. Pillai, R. Panchagnula, *J. Control. Release* **2003**, *89*, 127–140.

[86] H. V. A. N. Doorne, *Br. J. Dermatol.* **1985**, *112*, 461–467.

[87] S. M. Ali, G. Yosipovitch, *Acta Derm. Venereol.* **2013**, *93*, 261–267.

[88] S. S. Kwon, B. J. Kong, S. N. Park, *Eur. J. Pharm. Biopharm.* **2015**, *92*, 146–154.

[89] C. Gong, Q. Wu, Y. Wang, D. Zhang, F. Luo, X. Zhao, Y. Wei, Z. Qian, *Biomaterials* **2013**, *34*, 6377–6387.

[90] A. Sivaraman, A. K. Banga, *Drug Deliv. Transl. Res.* **2017**, 16–26.

[91] A. Concheiro, *Eur. J. Pharm. Biopharm.* **2007**, *66*, 55–62.

[92] S. Ata, U. Rahman, N. Sharma, M. Sciences, *Int. J. Innov. Sci. Technol.* **2018**, *3*, 13–25.

[93] Y. Sun, L. Du, Y. Liu, X. Li, M. Li, Y. Jin, *Int. J. Pharm.* **2014**, *469*, 31–39.

[94] J. C. Lang, F. Worth, *Adv. Drug Deliv. Rev.* **1995**, *16*, 39–43.

[95] D. Gulsen, A. Chauhan, *Int. J. Pharm.* **2005**, *292*, 95–117.

[96] J. Rosa, C. Álvarez-Lorenzo, M. Silva, L. Balsa, J. Couceiro, J. Torres-Labandeira, A. Concheiro, *Biomaterials* **2009**, *30*, 1348–1355.

Chapter 2

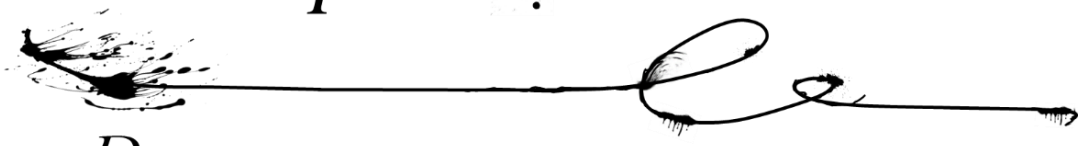

Diaminotriazines:

Novel Building Blocks

for Hydrophobic Hydrogels

2.1. Introduction

2.1.1. The triazine ring

The 1,3,5- or s-triazine unit and derivatives have been dubbed as very versatile units, both from a synthetic and supramolecular points of view.[1,2] As 6-member ring heterocycles consisting of C and N alternated atoms, the symmetric nature of this molecules allows them to form a wide variety of different host-guest interactions,[3] which involve either its nitrogen lone-pairs (coordination and H-bonds), its heteroaromatic π-electrons (π-π stacking and cationic-π interactions) or its σ backbone (anionic-σ and electron-rich-σ interactions) (Figure 1).

These interactions play a pertinent role in the formation of aggregates[4] and intricate H-bonding networks,[5] which have proven their great potential in the field of material chemistry, among others.

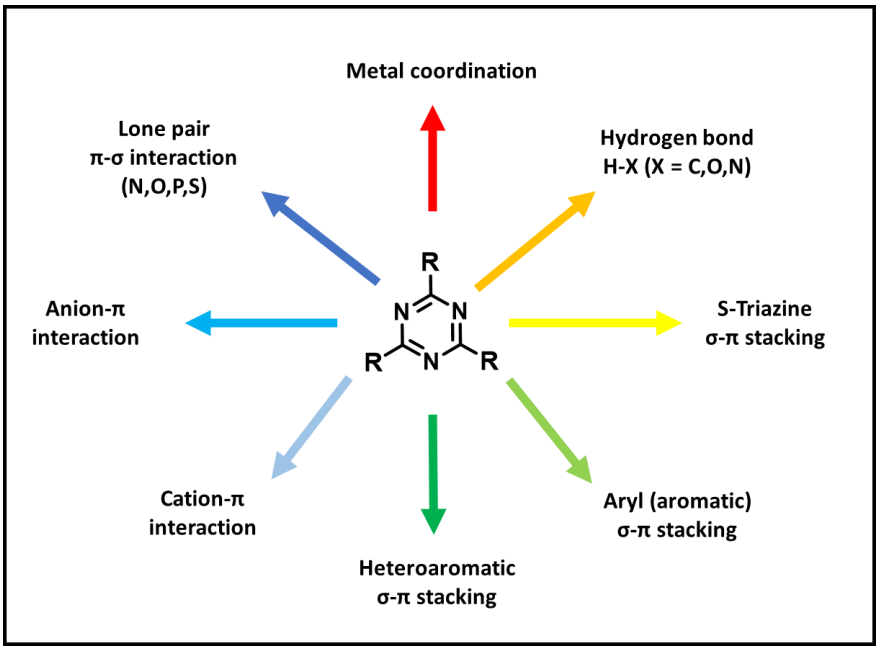

Figure 1. Intramolecular interactions of the 1,3,5-triazine ring.

The non-covalent versatility of the s-triazine ring is mainly due to its three nitrogen atoms. These lone pairs are expected to be capable of forming H bonds, and many examples have been reported where the triazine nitrogen atoms function as H bond acceptors.[6]

Further, as an heteroaromatic ligand with delocalized electronic structure and electron deficient character, the 1,3,5-triazine ring is expected to act both as a σ-donor and a π-acceptor.[7] Figure 2 shows the comparative interacting sites and polarizations between the triazine and benzene rings. It can be observed that the electron density is localized on the N atoms, whereas the C atoms are deficient in electronic charge.

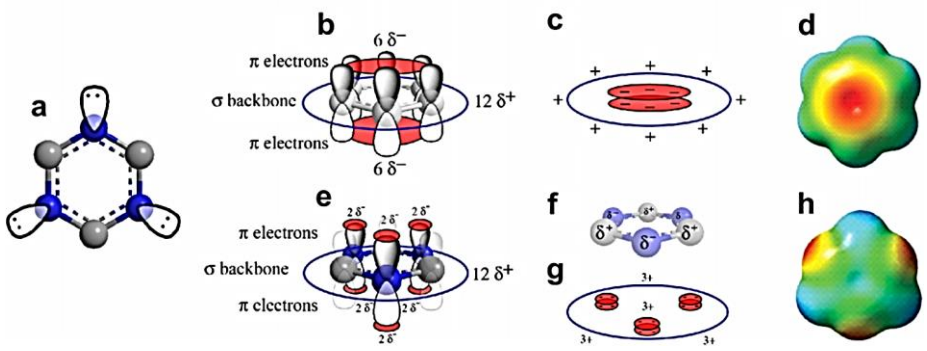

Figure 2. a) *s*-triazine ring. Schematic representations of the interacting sites, polarizations, and electrostatic potential surfaces of benzene (b, c, and d, respectively) and of s-triazine (e, f, g, and h, respectively).

Consequently, the multifunctionality of 1,3,5-triazine-containing compounds have allowed outstanding new developments in the area of tailored functional materials, as well as other fields such as medicinal chemistry, herbicides, catalysis or polymer chemistry.[2,8–11] In the following subsections, several kind of interactions are emphasized where the triazine ring plays an important role from a chemical point of view.[12]

- Hydrogen bonding

Due to its electron-sink capacity, the s-triazine ring acts as electron-withdrawing group on the terminal amines on aminotriazines. Thus, *s*-triazine nitrogen atoms appear electron richer whereas amino terminal groups display higher electron deficiency, and this allows the aminotriazine moiety to behave as a hydrogen bond Donor-Acceptor unit (Figure 3).

The hydrogen bonding aptitudes of these unique structures have since sparked the interest of the scientific community in the area of complex hydrogen-bonded supramolecules.[6]

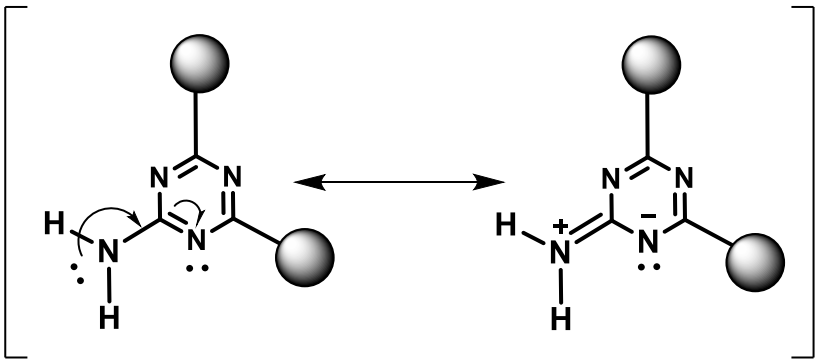

Figure 3. Electronic resonance in aminotriazine moieties.

Thus, melamine (2,4,6-triamino-1,3,5-triazine) can be regarded as a three Donor-Acceptor-Donor unit, which has been ingeniously used with Acceptor-Donor-Acceptor counterparts to generate "rosette-type" materials.[13] (Figure 4)

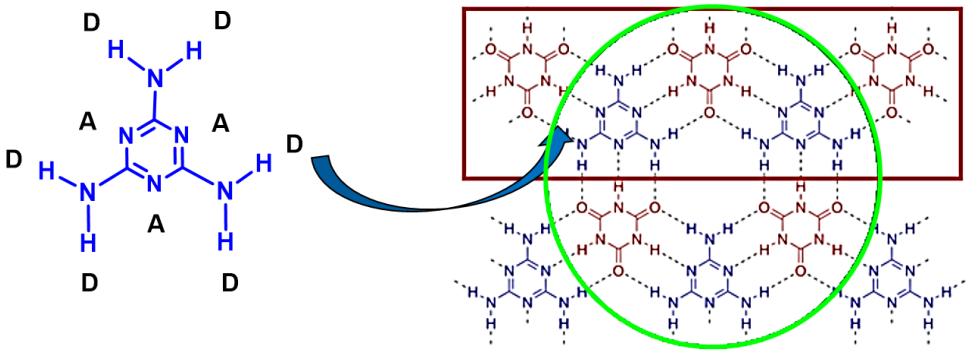

Figure 4. Melamine H bonding properties (left) and melamine-cyanuric acid rosettes (right, green) and linear ribbons (right, red).

Further research with melamine derivatives[14] have also taken the advantage of their outstanding abilities to form H-bonded architectures to generate helical supramolecular organizations. Accordingly, a 2,4-diamino-1,3,5-triazine derivative assembled with 3 units of benzoic acid moieties giving rise to propeller-like H-bonded supramolecules (Figure 5).

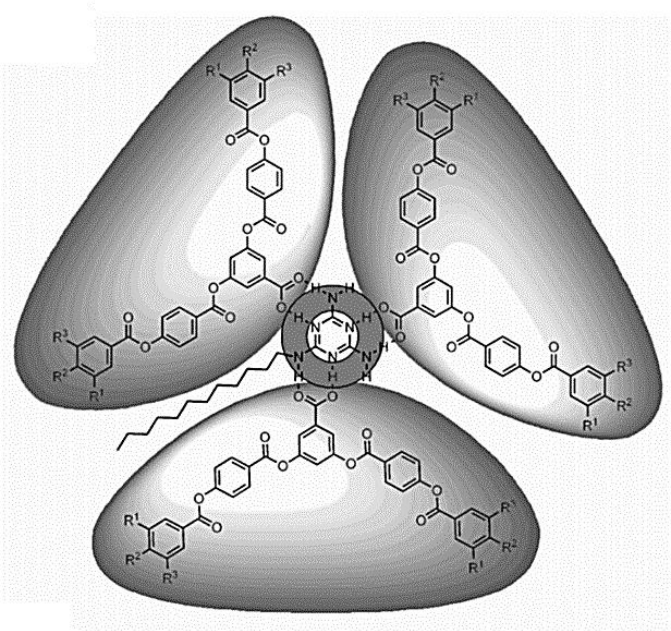

Figure 5. Representation of melamine tetrameric H-bonding complex.

- **π-π Stackings**

The π-π stacking between aromatic moieties is more stable when both partners are electron-poor, whereas electron donating substituents disfavor this interaction. The π-electron repulsion increases with the π-electron density within the aromatic rings.[15,16] Consequently, the order of stability related to the type of supramolecular contacts between two π-systems appears to be the following:[17]

π-deficient–π-deficient > π-deficient-π-rich > π-rich-π-rich.

N-containing heteroaromatic 6-member rings such as s-triazine are known to be electron-poor, and this electron-deficiency can be further increased upon coordination to a metal ion or when the aromatic molecules hold electron withdrawing substituents.

For these reasons, s-triazines represent excellent host or guest candidate molecules to generate stable aromatic stacking complexes. In this sense, Fujita and co-workers[18] reported a remarkable coordination network based on π-π interactions between aromatic rings and s-triazine units, generating pillars in the overall structure (Figure 6).

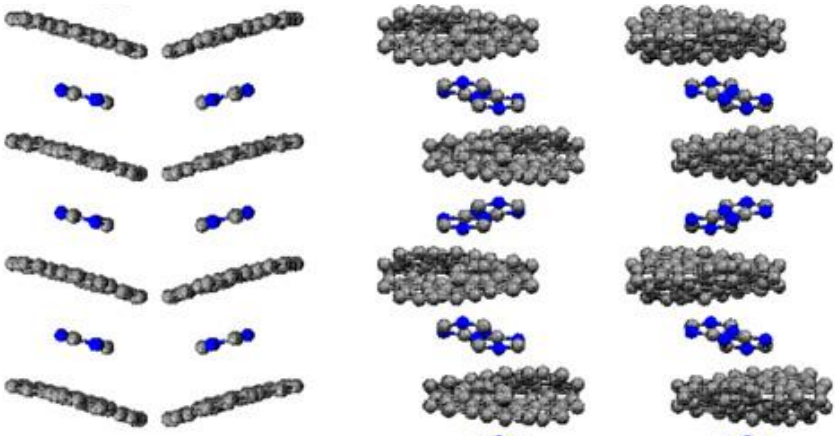

Figure 6. π-π stacked pillars of the overall structure between aromatic moieties and s-triazine rings. N are in blue and C are in grey.

- Coordination to a metal

The s-triazine N donor atoms have also been used to generate a number of coordination compounds. Electron donating substituents the s-triazine ring will increase the electron density on the ring N atoms, which will enhance their interaction with cations, whereas electron withdrawing substituents will conversely enhance the anion binding abilities of the ring N atoms.

An example of s-triazine-cation complexation was given by Rheingold and co-workers.[19] They described a self-assembled hexanuclear copper complex constituted of two Cu_3(s-triazine) units which are bridged by means of six chloride anions (Figure 7). The complex also showed that the s-triazine rings are perfectly stacked, the nitrogen atoms of one ring facing the carbon atoms of the other one.

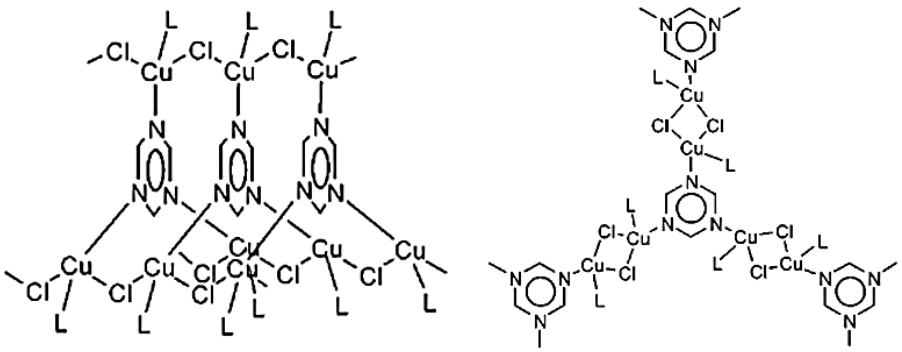

Figure 7. Molecular structure of s-triazine-copper complex.

2.1.1.1. Diaminotriazines

Among 1,3,5-triazine rings, amino-substituted-1,3,5-triazines stand out due to their ability to stablish strong intermolecular interactions, which give rise to complex supramolecular structures. A representative example are 4,6-diamino-1,3,5-triazines, commonly known as diaminotriazines (DATs), which are known to self-associate in solution, solid state and on surfaces *via* characteristic hydrogen bonding motifs, mainly by forming hydrogen-bonded dimers or higher-order aggregates.[20,21] (Figure 8).

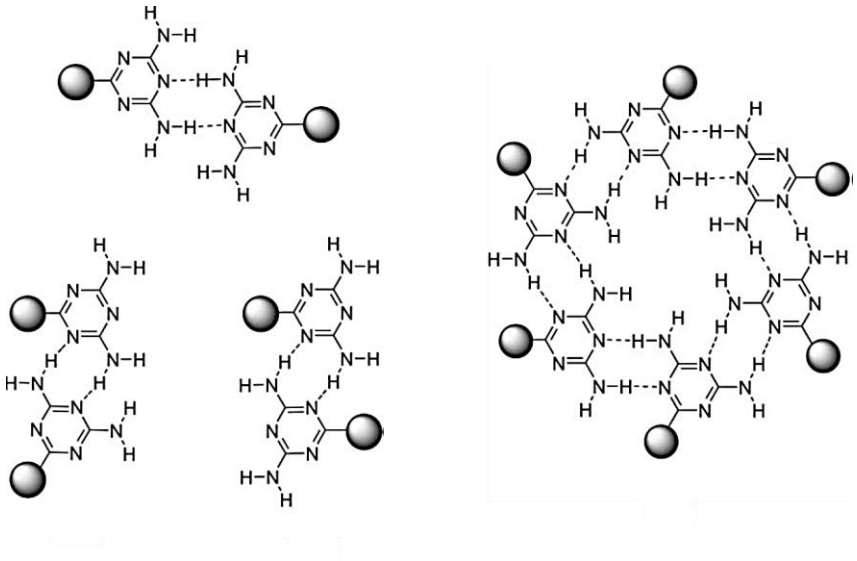

Figure 8. Self-assembled diaminotriazine (DAT) motifs: hydrogen-bonded dimers (left) and hydrogen-bonded hexameric rosettes (right).

The versatility of these associations is neatly represented in the work of Maly *et al*.[12] where 4,6-diamino-1,3,5-triazines were observed to self-associate in solution into disc-like hydrogen-bonded rosettes and columnar mesophases by stacking of an extended aromatic core (Figure 9).

In the proposed model, the diaminotriazine molecules associate by hydrogen bonding to form disc-like aggregates, which then stack in columns, each column constructed from six molecules per unit cell. It was found that the presence of additional phenyl rings appeared to be necessary for the formation of columnar mesophases, since the extended aromatic cores promote better π-stacking, which led to these columnar structures.

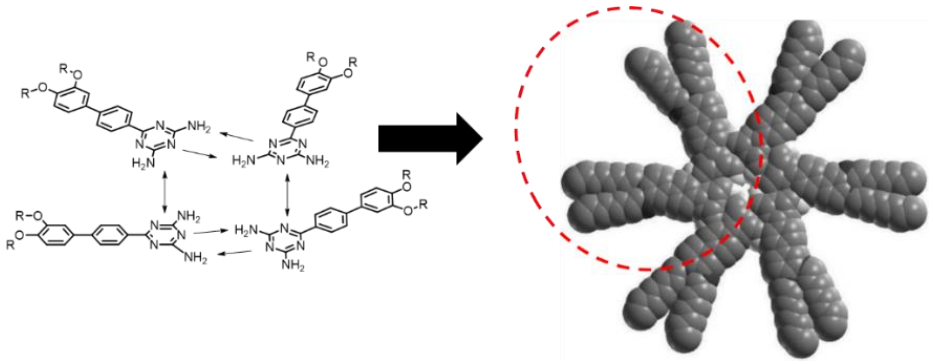

Figure 9. Proposed hydrogen-bonded hexameric rosette derived from biphenyl diaminotriazine derivatives.

In another example carried out in our group,[22] DAT units substituted in the 6-position were observed to arrange into secondary structures consisting of ribbons in which the molecules were connected through double N-H→N hydrogen bonds that resulted in a 3D network (Figure 10). Interestingly, the ribbon-like disposition between alternate DAT units was observed to prevail.

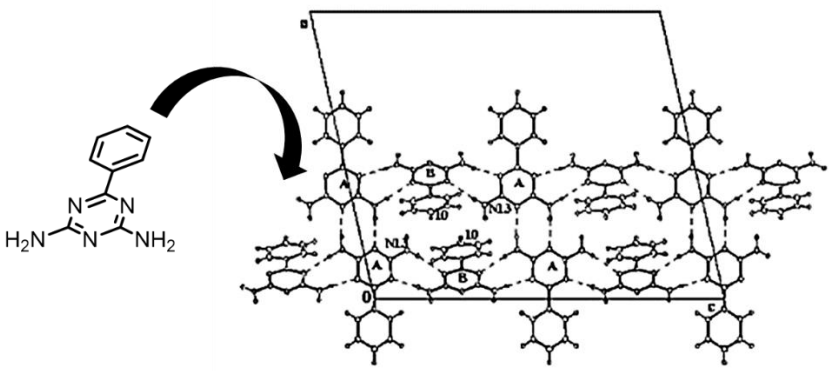

Figure 10. Fragment of hydrogen-bonded ribbons of 6-phenyl-2,4-diamino-1,3,5-triazine A and B projected along a plane.

2.1.1.2. Synthesis of diaminotriazines

In this section the most straightforward synthetic methodologies for the synthesis of DATs are shown.

a) Cycloaddition of 1-cyanoguanidines

One of the most versatile synthetic methods for obtention of DATs (**II**) is the cyclisation with nitriles and cyanoguanidines, which is favored under alkaline

conditions and allows easy obtention of symmetrical and unsymmetrical DATs (Scheme 1).

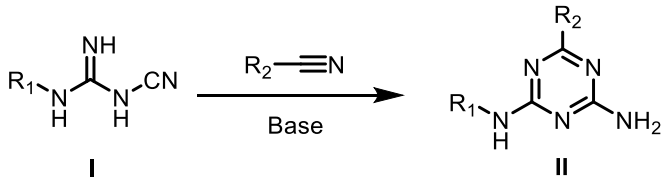

I II

Scheme 1. Synthesis of 2,4-diamino-1,3,5-triazines from 1-alkyl-3-cyanoguanidines.

Under basic catalysis, cyanoguanidine **I** is deprotonated and thus attack towards the nitrile *via* its imino group is favored. The resulting adduct **III** cycles upon nucleophilic attack to the remaining nitrile group of the cyaniguanidine, followed by restoration of aromaticity (Scheme 2).

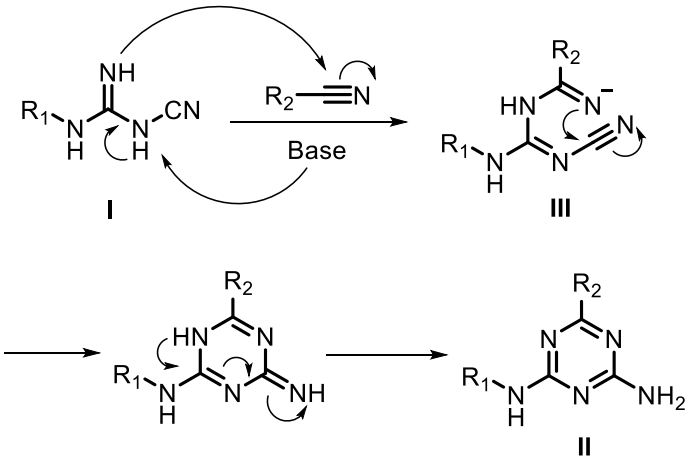

I III II

Scheme 2. Reaction mechanism of formation of 2,4-diamino-1,3,5-triazines from 1-alkyl-3-cyanoguanidines.

Our research group has carried out this methodology for synthesis of DATs substituted in the 6-position, both by conventional and microwave heating.[22,23] The reaction is carried out in polar solvents, giving high yields (≥ 70%). Maly *et al*[12] followed a similar methodology to afford biphenyldiaminotriazines with good yields (≥60%) under classical heating in order to incorporate additional phenyl spacers (Scheme 3).

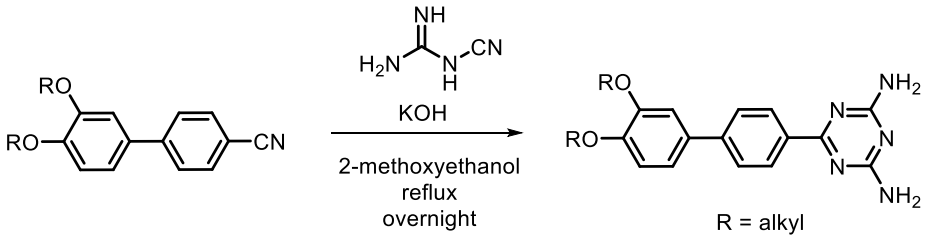

Scheme 3. Synthesis of biphenyldiaminotriazine derivatives starting from cyanoguanidine.

The substituents in the terminal amines may be easily tailored, allowing a wide variety of unsymmetrical DATs to be obtained with this methodology. Since many nitriles are commercially available, these substituents may be incorporated by choosing the suitable reactant.

On the other hand, precursor cyanoguanidines may also be synthesized by reaction with sodium dicyanamide **IV** and commercially available amines, a process patented by Cummings and Cohen.[24] Upon protonation of **IV**, nucleophilic attack of the amine affords the corresponding cyanoguanidine in a one-step easy procedure (Scheme 4).

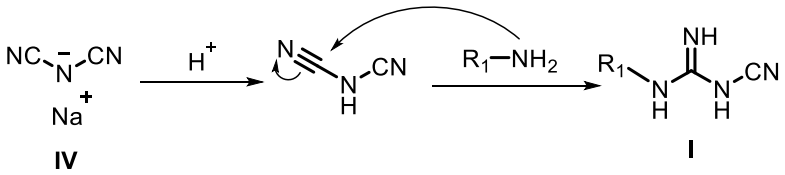

Scheme 4. Reaction mechanism for formation of 1-alkyl-3-cyanoguanidine **I**

b) Cycloaddition of biguanides

An alternative methodology for the synthesis of **II** consists in cyclisation between biguanide **V** and an acid derivative (acyl chlorides, esters, nitriles), catalyzed in basic medium (Scheme 5).

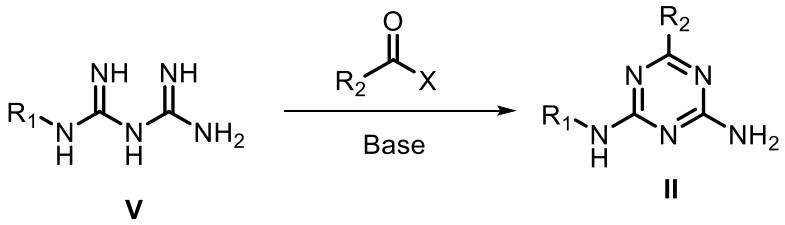

Scheme 5. Synthesis of 2,4-diamino-1,3,5-triazines from 1-alkyl-biguanide **V**

When deprotonated by an appropriate base, V performs double condensation to the acid derivative to afford the DAT after cyclisation (Scheme 6).

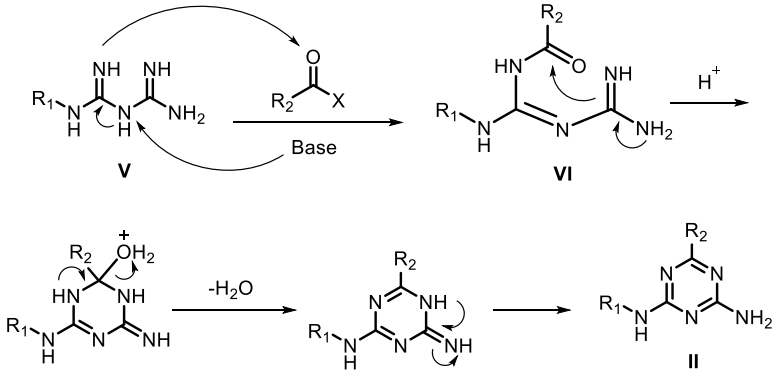

Scheme 6. Reaction mechanism of formation of 2,4-diamino-1,3,5-triazines from1-alkyl-biguanides

Since the biguanide intermediate VI resulting from the first condensation needs to adopt an unstable conformation for a second nucleophilic attack by the imino group, other side-products may be formed, such as polyacylated biguanides. For this reason, DAT synthesis starting from biguanides often requires harsher conditions than from cyanoguanidines.

The biguanide pathway was used by Brzozowski *et al*[25] to fabricate 2-amino-4-pyrazolidinyl-1,3,5-triazines with antitumoral activity from the corresponding pyrazolidinyl biguanide starting material and different esters (Scheme 7a).

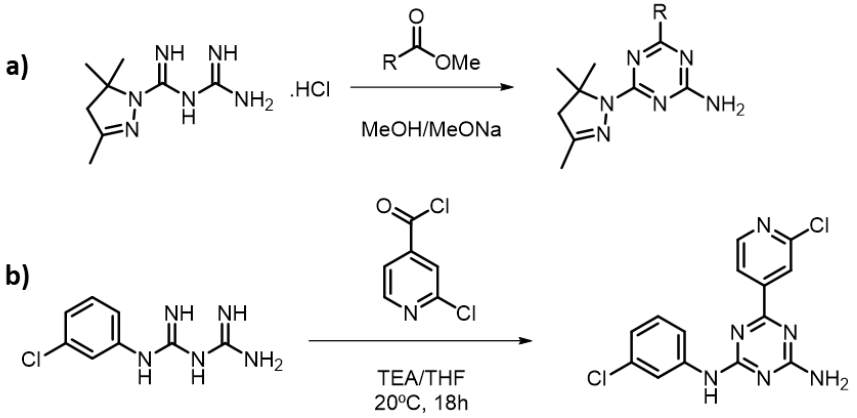

Scheme 7. Biguanide pathway a) synthesis of pyrazolidinyl DATs and b) synthesis of pyridine DAT derivatives

Kuo and coworkers[26] successfully synthesized pyridine DAT derivatives as potent Cyclin-Dependent Kinase (CDK) Inhibitors (Scheme 7b).

Similarly, biguanides may be synthesized from the corresponding cyanoguanidine starting materials and primary amines without further need of catalysis (Scheme 8).

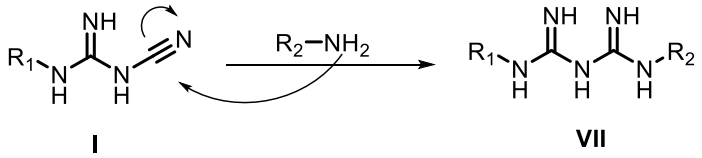

I VII

Scheme 8. Synthesis of 1,5-dialkyl-biguanide VII from 1-alkyl-3-cyanoguanidine

c) Nucleophilic aromatic substitution (S_NAr) to cyanuric chloride

Perhaps one of the most versatile methods for DAT synthesis is nucleophilic aromatic substitution of all kinds of nucleophiles, namely amines, alcohols, thiols, or Grignard reagents to cyanuric chloride.[3,6] This 1,3,5-triazine derivative is a strong electrophile that allows consecutive nucleophilic additions to each chloride atom in order to obtain the mono- di- or trisubstituted products upon regulation of reaction conditions (Scheme 9).

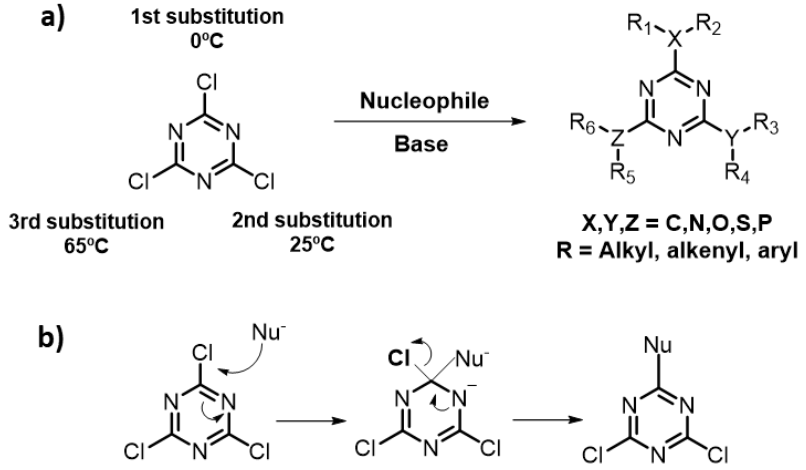

Scheme 9. a) Synthesis of polyfunctional 1,3,5-triazines from cyanuric chloride and b) reaction mechanism

This way, the first substitution takes place at 0ºC without heating, whereas following substitutions take place at around 25ºC and 65ºC, respectively, while usually excess base catalyst is needed. Therefore, by carefully controlling the temperature, 2,4,6- trisubstituted triazines may be sequentially synthesized.

For example, Cooke and coworkers[27] described a method for obtention of DATs from cyanuric chloride *via* Suzuki coupling in the presence of Pd catalyst and a boronic acid derivative (Scheme 10a). In another example, Arya and Dandia[28] prepared trisubstituted 1,3,5-triazines for cytotoxic studies by MW-assisted synthesis between cyanuric chloride and different nucleophiles in the presence of a Zeolite catalyst (Scheme 10b).

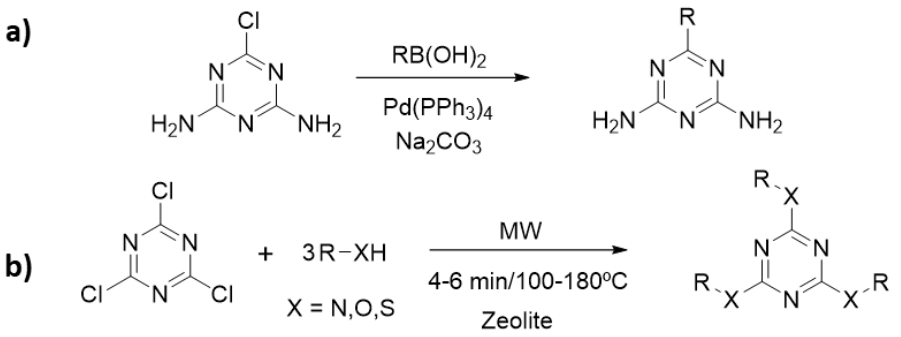

Scheme 10. a) Suzuki coupling for the obtention of 6-alkyl-2,4-diaminotriazines and b) S_NAr for obtention of trisubstituted triazines

Our group has also synthesized triazines 1,3,5-trisubstituted using this pathway under environmentally friendly conditions, using MW radiation as energy source and this way obtaining high yields and short reaction times. (Scheme 11).[29,30]

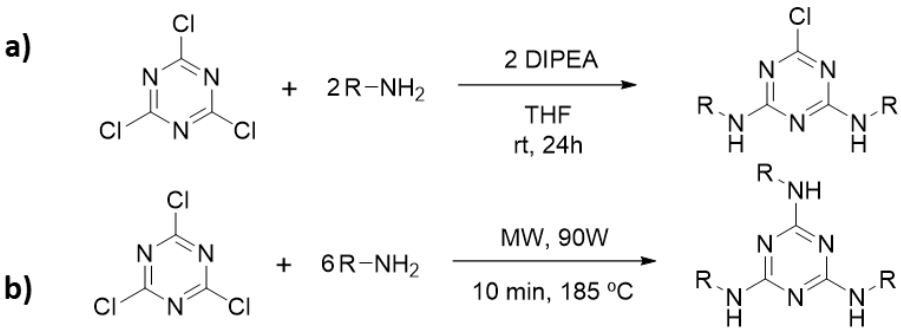

Scheme 11. S_NAr for obtention of a) 6-alkyl-2,4-diaminotriazines and b) trisubstituted triazines from cyanuric chloride

2.1.2. Diaminotriazine hydrogels

Despite the vast potential of this heterocycle, there are very few reported examples of hydrogels based on the diaminotriazine (DAT) core in literature. The reported hydrogels are constructed from the monomer 6-vinyl-2,4-diamino-1,3,5-triazine (VDAT) (Figure 11), which is commercially available, and they are commented below.

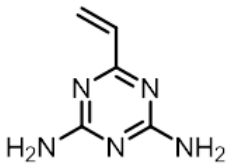

Figure 11. 6-vinyl-2,4-diamino-1,3,5-triazine (VDAT) monomer.

Zhang *et al.*[31] carried out the simplest attempts to fabricate DAT-based hydrogels *via* radical copolymerization between VDAT and polyethylene glycol diacrylate (PEGDA) (Figure 12a).

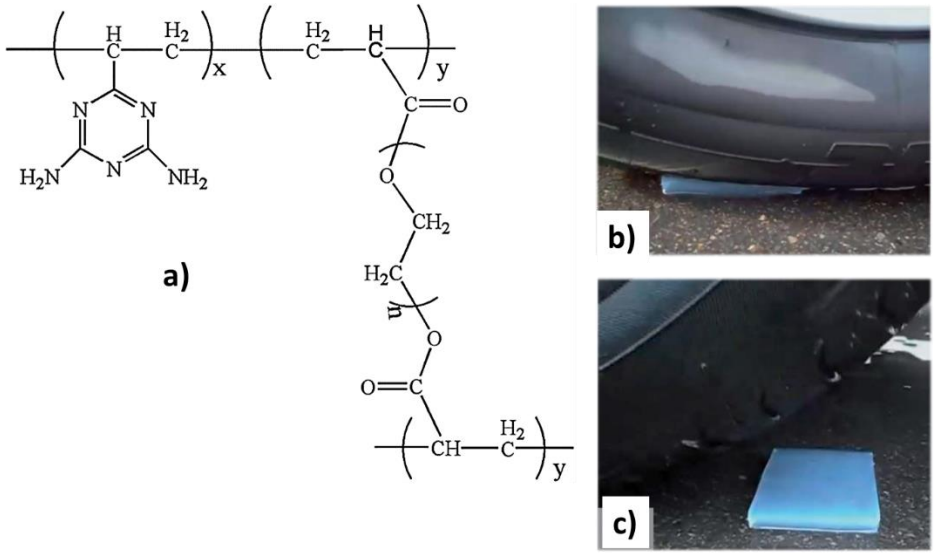

Figure 12. a) Schematic structure of poly(PEGDA-co-VDAT) hydrogels b) Hydrogel film compressed by a car c) and recovered after the car drove past.

These poly(PEGDA-co-VDAT) hydrogels showed enhanced mechanical properties, such as excellent elasticity and fatigue resistance, and were even able to recover their original shapes immediately after being ran over by a car

(Figure 12b-c). By appropriately combining VDAT with other monomers, DAT-based hydrogels in the absence of chemical crosslinking were also fabricated.

For example, *N*-acryloylglycinamide (NAGA) was copolymerized with VDAT (Figure 13a) in order to fabricate a hydrogel solely crosslinked by physical interactions, this is, a physically-crosslinked hydrogel ruled by the presence of multiple hydrogen bonding from both monomers.[32] Since the DAT moiety protonates at low pH (pKa VDAT = 5.15)[33], the poly(NAGA-co-VDAT) hydrogel exhibited pH response. In addition, they presented high mechanical performance, in fact, they could bend and twist as observed in Figure 13b-c.

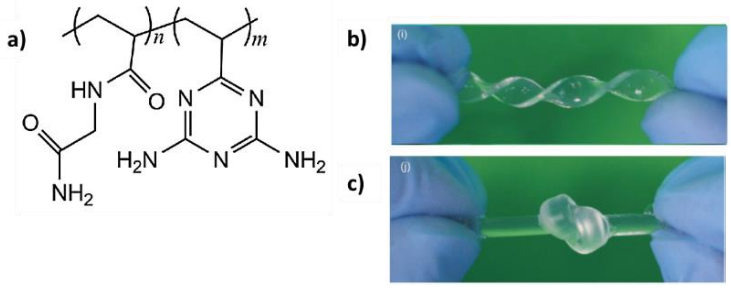

Figure 13. Schematic structure of p(NAGA-co-VDAT) hydrogel b) twisting and c) knotting of hydrogel samples.

Further, Xu *et al.*[34] fabricated DAT-based hydrogels with interesting CO_2-triggered shape memory behavior. The hydrogels presented mechanical properties that were tunable by bubbling CO_2 in aqueous media: by passing and degassing CO_2, a swelling/deswelling response of the hydrogel was induced and this allowed the material to present shape memory behavior (Figure 14).

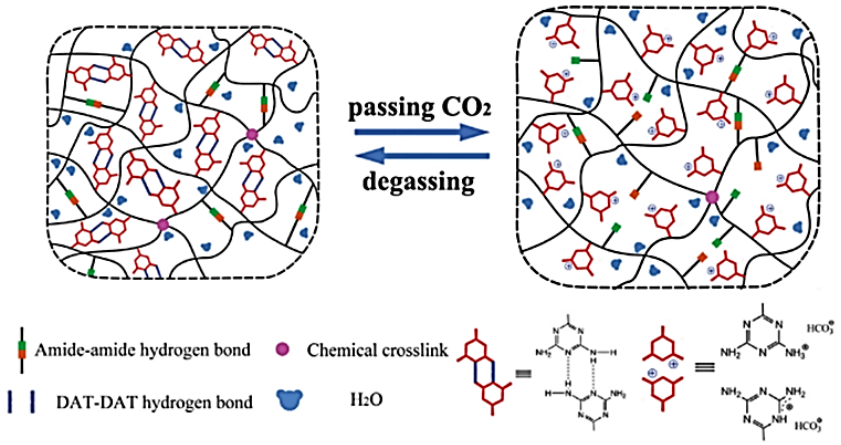

Figure 14. CO_2-triggered shape memory mechanism of DAT-based hydrogels.

The DAT-based were also harnessed for biosensing applications. For example, Liu and co-workers built a thymidine-responsive DAT-based hydrogel for controlled delivery of fluorescein isothiocyanate-bovine serum albumin (FITC-BSA).[35] The interaction between DAT and thymidine was shown to increase the swelling ratio of the hydrogels: within nucleic acid content increase, DAT and thymidine formed complementary H-bonds at the expense of breaking DAT–DAT physical crosslinks, loosening the network and increasing the swelling capacity of the hydrogel (Figure 15).

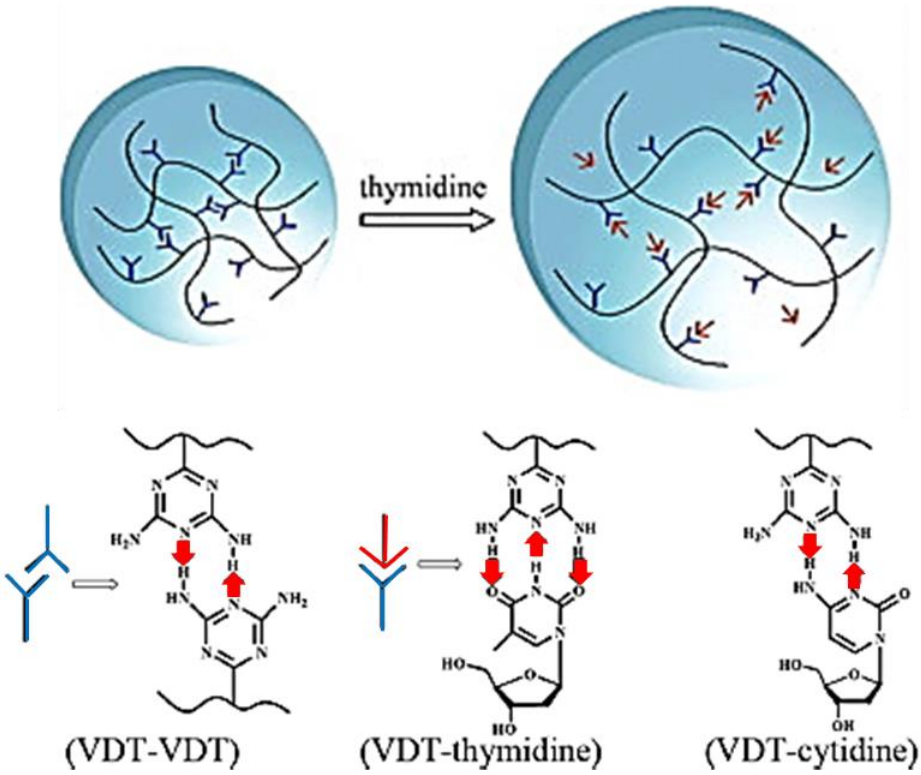

Figure 15. Schematic depiction of thymidine-responsive swelling mechanism of the DAT-based hydrogels. H-bonds are represented in red.

The hydrogel was observed to selectively release bovine serum albumin (BSA) in response to addition of thymidine, and not with cytidine. This result was owed to the sensoring abilities of the DATs: DAT-thymidine complexes form three H-bonds, and this occurs at the expense of breaking the DAT-DAT H-bond network, which now becomes looser and facilitates BSA permeation.

The VDT-cytidine interaction formed only two H-bonds, which is unable to break stronger DAT-DAT interactions. As a result, BSA was not released with cytidine (Figure 16).

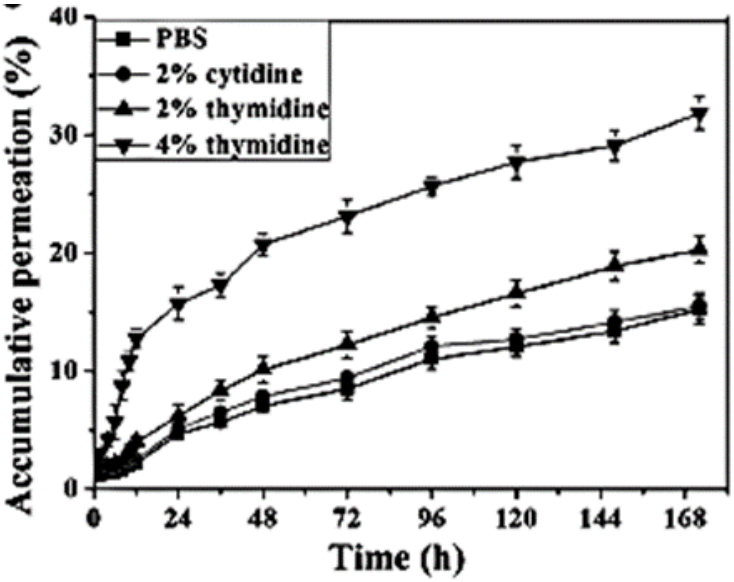

Figure 16. BSA diffusion release from DAT-based hydrogels.

Further verification of the ability of DNA transfection of DAT-based hydrogels was carried out by Tang *et al*, who built a thermoresponsive and biocompatible 2-(2-methoxyethoxy)ethyl methacrylate (MEO_2MA)-VDAT hydrogel (Figure 17a) capable of DNA delivery into fibroblasts by reverse-transfection.[36]

Through complementary H-bonding between base pairs and DAT residues, plasmid DNA (pDNA) was anchored to the surface of the hydrogel. At 37ºC, where the swelling of the hydrogel remains low, cultured cells could then attach to the hydrogel surface, wherein cellular internalization of pDNA takes place by direct contact.

After transfection, the cells could be detached from the hydrogel by cooling down to 20ºC, where the hydrogel swells due to the thermo-responsiveness (Figure 17b). It was observed that both highly hydrated hydrophilic or highly hydrophobic surfaces were not suitable for cell adhesion.

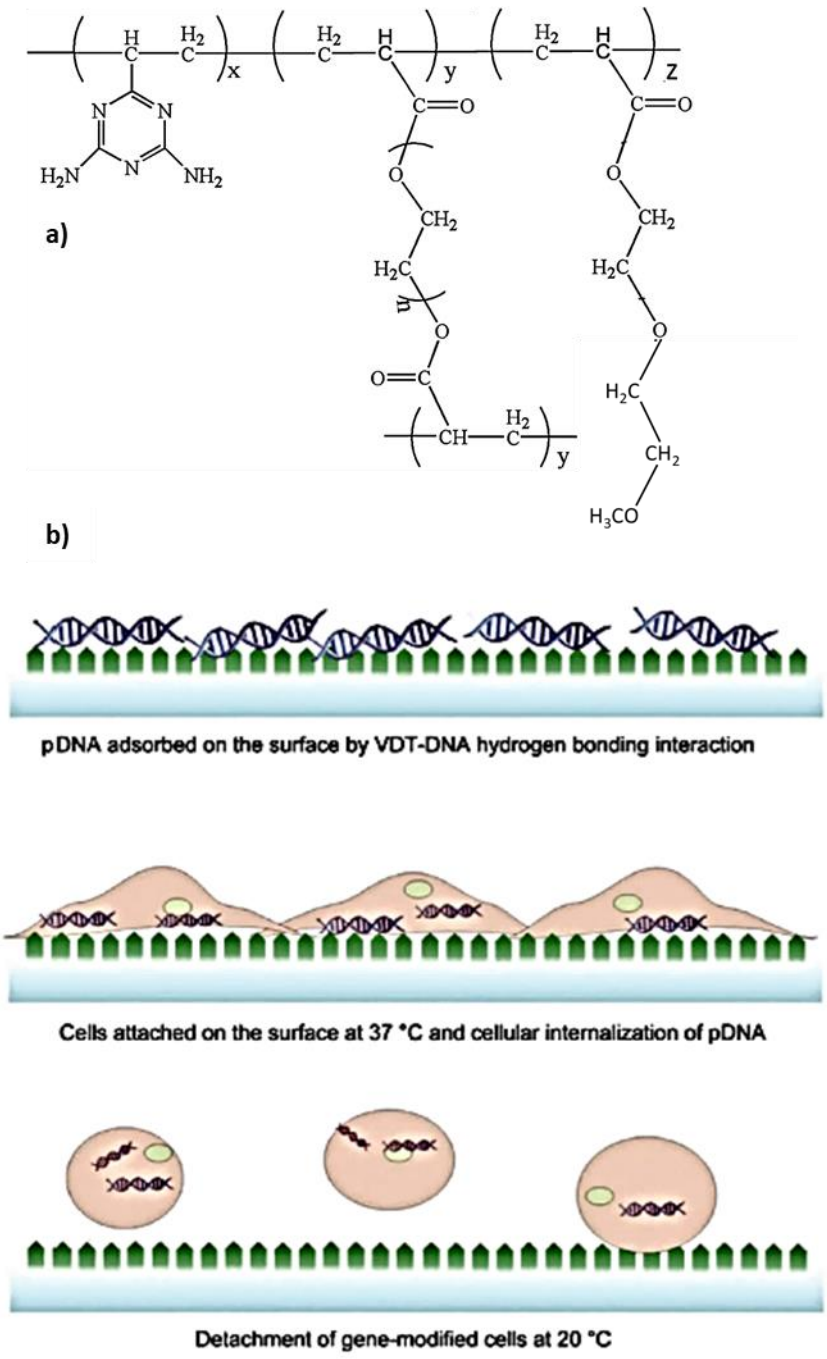

Figure 17. a) Schematic structure of p(MEO_2MA-co-VDAT) hydrogels. b) Schematic diagram depicting the procedure of DNA anchoring, cell transfection, and detachment.

The strong H-bonds interactions that take place inside the DAT hydrogels are responsible for the excellent mechanical properties of these hydrogels. These strong H-bond interactions are hydrophobic in nature and in turn confer these hydrogels with hydrophobicity by limiting their water content.[36–38] In a proposed mechanism, Komiyama and coworkers[33] suggested that poly(vinyldiaminotriazine) (PVDAT) provides hydrophobic microdomains inside which DATs form complementary H-bonds (Figure 18). Since the inside of the microspheres is apolar, water molecules are excluded from the DAT residues.

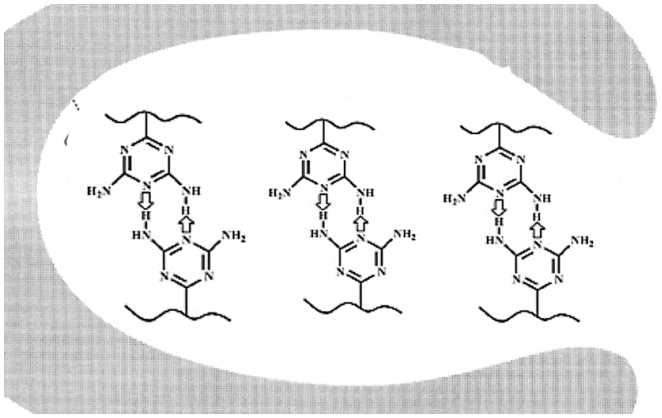

Figure 18. Hydrophobic microdomains in PVDAT.

This principle suggests that DAT hydrogels could be suitable candidates to circumvent the poor tolerance that conventional hydrogels show for hydrophobic drugs. Despite their intrinsic hydrophobicity, however, their potential for hydrophobic drug delivery applications remains unexplored.

2.2. Results and Discussion

In this chapter, diaminotriazines (DATs) are evaluated as building blocks for the preparation of hydrophobic hydrogels. First, the synthetic design and characterization of DATs and DAT-based hydrogels are discussed. Moreover, the capability of the hydrogels towards hydrophobic drug delivery is for the first time studied.

2.2.1. The 6-vinyl-2,4-diamino-1,3,5-triazine monomer

In order to incorporate the DAT moiety into the hydrogel structure *via* polymerization process, we decided to synthesize the simplest DAT-based monomer, 6-vinyl-2,4-diamino-1,3,5-triazine (VDAT) **4**. This compound is nowadays scarcely available for purchase and so synthetic methods for this monomer were previously developed in literature, although they afforded very low yields (Figure 19).[39]

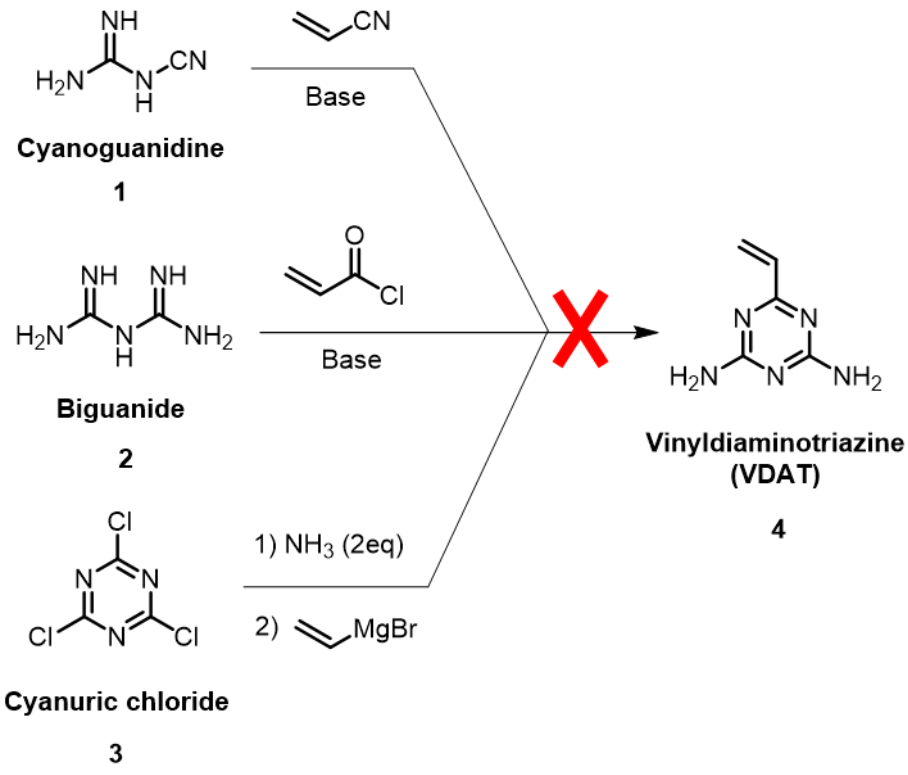

Figure 19. Standard routes attempted in literature for synthesis of **4**.

Due to the difficulty to synthesize VDAT following the standard methodologies, we carried out an alternative methodology described in the Japanese patent publication No. 36391/1972.[40] In this procedure, 2,4-diamino-6-[2-(2-methyl-1-imidazolyl)ethyl]-1,3,5-triazine **5** reacts with epichlorohydrin **6** under water reflux in order to give pure crystals of VDAT in good yields (50%) (Scheme 12).

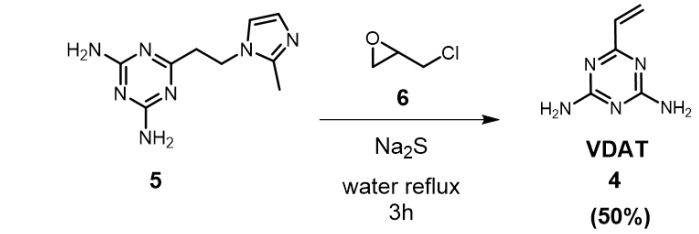

Reaction Mechanism

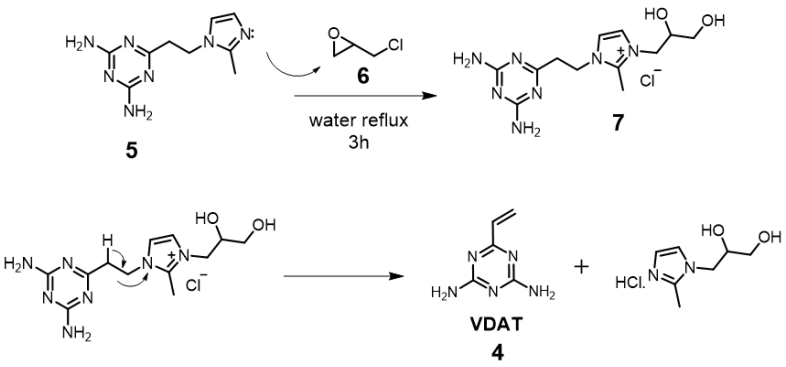

Scheme 12. Synthesis of VDAT and reaction mechanism.

As seen in the reaction mechanism depicted in Scheme 12, the imidazole group of **5** undergoes nucleophilic substitution to **6**, and the water-soluble intermediate **7** is formed. Immediately after, the imidazolium group leaves the molecule *via* elimination process and pure VDAT precipitates in aqueous media as a white solid. It is noteworthy mentioning that a catalytic amount of sodium sulfide is added in order to avoid side-oligomerizations.[10]

The structure of VDAT was confirmed with spectroscopic techniques. Proton nuclear magnetic resonance (^{1}H-NMR) shows a broad signal at 6.67 ppm corresponding to the -NH_2 protons and the signals corresponding to the vinyl group (5.5-6.5 ppm). ^{13}C-NMR spectrum shows two signals around 168 ppm which correspond to the triazine ring (see chapter 6, experimental section).

FT-IR spectroscopy reveals the presence of bands around 3300 cm^{-1} corresponding to the N-H stretching vibrations, as well as the ring C=N stretchings between 1500-1400 cm^{-1} (see chapter 6, experimental section).

2.2.2. The diaminotriazine hydrogel

Once the VDAT monomer was synthesized, we attempted the preparation of an hydrogel containing the DAT moiety, which was carried out *via* radical polymerization process. In order to optimize the synthesis of the hydrogels towards their application for drug delivery, we first studied several parameters that were necessary for this purpose, namely:

- The influence of the different monomers
- The role of pH
- The role of the different crosslinkers

2.2.2.1. The role of the monomers

The synthesis of the hydrogels was carried out by dissolving the monomers and casting the resulting solution into silicon molds, which was then heated in an oven for the polymerization to occur. Some of the results are shown in Table 1.

In this work, the prepared hydrogels have been named after the acronyms of the corresponding monomers used for their synthesis as exemplified in Figure 20.

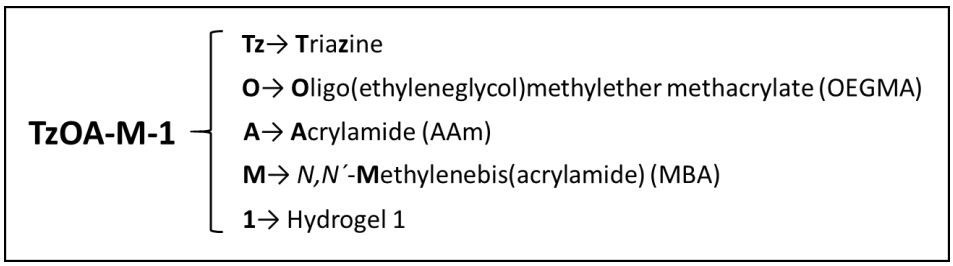

Figure 20. Nomenclature of the hydrogels.

The first attempts tried to carry out the thermal polymerization of the VDAT monomer in the presence of the crosslinker *N,N´*-methylenebis(acrylamide) (MBA) **8** and potassium persulfate (KPS) initiator in dimethyl sulfoxide (DMSO), due to the poor solubility of the triazine monomer in aqueous medium. Under these conditions, (entry 1, Table 1), however, no hydrogel was observed, but instead a whitish opaque polymer insoluble in water (Scheme 13).

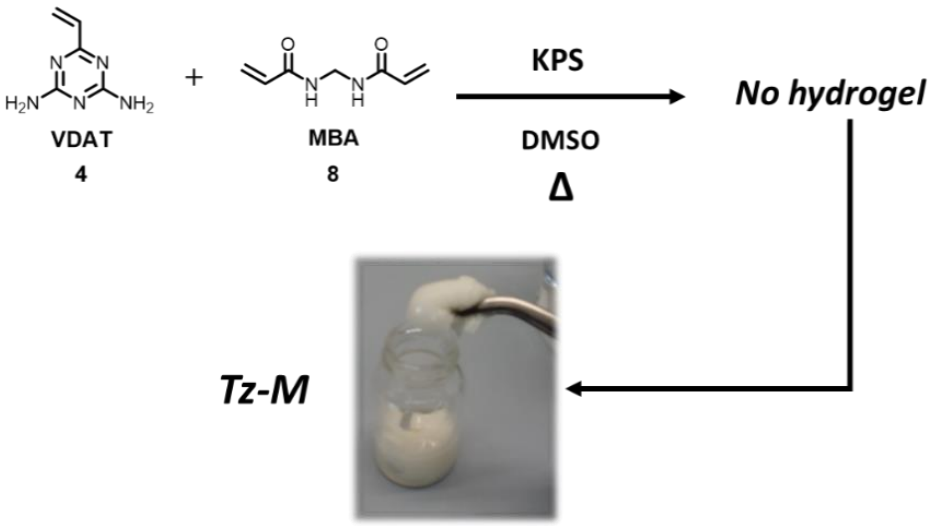

Scheme 13. Synthesis of Tz-M.

In light of these results, we decided to incorporate in the synthetic procedure an additional monomer, oligo(ethyleneglycol)methylether methacrylate (OEGMA) **9**, whose hydrophilic character could compensate the strong hydrophobicity of the VDAT (entry 2, Table 1, **TzO-M-1**).[37] It is important to mention in this point that, since the polymerization is carried out in DMSO, the materials obtained were initially organogels. The corresponding hydrogels were obtained by immersing the organogels in water, where the DMSO is expelled and replaced by the former (Scheme 14).[31]

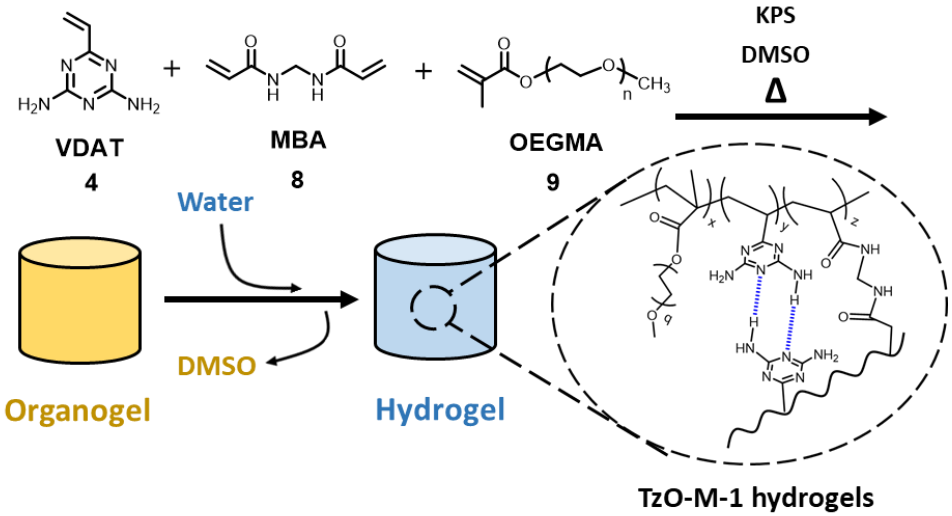

Scheme 14. Synthesis of **TzO-M-1**

Table 1. Synthesis of DAT-based hydrogels

Entry[a]	Name	[OEGMA] (mg/ml)	[VDAT] (mg/ml)	[AAm] (mg/ml)	[MBA] (mg/ml)	MW (% w/w)
1	**Tz-M**	-	82	-	2	<10
2	**TzO-M-1**	41.7	41.7	-	16.7	10
3[b]	**TzO-M-2**	41.7	41.7	-	0.5	10
4[b]	**TzO-M-3**	41.7	41.7	-	2	<10
5	**TzO-M-4**	150	150	-	2	30
6	**TzO-M-5**	225	75	-	2	30
7	**TzO-M-6**	270	30	-	2	30
8	**TzOA-M-1**	135	30	135	2	30
9	**TzA-M-1**	-	150	150	2	30
10	**TzA-M-2**	-	120	180	2	30

[a]T[a] = 70ºC, t = 15 min, [KPS] = 2 mg/ml. [b]no hydrogel

The incapacity of **TzO-M-1** to swell in water suggested a dense and compacted network. Thus, the following attempts focused on lowering the content of crosslinker MBA from 16.7 mg/ml → 0.5 mg/ml, while fixating the rest of the monomer content in order to keep this value constant at 10%. Too low MBA contents resulted in no polymerization (entry 2 *vs* 3, Table 1), whereas medium contents of MBA (2 mg/ml) yielded a sticky polymer **TzO-M-3,** that lost its consistency once removed from the mold (entry 4, Table 1).

The results obtained led us to approach the synthesis of the hydrogel considering a different factor, the total mass of the monomers in the solution, defined as the monomer weight (MW, w/w %). Thus, we increased the MW from 10% to 30%, accordingly increasing the concentrations of VDAT and OEGMA from 41.7 mg/ml to 150 mg/ml (entry 5, Table 1). The resulting organogel was able to expel DMSO from its network and swell in water when immersed in the latter, thus affording a hydrogel (**TzO-M-4**) for the first time.

Despite this achievement, the material appeared a brittle, semi-transparent hydrogel with a very limited ability to swell in water (Figure 21a). The swelling capacity of the hydrogels is a very important factor that determines their applicability in the biomedical field.[41]

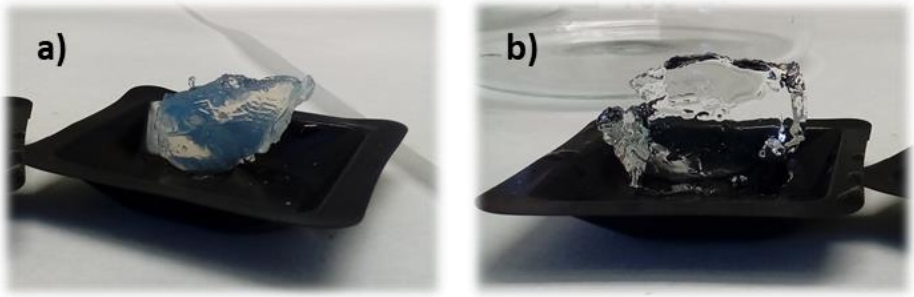

Figure 21. Digital images of DAT hydrogels at a) 50% VDAT content (**TzO-M-4**) and b) 10% VDAT content (**TzO-M-6**).

For this reason, the next step focused on studying the influence of the VDAT monomer in the swelling ability of the hydrogel. By decreasing the VDAT content from 150 mg/ml, to 75 mg/ml and 30 mg/ml (entries 6 and 7 *vs* entry 5, Table 1), the three corresponding, respectively, to a 50%, 25% and 10% of VDAT content, a clear difference was observed: with only 30 mg/ml (10% VDAT) a more transparent hydrogel with the ability to swell in water was obtained (Figure 21b). The monomer weight (mw) was always fixed to 30% in these experiments.

At this point, it is important to define the swelling capacity of a hydrogel, which is quantified by the swelling degree (SD). The SD determines the amount of water that can be held inside the porous structure of the network. The SD depends on several parameters such as pore and mesh sizes, density of crosslinking, functional hydrophilicity, and monomer weight (MW) of the hydrogel. The SD is calculated according to the following equation (Equation 1):

$$SD = \frac{W_t - W_0}{W_0}$$

$W_0 = \text{initial hydrogel weight}$

$W_t = \text{hydrogel weight at time t}$

Equation 1. Swelling Degree (SD)

The SD was calculated by weighting the hydrogels in their maximum swollen state and the weight of the hydrogels until complete dryness. Based on

this formula, the SD of the hydrogels with respect to their VDAT content was plotted (Figure 22).

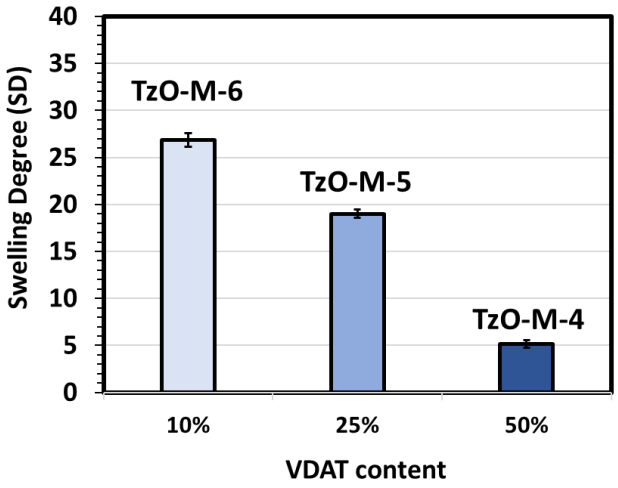

Figure 22. SD study of hydrogels **TzO-M-6, TzO-M-5** and **TzO-M-4**. Total MW was fixed at 30%.

The results show an inverse trend, where increasing the VDAT content results in a sharp decrease in the SD. In fact, hydrogels with a 50% of triazine content swell up to five times less than hydrogels with only 10% content.

Despite clear hydrogels with the ability to swell were already successfully prepared, however, they still showed brittleness and easily broke once swollen in water. To overcome this setback, the monomer acrylamide (AAm) was introduced in the hydrogel formula, which helps maintain consistency in the swollen state. The result showed a hydrogel (**TzOA-M-1**) that withstood from breaking (entry 8, Table 1) and was easily manipulated even in its maximum swollen state (Figure 23).

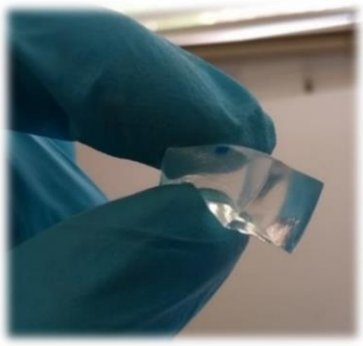

Figure 23. TzOAM-1 hydrogels.

In order to quantify the mechanical improvement that the introduction of the acrylamide monomer conferred the hydrogel, two hydrogel formulations, one in the absence (TzO-M-6) and one in the presence (TzOAM-1) of acrylamide (entries 7 and 8, Table 1) where subjected to 100 fatigue cycles of mechanical compression. The fatigue experiments were carried out by performing 100 compressive cycles on hydrogel probes with a rate of 40 mm/min and a 50 N cell load.

The results showed that hydrogels containing acrylamide (AAm) absorbed higher energies than the hydrogels in the absence of acrylamide (Figure 24).

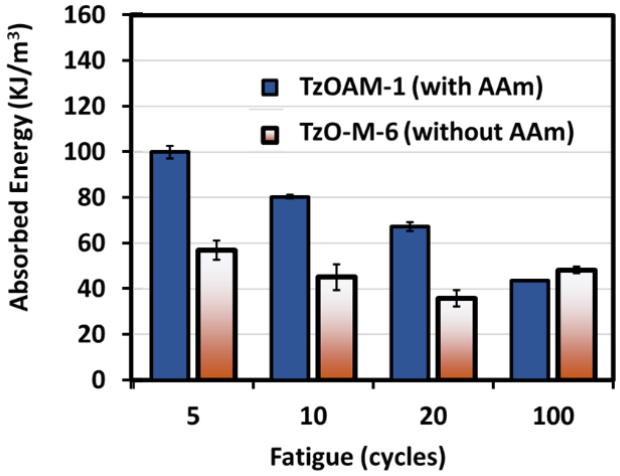

Figure 24. Fatigue test of hydrogels TzOAM-1 and TzO-M-6.

A possible explanation to this phenomenon lies in the ability of AAm to form reversible H-bonds with neighboring acrylamide monomer units. When this molecule is introduced into the DAT-based hydrogel network, weak AAm-AAm H-bond dimers are formed (Figure 25a, depicted in blue), which co-exist with the stronger DAT-DAT H-bonds (Figure 25a. red). When subjected to a load, these weak AAm H-bonds break, but reversibly recover after the load is removed. On the contrary, DAT-DAT H-bonds, which are stronger in nature, do not recover upon lifting the load (Figure 25b).

It follows that, from a mechanical point of view, the reversible disruption-formation of weak H-bonds such as those provided by acrylamide allows additional pathways to absorb mechanical energy and this helps improve the mechanical performance of DAT-based hydrogels.[34,42]

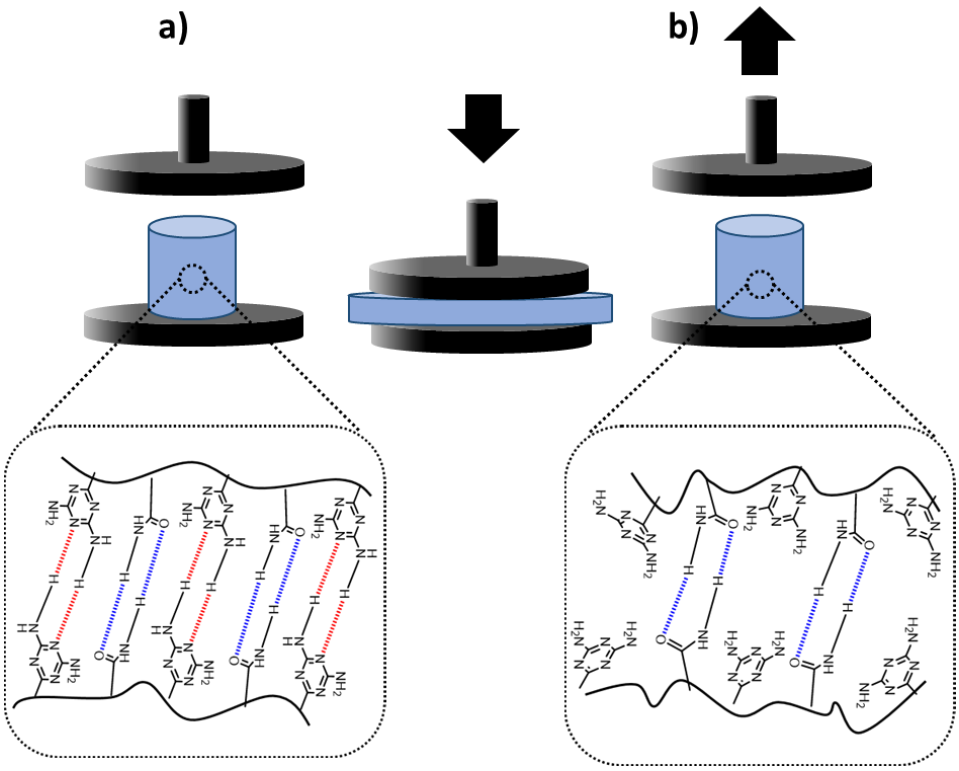

Figure 25. Reversible formation of weak AAm H-bonds (blue) in **TzOAM-1** hydrogels a) before the load is applied b) after the load is applied.

Further, since AAm is also slightly hydrophilic and in order to simplify the hydrogel formula, we wished to determine whether this monomer could replace the role of hydrophilicity of the OEGMA monomer instead. For this purpose, we synthesized a hydrogel where OEGMA was replaced for AAm in increasing amounts while maintaining the MW fixed to a 30%, **TzA-M-1** and **TzA-M-2** (entries 9 and 10, Table 1).

It was observed, however, that upon removing OEGMA the hydrogels were unable to swell, and rather behaved as semi-swollen polymers, thus evidencing that the presence of OEGMA in the hydrogel formulation was necessary for proper water uptake.

Up to this point, the formulation **TzOA-M-1** (entry 8, table 1) was chosen as the optimal hydrogel recipe, since it was the first hydrogel formula to maintain consistency in its maximum swollen state.

The final recipe for the synthesis of **TzOA-M-1** is shown in Scheme 15. In order of addition, VDAT was first added, followed by co-monomers OEGMA **9**,

AAm **10**, and crosslinker MBA **8** until total dissolution. Radical initiator KPS was then added prior to casting the solution into silicon molds in an oven. The resulting organogels were then immersed in water in order to phase-invert the DMSO and swell in the former, thus yielding the corresponding hydrogels.

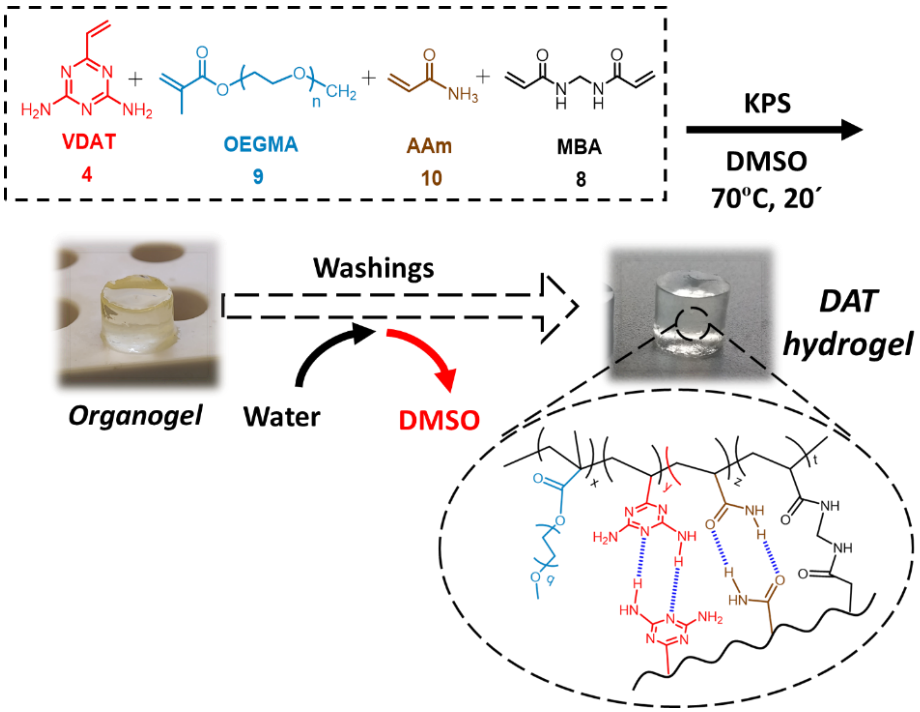

Scheme 15. Synthesis of **TzOA-M-1** hydrogels.

At this point, it is important to mention the **double role of the washings in water:**

- Immersion in water allows the DMSO in the organogels to be expelled and be replaced by water, and therefore carry out the necessary transformation from organogel to hydrogel.

- Systematic washings in water remove all the unreacted monomers and oligomers that did not react during polymerization and would otherwise pose additional toxicity for future biomedical applications.

In order to determine the number of water replacements required to clear all unreacted species, we monitored each washing with UV/VIS spectroscopy. For this experiment, water was replenished twice a day, for a total of 4 days (Figure 26).

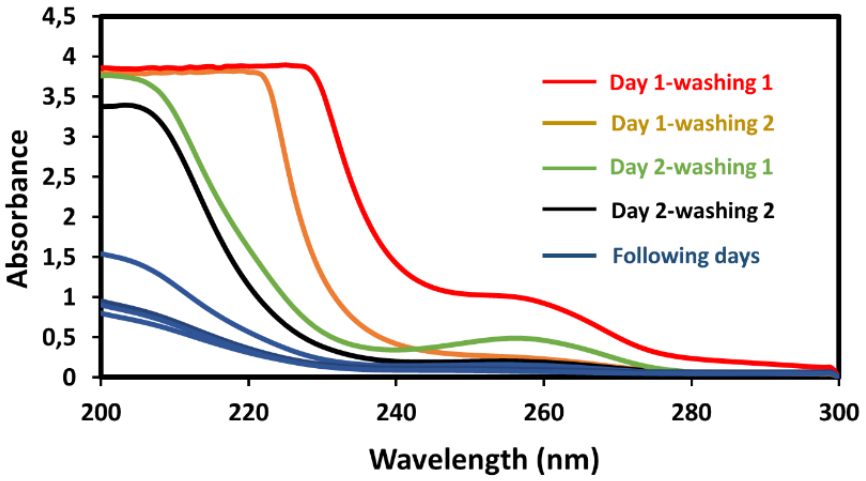

Figure 26. UV/VIS spectra follow-up for the washings of the hydrogels.

It was found that the presence of organic compounds at around 260 nm drastically decreases during the first two days, corresponding to the first four washings.

2.2.2.2. The role of pH

Given that one of the main objectives of this work is to design drug delivery vehicles capable of responding to external stimuli, we wished to exploit the capacity of the DAT hydrogel in this sense.

As explained in the introduction of this thesis, smart hydrogels respond to a variety of chemical and physical stimuli, such as pH,[43] temperature,[44] enzyme activity,[45] or mechanical deformation,[46] to name a few. These stimuli typically modify the porous network of the hydrogels *via* several mechanisms in order to release the compound from the reservoir.

Since the pyridinic nitrogen atoms of the triazine ring protonate under low pH conditions (pKa of the VDAT = 5.15),[33] and with the aim of carrying out drug delivery studies, we then decided to test the tolerance and swelling behavior of the TzOA-M hydrogels towards the acidic pH. The different hydrogels prepared are shown in Table 2.

For this, two different pH were studied, namely pH =1.2, known as Simulated Gastric Fluid, or SGF, which simulates the pH that occurs in the human gastric system and neutral pH =7 for the sake of comparison.

The **TzOA-M-1** hydrogels showed similar swelling degree (SD) values in neutral and SGF medium. (Figure 27a). Upon increasing the VDAT content to 30% (90 mg/ml) **TzOA-M-2,** however, a clear difference in their capacity to swell in both media was observed (entry 2, table 2 and Figure 27b).

Table 2. Synthesis of DAT-based hydrogels

Entry[a]	Name	[OEGMA] (mg/ml)	[VDAT] (mg/ml)	[AAm] (mg/ml)	MW (% w/w)
1	TzOA-M-1	135	30	135	30
2	TzOA-M-2	105	90	105	30
3	TzOA-M-3	75	150	75	30
4	TzOA-M-4	135	60	135	33
5	TzOA-M-5	135	90	135	36
6	TzOA-M-6	135	150	135	42

[a]T[a] = 70ºC, t = 15 min, [KPS] = [MBA] = 2 mg/ml

Finally, the SD difference between pH = 7 and pH = 1.2 became quite significant when the VDAT content was increased to 50% (150 mg/ml) (entry 3, table 2). However, the improvement in the capacity of the **TzOA-M-3** hydrogels to swell in SGF buffer occurred at the expense of collapsing its structure in this medium, as it is evidenced in Figure 27c.

These observations are predicated on the pH-responsive behavior of the DAT moiety. DAT hydrophobic interactions (namely H-bonds and π-π stackings) in neutral aqueous media behave as "water barriers" that impede water from penetrating the network (Figure 28, left).

However, in SGF media, DAT molecules protonate *via* N ring atom and thus intermolecular H-bonds between the terminal -NH_2 and pyridine N are disrupted. The protonated DATs now suffer charge repulsion from one another and are repelled, consequently breaking π-π stackings as well. In this scenario, the hydrophobic "water blockades" are removed and water infiltrates the network in higher amounts, thus increasing considerably the SD values (Figure 28, right).

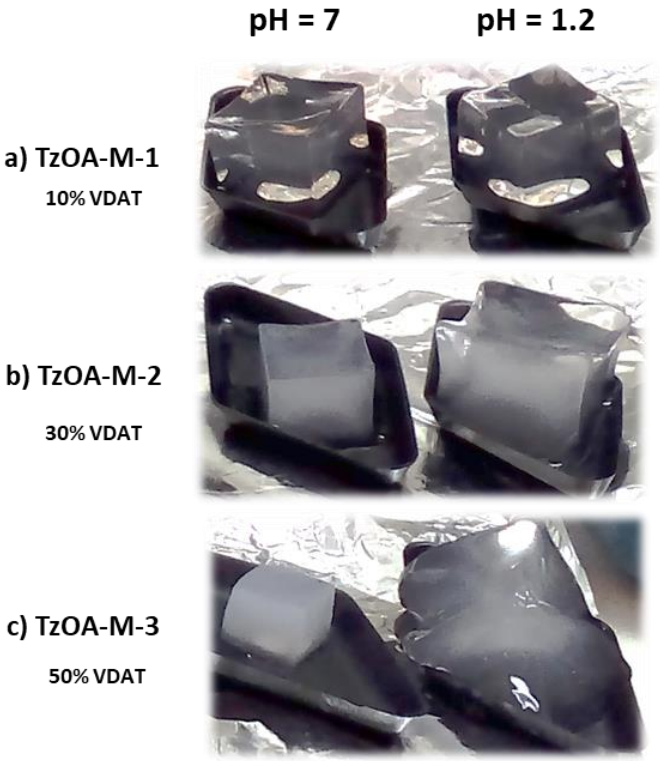

Figure 27. SD of DAT hydrogels in neutral aqueous medium (left) and SGF (right) for a) 10% VDAT b) 30% VDAT and c) 50% VDAT.

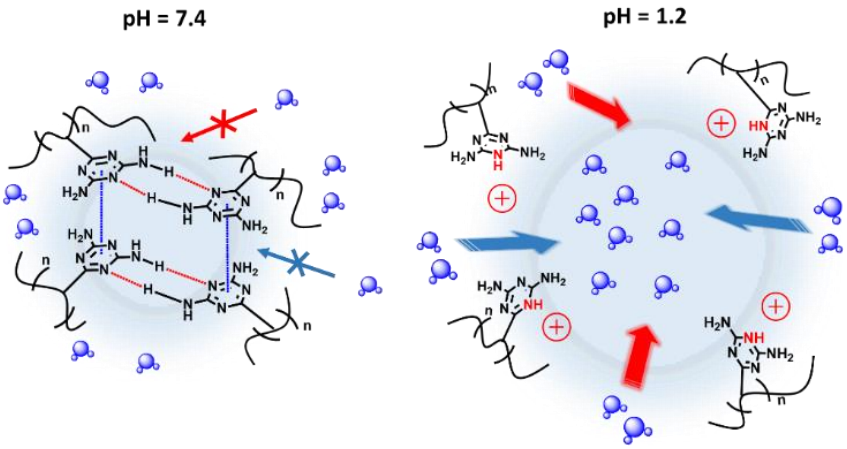

Figure 28. pH-induced swelling mechanism of the DAT-based hydrogels. Swelling in aqueous media (left) and in SGF medium (right).

The marked swelling of the DAT hydrogels in SGF also explains why the hydrogel scaffolding worsens dramatically in this medium. Since the repulsion of the DATs in SGF medium occurs at the expense of dismantling the DAT-DAT

H-bond strengthening network, as observed in the TzOA-M-3 hydrogels, the scaffold collapses in this medium.

In order to avoid this scenario, we hypothesized that an additional source of H-bonds that could withstand in acidic medium, such as acrylamide (pKa = 16.7), would compensate for the disruption of the DAT H-bond network and stabilize the hydrogels with high VDAT content. For this purpose, we decided to increase both contents of OEGMA and AAm from 75 mg/ml to 135 mg/ml, with different VDAT contents, namely, 60 mg/ml, 90 mg/ml and 150 mg/ml (entries 5 and 6 *vs* 4, table 2). For this transformation to occur, the total polymer content was increased above 30%.

The results showed that the hydrogels could swell in SGF medium, this time maintaining their consistency, therefore highlighting again the important role of the AAm monomer. The hydrogel formulation TzOA-M-6 showed the best consistency both in aqueous and SGF medium as well as an optimal response under acidic pH. For this reason, we performed the SD studies in both media in order to quantify their swelling capacity.

Figure 29a reveals that TzOA-M-6 hydrogels in SGF swelled considerably faster than in neutral media, until around 10-fold after 4 days, while maintaining their physical integrity (Figure 29b).

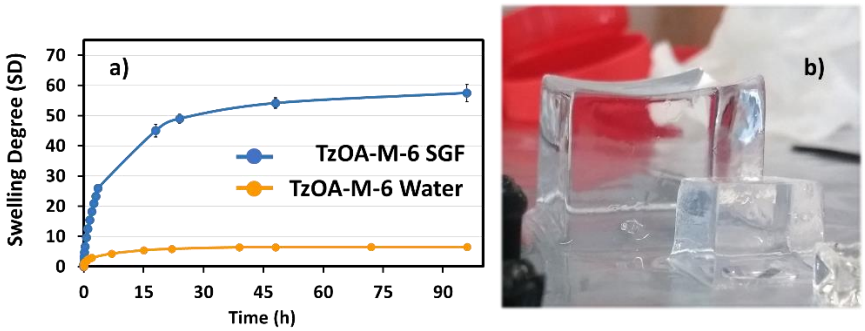

Figure 29. Swelling studies for TzOA-M-6 hydrogels in water and SGF (Simulated Gastric Fluid): a) SD study b) Hydrogels swollen in SGF (left) and water (right).

The excellent responsiveness of these hydrogels to the pH stimulus encouraged us to choose them as potential candidates for drug delivery applications, which will be discussed further in detail.

2.2.2.3. The role of the crosslinker

The bio-applications of hydrogels are determined by parameters such as the swelling degree, as well as their porous structure, among others. These, in turn, are both largely dependent on the crosslinker employed for the formation of the polymer network.

In order to ascertain the influence of the crosslinker agent in our DAT-based hydrogels, we prepared and characterized several hydrogels with different crosslinker agents:

- The short chain *N,N'*-Methylenebisacrylamide (MBA) **8**
- The long chain polyethylene glycol diacrylate (PEGDA) **11**
- In the absence of chemical crosslinker, this is, a physically-crosslinked hydrogel

A possible representation of the structure of each of the hydrogels is provided in Figure 30.

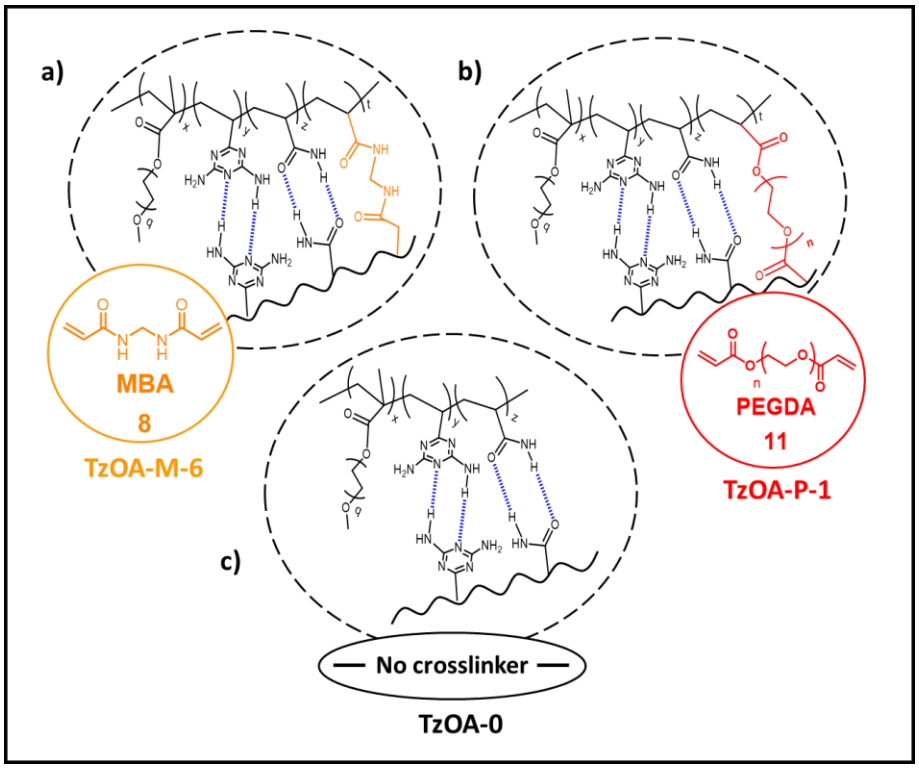

Figure 30. Structure of hydrogels a) chemically-crosslinked **TzOA-M-6** b) chemically-crosslinked **TzOA-P-1** and c) physically-crosslinked **TzOA-0.**

Several experiments with a range of different crosslinker concentrations were attempted. For the short crosslinker MBA, hydrogels appeared consistent for a range between [MBA] = 0.5-2 mg/ml; the optimal concentration being the formula previously optimized (Table 3, entry 1, **TzOA-M-6**).

Table 3. Synthesis of DAT-based hydrogels

Entry[a]	Name	[MBA] (mg/ml)	[PEGDA] (mg/ml)	Crosslinker length	Crosslinking
1	**TzOA-M-6**	2	-	Short	Chemically crosslinked
2	**TzOA-P-1**	-	2	Long	Chemically crosslinked
3	**TzOA-0**	-	-	-	Physically crosslinked

[a]T[a] = 70ºC, t = 15 min, [VDAT] = 150 mg/ml, [OEGMA] = [AAm] = 135 mg/ml, [KPS] = 2 mg/ml, MW = 42 %

For the longer crosslinker PEGDA, the appropriate concentrations ranged between [PEGDA] = 1-5 mg/ml, being this value of 2 mg/ml for the optimal conditions (Table 3, entry 2, **TzOA-P-1**).

Entry 3 shows the conditions under which a physically-crosslinked hydrogel based on VDAT (triazine **4**) was obtained (Table 3, entry 3, **TzOA-0**). This hydrogel was ruled purely by H-bonds arising from the DAT and AAm moieties.

All three **TzOA-M-6, TzOA-P-1** and **TzOA-0** hydrogels were then characterized with swelling and pore size studies, both in neutral and SGF medium.

a) In neutral medium

As commented earlier, the swelling degree (SD) defines the amount of water that the porous network of a hydrogel can incorporate. Of all three hydrogels studied, the physically crosslinked hydrogels were shown the highest SD values (**TzOA-0)** in water, followed by long chain PEGDA-crosslinked (**TzOA-P-1)** and short chain MBA-crosslinked hydrogels (**TzOA-M-6)** and all of them reached a maximum SD value at around 3 days (Figure 31a).

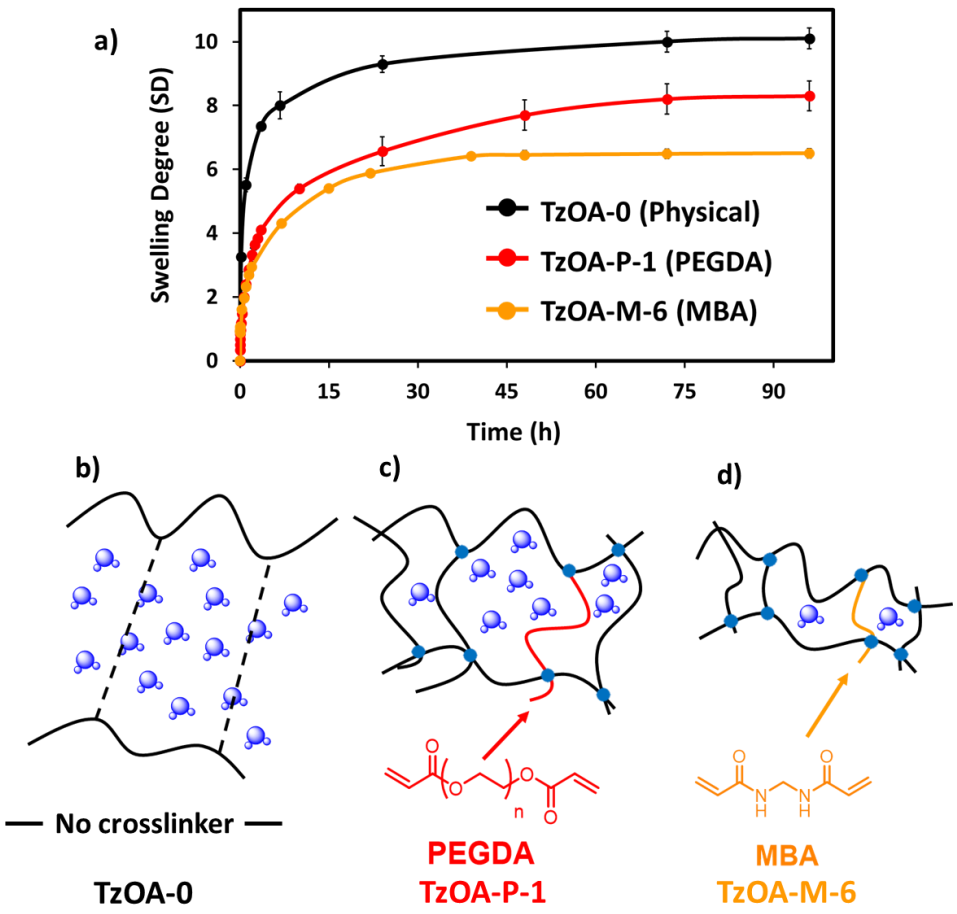

Figure 31. *a*) SD study of physically-(**TzOA-0**), PEGDA-(**TzOA-P-1**) and MBA-(**TzOA-M-6**) crosslinked hydrogels in aqueous media. Depiction of porous network for b) **TzOA-0** c) **TzOA-P-1** and d) **TzOA-M-6** hydrogels.

These results agree with the expected trend: in the absence of chemical crosslinker, the polymer network is less compact, since there are no covalent joints that bind the polymer chains. As a result, the pore sizes will be the largest in comparison and more water will be allowed inside (Figure 31b). With long PEGDA crosslinker, the polymer chains will be covalently bound, although through large chains. The pore size will be still large, but still smaller than in the absence of crosslinker, and thus smaller SD values are expected (Figure 31c). Finally, with short chain MBA crosslinker, the smallest pore sizes are formed and therefore the smallest SD values are observed (Figure 31d).[47]

The confirmation of the porous microstructure of the hydrogels was performed by scanning electron microscopy (SEM). For proper imaging,

washed hydrogels were completely swollen and lyophilized, prior to introduction in the SEM chamber. Figure 32a shows the pore size distributions of our hydrogels.

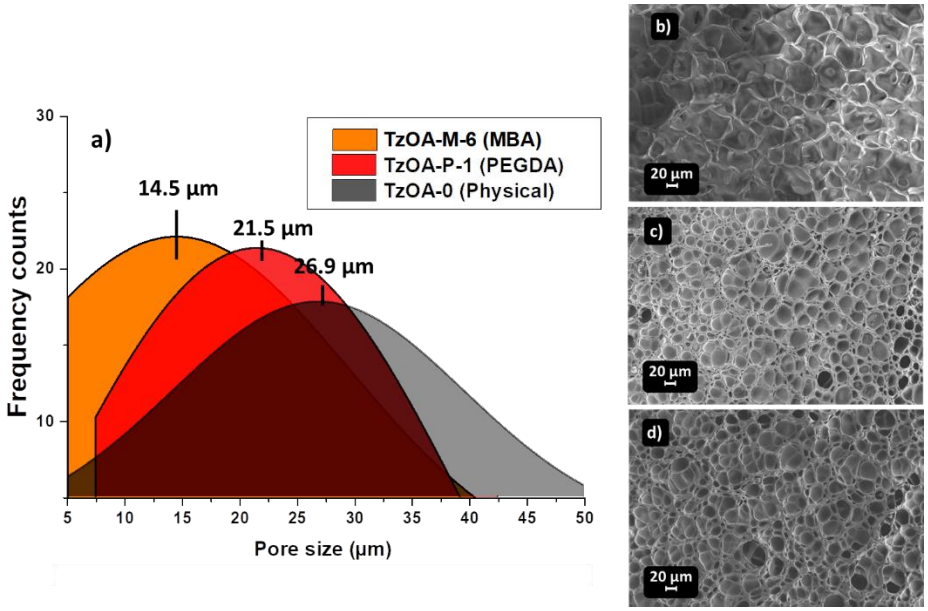

Figure 32. a) Pore size distributions and porous microstructure for b) physically-(**TzOA-0**) crosslinked c) PEGDA-(**TzOA-P-1**) crosslinked and d) MBA-(**TzOA-M-6**) crosslinked hydrogels.

As it can be observed, the pore sizes of the three hydrogel formulations were in accordance with the swelling degree studies. Pore size values of 14.5 µm, 21.5 µm and 26.9 µm were observed for smaller chain MBA-crosslinked, longer chain PEGDA-crosslinked and physically crosslinked hydrogels, respectively, thus confirming the expected trend.

The porous microstructure is shown in Figure 32b-d. All hydrogel formulations show irregular pore sizes, which is a typical feature for DAT-based hydrogels: DATs tend to aggregate into amorphous domains and porous distributions in DAT-based hydrogels thus tend to be heterogeneous.[48]

b) In SGF medium

In SGF medium, DAT hydrogels showed a considerable increase in the SD values from early hours, until reaching a plateau after 5 days (Figure 33a).

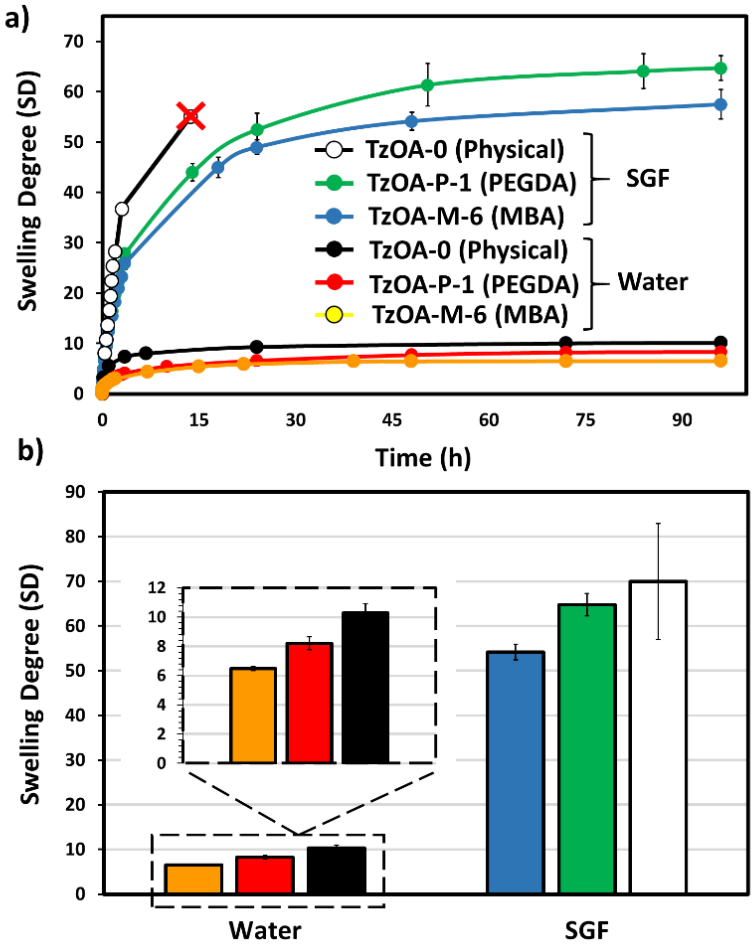

Figure 33. Swelling study in neutral and acidic media: swelling study with respect to time (up) and maximum swelling degree (SD) of DAT-based hydrogels (down).

Further, maximum SD studies show that DAT-based hydrogels in SGF media reach around 7 to 10 times higher SD values than in neutral aqueous media, as expected for their pH-responsiveness (Figure 33b).

In addition, the expected upward trend in the swelling degree was observed when the crosslinker chain length increases. Note that the SD curves for the physically crosslinked hydrogel in SGF medium is incomplete (Figure 33a) and the corresponding maximum SD values bear considerably high error bars (Figure 33b). It was observed for these hydrogels that, unlike in neutral media, the sole physical junctions were not able to withhold the hydrogel from breaking at such high SD values.

This highlights the crucial role of the crosslinkers in hydrogels of conferring mechanical consistency, since these materials are usually fabricated with dilute polymers and their nature in their swollen state is normally brittle.[49]

Pore studies in SGF media were obtained with SEM imaging. Figure 34 shows that pore sizes increase around 3-5 fold in SGF medium with respect to neutral aqueous medium.

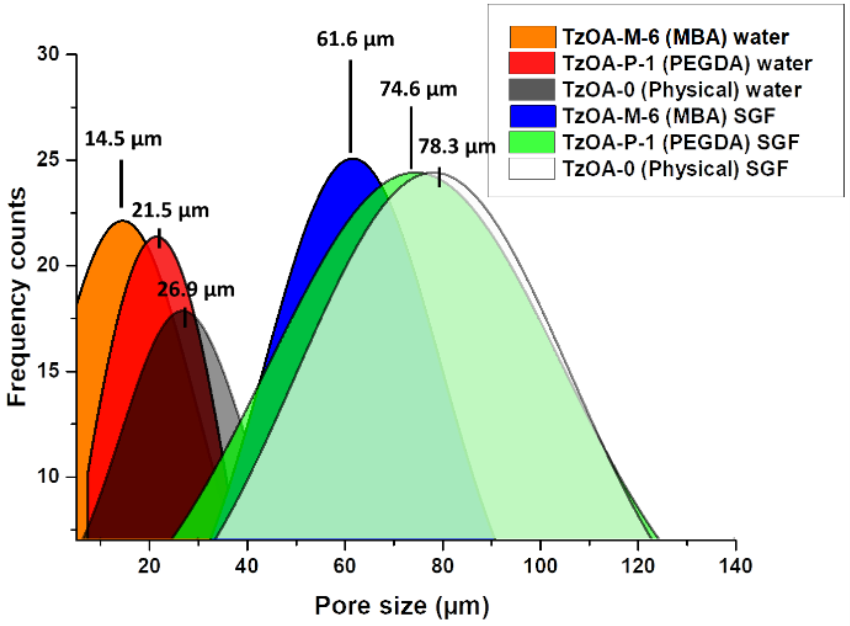

Figure 34. Pore size distributions for physically-crosslinked (TzOA-0), PEGDA-crosslinked (TzOA-P-1) and MBA-crosslinked (TzOA-M-6) hydrogels both in water and SGF media.

Similarly, hydrogels **TzOA-0, TzOA-P-1** and **TzOA-M-6** showed the same trend in pore sizes so far observed: 78.3 µm > 74.6 µm > 61.6 µm, respectively, corresponding to physically crosslinked, PEGDA-crosslinked and MBA-crosslinked hydrogels, confirming the data of the SD studies.

Porous microstructure clearly shows the pore size expansion of the DAT-based hydrogels in SGF media for the three hydrogel formulations (Figure 35). In addition, heterogeneous porosity is also present in SGF medium since DAT tend to aggregate into amorphous microdomains.

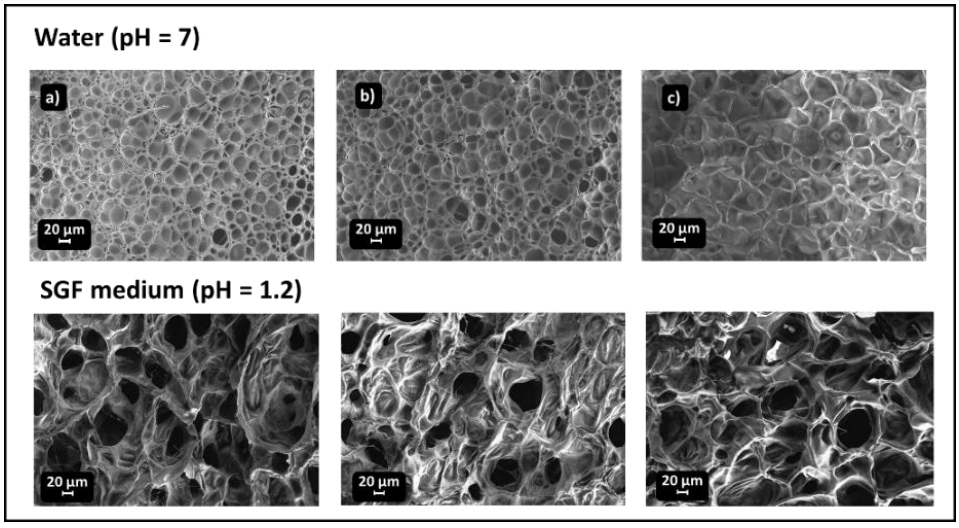

Figure 35. Porous microstructure for a) MBA-crosslinked hydrogels (**TzOA-M-6**) b) PEGDA-crosslinked hydrogels (**TzOA-P-1**) and c) physically-crosslinked hydrogels (**TzOA-0**) both for water (up) and SGF medium (down).

2.2.3. Other diaminotriazine-based hydrogels

In order to expand the scope of the methodology for the synthesis of DAT-based hydrogels recently optimized, we attempted to fabricate hydrogels based on DAT backbones other than 6-vinyl-2,4-diamino-1,3,5-triazine (VDAT).

For this, we started from different vinyl DATs previously synthesized in our group based on published protocols.[22,29,30] Bis- and tris-(allyl)aminotriazines **13** and **14** were synthesized by S_NAr reaction between cyanuric chloride **3** and allyl amine **12** (Scheme 16a), whereas the vinyl phenyl derivative **16** was synthesized from cyclisation reaction between cyanoguanidine **1** and cyanostyrene **15** (Scheme 16b).

Table 4 summarizes the experiments carried out for the synthesis of the hydrogels based on the triazines **13**, **14**, and **16**, which were attempted following the recipe for the hydrogel **TzOA-M-6**.

However, due to the higher insolubility of these triazine derivatives in DMSO, their concentration was lowered from 150 mg/ml down to 30 mg/ml in each case in order to avoid precipitation.

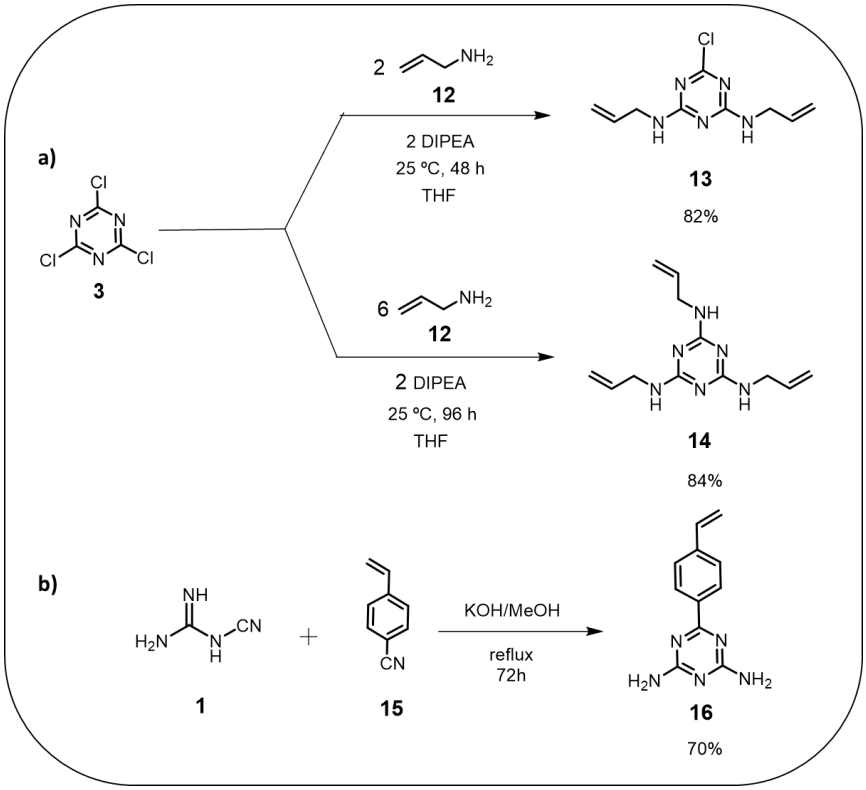

Scheme 16. Synthetic methodologies for a) bis- and tris-allyl diaminotriazines **13** and **14** and b) phenyl vinyl diaminotriazine **16**

Table 4. Synthesis of DAT-based hydrogels

Entry[a]	Name	[KPS] (mg/ml)	t (min)	Triazine derivative
1	Tz_1OA-M	2	15	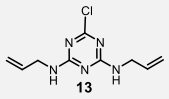
2	Tz_2OA-M	2	15	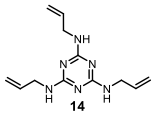
3[b]	Tz_3OA-M-1	2	30	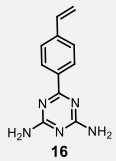
4	Tz_3OA-M-2	8	30	

[a]T = 70ºC, [triazine] = 30 mg/ml, [OEGMA] = [AAm] = 135 mg/ml, [MBA] = 2 mg/ml, MW = 30%. [b]no hydrogel

The hydrogels obtained with the bis- and tris-(allyl)aminotriazines **13** and **14** turned out whitish and opaque and showed limited swelling degrees **Tz1OA-M** and **Tz2OA-M** (Table 4, entries 1 and 2 and Figure 36a-b).

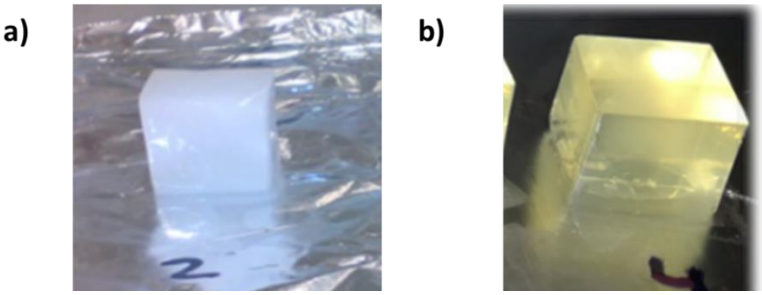

Figure 36. Hydrogels based on triazine derivatives: a) **Tz_1OA-M-1** (triazine **13**) b) **Tz_2OA-M-2** (triazine **14**).

Both the lack of transparency and the restricted swelling denoted a very high degree of crosslinking of the polymer network; indeed, since the triazine derivatives **13** and **14** have several pendant vinyl moieties, they behave as crosslinkers instead than as monomers. In consequence, the polymer network becomes more compacted and allows less water inside, and thus hydrogels appear less transparent and more opaque.

Hydrogels based on the phenyl vinyl triazine **16** were also attempted following the same recipe with low triazine contents of 30 mg/ml, but the polymerization did not take place (entry 3, Table 4). After several attempts, we opted the simpler strategy of increasing the amount of KPS initiator 4-fold (2 mg/ml → 8 mg/ml) and the solution polymerized after 30 min into an organogel. Subsequent washings in water afforded the corresponding hydrogel (entry 4, Table 4) (Figure 37), which resulted mechanically consistent.

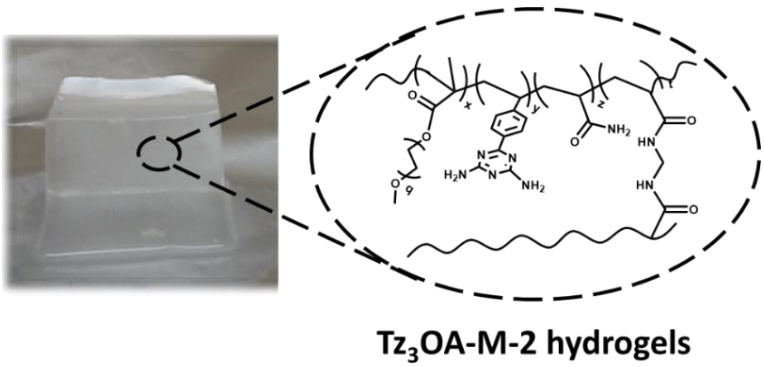

Figure 37. The **Tz_3OA-M-2 hydrogel** (triazine **16**).

With these experiments, therefore, we demonstrated that our present formula is a feasible and universal approach to synthesize triazine-based hydrogels for an array of applications.

2.2.4. Diaminotriazine hydrogels for drug delivery

Nowadays, the controlled delivery of hydrophobic drugs still remains one of the main challenges in the drug delivery literature; being intrinsically hydrophilic, hydrogels present poor drug loading and delivery performances for these compounds.[50,51] Chapter 1 summarized the strategies that have been attempted over the years to overcome these setbacks, namely, incorporation of hydrophobic blocks[52] and hydrophobic moieties[53] into the hydrogel network. However, the weak nature of the non-covalent dispersive forces underlying these methodologies may lead to supramolecular disassembly and consequently undesired burst release of drug molecules.[54,55]

Encouraged by our findings, we wished to investigate the outstanding hydrophobic character of the DAT-based hydrogels in order to find a novel material that allows release of hydrophobic drugs in a stable and controlled manner. For these studies, we chose as starting point the hydrogel formulation **TzOA-M-6** due to its high content in VDAT, optimal responsiveness to pH stimulus and excellent consistency in its maximum swollen state.

Further, a series of commercially available drugs of decreasing water solubilities were tested (Figure 38).

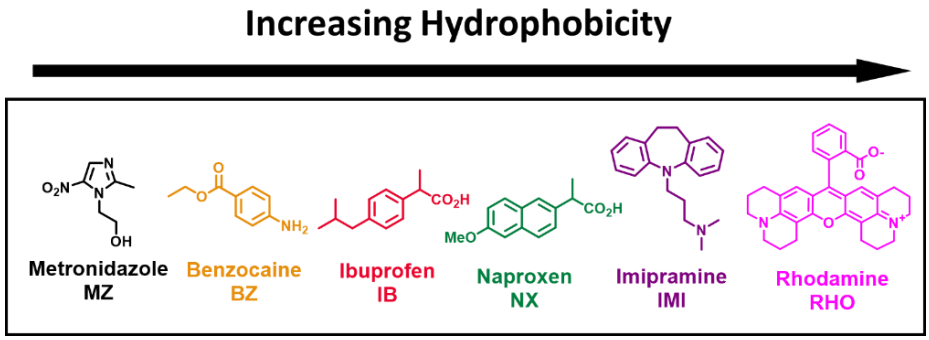

Figure 38. Drugs of different water solubilities used for the delivery tests.

Metronidazole (MZ), an antibiotic commonly used for gastric infections, **benzocaine (BZ)** a local anesthetic, **ibuprofen (IB)** a widely used non-steroideal anti-inflamatory (NSAID) drug, **naproxene (NX)** a more hydrophobic NSAID

derivative of **IB**, **imipramine (IMI)**, a phenyl-rich antidepressant belonging to the tricyclic antidepressant class and **rhodamine 101 (RHO),** a phenyl-rich fluorophore.

To carry out the *in vitro* drug delivery experiments, two steps are followed:

- The drug loadings, where the drugs are first incorporated inside the porous network of the hydrogel.
- The drug release, where the drugs are then released from the porous network to the outer media, typically mediated by simple diffusion.

For the drug loadings, the dried hydrogels (xerogel) were swollen with a known amount of drug solution until all of it was sucked up by the hydrogel. Further, the release experiments were carried out immersing the drug-loaded hydrogels in phosphate buffered saline PBS buffer in an orbital mixer and shaker with a heating platform, operating at 70 rpm and 37 ºC in order to simulate physiological temperatures. At each time point, an aliquot was taken from the release medium and taken to UV/VIS spectrophotometry for absorbance measurement (Figure 39).

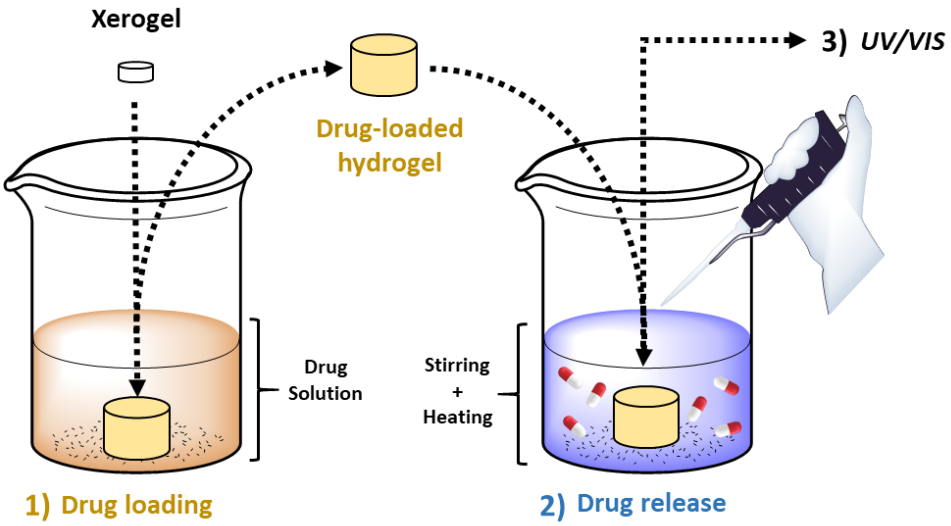

Figure 39. Drug loading and drug release experiments.

Immediately after each measuring, the aliquot was replaced with the same volume of buffer, accordingly, in order to keep the final volume constant. The absorbance readings were then interpolated in a calibration curve of the

corresponding drug solution under study. As a mode of example, the UV/VIS spectrum of imipramine (IMI) drug in PBS buffer and its calibration curve are provided in Figure 40. Finally, the percentage drug release values are plotted with respect to time.

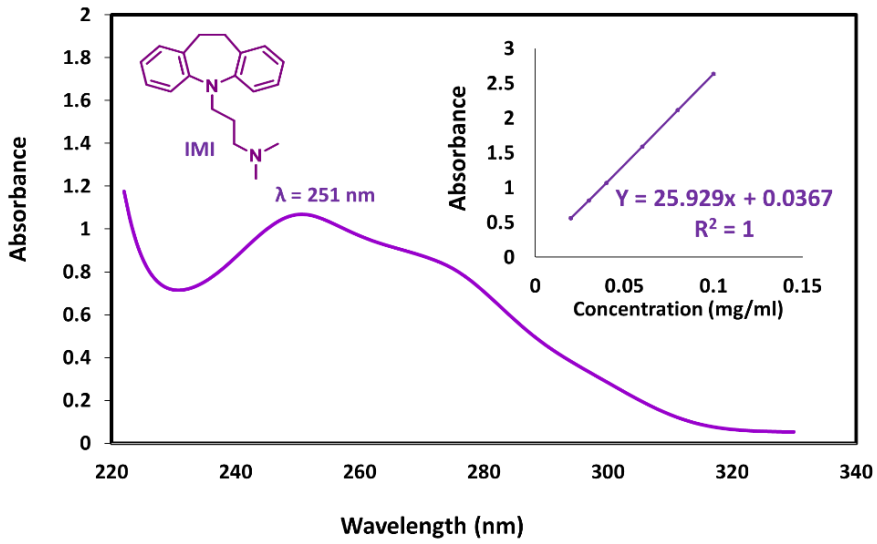

Figure 40. UV/VIS spectrum of imipramine (IMI) drug and calibration curve in PBS medium.

2.2.4.1. Parameters that influence drug delivery

We first studied a series of parameters that are essential for the drug delivery performance of the hydrogels. These are:

- The role of the triazine monomer
- The role of pH
- The role of the crosslinker
- The role of the pores

a) The role of the triazine monomer

It has been stated that the VDAT monomer induces hydrophobicity in the DAT-based hydrogels by assembly of hydrophobic microdomains.[56,57] By performing a simple experiment, we evaluated the release of drugs of different water solubility in hydrogels in the presence and absence of the VDAT monomer.

Figure 41 shows the release in PBS medium of drugs **MZ** and **IB** from hydrogels **TzOA-M-6** and from the same hydrogels in the absence of the triazine **OA-M-6**. It is clearly observed for both drugs that hydrogels with VDAT in their structure slow down the release of the payload with respect to their VDAT-free counterparts. This implies that the drugs interact notably with the DAT molecules *via* non-covalent interactions, and this results in a slower diffusion of the drug through the porous channels.

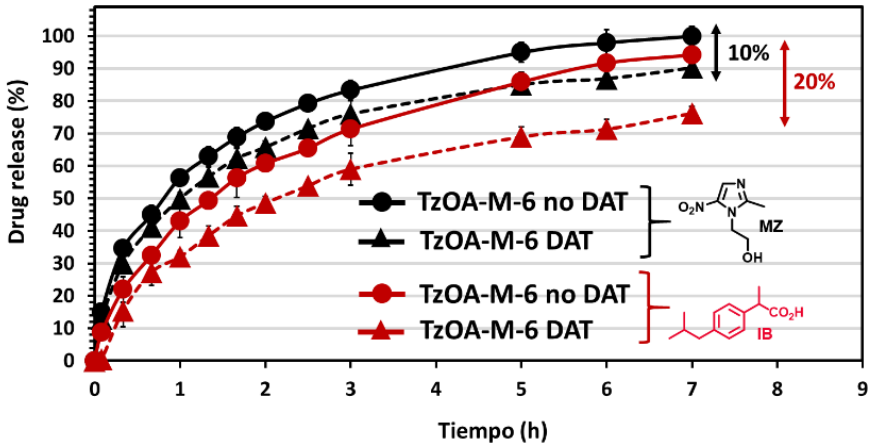

Figure 41. MZ release (black) and IB release (red) of DAT and DAT-free hydrogel formulations.

Importantly, the gap in the release between VDAT hydrogels and VDAT-free hydrogels is higher for **IB** (~20%) than for **MZ** (~10%). This is a strong evidence of the hydrophobic character of the VDAT monomer: since **IB** is more hydrophobic than **MZ**, it will interact stronger with the DAT matrix and thus the difference between the drug release with and without VDAT will become more accused than with the more hydrophilic drug.

b) The role of pH

The pH-responsiveness of the DAT-based hydrogel makes them appealing candidates for pH-responsive drug delivery. We wished to determine whether the ability of the DAT hydrogel to increase its SD on low acidic pH could be harnessed as a chemical trigger to deliver a drug on demand.

For this purpose, we loaded **TzOA-M-6** hydrogels with a different model drug, **imipramine** (**IMI**), following the same protocol for drug loadings used so far. Figure 42 shows the release profiles for **IMI** from the hydrogels both in SGF buffer and water. The profiles reveal that when the pH trigger is applied, more

than a 10% release payload is released with respect to neutral medium at early times.

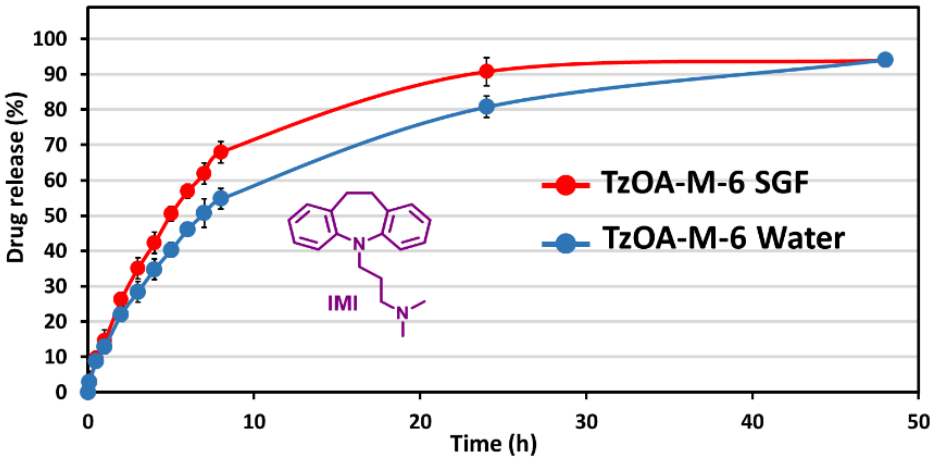

Figure 42. Influence of the pH-responsiveness on the release of model drug **IMI** from **TzOA-M-6** hydrogels in aqueous and SGF media.

This result is predicated on the pH-responsive nature of the DATs in the hydrogel. In neutral medium, the DATs retain drugs *via* strong hydrophobic interactions (namely, H-bonds and π-π stackings), particularly if the drug has aromatic rings, such as for the case of **IMI** (Figure 43 left).

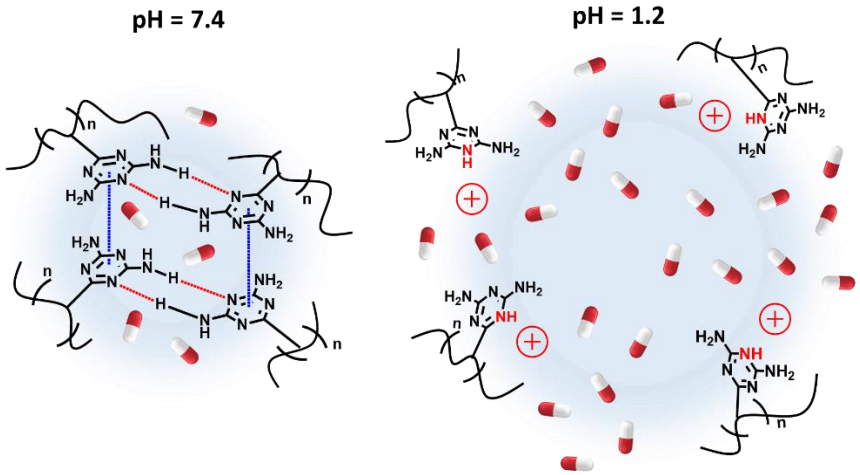

Figure 43. Mechanism for the pH-triggered drug release of model drug from the **TzOA-M-6** hydrogels.

In SGF medium, where the DATs protonate and the hydrophobic domains are disrupted, the drug is released from its hydrophobic entrapment (Figure 43 right).

These results thus corroborate that DAT-based hydrogels may be used for targeted drug delivery, for example to deliver a cargo selectively on the gastrointestinal (GI) tract, where the pH oscillates between 1-3.

It is worth mentioning the importance of choosing the appropriate drug depending on the pH of the release medium. The model drug **IMI** is an alkaline drug, and thus in SGF medium it will protonate and enhance its solubility. Upon releasing other acidic drugs in SGF buffer, such as **naproxene** (**NX**) or **ibuprofen (IB)**, we observed that the drugs precipitated into crystals inside the hydrogel during drug release (Figure 44), and thus these were ruled out for pH-responsive drug delivery experiments.

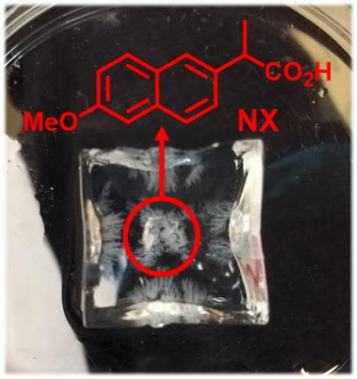

Figure 44. Crystals of **NX** precipitate inside the SGF-swollen hydrogels.

c) The role of the crosslinker

In order to study the impact of the crosslinker in the drug release, we conducted an experiment where we measured the release of **ibuprofen (IB)** from two hydrogels containing different crosslinker agents, namely, **TzOA-M-6** (containing MBA) and **TzOA-P-1** hydrogels (containing PEGDA), and allowed the release of drug in phosphate saline buffer (PBS, pH = 7.4) (Figure 45a).

The results show there is a mild 10% increase of **IB** release for **TzOA-P-1** hydrogels than for **TzOA-M-6** counterparts. This observation is explained by the type of crosslinker used: for longer crosslinker PEGDA, pore sizes will be larger and so the drug will be less restrained inside the crosslinked network (Figure

45b). Conversely, for shorter MBA crosslinker, pore sizes will be smaller and the drug will be more retained within the polymer network, thus the release of drug is this way more contained.

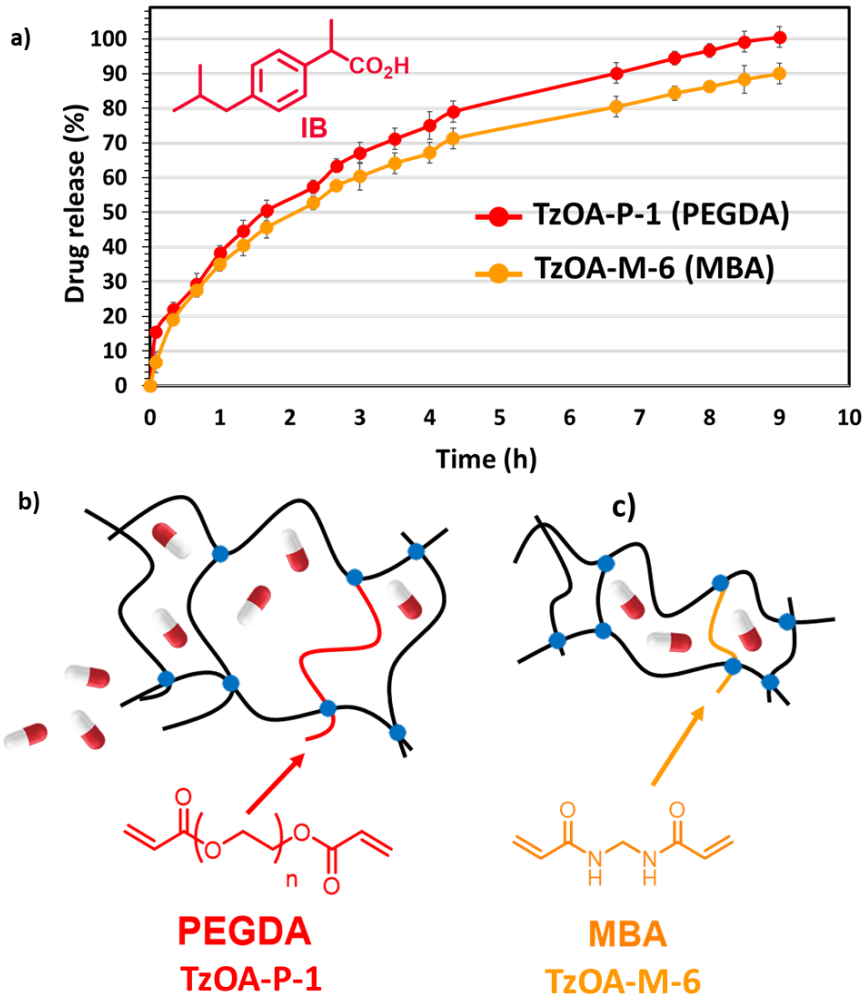

Figure 45. Influence of the crosslinker agent in the drug release of model drug IB a) Drug release from the hydrogels and depiction of the release from b) TzOA-P-1 hydrogels and c) TzOA-M-6 hydrogels.

d) The role of the pores

Another parameter that determines the drug release rates is the state in which the pores of the hydrogels are. By modulating the water content inside the network of the hydrogels, the pores may shrink or expand depending on the methodology employed to remove the water from them.

Three different type of hydrogels may be observed according to the state of their porous structure (Table 5):

Table 5. Type of hydrogels according to their pore shape.

Type of gel	Aerogel	Hydrogel	Xerogel
Preparation	Freeze-drying	Swelling	Drying
Pore shape	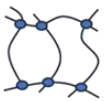 Lyophilized pore	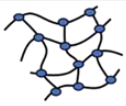 Swollen pore	 Collapsed pore
Appearance		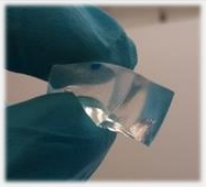	
	Pore size decrease		

- **Aerogels** are water-swollen hydrogel that have been freeze-dried in a lyophilizer. Since the hydrogel was swollen to its maximum state prior to freeze-drying, the pores remain maximally expanded even after the water has been removed.

- **Xerogels** are obtained once the water-swollen hydrogel are heated to complete dryness and all the water is fully evaporated. In this process, the pores of the hydrogels collapse to their minimum size.

- Finally, **hydrogels** are the most common formulation for these materials; these may be obtained by immersing the corresponding xerogel counterpart in water until all the water has filled their porous network to their maximum capacity.

These three scenarios may also determine the ratio of drug delivery, since the size of the pores varies in each case. In order to ascertain this, we prepared the three hydrogel formulations using the recipe **TzOA-M-6**.

First, we loaded the hydrogels with **MZ** model drug**,** by simply immersing the corresponding xerogel in an aqueous solution of the drug until it reached

the maximum swollen state (hydrogel). In a parallel experiment, another MZ-loaded hydrogel was lyophilized in a freeze-drier (aerogel). Finally, a third drug-loaded hydrogel was placed in an oven until total dryness (xerogel). The three hydrogel formulations were then immersed in water and their release rates with respect to time were measured (Figure 46).

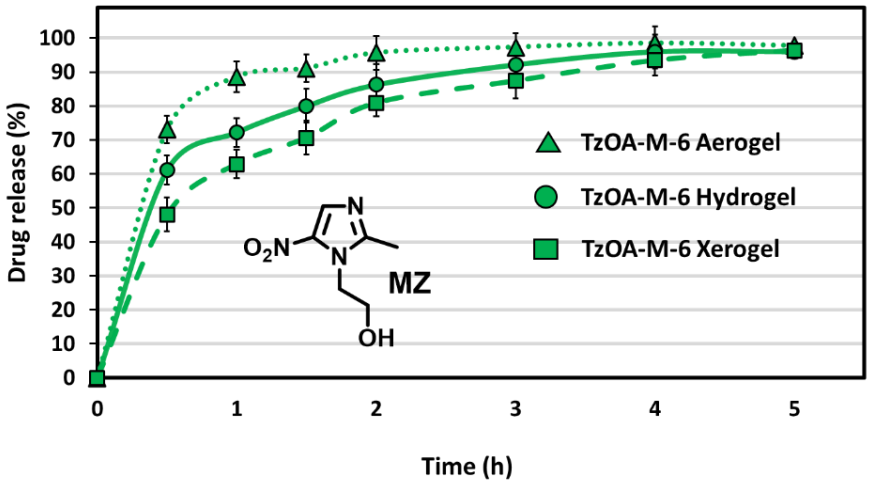

Figure 46. Influence of the pore shapes on the release of model drug MZ from aerogels, hydrogels and xerogels.

The results show that aerogels release the fastest drug rates, followed by hydrogels and xerogels, respectively, which correlates with the expected trend.

The reason behind this result is the pore sizes: aerogels, which have the pores expanded to their maximum, quickly release the drug to the medium. On the opposite scenario, xerogels release the drug at the slowest pace, since their pores are in the collapsed state. It follows that, depending on the porous state, the release of the drug from the hydrogel can be tailored to be faster or slower.

2.2.4.2. Delivery of hydrophobic drugs

To determine experimentally the hydrophobic character of the DAT-based hydrogels, we compared both their drug loading capacities and their drug release rates mediated by diffusion of the six drugs of increasing hydrophobicity (see Figure 38).

The choice of the drugs under study was made based on their polar character and hydrophobicity: MZ is a small imidazole drug with highly polar -

NO_2 and -OH groups. **BZ** has two polar ester and amine groups, however is less polar than **MZ** due to the phenyl ring. **IB** has both a phenyl ring and a sec-butyl group which account for higher apolar character and higher hydrophobicity. **NX** is highly apolar due to the presence of a napthtalene moiety. Further, **IMI** has a tricyclic bulky core. Finally, **RHO** is an 8-member ring dye with highly hydrophobic character.

a) Drug loadings

For the calculations of the drug loadings, dried hydrogel samples were immersed in a $2x10^{-3}$ M solution of the corresponding drug in PBS at room temperature until a hydrogel in its maximum swelling was obtained. The drug loading was then calculated by an indirect method (Equation 2):

$$Drug\ loading\ (\%) = \left(\frac{m_0 - m_u}{m_0}\right) \mathrm{x}\ 100$$

Equation 2. Formula for drug loading calculation.

Where m_0 is the initial drug mass present in the loading medium and m_u is the mass of the unloaded drug remaining after the hydrogel had incorporated the drug.

Figure 47 shows the drug loading profiles for the chosen commercial drugs in the DAT-based hydrogels.

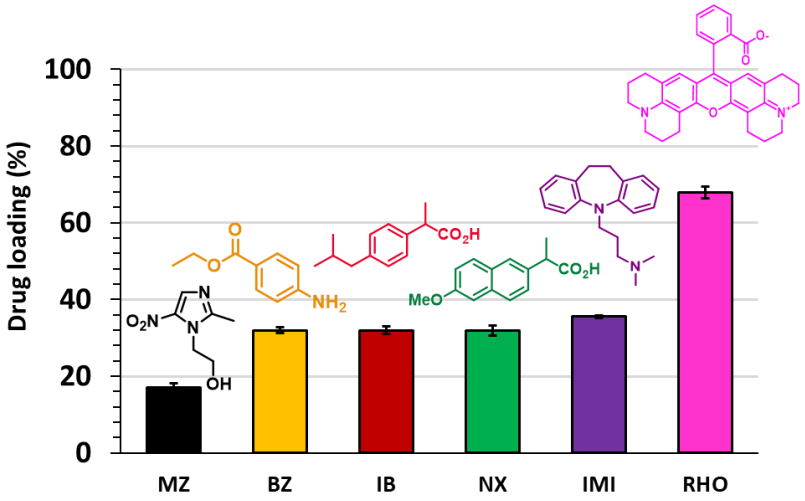

Figure 47. Drug loadings for drugs of increasing hydrophobicity.

There is a clear growing trend in the hydrogel loadings as the hydrophobicity of the drug increases: only loadings of 17% were registered for MZ, a small and highly hydrophilic drug, whereas for IMI, a bulky three-membered ring hydrophobic drug, loadings reached up to 35%. Finally, for RHO, the most hydrophobic drug studied here, drug loadings peaked to 68%.

This suggested the suitability of the DAT matrix for hosting hydrophobic drugs within the porous hydrogel network, possibly due to hydrophobic non-covalent interactions between the drug and the DAT molecules.

b) Drug release

The *in vitro* drug release experiments were carried out by immersion of drug-loaded hydrogels in 50 mL of PBS media. The samples were placed in an orbital mixer and shaker operating at 70 rpm and heating at 37 ºC (Figure 48), which simulated the conditions that occur in physiological environments. At defined time intervals, aliquots of 5 mL were withdrawn and replaced with the same volume of fresh buffer.

Figure 48. Orbital mixer and shaker with the drug release vessels operating at 70 rpm and heating at 37 ºC.

The drug release took place by diffusion of the drug from inside the DAT hydrogel network out onto the PBS buffer solution (Figure 49). The results showed an obvious downward trend where the release rates became slower as the hydrophobicity of the drug increased.

The drug RHO showed a particularly slower permeation than the rest of the drugs, with only a 10% payload released after 7h, in contrast with the 90% released by MZ by that same time. As suggested the loading studies, the release experiments point a stronger drug-hydrogel affinity with the highly

hydrophobic drugs, possibly through non-covalent interactions, and this causes the release to pace down.

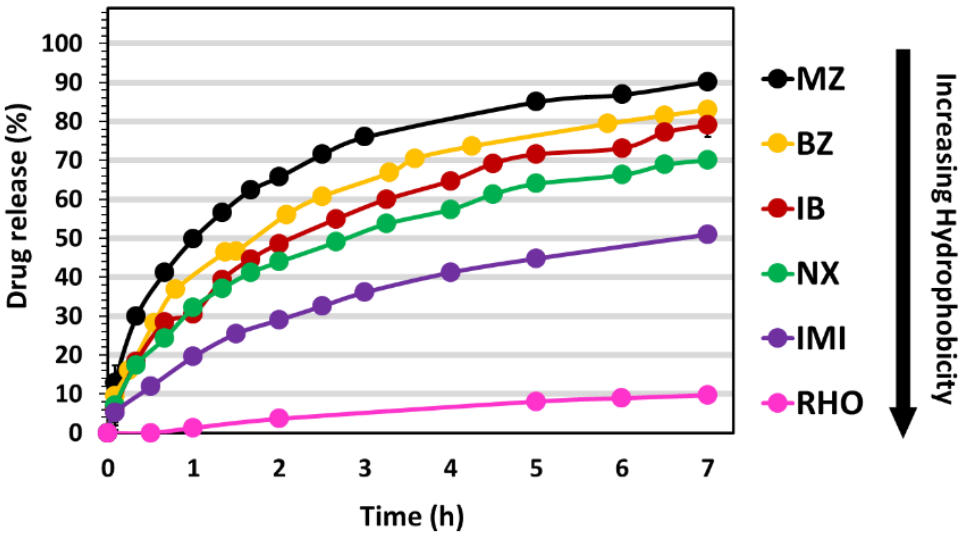

Figure 49. Drug release for drugs of increasing hydrophobicity.

The results obtained with both experiments suggest DAT hydrogels may be promising candidates for hydrophobic drug delivery for several reasons: first, the drug loadings for hydrophobic drugs are significantly increased in DAT hydrogels, which is one of the main setbacks of hydrogels, being intrinsically hydrophilic.[58] Further, since DAT hydrogels pace down the release of hydrophobic drugs, they may avoid burst release, this is, the sudden initial rapid release typically observed at the early moments on the release profiles in hydrogel matrices.[59]

c) Delivery of growth factors: retinoic acid

The scope of DAT-based hydrogels for controlled release of common hydrophobic drugs can be further expanded to other compounds of broader biological significance, such as growth factors. In this study, we proposed **retinoic acid (RA)** as a model hydrophobic active compound for growth factor delivery in DAT-based hydrogels (Figure 50). Retinoic Acid is a metabolite of vitamin A required for growth and development; it acts as an intracellular signaling molecule that guides development of the embryo through Hox genes.[60]

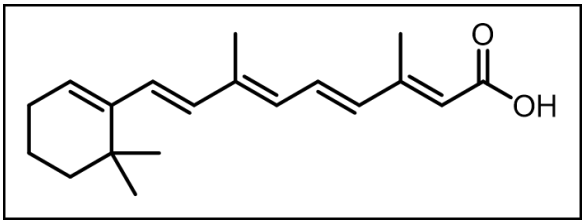

Figure 50. Chemical structure of retinoic acid RA.

RA resulted in the highest hydrophobicity tested so far and so it was required to conduct the loading and release experiments in PBS and in the presence of a surfactant, namely, sodium dodecyl sulfate (SDS). Due to their amphiphilic nature, long-chain surfactants like SDS help dissolve compounds of high hydrophobicity such as RA through micellization.

The drug loadings were performed by immersing dried hydrogel samples in a $1.7x10^{-4}$ M solution of RA in PBS/SDS (0.1M) at room temperature until maximum swelling had occurred. Both the UV/VIS spectrum and calibration curves for RA in PBS/SDS 0.1M are shown in Figure 51.

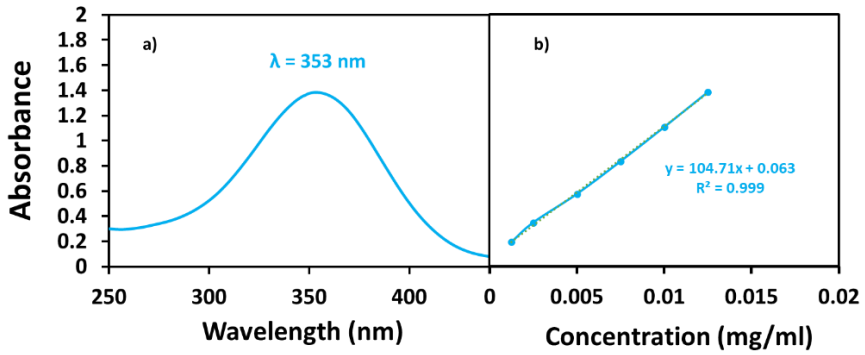

Figure 51. Retinoic acid (RA) a) UV/VIS spectrum and b) calibration curves in PBS medium.

Only RA loadings of up to 25% were observed, which is below expected for the trend observed in the previous drugs. Despite the presence of surfactant, the RA loading solution was 10 times more diluted than the drugs studied so far, due to the singular hydrophobicity of the growth factor. The smaller drug concentrations of the loading solution along with the presence of bulky surfactants may account for the low loading values observed for RA in DAT hydrogels.

The release experiments of **RA** in PBS/SDS medium for 24h are shown in Figure 52, which were overlaid with the release profiles of the smaller drugs **MZ, BZ, IB, NX, IMI**, and **RHO**, previously studied.

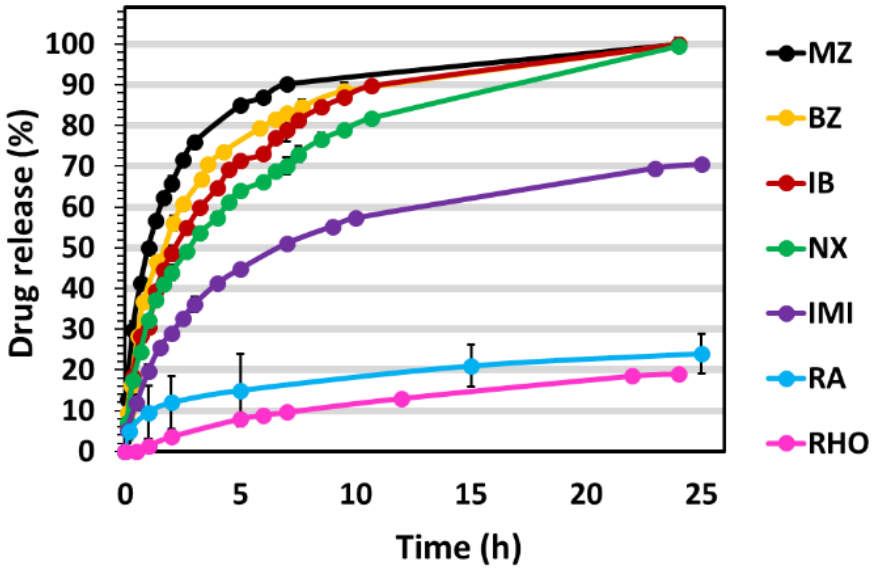

Figure 52. Comparison of drug release profiles for drugs of increasing hydrophobicity and retinoic acid (RA).

RA was released from the DAT hydrogels at the slow rate close to **RHO**; in comparison, barely a 20% of **RA** was released after 24h, whereas a 70% and a 100% were released for **IMI** and the rest of drugs, respectively, by that time.

It is likely that **RA** is strongly retained inside the DAT hydrophobic cavities through non-covalent interactions between the DATs and the unsaturated double bonds of the growth factor. The ability of the DAT hydrogels to pace down the release of drugs may be harnessed for cell differentiation, which is strongly determined by the release rates of growth factors, such as **RA**, incoming to the cell.[61] By modulating these release rates, for example, tailoring the amount of VDAT monomer in the hydrogel formulation, different cell responses may be achieved.

2.2.4.3. Theoretical calculations of the hydrophobic domains

Based on the previous drug loading and release studies, which point out that hydrophobic drugs interact more favorably with the DAT matrix, we have attempted to model the hydrophobic microenvironments that take place inside

the hydrogels and theorised whether these could function as suitable hydrophobic cavities to host poor-water soluble drugs.

For this, we have aimed to theoretically study how triamine triazine (or melamine) can modify their supramolecular behaviour when implemented into a polymeric structure. For such case, we envisioned the used of advance first principle methodologies to compare the interaction between a supramolecular construct of melamine and a modified triazine with an aliphatic residue (to model the polymeric chains, which herein represent the DAT-based matrix). We then carried out two different sets of modellizations:

- A first aproximation in which the triazines are modelled into circular stacked hexamers, based on the motifs in which DATs associate.[12]

- A further calculation of the stability and interactions of these hexamers with both a hydrophobic and a hydrophilic drug species. Following the line of this study, we chose the most hydrophobic drug **RHO** and the most hydrophilic drug **MZ** as candidate drugs for the modelization.

The *ab initio* calculations presented in this work have been produced using SIESTA code[62] which is a highly efficient program for studying the structural and electronic calculation of molecules and solids. In the case of the hexamer systems (Figure 53a), we computed the total adsorption energies ($E_{Hexamer}$) as shown in Equation 3:

$$E_{Hexamer} = E_{triazine\text{-}triazine} - \mathrm{n\ x}\ E_{triazine}$$

Equation 3. Total adsorption energy of hexamers.

where $E_{triazine\text{-}triazine}$, and $E_{triazine}$ are the triazine supramolecular hexamers and the triazine molecule, respectively. The n index is the number of triazine molecules.

The stability of these systems is very similar, and it is based on the four hydrogen bonds connecting each of the triazines molecules to the neighbouring units (Figure 53a, dashed lines). In this case, the aliphatic residue to simulate the polymeric chain was placed on the outside of the hexamer, and it doesn't affect the stability of the system concerning the melamine free hexamer ($E_{Hexamer}$ = -2.29 vs -2.27 eV for the free and polymerised hexamers, respectively; see Figure 53c).

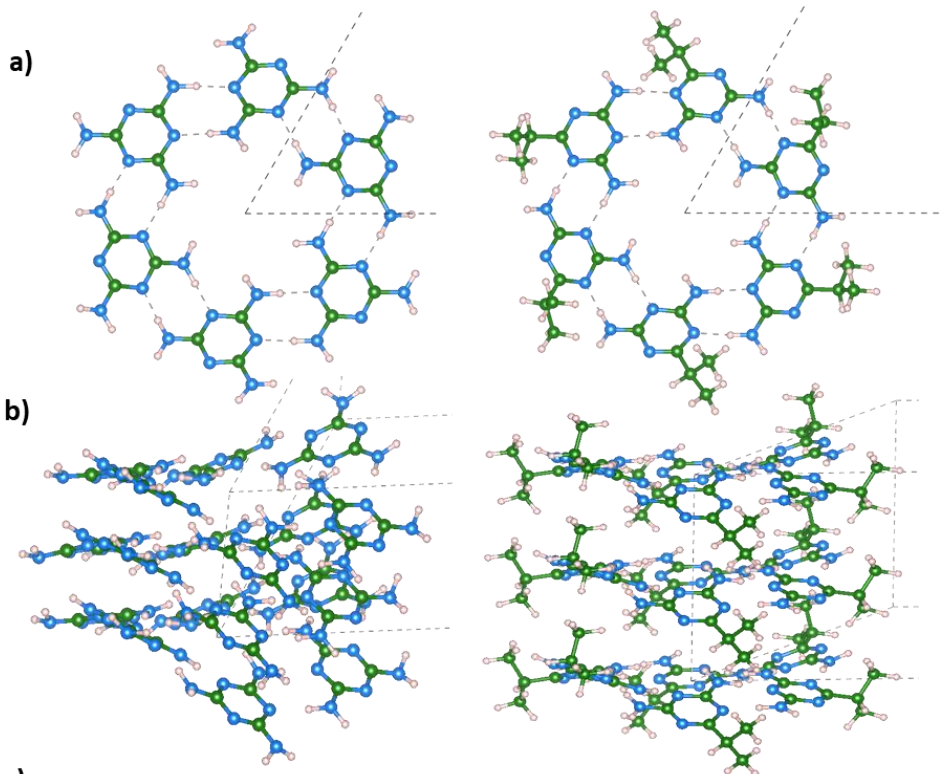

c)

System	E[hexamer] (eV)	E[triazine-stacking] (eV)
Melamin	-2.29	-2.00
Polymer	-2.27	-1.17

Figure 53. Calculated structures in DAT-based hydrogels: a) Hexameric rosettes and b) Hexameric rosette stackings for melamine (left) and polymerised melamine (right) supramolecules and c) total energies of the systems.

These data reflect that the formation of H-bonded-driven DAT hexamers also likely occurs within a polymerised environment in the DAT-based hydrogels.

Further, in the case of the stacking of several of these triazine hexamer supramolecules (Figure 53b) we computed the total stacking energies of these systems ($E_{triazine\text{-}stacking}$) as shown in Equation 4:

$$E_{triazine\text{-}stacking} = E_{Stacking} - 2\ x\ E_{triazine\text{-}triazine}$$

Equation 4. Total stacking energy between hexamers.

where $E_{Stacking}$ and $E_{triazine\text{-}triazine}$, are the total energies of the systems, and the triazine supramolecular hexamers, respectively.

The results show that stackings between melamine hexamers rely mainly on π - π interactions, as also corroborated by the average interlayer distance between melamine molecules (around 3.5 Å), whereas for polymerised melamine systems, less degree of interaction is observed ($E_{triazine\text{-}stacking}$ = -2.00 *vs* -1.17 eV for the free and polymerised melamine hexamers, respectively (see Figure 53c), with CH - π interactions as the main stability forces, which can be deduced from the stability energies and the longer average distance between the layers (around 5.6 Å).

Based on these results, we can assume that in terms of stability, isolate melamine systems could tend to aggregate into these supramolecular circular systems, forming rods (or fibres).

When these molecules are incorporated into a polymeric matrix, there is some loss of a degree of freedom to the assembly of these systems. Still, given the flexibility and fluency of the polymeric chains, it can be reasonably assumed that these supramolecular systems could form between adjacent triazine molecules, assembling into aggregates inside the hydrogels, as suggested in the literature.[38]

We then replaced one layer of these triazine hexamers with the hydrophobic drug **RHO** and hydrophilic drug **MZ**, which represents the hydrophobic "pockets" and re-optimised the systems to a new minimum. For the stacking of the drug compounds into these supramolecules, we computed the total interaction energies of these systems ($E_{stacking\text{-}drug}$) as shown in Equation 5:

$$E_{Stacking\text{-}Drug} = E'_{Stacking} - E_{triazine\text{-}triazine} - E_{Drug}$$

Equation 5. Total stacking energy between hexamers and drug.

where $E'_{stacking}$, $E_{triazine\text{-}triazine}$, and E_{Drug} are the total energies of the systems, the triazine supramolecular hexamers and the isolated drug molecules, namely, **MZ** and **RHO**.

The hydrophilic drug **MZ** appears to interact only poorly with triazine supramolecular structures, both in free and polymerised states, given their small absorption energies (Figure 54a,c).

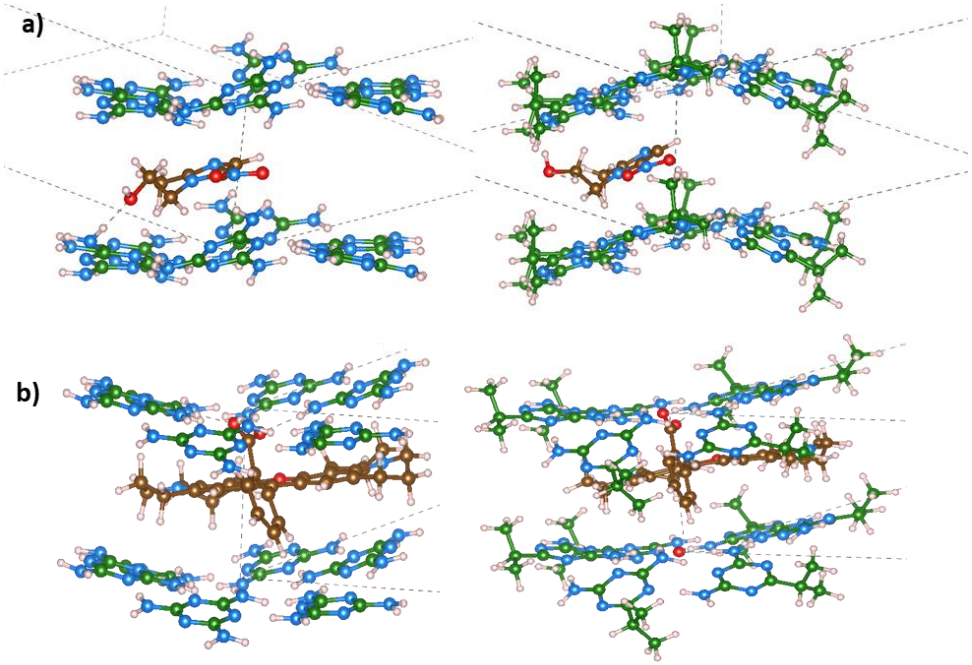

c)

System	E[Stacking-MZ] (eV)	E[Stacking-RHO] (eV)
Melamin	-0.58	-2.46
Polymer	-0.69	-2.90

Figure 54. Calculated structures in DAT-based hydrogels: a) **MZ** stacking sandwiches b) **RHO** stacking sandwiches for melamine (left) and polymerised melamine (right) supramolecules and c) total energies of the systems.

This poor stabilization is related to a reduced number of long-range interactions, the latter corresponding to a hydrogen bond interaction between the hydroxyl groups of metronidazole and the amino groups in the melamine.

In contrast, the hydrophobic compound **RHO** interacts quite favourably with both melamine and polymerised melamine (Figure 54b,c): both systems rely on reduced π–π interactions between the triazine hexamers and the rhodamine, as well as interactions between the NH_2 groups of the melamine with the COO^- residues in the fluorescent compound.

In the case of polymerised melamine, the sandwich-like system is slightly less compact (variation of 0.3 Å) due to the flexibility of the isopropyl residues, which flex to find CH - π interactions with the rhodamine phenyl group and confer additional stability to the supramolecular construct ($E_{Stacking\text{-}RHO}$ = -2.46 *vs* -2.90 eV for the free and polymerised melamine hexamers, respectively (see Figure 54c).

The calculations matched with the experimental data: drug loadings in the hydrogels increased 4-fold for the hydrophobic drug **RHO** with respect to hydrophilic **MZ** (68% *vs* 17%, respectively) (Figure 55).

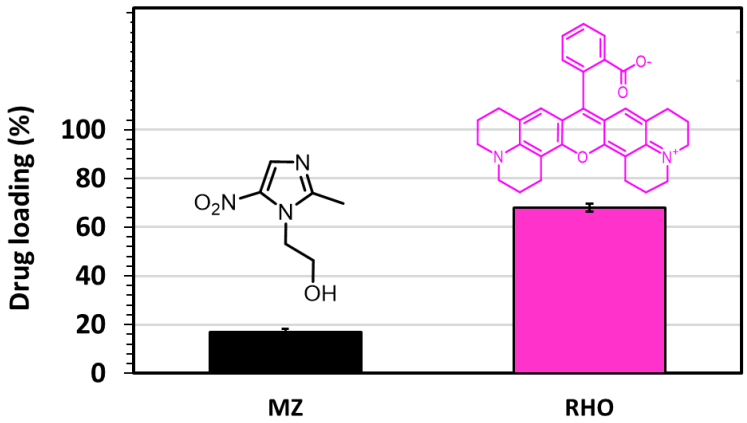

Figure 55. Experimental drug loadings for MZ and RHO in pristine DAT hydrogels.

In summary, the performed calculations strongly suggest that in these hydrogels, DATs tend to aggregate into stacked hexameric "pockets" inside which drugs of higher hydrophobic character stabilize. This stabilization occurs through favorable π-π and *CH*-π interactions between the DATs and the drug and are responsible for the affinity of the DAT-based hydrogels for hydrophobic compounds, in accordance with the experimental data.

2.3. References

[1] B. Klenke, M. Stewart, M. P. Barrett, R. Brun, I. H. Gilbert, *J. Med. Chem.* **2001**, *44*, 3440–3452.

[2] X. P. Hu, H. L. Chen, Z. Zheng, *Adv. Synth. Catal.* **2005**, *347*, 541–548.

[3] T. J. Mooibroek, P. Gamez, *Inorganica Chim. Acta* **2007**, *360*, 381–404.

[4] B. F. Abrahams, S. R. Batten, H. Hamit, B. F. Hoskins, R. Robson, *Chem. Commun.* **1996**, 1313–1314.

[5] J. A. Zerkowski, C. T. Seto, G. M. Whitesides, *J. Am. Chem. Soc.* **1992**, *114*, 5473–5475.

[6] P. Gamez, J. Reedijk, *Eur. J. Inorg. Chem.* **2006**, 29–42.

[7] F. Ugozzoli, C. Massera, *Cryst. Eng. Commun.* **2005**, *7*, 121–128.

[8] S. Ronchi, D. Prosperi, F. Compostella, L. Panza, *Synlett* **2004**, *6*, 1007–1010.

[9] J. M. Oliva, M. E. D. G. Azenha, H. D. Burrows, R. Coimbra, J. S. S. De Melo, M. Canle L, M. I. Fernández, J. A. Santaballa, L. Serrano-Andrés, *ChemPhysChem* **2005**, *6*, 306–314.

[10] L. M. Pedroso, M. M. C. A. Castro, P. Simões, A. Portugal, *Polymer (Guildf).* **2005**, *46*, 1766–1774.

[11] M. Yoshizawa, T. Kusukawa, M. Kawano, T. Ohhara, I. Tanaka, K. Kurihara, N. Niimura, M. Fujita, *J. Am. Chem. Soc.* **2005**, *127*, 2798–2799.

[12] K. E. Maly, C. Dauphin, J. D. Wuest, *J. Mater. Chem.* **2006**, *16*, 4695.

[13] G. M. Whitesides, J. P. Mathias, C. T. Seto, *Science (80-.).* **1991**, *254*, 1312–1319.

[14] J. Barberá, L. Puig, P. Romero, J. L. Serrano, T. Sierra, *J. Am. Chem. Soc.* **2006**, *128*, 4487–4492.

[15] J. S. Siegel, F. Cozzi, *Pure Appl. Chem.* **1995**, *67*, 683–689.

[16] C. A. Hunter, *Angew. Chemie Int. Ed. English* **1993**, *32*, 1584–1586.

[17] F. Cozzi, M. Cinquini, R. Annuziata, J. S. Siegel, *J. Am. Chem. Soc.* **1993**, *115*, 5330–5331.

[18] O. Ohmori, M. Kawano, M. Fujita, *Cryst. Eng. Commun.* **2005**, *7*, 255–259.

[19] R. D. Pike, B. D. Borne, J. T. Maeyer, A. L. Rheingold, *Inorg. Chem.* **2002**, *41*, 631–633.

[20] R. Deans, G. Cooke, V. M. Rotello, *J. Org. Chem.* **1997**, *62*, 836–839.

[21] F. H. Beijer, R. P. Sijbesma, J. A. J. M. Vekemans, E. W. Meijer, H. Kooijman, A. L. Spek, *J. Org. Chem.* **1996**, *61*, 6371–6380.

[22] A. Díaz-Ortiz, J. Elguero, C. Foces-Foces, A. de la Hoz, A. Moreno, M. C. Mateo, A. Sánchez-Migallón, G. Valiente, *New. J. Chem.* **2004**, *28*, 952–958.

[23] J. M. Galindo, J. Leganés, J. Patinõ, A. M. Rodríguez, M. A. Herrero, E. Diéz-Barra, S. Merino, A. M. Sánchez-Migallón, E. Vázquez, *ACS Macro Lett.* **2019**, *8*, 1391–1395.

[24] J. R. Cummings, E. Cohen, *Novel Hypotensive Compositions Containing 1-Substituted-3-Cyanoguanidines*, **1967**, Cummings, J. R.; Cohen, E.; US Patent, US3308022.

[25] Z. Brzozowski, F. Sa, *Eur. J. Med. Chem.* **2002**, *37*, 709–720.

[26] G. H. Kuo, A. DeAngelis, S. Emanuel, A. Wang, Y. Zhang, P. J. Connolly, X. Chen, R. H. Gruninger, C. Rugg, A. Fuentes-Pesquera, et al., *J. Med. Chem.* **2005**, *48*, 4535–4546.

[27] G. Cooke, H. Augier de Cremiers, V. M. Rotello, B. Tarbit, P. E. Vanderstraeten, *Tetrahedron* **2001**, *57*, 2787–2789.

[28] K. Arya, A. Dandia, *Bioorganic Med. Chem. Lett.* **2007**, *17*, 3298–3304.

[29] A. Díaz-Ortiz, J. Elguero, A. De La Hoz, A. Jiménez, A. Moreno, S. Moreno, A. Sánchez-Migallón, *QSAR Comb. Sci.* **2005**, *24*, 649–659.

[30] A. Díaz-Ortiz, J. Elguero, C. Foces-Foces, A. De la Hoz, A. Moreno, S. Moreno, A. Sánchez-Migallón, G. Valiente, *Org. Biomol. Chem.* **2003**, *1*, 4451–4457.

[31] B. Liu, W. Liu, *Macromol. Rapid Commun.* **2018**, *39*, 1–11.

[32] Q. Wang, Y. Zhang, X. Dai, X. Shi, W. Liu, *Sci. China Technol. Sci.* **2017**, *60*, 78–83.

[33] H. Asanuma, T. Ban, S. Gotoh, T. Hishiya, M. Komiyama, *Macromolecules* **1998**, *31*, 371–377.

[34] B. Xu, Y. Zhang, W. Liu, *Macromol. Rapid Commun.* **2015**, *36*, 1585–1591.

[35] P. Wang, J. Zhang, Y. Li, N. Wang, W. Liu, *Mater. Lett.* **2015**, *142*, 71–74.

[36] L. Tang, Y. Yang, T. Bai, W. Liu, *Biomaterials* **2011**, *32*, 1943–1949.

[37] N. Wang, Y. Han, Y. Liu, T. Bai, H. Gao, P. Zhang, W. Wang, W. Liu, *J. Hazard. Mater.* **2012**, *213–214*, 258–264.

[38] L. Tang, W. Liu, G. Liu, *Adv. Mater.* **2010**, *22*, 2652–2656.

[39] C. G. Overberger, F. W. Michelotti, *J. Am. Chem. Soc.* **1958**, *80*, 988–991.

[40] N. Sawa, Wakaba-cho, Tadotsu-cho, N. Kagawa-kan, T. Masuda, Kitahirayama-cho, M. K, *Process for Synthesizing 2-Vinyl-4,6-Diamino-s-Triazine*, **1987**, Sawa, N., Masuda, T. Japan. Application. No. 85305954.1.

[41] J. L. Drury, D. J. Mooney, *Biomaterials* **2003**, *24*, 4337–4351.

[42] X. Zhao, *Soft Matter* **2014**, *10*, 672–687.

[43] A. M. L. S. M. Christopher, *Physiol. Behav.* **2016**, *176*, 100–106.

[44] C. Gong, T. Qi, X. Wei, Y. Qu, Q. Wu, F. Luo, Z. Qian, *Curr. Med. Chem.* **2013**, *20*, 79–94.

[45] M. Ishihara, K. Obara, T. Ishizuka, M. Fujita, M. Sato, K. Masuoka, Y. Saito, H. Yura, T. Matsui, H. Hattori, et al., *J. Biomed. Mater. Res. - Part A* **2003**, *64*, 551–559.

[46] N. Huebsch, C. Kearney, X. Zhao, C. Cezar, *Proc. Natl. Acad. Sci.* **2014**, *111*, 9762–9767.

[47] J. Li, D. J. Mooney, *Nat. Rev. Mater.* **2016**, *1*, 16071.

[48] J. Zhang, N. Wang, W. Liu, X. Zhao, W. Lu, *Soft Matter* **2013**, *9*, 6331.

[49] X. Zhao, *Soft Matter* **2014**, *10*, 672–687.

[50] W. Xu, P. Ling, T. Zhang, *J. Drug Deliv.* **2013**, *2013*, 1–15.

[51] E. Larrañeta, S. Stewart, M. Ervine, R. Al-Kasasbeh, R. F. Donnelly, *J. Funct. Biomater.* **2018**, *9*, 13.

[52] M. McKenzie, D. Betts, A. Suh, K. Bui, L. D. Kim, H. Cho, *Molecules* **2015**, *20*, 20397–20408.

[53] R. Mateen, T. Hoare, *J. Mater. Chem. B* **2014**, *2*, 5157–5167.

[54] M. Cai, K. Zhu, Y. Qiu, X. Liu, Y. Chen, X. Luo, *Colloids Surfaces B Biointerfaces* **2014**, *116*, 424–431.

[55] E. G. Bellomo, M. D. Wyrsta, L. Pakstis, D. J. Pochan, T. J. Deming, *Nat. Mater.* **2004**, *3*, 244–248.

[56] B. Liu, W. Liu, *Macromol. Rapid Commun.* **2018**, *39*, 1–11.

[57] J. Leganés, A. Sánchez-Migallón, S. Merino, E. Vázquez, *Nanoscale* **2020**, *12*, 7072–7081.

[58] T. R. Hoare, D. S. Kohane, *Polym. with aligned carbon Nanotub. Act. Compos. Mater.* **2008**, *49*, 1993–2007.

[59] N. A. Peppas, *Curr. Opin. Colloid Interface Sci.* **1997**, *2*, 531–537.

[60] L. Z. Holland, *Nature* 2007, *447*, 153–155.

[61] C. Del Angel-Mosqueda, Y. Gutiérrez-Puente, A. P. López-Lozano, R. E. Romero-Zavaleta, A. Mendiola-Jiménez, C. E. Medina-De la Garza, M. Márquez-M, M. A. De la Garza-Ramos, *Head Face Med.* 2015, *11*, 1–9.

[62] J. M. Soler, E. Artacho, J. D. Gale, A. García, J. Junquera, P. Ordejón, D. Sánchez-Portal, *J. Phys. Condens. Matter* 2002, *14*, 2745–2779.

Chapter 3

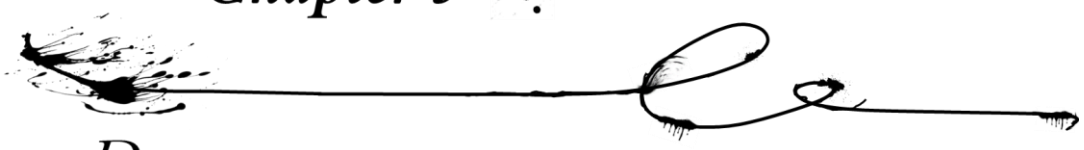

Diaminotriazine Hybrid Hydrogels: Synthesis and Characterization

3.1. Introduction

3.1.1. Nanomaterials

Nanomaterials (NMs) describe the materials sized between 1 and 100 nm encompassing the nanoscale region, including small molecules (Figure 1). These materials are small enough to fit into cells and complex cellular forms, which in the past decades has granted them increasing scientific attention, especially in the biomedical field.[1]

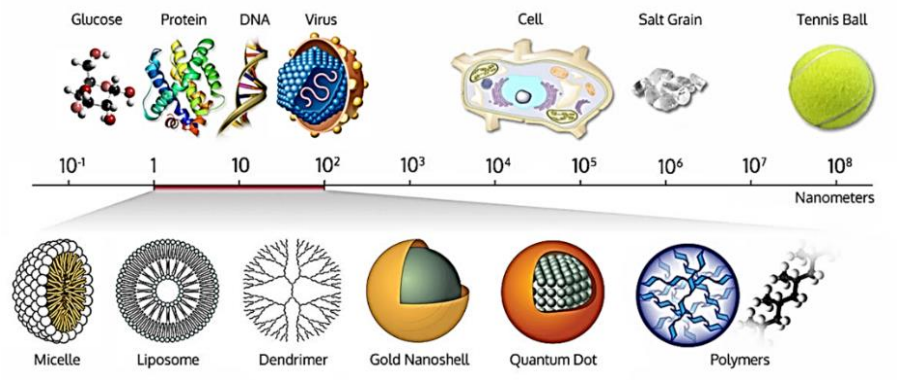

Figure 1. Scale of nanomaterials and various objects.

Surprisingly, the nanomaterials produce a unique character with new characteristics and capabilities by modifying the shape and size at the nanoscale level. Nanomaterials may be of different shapes, such as small nanoparticles (NPs), nanorods or nanotubes and nanosheets, which can be characterized based on their dimensionality (0D,1D and 2D, respectively). By the interaction of two or more particles, their physical properties will be altered and more complex structures may arise, which generally fall into the 3D domain. Based on their morphology, size and properties, nanomaterials may be classified into different types.[2] These will be briefly explained in the following sub-sections.

3.1.1.1. Carbon-based nanomaterials

The main constituent in this type of nanomaterials is the carbon atom, which is one of the most common elements in nature. The natural allotropes of carbon are amorphous carbon, diamond and graphite, which all differ in their crystalline

structure: while diamond has a sp^3-defined and extended network, graphite consists in sp^2-stacked hexagonal honeycombs.

On the contrary, amorphous carbon has no defined structure. The main types of carbon nanomaterials are carbon nanotubes, fullerenes, graphite and graphene, which all present remarkably different shapes (Figure 2). Carbon nanotubes (CNTs) are graphene sheets which are rolled into a tube; they may be single-walled (SWCNT) or multi-walled (MWCNTs), which have several concentric sheets. These are much stronger than steel and can be useful for structural enhancement.[3] Fullerenes, on the other hand, are hollow cage particles with sixty or more sp^2 -hybridized carbon atoms. Its structure is similar to a hollow football with pentagonal and hexagonal carbon units organized in a regular pattern. They show good electrical conductivity, electron affinity, and high strength.[4]

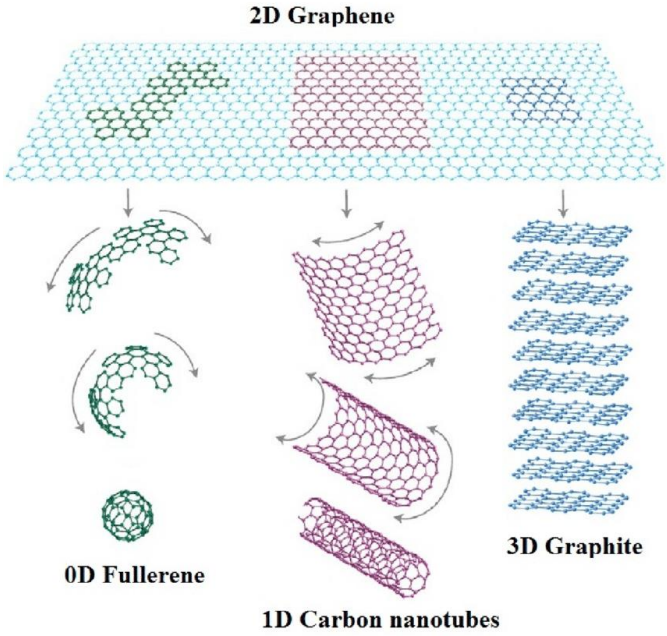

Figure 2. Theoretical conceptualization of fullerene, carbon nanotubes and graphite from graphene.

Graphene is composed of a single atomic layer of sp^2 hybridized carbon atoms in a honeycomb-fashion crystal lattice. According to the number of graphene layers, graphene may be categorized as few-layer graphene (FLG) (2-5 stacked graphene sheets) or multi-layer graphene, with a number of layers similar to that of graphite.[5] Each layer presents a 2D structure with high specific surface area, which allows these materials to display remarkable electronic, thermal, mechanical and optical properties.[6]

For example, graphene presents an unusually high conductivity as a result of the way electrons propagate through the graphene sheet. This is possible due to the point where the conduction and valence bands meet, known as the Brillouin Zone.[7] Due to the conical shape of these bands, graphene is referred to as a semiconductor of zero band gap (Figure 3).

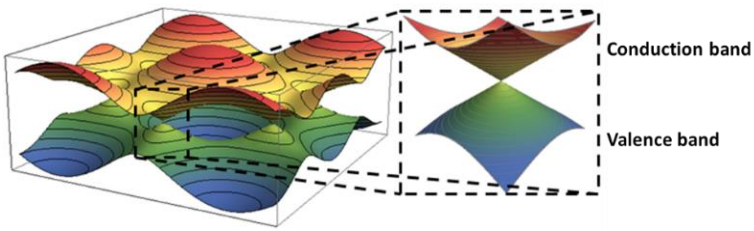

Figure 3. Conduction and valence bands of single-layer graphene.

Graphene also has an excellent mechanical strength. According to atomic force microscopy (AFM) measurements, the Young´s Modulus of a single-layer graphene was shown to be amongst the strongest materials measured so far.[8] This was attributed to its particular two-dimensional geometry, high surface to volume ratio and interface interactions. Additional outstanding properties of this material are its high thermal conductivity and high optical transparency.[9]

3.1.1.2. Metal-based nanomaterials

These nanomaterials include metal and metal oxide nanoparticles and other nanostructured materials. These are fabricated from metal ions, such as Au or Ag or metal oxides such as TiO_2 and ZnO, usually from chemical or photochemical methods.

By using reducing agents the metal oxides are reduced to metal nanoparticles, which have a high surface area and good adsorption ability of certain molecules.[10] Several types of inorganic NPs exhibiting photothermal, photochemical and magnetic properties have been widely used for detection and diagnostic applications (Figure 4).

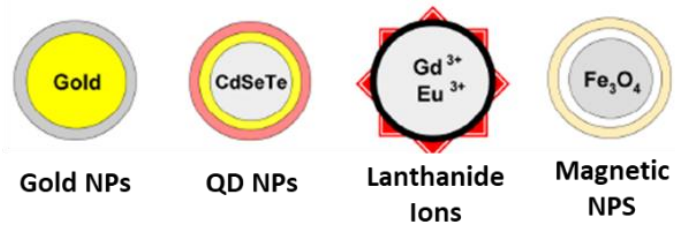

Figure 4. Metal-based nanoparticles.

For example, gold NPs are interesting biomedical tools for tumor imaging, due to their optical and electrical properties.[11]

Quantum dots (QDs) are semiconductors which have an appropriate range of absorption bands for use as imaging probes.[12] Lanthanide-doped NPs, on the other hand, allow the conversion of low energy light, such as near infrared (NIR), to high energy visible or ultraviolet (UV) light and have also been studied for treatment of tumors.[13]

One of the most studied inorganic-based nanoparticles are magnetic nanoparticles (MNPs), which can be manipulated using magnetic fields. Such nanoparticles typically consist of a magnetic material, often iron, nickel and cobalt, and typically range in size between 1-100 nm (Figure 5).

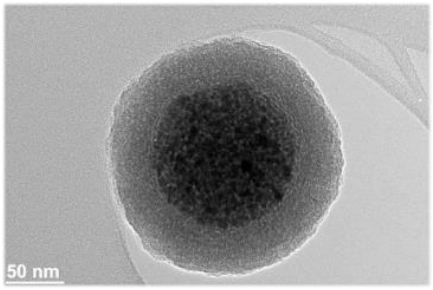

Figure 5. TEM image of a magnetite nanoparticle.

MNPs have been widely studied for use in catalysis,[14] biomedicine,[15] magnetic resonance imaging,[16] or environmental applications,[17] among many others. Perhaps the most common kind of MNPs are the iron oxide (Fe_3O_4)-based NPs, commonly referred to as superparamagnetic iron oxide nanoparticles (SPIONs).

The main methodology for SPIONs synthesis is the co-precipitation method, which is a straightforward way to synthesize iron oxides from Fe^{3+}/Fe^{2+} salt solutions in alkali media under elevated or ambient temperature. The size, shape, and composition of the SPIONs depend on several parameters: type of salts used (chlorides, sulfates or nitrates), the Fe^{3+}/Fe^{2+} ratio, temperature, pH value or ionic strength, among others. This methodology has been used extensively to produce magnetite nanoparticles of controlled sizes and magnetic properties.[18,19]

3.1.1.3. Organic-based nanomaterials

These include nanomaterials (NMs) made mostly from organic matter that may self-assemble into complex structures such as micelles, liposomes, polymer NPs and dendrimers.[1] These are attractive building blocks for use in the drug delivery field, due to their surface functionality, biodegradability, cell interaction and high drug loading efficiency.

Micellar NPs, for example, can encapsulate in their core hydrophobic drugs, due to their amphiphilic nature (Figure 6a). Liposomes are constructed from bilayer-spherical structures, such as phospholipids, cholesterol and other fatty acids and are suitable candidates for DNA transfection in their hydrophilic cores to target tumor sites (Figure 6b).[20]

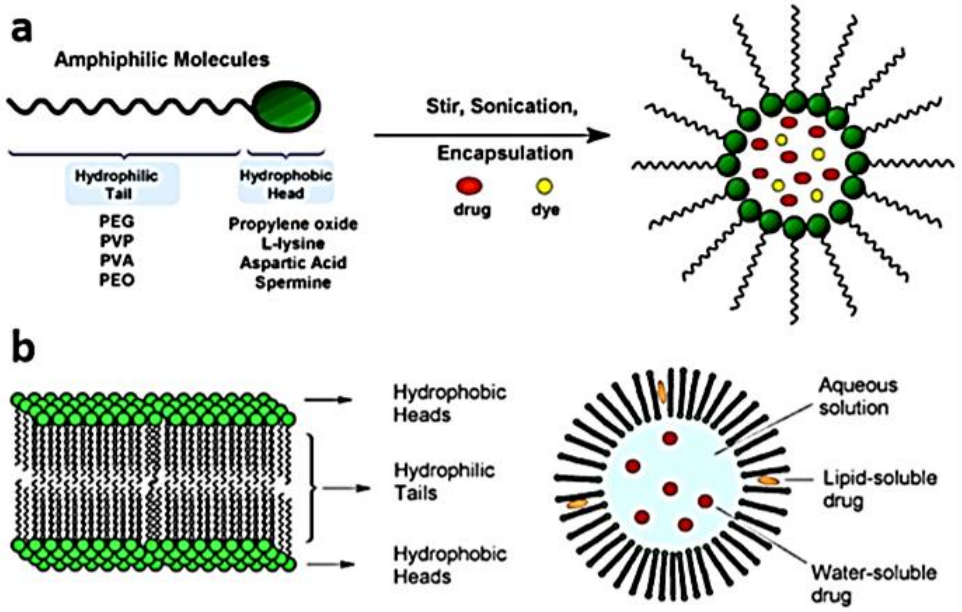

Figure 6. Organic nanoparticles: a) Nanomicelles and b) Liposomes.

Moreover, polymeric nanogels are porous substances created by crosslinking of polymer chains in the nanometer range, which can assemble into nanometer-sized drug reservoirs that may be easily functionalized (Figure 7a).[21]

Further, dendrimers, branched tree-like polymeric structures, can also encapsulate drugs in their internal structure, while the surface may be easily modified for targeting or molecular recognition (Figure 7b).[22]

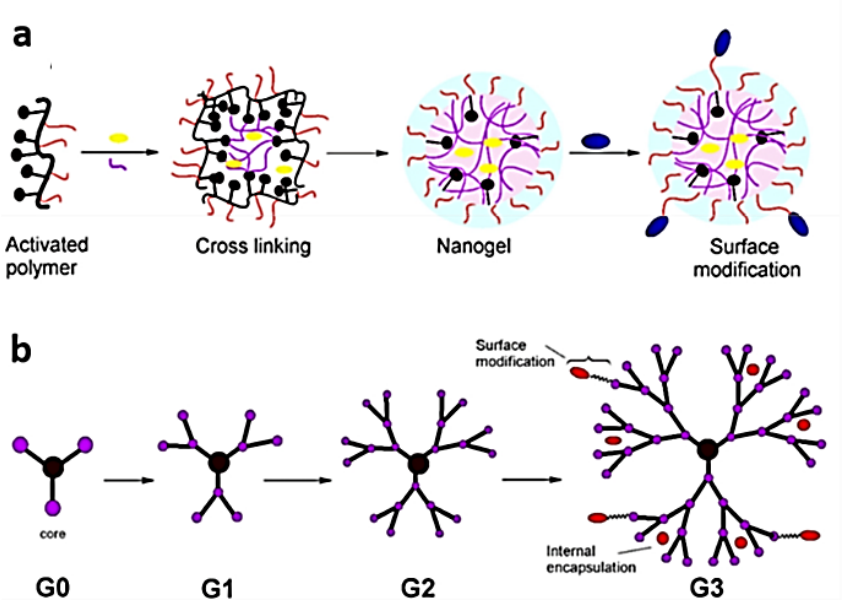

Figure 7. Organic nanoparticles: a) Polymer nanoparticles b) Dendrimers.

3.1.2. Hybrid nanocomposite hydrogels

Hybrid nanocomposite hydrogels are hydrated polymeric networks of synthetic or natural origins, which incorporate nanostructures in their scaffold, such as carbon-based materials, polymeric particles or metal/metal oxide nanoparticles (Figure 8).[23]

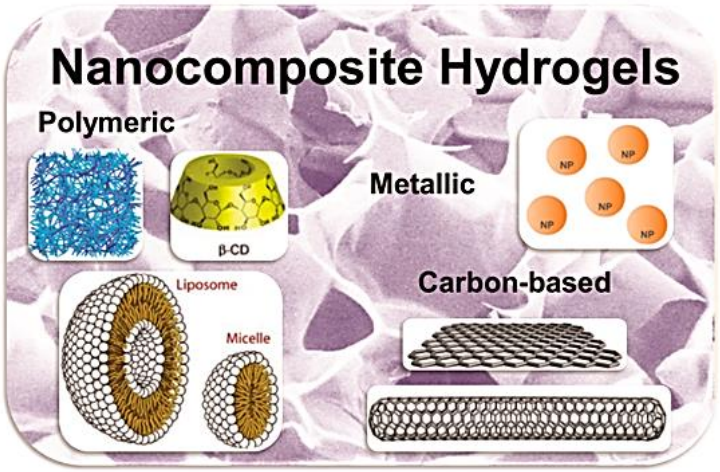

Figure 8. Hybrid nanocomposite hydrogels.

The nanoparticles interact with the hydrogel scaffold and confer novel properties to the nanocomposite;[24] as a result these materials offer a wide variety of applications in many fields, such as biomedicine, drug delivery, biosensors, and bioactuators.[25]

3.1.2.1. Hybrid hydrogels from carbon-based nanomaterials

Carbon-based nanomaterials such as CNTs, graphene or fullerenes have been widely investigated to enhance the properties of hybrid hydrogels, such as high mechanical and optical properties or electrical conductivity.[26]

For example, due to their high electrical conductivity, CNTs-filled nanocomposite hydrogels have been used to fabricate electrically conductive tissues such as nerve, muscle, and cardiac tissues by inducing formation of conductive networks within the hybrids (Figure 9).

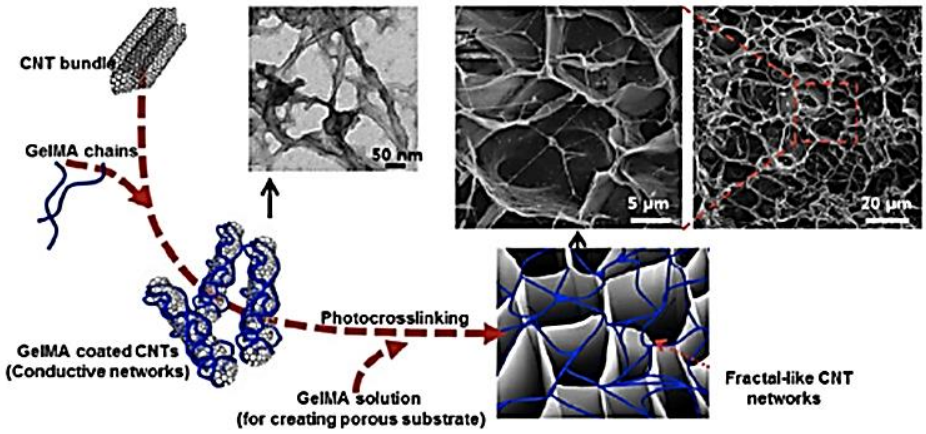

Figure 9. Electrically conductive hybrid hydrogels by formation of CNTs-embedded conductive networks.

Due to their hydrophobic nature, CNTs tend to aggregate inside the hydrophilic hydrogel scaffold and for this reason they are usually functionalized with hydrophilic polar groups to facilitate dispersion within the network.[28]

The enhancement of the hybrid properties has been also achieved by incorporating graphene into soft hydrogel scaffolds. For example, toughness, stiffness and self-healing capacities of the hybrids have been improved by interaction between the graphene sheets and the elastic polymer chains of the hydrogel.[29]

Moreover, the exceptional electric conductivity of graphene has been harnessed to fabricate electrically conductive hydrogels for drug delivery and tissue engineering applications. In this sense, our group designed graphene-based hydrogels as electroactive scaffolds which were able to control drug release in a pulsatile fashion upon the ON/OFF application of low electrical voltages (Figure 10).[30]

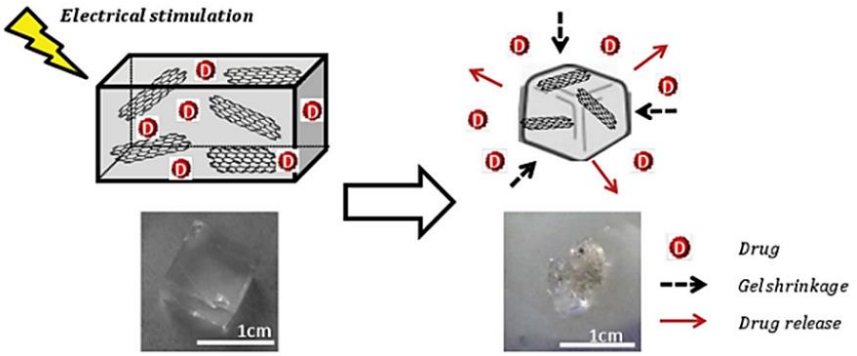

Figure 10. Electrically stimulated drug release from graphene hydrogel scaffolds.

Similarly, graphene-embedded hydrogels were able to support the growth of cultured brain cells and development of synaptic activity by building conductive networks within the polymer scaffold.[31]

3.1.2.2. Hybrid hydrogels from metal and metal/oxide nanoparticles

Inorganic-based NPs have also been incorporated into hydrogel scaffolds and proven useful for biomedical applications. These NPs may include Au, Ag or metal-oxide NPs, such as iron oxide (Fe_3O_4), titania (TiO_2) or zirconia (ZrO_2).[32] These inorganic-based NPs possess desired physical properties such as electrical conductivity (Au nanorods), magnetic properties (Fe_3O_4) and antimicrobial properties (Ag) and thus hydrogels containing these NPs are extensively used as imaging agents, drug delivery systems, conductive scaffolds and sensors/actuators.[32]

Ferromagnetic hydrogels, this is, hydrogels containing iron oxide NPs, can be used to construct tissue networks in a controlled manner using external magnetic fields (EMF) in order to attract biological agents bound to the NPs.[33] For example, by modification of a hydrogel with SPIONs, mechanical variations may be induced by application of an alternating magnetic field (AMF), which could be employed to induce angiogenesis.[34]

Magnetic-responsive hydrogels may also be used for controlled drug delivery upon application of a magnetic field. By introduction of SPIONs into the hydrogel network, the release of levodopa (LD) from the polymer network was enhanced under an EMF, which stimulated viability, proliferation and expression of dopaminergic markers of human neuroblastoma (Figure 11).[35]

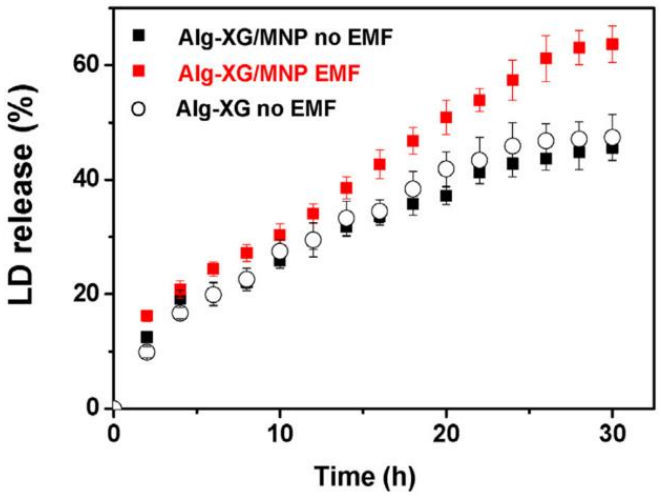

Figure 11. Magnetic-triggered levodopa release from alginate/xanthan gum hydrogels embedded with SPIONs upon application of an external magnetic field (EMF).

3.1.2.3. Hybrid hydrogels from polymer nanoparticles

Hybrid hydrogels may also be fabricated by incorporation of polymeric nanoparticles into crosslinked networks. For example, dendrimer-shaped nanoparticles can be used to reinforce the hydrogel network through interactions with the polymer chains.

In this sense, hyperbranched polyester (HPE) NPs modified with acrylic terminal groups were fabricated, which crosslinked under UV exposure. Depending on the crosslinking degree, the mechanical strength was tuned. Additionally, these hydrogels were able to encapsulate hydrophobic drugs within the inner core and release the compound for periods longer than a week (Figure 12).[36]

In another example, polyamidoamine (PAMAM) dendritic NPs were incorporated into collagen hydrogels to improve mechanical performances, which resulted in fibroblast proliferation inside the scaffolds.[36]

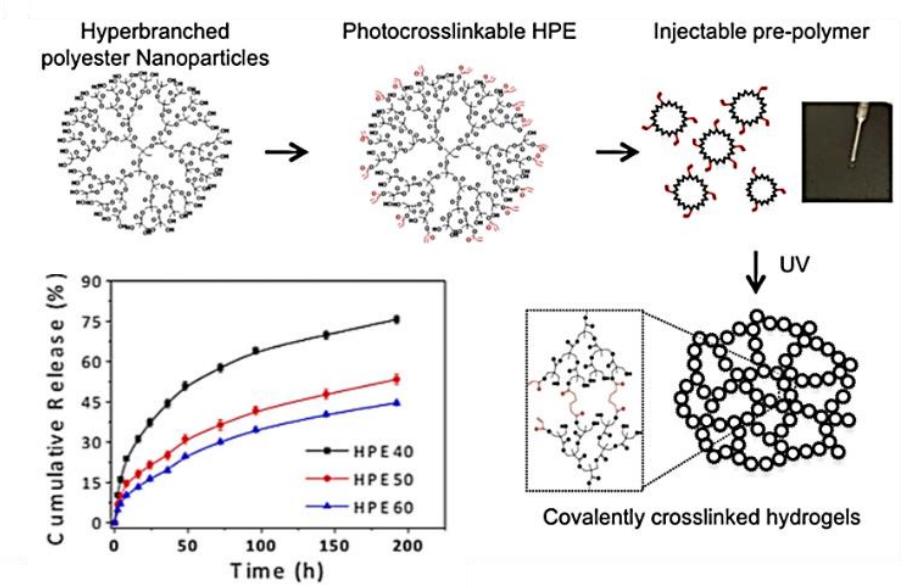

Figure 12. Hyperbranched photo-crosslinked hydrogels for hydrophobic drug delivery.

3.1.3. Diaminotriazines for hybrid materials

The versatility of DATs towards interaction with other H-bonding molecules, metal ions or aromatic moieties suggests that hydrogels based in the DAT core can be suitable scaffolds for the fabrication of hybrid materials. This way, through favorable interactions, DAT hydrogels could harbor nanomaterials within the polymer network and acquire enhanced properties, such as stimuli-responsiveness.

3.1.3.1. Carbon-based nanomaterials

Melamine (2,4,6-diamino-1,3,5-triazine) was shown to stablish favorable π-π interactions between its aromatic nucleus and the surface of few-layer graphene sheets (Figure 13a).[37,38]

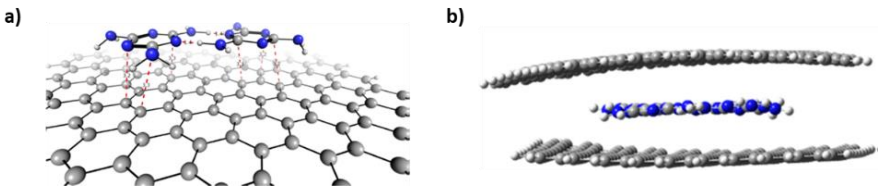

Figure 13. Melamine-graphene interactions: a) π-π stacking interactions b) intercalation of DAT H-bond networks between graphite layers.

The triazine derivatives formed an extended H-bond 2D network on the top of graphene surface, which in turn reduced van der Waals forces between the layers (Figure 13b) and served as efficient exfoliating agent of graphite. The melamine "exfoliating effect" played a decisive role in the mechanochemical treatment employed to obtain good-quality non oxidized graphene.[39]

3.1.3.2. Metal nanoparticles

As already commented, DATs may coordinate metal atoms due to the electron-donor character of the s-triazine N atoms and the electron-acceptor character of the metal centers. This was exemplified in the work carried out by Liu and coworkers[40] who built a DAT-based hydrogel with the capacity to complex Cu^{2+} ions and operate as sensors for water contaminants. The hydrogels adopted typical blue coloration of copper (II) salts the upon sequestering the Cu^{2+} ions (Figure 14a).

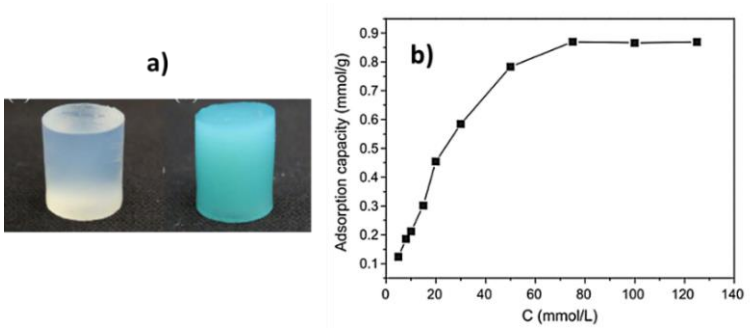

Figure 14. Copper adsorption of DAT-based hydrogels a) before (left) and after (right) metal absorption b) absorption capacity with respect to concentration.

It was observed that the metal complexing capacity of the hydrogels increased within Cu^{2+} ion concentration in the medium, until it reached saturation when all the coordination sites were occupied (Figure 14b).

These findings point that DAT hybrid hydrogels could be built by favorable interaction between the DATs and graphene or metal nanoparticles, endowing the hydrogels with interesting properties.

3.2. Results and discussion

In this chapter, we incorporate nanomaterials to DAT hydrogels in order to synthesize and characterize DAT hybrid nanocomposite hydrogels with novel properties. First, the study of the nanomaterials is covered, namely, graphene and superparamagnetic iron oxide nanoparticles (SPIONs). Moreover, the corresponding graphene- and magnetite- hybrid diaminotriazine hydrogels are studied.

3.2.1. Nanomaterials

3.2.1.1. Few-layer graphene

a) Synthesis

Few-layer graphene was obtained by a mechano-chemical exfoliation process previously reported in our group.[39,41] Graphite is ball-milled in solvent-free conditions under 30 min (100 rpm) and in the presence of melamine as an exfoliating agent (Scheme 1).

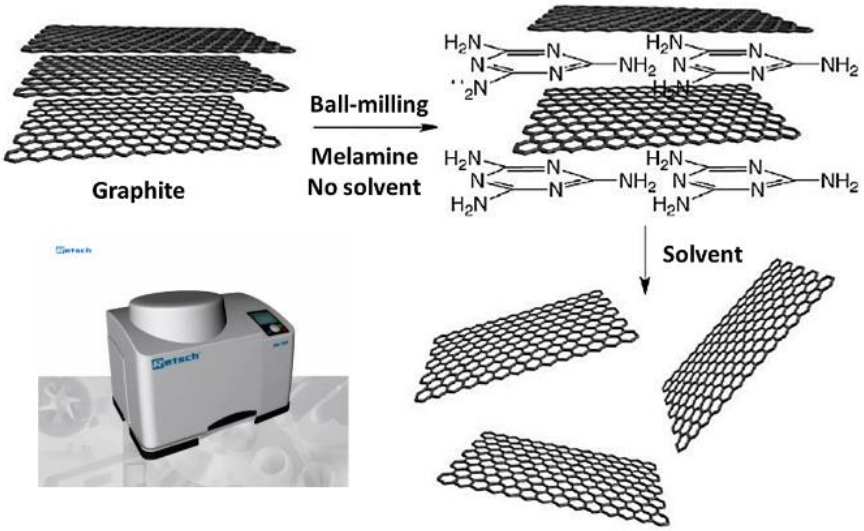

Scheme 1. Obtention of few-layer graphene in a planetary mill under solvent-free conditions.

Theoretical and experimental studies showed that the interaction of diaminotriazines with graphitic layers facilitates the exfoliation, due to π-π favourable and graphene-NH_2 interactions between diaminotriazines and graphene layers. [37,38]

The exfoliated graphene is then dialyzed in hot water to remove the melamine, after which the suspension is left to sediment in order to separate the non-exfoliated graphite from the graphene. Finally, these aqueous suspensions were lyophilized to obtain few-layer graphene powders.

b) Characterization

The nanomaterial was then characterized by Raman spectroscopy, thermogravimetric analysis (TGA), elemental analysis, and transmission electron microscopy (TEM). Raman spectroscopy provided deep-insight into the few-layer graphene structure (Figure 15).

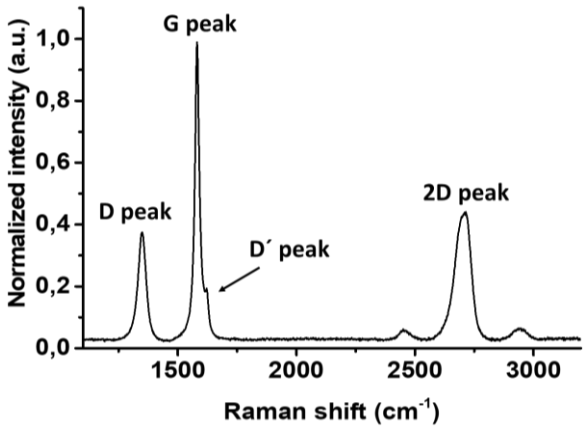

Figure 15. Raman spectrum of few-layer graphene.

The spectrum reveals the typical D, G and 2D bands ascribed to a few-layer graphene at 1345, 1580 and 2700 cm^{-1}, respectively. The G band represents the C-C sp^2 stretchings, which confirms the graphitic nature of the sample. The D band informs of the C-C sp^3 defects of the sample; by comparing the intensities of the D and G bands, a I_D/I_G ratio of 0.38 is obtained, which endorses a low presence of sp^3 hybridization in the nanomaterial.[42] Moreover, the presence of the D´ shoulder at 1600 cm^{-1} confirms the distortion of the C-C sp^2 symmetry. The width of the 2D band informs of the approximate number of layers; 4 layers were observed for the few-layer graphene following this methodology, according to the formula from Paton *et al.*[43]

Elemental analysis shows both very low oxygen and nitrogen contents, revealing a low degree of oxidation in the graphene layers as well as negligible traces of melamine remaining from the exfoliation process (Table 1).

Table 1. Elemental analysis of few-layer graphene.

	C (%)	H (%)	O (%)	N (%)
	95.66 ± 0.04	0.51 ± 0.04	3.11 ± 0.08	0.56 ± 0.02

TGA analysis reveals a 7.5% weight loss at 600ºC, complementing the low oxygen content as confirmed by elemental analysis (Figure 16).

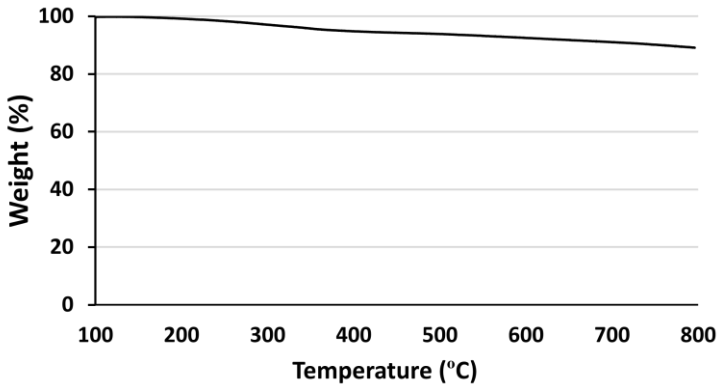

Figure 16. TGA analysis of few-layer graphene.

TEM imaging reveals a lateral size distribution of around 350 nm; additionally, a TEM image of the graphene flakes is provided (Figure 17).

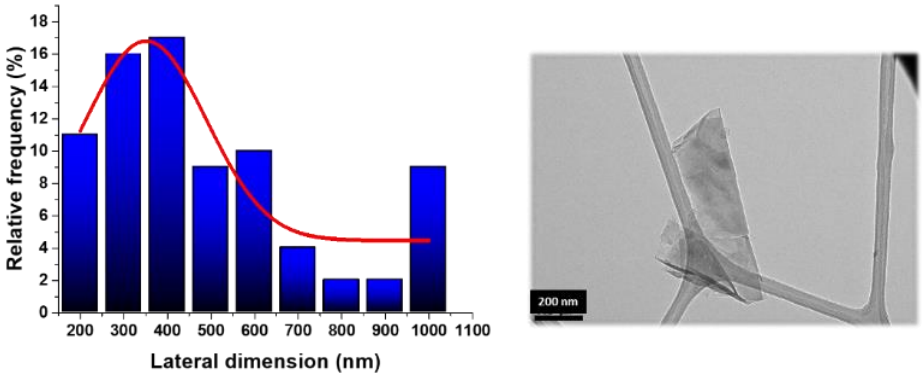

Figure 17. TEM characterization: Lateral size distribution (left) and TEM representative image (right).

3.2.1.2. Magnetite nanoparticles

a) Blending method

- **Synthesis**

The first method attempted for the synthesis of superparamagnetic iron oxide nanoparticles (SPIONs) was the blending method. This consists in the preparation of the SPIONs during the formation of the hydrogels, mostly following a co-precipitation method for preparing water-soluble iron NPs. Due to the tendency of these NPs to aggregate in aqueous media, they are normally coated during synthesis with hydrophilic polymers or surfactants, such as protein, starch or glucan, in order to increase their water solubility and dispersibility.[44]

The coated-NPs synthesized this way usually have around 30-150 nm in size and in aggregate form. In this case, the preparation of the NPs was carried out elsewhere in our group following a patented protocol (Figure 18).[45]

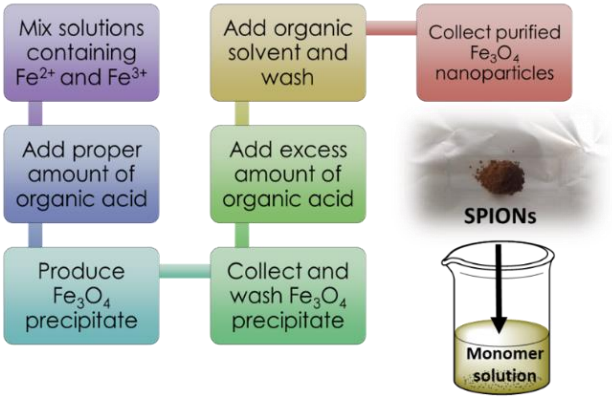

Figure 18. Synthesis of SPIONs *via* blending method.

First, Fe^{3+}/Fe^{2+} solutions were mixed in a 2:1 ratio in HCl solution, followed by addition of glycine, which served as surfactant in order to avoid NP aggregation. The pH was then adjusted to 10 by addition of NaOH until precipitation of magnetite (Fe_3O_4) was observed. The precipitate was washed with deionized (DI) water several times and excess glycine was added while stirring in order to complete the micellization of the NPs. Finally, excess glycine was rinsed with organic solvent and the suspension was centrifuged to obtain the purified SPIONs.

- Characterization

The water-soluble SPIONs were subsequently characterized by SQUID (superconducting quantum interference device) and TEM techniques. TEM imaging shows two diameter size distributions ranging between 0-20 nm, which is expected for average magnetite aggregates (Figure 19).[46]

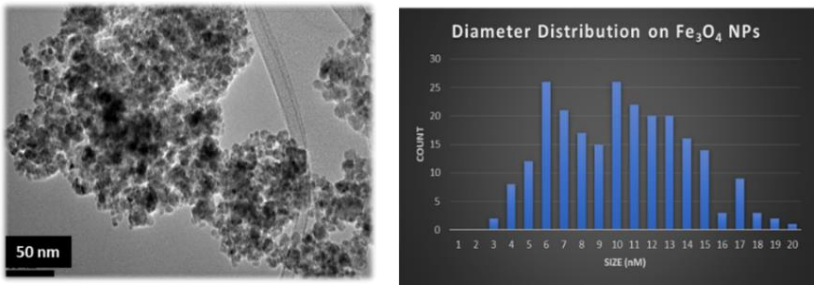

Figure 19. TEM imaging and diameter distributions for SPIONs.

Further characterization by SQUID magnetometry shows the SPIONs have superparamagnetic character with no coercitivity within the studied range, thus confirming that they behave as superparamagnetic single-domain aggregates rather than multi-domain clusters (Figure 20).

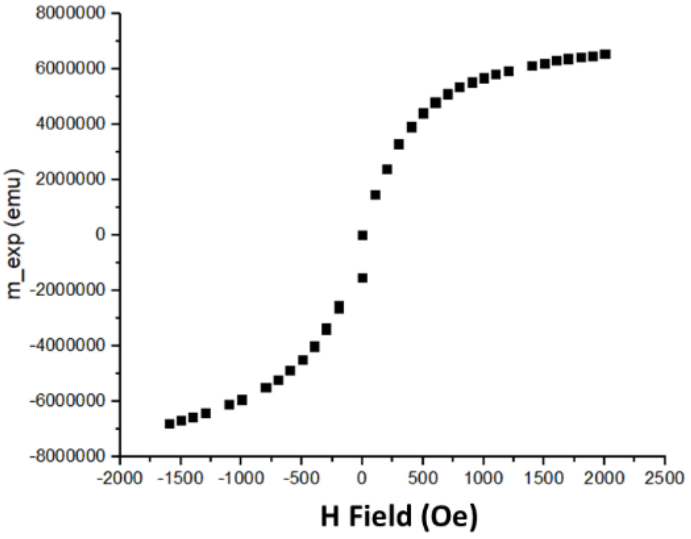

Figure 20. SQUID of SPIONs synthesized *via* blending method.

b) In situ co-precipitation method

- Synthesis

The second methodology followed for the synthesis of SPIONs is the *in situ* co-precipitation. The process is similar to the blending method, however, the SPIONs are synthesized after the hydrogel has already been fabricated.

First, a dried hydrogel is immersed in a Fe^{3+}: Fe^{2+} (2:1) aqueous solution until the hydrogel achieves maximum swelling in this solution. Subsequently, the iron-loaded hydrogels are fully immersed in alkali media, where the co-precipitation reaction takes place immediately (Figure 21).

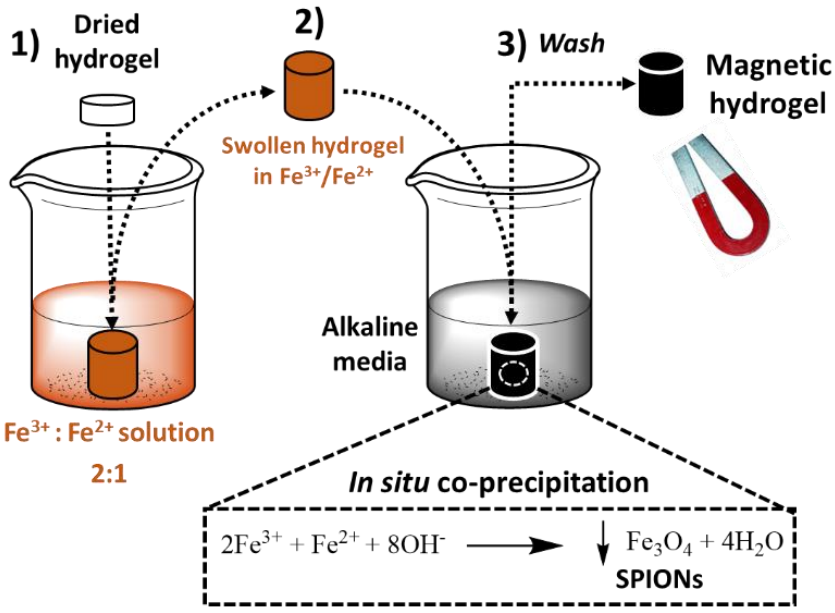

Figure 21. Synthesis of SPIONs *via in situ* co-precipitation method.

The magnetic hydrogel is then washed in water several times until no excess magnetite NPs are observed leaking out from the hydrogel.

The characterization of these magnetite nanoparticles is discussed thoroughly during the study of the corresponding magnetic hybrid hydrogels prepared with the *in situ* co-precipitation method.

3.2.2. Hybrid nanocomposite hydrogels

3.2.2.1. Graphene hybrid hydrogels

For these studies, we have chosen the standard chemically-crosslinked hydrogel **TzOA-M-6** as starting point. Then, we prepared the corresponding the graphene hybrid hydrogels **G-TzOA-M-6**.

a) Synthesis

The hydrogels were fabricated following previous recipes optimized in chapter 2: 2-vinyl-4,6-diamino-1,3,5-triazine (VDAT), oligo(ethylene glycol) methyl ether methacrylate (OEGMA), acrylamide (AAm), *N,N´*-methylenebis(acrylamide) (MBA) and potassium peroxydisulfate (KPS) were dissolved in DMSO and casted in an oven. The graphene hybrids were instead prepared from few-layer graphene (FLG)/DMSO homogeneous dispersions (Scheme 2).

After washings in water, three hydrogels were this way synthesized: **TzOA-M-6** hydrogels with 0% w/w FLG (Table 2, entry 1), **$G_{0.1}$-TzOA-M-6** hydrogels with 0.1% w/w FLG (Table 2, entry 2) and **$G_{0.5}$-TzOA-M-6** hydrogels with 0.5 % w/w FLG (Table 2, entry 3).

Importantly, the nanomaterial appeared homogeneous inside the hydrogel, which pointed that it did not aggregate during polymerization. In addition, the graphene sheets did not leak out of the hydrogel after washings and remained embedded in the polymeric structure, as reported for the previous preparation of hybrid hydrogels by our group.[47]

Table 2. Synthesis of **TzOA-M-6** and **G-TzOA-M-6** hydrogels.

Entry[a]	Name	[FLG/DMSO] (mg/ml)	[FLG] (% w/w)
1	TzOA-M-6	-	-
2	$G_{0.1}$-TzOA-M-6	0.42	0.1
3	$G_{0.5}$-TzOA-M-6	2.1	0.5

[a]T = 70ºC, t = 15 min, [MBA] = [KPS] = 2 mg/ml, [OEGMA] = [AAm] = 135 mg/ml, [VDAT] = 150 mg/ml, MW = 42 %.

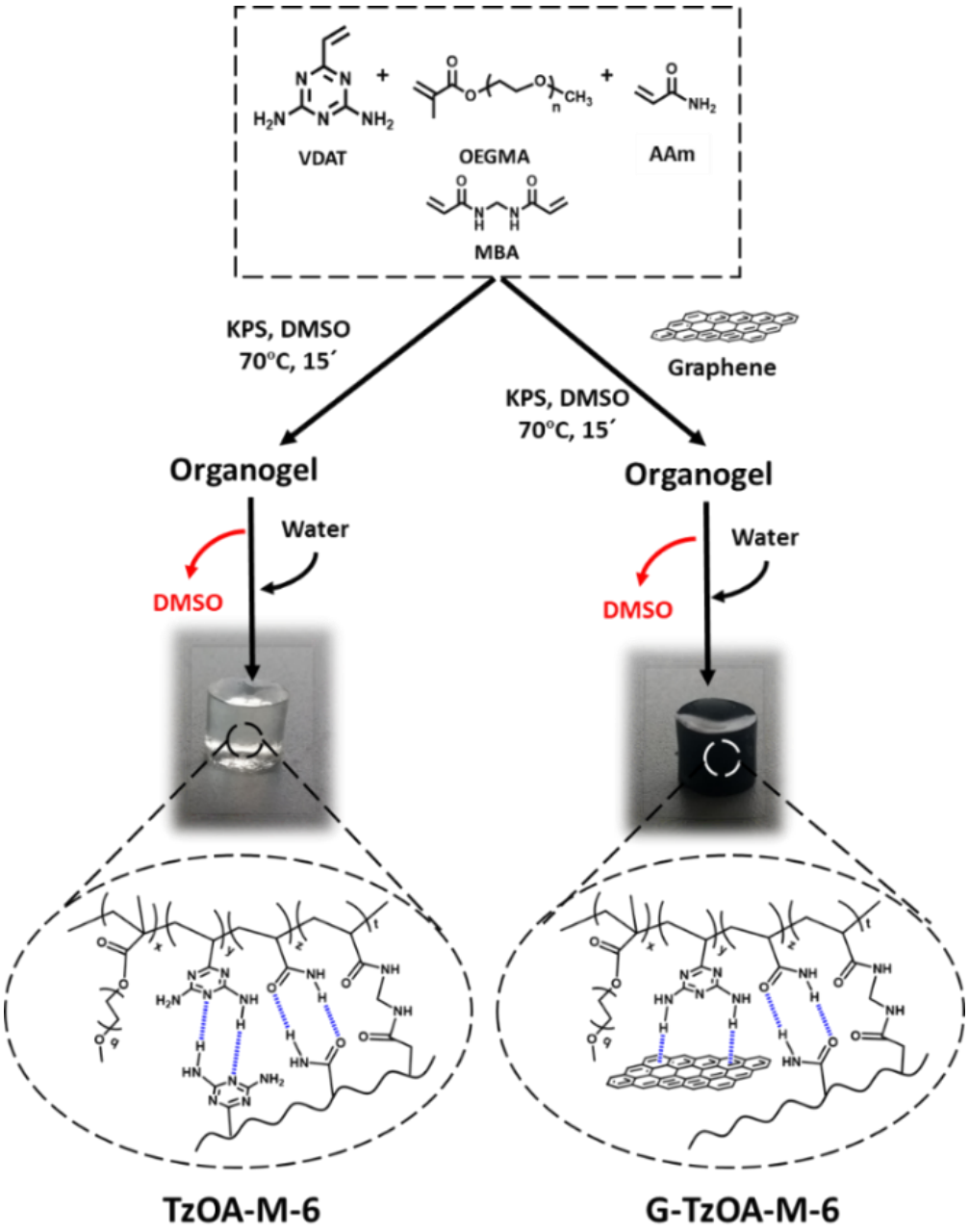

Scheme 2. Synthesis of TzOA-M-6 and G-TzOA-M-6 hydrogels.

b) Characterization

The hydrogels were fully characterized by swelling studies, scanning electron microscopy (SEM), thermogravimetric analysis/differential scanning calorimetry (TGA/DSC), Fourier transform Infrared spectroscopy (FT-IR) spectroscopy, and mechanical tests.

- Swelling studies

The swelling studies were carried out both in aqueous neutral medium and Simulated Gastric Fluid (SGF), which is a buffer that mimics the harsh acidic conditions that occur in the gut.[48] The results show that both **TzOA-M-6** and **G-TzOA-M-6** hydrogels swell up to 10-fold in SGF medium in comparison with neutral aqueous medium (Figure 22), due to the ability of DATs to protonate under acidic media (pKa VDAT = 5.15).[49]

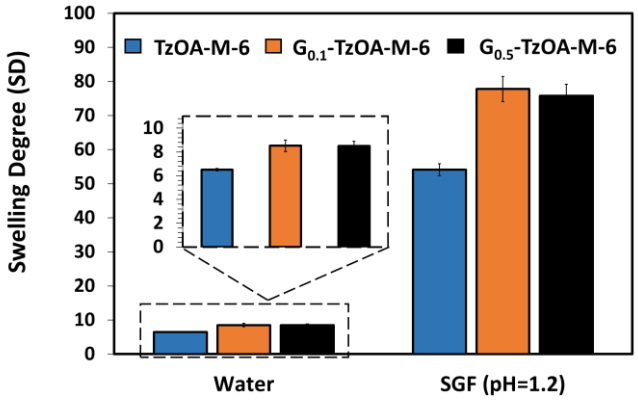

Figure 22. Swelling degree of **TzOA-M-6** and **G-TzOA-M-6** hydrogels.

Moreover, an interesting trend was observed whereby increasing graphene content resulted in higher SD values in both neutral and acidic media, thus suggesting that graphene is exerting a distinctive effect in the polymeric network.

A possible mechanism for the effect of graphene on DAT-based hydrogels is depicted in Figure 23. In neutral aqueous media, the DAT hydrophobic microdomains act as "hydrophobic barriers" for small protic molecules like water, thus restraining water uptake (Figure 23a).

When graphene is introduced into the DAT hydrogels, favorable π-π stacking is likely to occur between triazine molecules and graphene sheets, together with NH_2-graphene interactions.[37,38] These graphene-diaminotriazine engagements may disrupt the DAT-DAT network to a certain extent and water is allowed inside. As a consequence, the SD is observed to increase for **G-TzOA-M-6** hydrogels (Figure 23b).

When both hydrogels are immersed in SGF buffer, protonation of DATs breaks the entirety of the DAT-DAT π-π and H-bonding hydrophobic network and the water uptake increases drastically. The combination of both the effects of graphene and acidic medium could explain the highest SD values achieved

with **G-TzOA-M-6** hydrogels in SGF buffer with respect to **TzOA-M-6** hydrogels in SGF buffer (Figure 23c).

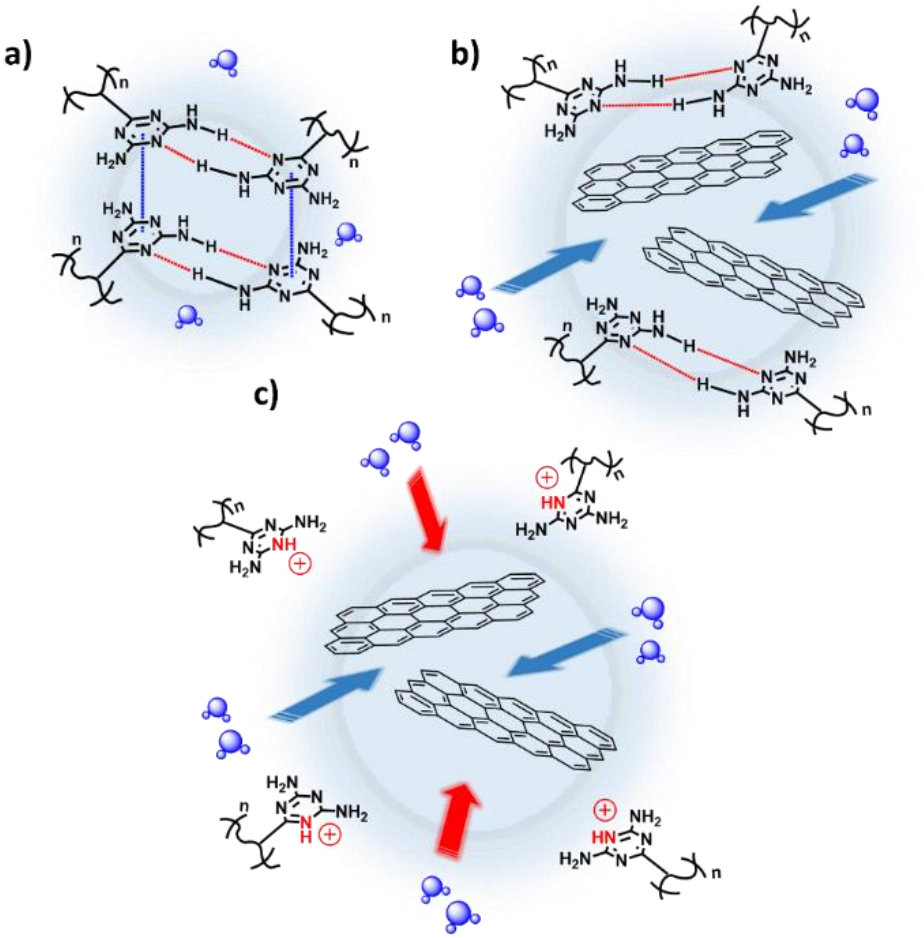

Figure 23. Proposed swelling mechanism for DAT-based hydrogels a) in neutral media b) in neutral media and in the presence of graphene c) in the presence of graphene and in SGF media.

The trends described above can be observed macroscopically in the digital images of the DAT-based hydrogels (Figure 24). In the presence of graphene, hydrogels slightly increase their overall volume, while in SGF media this increase is more pronounced.

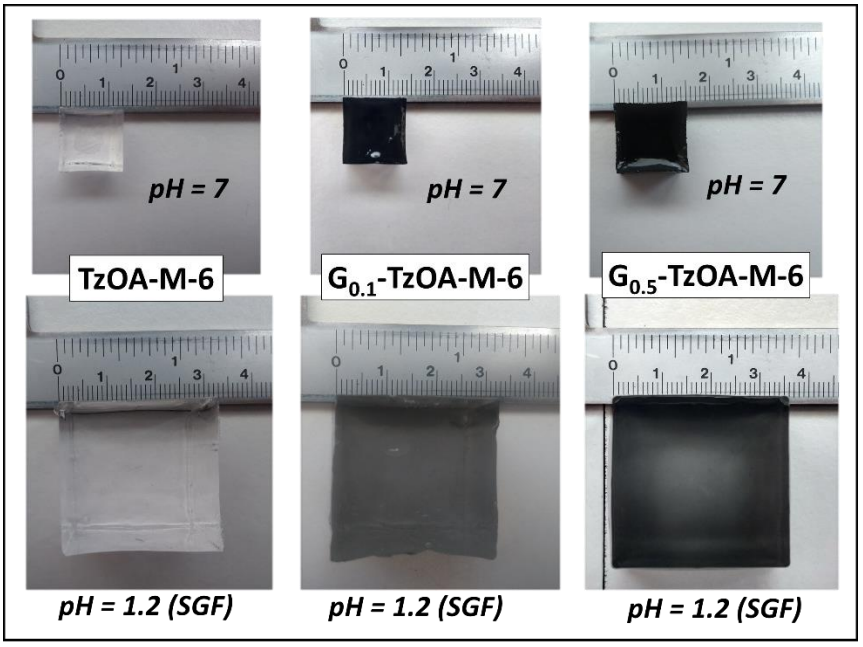

Figure 24. Digital images of DAT-based hydrogels. From left to right: **TzOA-M-6**, **$G_{0.1}$-TzOA-M-6** and **$G_{0.5}$-TzOA-M-6** hydrogels in neutral media (pH=7) (up) and SGF media (pH=1.2) (down).

- **Scanning Electron Microscopy (SEM)**

SEM was used to measure the pore sizes of the hydrogels. The latter were swollen until maximum state and lyophilized *prior* to imaging. Figure 25 shows the pore size distributions of the **TzOA-M-6** and **G-TzOA-M-6** hydrogels in water and SGF media.

In neutral aqueous media, the **$G_{0.1}$-TzOA-M-6** and **$G_{0.5}$-TzOA-M-6** hydrogels containing graphene have very low polydispersities with pore sizes of 4.37±0.45μm and 3.99±0.51μm (Figure 25, bold orange and black, respectively). This pronounced narrowing of the pore sizes when graphene is introduced can be attributed to the graphene-DAT interactions.

In SGF medium, the polydispersity and the pore sizes increase for all hydrogels (Figure 25, dashed blue, orange and black, respectively).

DAT hydrogels typically show amorphous porosity attributed to the DAT aggregates.[50] In **G-TzOA-M-6** hybrids, DATs could arrange in extended 2D hydrogen-bonded films on top of the graphene surface, as occurs with melamine,[37,38] and rearrange the amorphous porosity of the hydrogels .

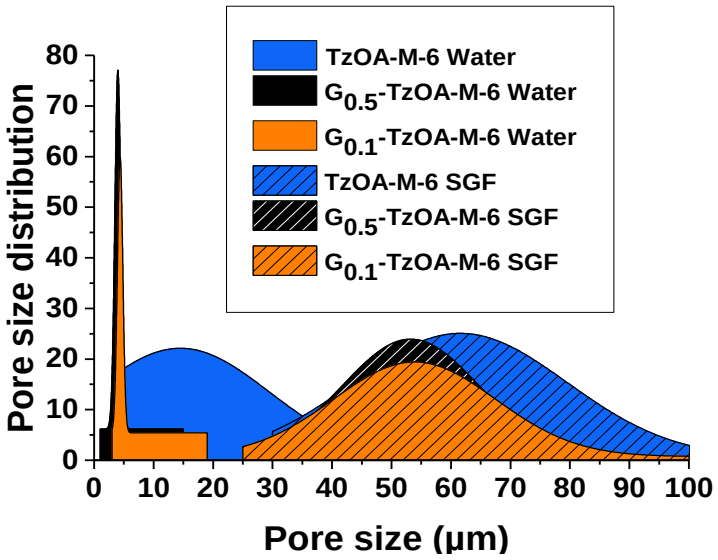

Figure 25. Pore size distribution of TzOA-M-6, G-TzOA-M-6 hydrogels.

In SGF media, however, protonated DATs are repelled and distant from one another and may not form 2D H-bond films on the surface of graphene. Thus, no rearrangement of pore sizes is observed.

The digital SEM images of the TzOA-M-6 and G-TzOA-M-6 hydrogels in PBS and SGF media are shown in Figure 26a-f.

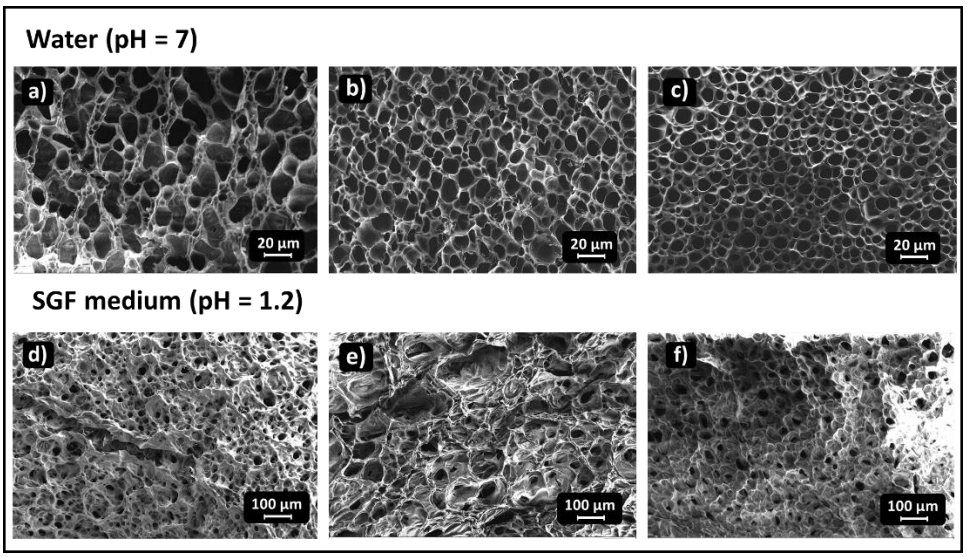

Figure 26. Porous morphology of DAT-based hydrogels for a) TzOA-M-6, b) $G_{0.1}$-TzOA-M-6 c) $G_{0.5}$-TzOA-M-6 in neutral medium and for d) TzOA-M-6, e) $G_{0.1}$-TzOA-M-6 and f) $G_{0.5}$-TzOA-M-6 in SGF medium.

- Infrared spectroscopy (IR)

IR spectroscopy confirmed the structure of the hydrogels (Figure 27). The two bands at 958 and 830 cm^{-1}, corresponding to the vinyl group of the VDAT monomer, both disappear in the spectra of the hydrogels, confirming that the monomer has effectively polymerized.

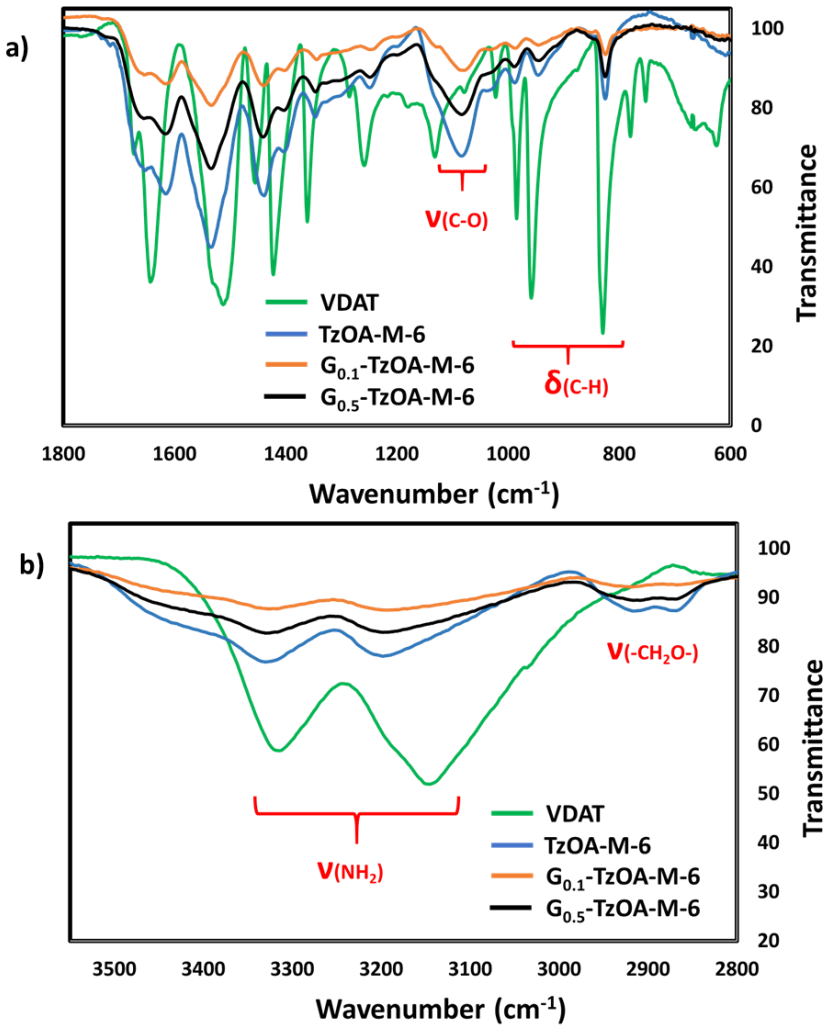

Figure 27. a) FT-IR spectra of VDAT monomer and DAT-based hydrogels b) zoom in in the 3500-2800 cm^{-1} region.

Moreover, the C-O and -CH_2O- stretching vibrations at 1077 and 2860 cm^{-1}, respectively, confirm the incorporation of the polyethylene glycol (PEG) backbone in the hydrogels.

The NH stretchings at 3300-3150 cm^{-1} in the VDAT monomer both experience a shift and broadening in all DAT-based hydrogels (Figure 27b). This

supports evidence of self-H bonding between DATs,[51] and indicates that self H-bonding occurs when the DATs are polymerized into the hydrogel. This finding supports the existence of hydrophobic aggregates inside the DAT hydrogels, where the H-bond formation is favored.

- Thermogravimetric Analysis (TGA)

TGA studies were performed to study the decomposition of the TzOA-M-6 and G-TzOA-M-6 hydrogels. Two major significant weight losses occur for all the hydrogels, namely, a 7.4% and a 60.8% loss between 0-100ºC and between 300-450ºC, respectively (Figure 28, bold curves). The first loss is attributed to the remnant water in the hydrogels, whereas the 61% loss is attributed to the polymer backbone decomposition.

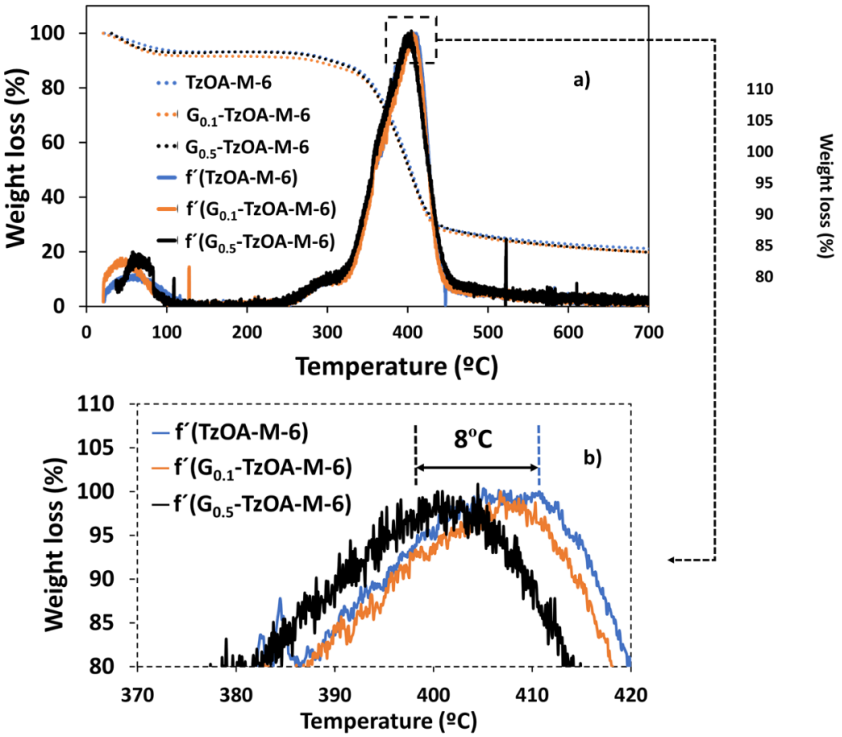

Figure 28. TGA curves of TzOA-M-6 and G-TzOA-M-6 hydrogels a) TGA curves (dashed) and derivatives (bold) b) peak maxima.

A closer look in the peak maxima shows that $G_{0.5}$-TzOA-M-6 hydrogels decompose 8ºC below than TzOA-M-6 hydrogels (Figure 28b). This finding shows that the presence of graphene favors early decomposition of the hydrogels. Since the DAT H-bonding network is responsible of the hydrogel

consistency, it follows that graphene is disrupting this network and weakening the structure, in accordance with the SD and pore studies.[52]

Density scanning calorimetry (DSC) further provided the pyrolysis energy profile of the hydrogels (Figure 29). A downward trend is observed for the first 300ºC, which indicates an endothermic process. A shift in the DSC profile from 300–450ºC, with a maximum at 430ºC, shows that the decomposition of the polymer backbone is however an exothermic process.

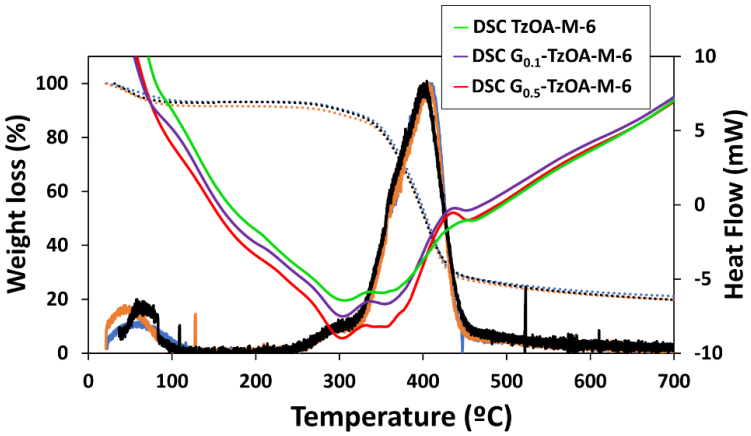

Figure 29. Coupled TGA-DSC curves. DSC curves are represented in red, purple and green for **TzOA-M-6**, **$G_{0.1}$-TzOA-M-6** and **$G_{0.5}$-TzOA-M-6** hydrogels, respectively.

Finally, a mass detector was coupled to the TGA to reveal the chemical background of the thermal decompositions; the mass curves are overlaid with the TGA curves for better clarity (Figure 30).

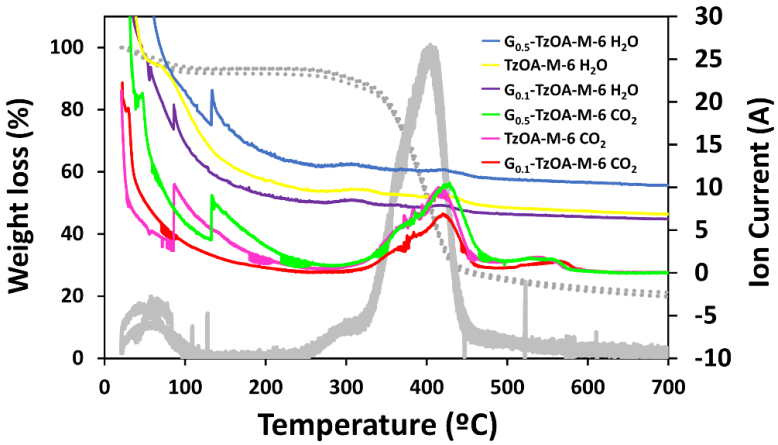

Figure 30. Coupled TGA-mass curves. H_2O loss (yellow, purple, blue) and CO_2 loss (pink, red and green) is represented for **TzOA-M-6**, **$G_{0.1}$-TzOA-M-6** and **$G_{0.5}$-TzOA-M-6** hydrogels, respectively.

Vaporized water is shown to predominate during the first 100ºC (Figure 30, curves blue, yellow and purple). Moreover, a carbon dioxide peak is observed between 350-450ºC corresponding to the polymer backbone decomposition (Figure 30, green, pink and red). The latter is attributed to the pyrolysis of the amide and ester groups of the hydrogels.

- Mechanical properties

The mechanical properties were carried out to further study the influence of graphene on the structure of the DAT hydrogels. First, compressive tests were carried out on cylindrical-shaped hydrogels at constant speed until reaching 90% initial compression.

The stress-strain curves show that introduction of 0.1%G content in TzOA-M-6 hydrogels leads to higher compressive strains, whereas further increase to 0.5%G leads to less strain (Figure 31).

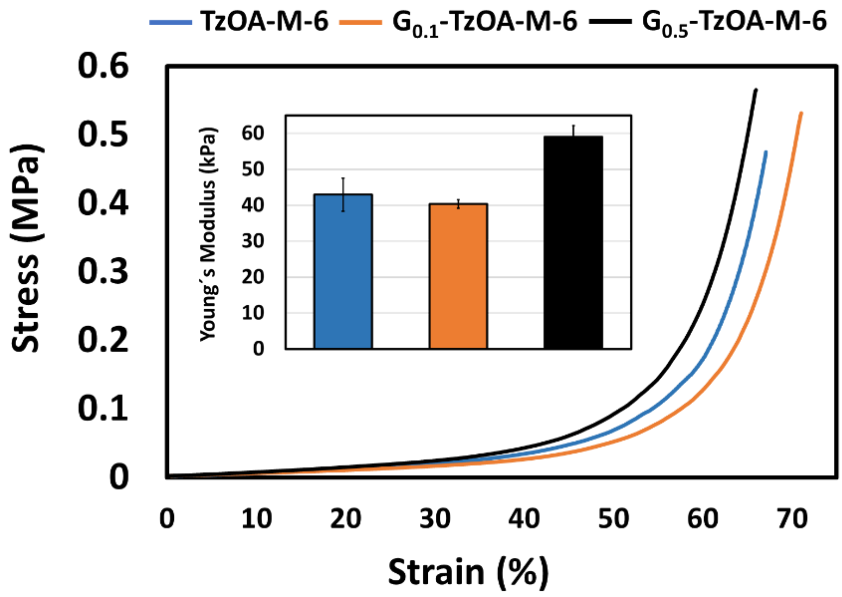

Figure 31. Compressive strength of DAT-based hydrogels: a) Stress-strain curves and b) Young´s Modulus.

Further, the Young moduli values in the 2-10% strain range were recorded, which provided insight on the stiffness of the material (Figure 31 inset). The moduli initially dropped from hydrogels without graphene to hydrogels with 0.1%G, whereas they increase again with 0.5%G. The observations shown in Figure 31 point that at 0.1%G contents, the polymer scaffold becomes loosened, whereas at 0.5%G the scaffold stiffens back. A possible explanation

is that related to the graphene-DAT interactions: at low concentrations, graphene disrupts the DAT strengthening H-bond network and the rigidity of the material decreases. At higher concentrations, graphene could be acting as crosslinker agent and this increases the compactness and stiffness of the hydrogel, thus offsetting the previous effect.

Moreover, tensile strengths were also performed. The fracture toughness values were then calculated from the area under the stress-strain curves. Tensile stress-strain curves show that introduction of graphene decreases the tensile strength, which supports the disruption of the DAT-DAT strengthening network (Figure 32a).

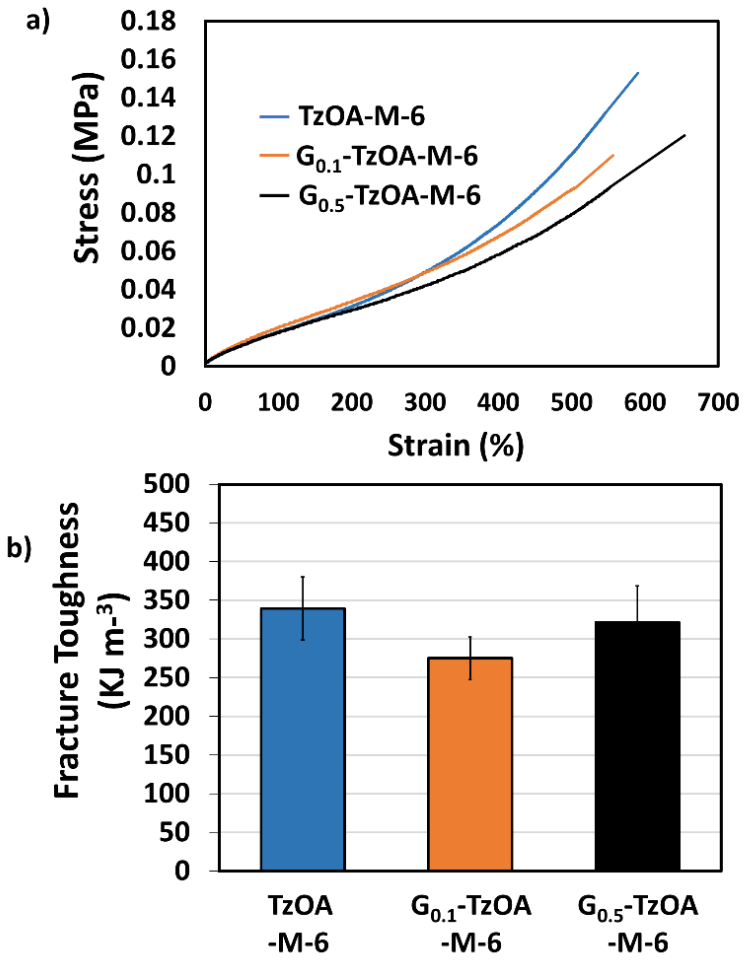

Figure 32. Tensile strength of DAT-based hydrogels: a) stress-strain curves and b) fracture toughness.

However, when graphene content is increased to 0.5%G, the ductility as well as fracture toughness values increase, suggesting again that graphene

reinforces the mechanical strength of the hydrogels *via* alternative load transfer mechanisms (Figure 32b).[53–55]

Finally, fatigue tests were carried out by compressing hydrogels samples between two plates for 100 cycles at a constant rate. The results confirm the observations of the compressive studies explained above: upon introducing only 0.1%G contents, the energy absorbed in each cycle increases, suggesting a higher elastic network. Further increase to 0.5%G contents decreases these values, meaning that the network becomes again strengthened (Figure 33).

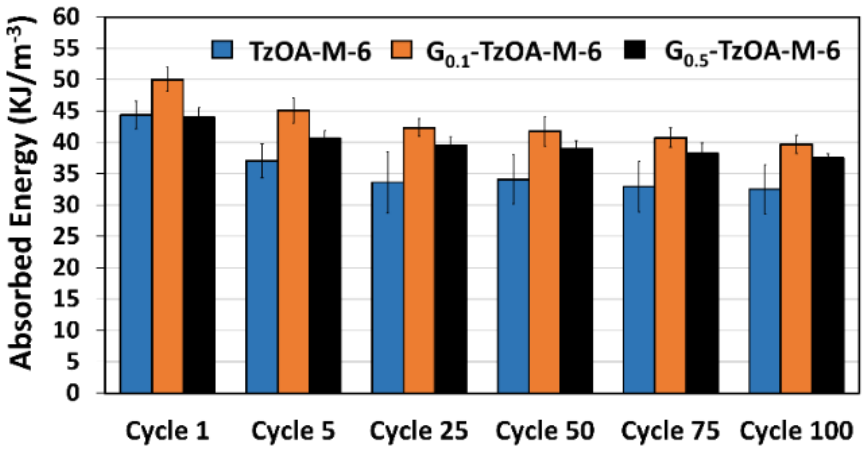

Figure 33. Fatigue tests of DAT-based hydrogels.

It is noteworthy that the difference in energy absorption between the 1st and the 100th cycle is lowest in **$G_{0.5}$-TzOA-M-6** hydrogels than in **TzOA-M-6** hydrogels. This evidences the anti-fatigue character of the hybrid hydrogels, which is caused by the mechanical improvement of graphene.

3.2.2.2. Magnetite hybrid hydrogels

a) Via blending method

For these studies, two hydrogel series were studied: **TzOA-P-1** hydrogels and their corresponding magnetite counterparts, **Mag-TzOA-P-1**.

- **Synthesis**

In the blending method, superparamagnetic iron oxide nanoparticles (SPIONs) were introduced with the rest of the reactants during polymerization following previous recipes optimized in chapter 2: VDAT (150 mg/ml), OEGMA

(135 mg/ml), AAm (135 mg/ml), crosslinker poly(ethylene glycol) diacrylate (PEGDA, 2 mg/ml) and KPS initiator (2 mg/ml) were dissolved in DMSO and the mixture casted in an oven. The magnetite hydrogels were instead prepared from SPION/DMSO dispersions, which were under constant sonication to avoid NP aggregation (Scheme 3).

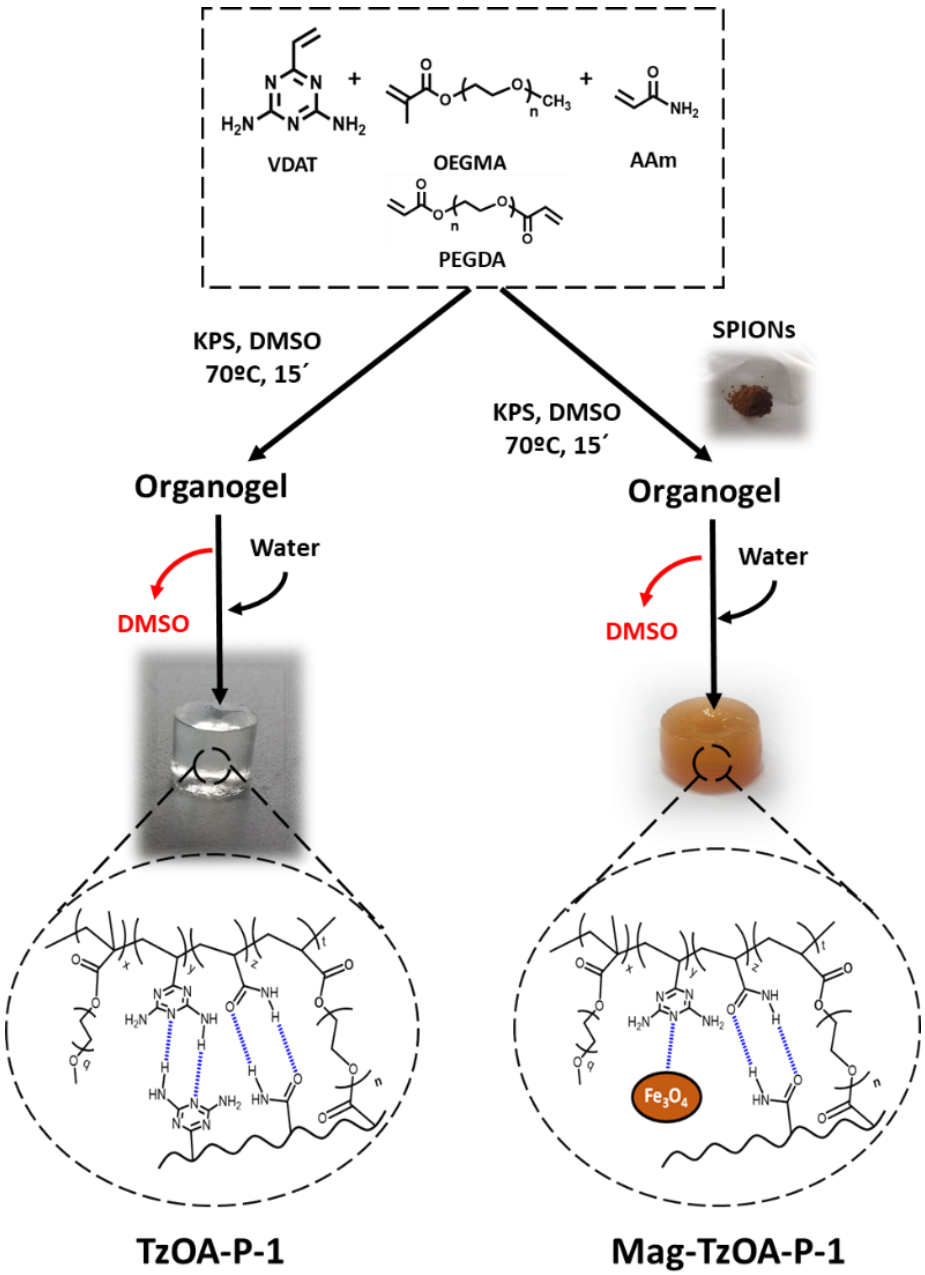

Scheme 3. Synthesis of **TzOA-P-1** and **Mag-TzOA-P-1** hydrogels prepared *via* blending method.

After washings in water, three hydrogels were this way synthesized: **TzOA-P-1** hydrogels, in the absence of SPIONs (Table 3, entry 1), **Mag$_2$-TzOA-P-1** hydrogels, prepared from 2 mg/ml SPIONs/DMSO (Table 3, entry 2) and **Mag$_4$-TzOA-P-1** hydrogels, prepared from 4 mg/ml SPIONs/DMSO (Table 3, entry 3).

Additionally, as occurred with graphene, the distribution of the nanoparticles in the hydrogel turned homogeneous, and no SPION leaking was observed after synthesis, confirming that the latter were effectively trapped within the crosslinked network.

Table 3. Synthesis of **TzOA-P-1** and **Mag-TzOA-P-1** hydrogels.

Entry[a]	Name	[SPIONs/DMSO] (mg/ml)	[SPIONs] (% w/w)
1	TzOA-P-1	-	-
2	Mag$_2$-TzOA-P-1	2	0.95
3	Mag$_4$-TzOA-P-1	4	1.9

[a]T = 70ºC, t = 15 min, [DAT] = 30 mg/ml, [OEGMA] = [AAm] = 135 mg/ml, [PEGDA] = 2 mg/ml, MW = 30 %

- **Characterization**

The hydrogels were characterized by swelling studies, scanning electron microscopy (SEM) and superconductive quantum interference device (SQUID) measurements.

➢ **Swelling studies**

Swelling studies revealed that the capacity of the materials to incorporate water increased notably as the SPION concentration in the hydrogels increased from **TzOA-P-1** hydrogels (0 mg/ml nanoparticles) to **Mag$_2$-TzOA-P-1** (2 mg/ml) and **Mag$_4$-TzOA-P-1** (4 mg/ml) hydrogels (Figure 34).

In fact, it was observed that **Mag$_4$-TzOA-P-1** had poorer consistencies than **Mag$_2$-TzOA-P-1** counterparts. These observations suggested that the SPIONs could be affecting the polymer scaffold during formation of the hydrogels.

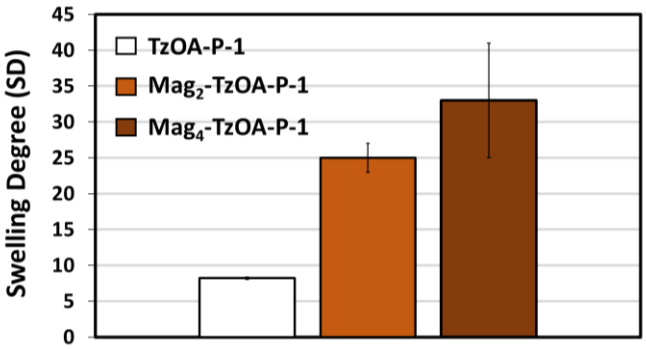

Figure 34. Swelling studies in water for TzOA-P-1 and Mag-TzOA-P-1 hydrogels.

➢ Scanning Electron Microscopy

Further analysis of the hydrogels was carried out with SEM studies. The results show that a marked increase in pore sizes occurs when SPIONs are increasingly incorporated into TzOA-P-1 hydrogels, leading to pore sizes of 24.2 ± 8.5 µm, 79.4 ± 22.3 µm and 102.8 ± 27 µm for TzOA-P-1, Mag_2-TzOA-P-1 and Mag_4-TzOA-P-1 hydrogels, respectively (Figure 35).

In accordance with the SD studies, upon increasing the SPION content the pore sizes increase, which is likely due to a loosening of the polymer network that occurs when introducing the NPs during synthesis

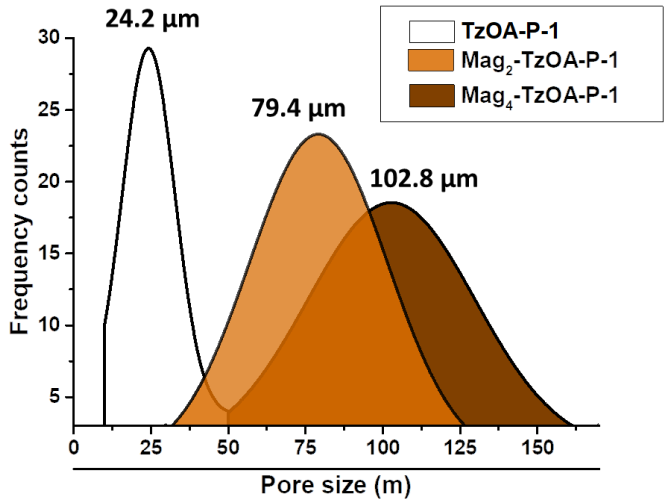

Figure 35. Pore size studies of TzOA-P-1 and Mag-TzOA-P-1 hydrogels.

. In addition, SEM images revealed morphology alterations of the pores, particularly for Mag_4-TzOA-P-1 hydrogels (Figure 36).

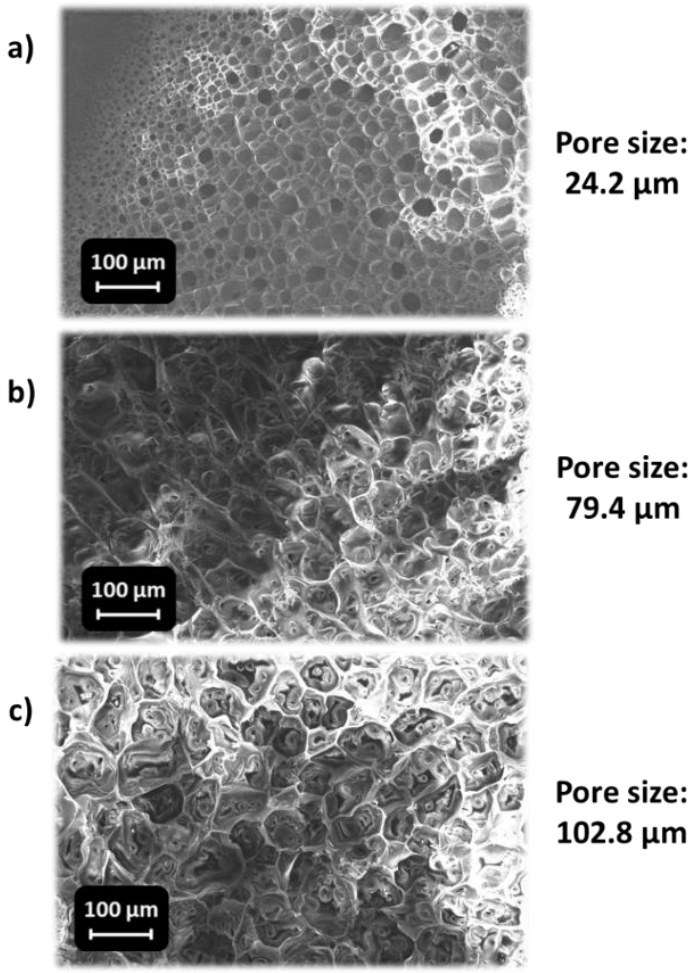

Figure 36. Pore SEM images for a) **TzOA-P-1** b) **Mag$_2$-TzOA-P-1** and c) **Mag$_4$-TzOA-P-1** hydrogels.

- **SQUID magnetometry**

Superconducting Quantum Interference Device (SQUID) measurements showed magnetic hysteresis behavior for both **Mag$_2$-TzOA-P-1** and **Mag$_4$-TzOA-P-1** hydrogels whereas **TzOA-P-1** hydrogels showed no response to the applied magnetic field (Figure 37).

Additionally, **Mag-TzOA-P-1** hydrogels present no coercitivity, this means, when the applied field is zero, no residual magnetization was observed,[35] which implies that the SPIONs embedded in the hydrogels behaved as single magnetic domains.[46]

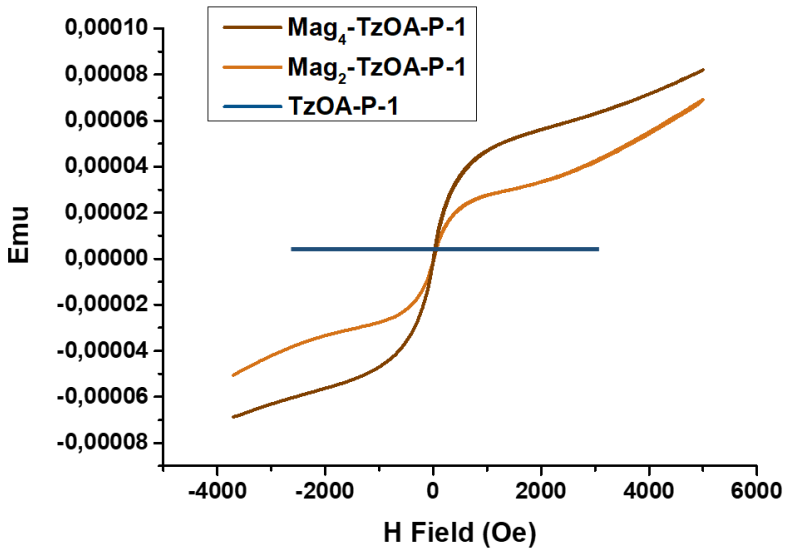

Figure 37. SQUID test for **TzOA-P-1** and **Mag-TzOA-P-1** hydrogels.

b) In situ co-precipitation method

For these studies, two hydrogel series were studied: **TzOA-0** hydrogels and their corresponding magnetite counterparts, **Mag-TzOA-0** hydrogels.

- **Synthesis**

In the *in situ* co-precipitation method, the recipe for the synthesis of physically-crosslinked **TzOA-0** hydrogels was followed: VDAT (150 mg/ml), OEGMA (135 mg/ml), AAm (135 mg/ml) and KPS initiator (2 mg/ml) were dissolved in DMSO and the mixture casted in an oven. After washing of the organogels, the **TzOA-0** hydrogels were obtained (Scheme 4a). The **Mag-TzOA-0** hydrogels were prepared following an experimental procedure based on literature.[56] First, **TzOA-0** dried xerogels were immersed in a 0.7/0.35 M $FeCl_3$/$FeCl_2$ aqueous solution for several days until maximum swelling, after which the hydrogels acquired a brown coloration. The iron-swollen hydrogels were then immersed in a 1.25 M NaOH solution (pH = 14), where the co-precipitation reaction takes place:

$$2Fe^{3+} + Fe^{2+} + 8(OH)^{-} \longrightarrow \downarrow Fe_3O_4 + 4H_2O$$

Immediately after immersion in alkali medium, the brownish hydrogels turn black due to the formation of the SPIONs and the magnetic hydrogels **$Mag_{0.35}$-TzOA-0-a** were obtained (Scheme 4b and Table 4, entry 1).

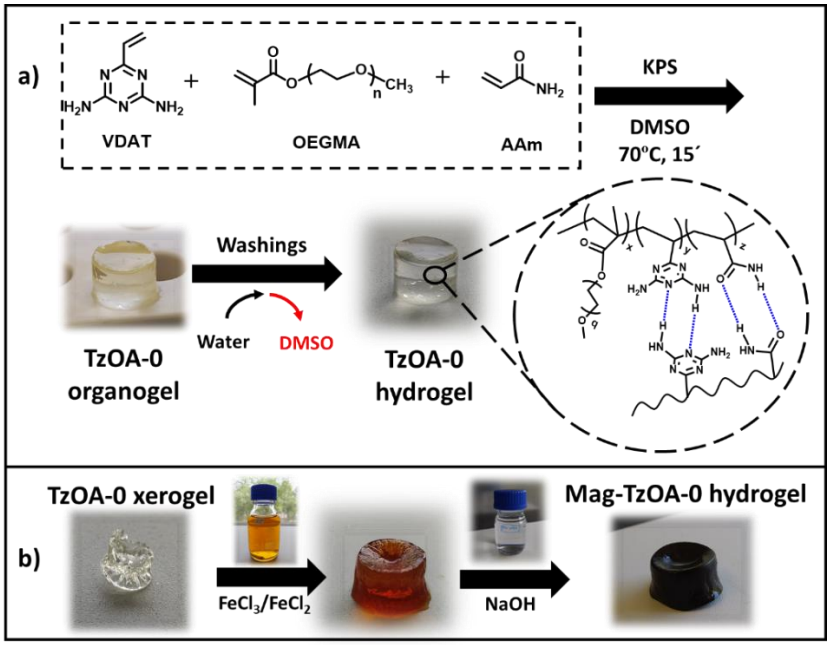

Scheme 4. Synthesis of a) **TzOA-0** and b) **Mag-TzOA-0** hydrogels.

Table 4. Synthesis of **Mag-TzOA-0** hydrogels

Entry[a]	Hydrogel	Fe^{3+}/Fe^{2+} solution	Alkaline solution	pH
1	$Mag_{0.35}$-TzOA-0-a	0.7/0.35 M	NaOH = 1.25 M	14
2	$Mag_{0.35}$-TzOA-0-b	0.7/0.35 M	NH_4OH = 0.5 M	11.7
3	$Mag_{0.25}$-TzOA-0	0.5/0.25 M	NH_4OH = 0.5 M	11.7
4	$Mag_{0.05}$-TzOA-0	0.1/0.05 M	NH_4OH = 0.5 M	11.7

[a]Hydrogels were immersed 4 and 2 days in Fe^{3+}/Fe^{2+} and alkaline solutions, respectively.

The hydrogels were strongly attracted to a neodymium static magnet, however, the materials eventually broke into pieces in the alkali solution (Figure 38).

Inspired by literature,[57,58] we hypothesized that the harsh alkaline conditions used for the co-precipitation process could be causing hydrolysis of the polymer network.

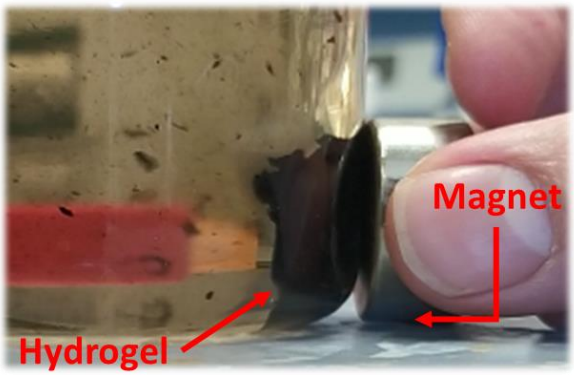

Figure 38. Breaking of **Mag0.35-TzOA-0-a** hydrogels after immersion in alkali solution.

Thus, we lowered the pH of the alkali solution from 14 to 11.7 by switching from strongly basic NaOH to ammonia weak base. The resulting **$Mag_{0.35}$-TzOA-0-b** hydrogels did not break after immersion in alkali medium and maintained consistency (Table 4, entry 2, Figure 39a).

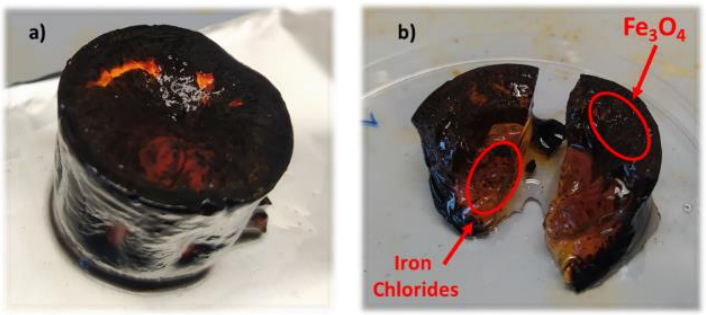

Figure 39. Mag0.35-TzOA-0-b hydrogels a) from the outside b) from the inside.

Despite the **$Mag_{0.35}$-TzOA-0-b** hydrogels were resistant to breaking, they showed important heterogeneity to the naked eye. The outer layers of the hydrogel appeared black whereas the closest area to the core remained brown, which pointed that only the external bulk of the hydrogel had converted the iron chloride precursor into Fe_3O_4 nanoparticles, while the inside remained unreacted (Figure 39b). We further confirmed this by cutting one of the central unreacted brown pieces and placing it close to the magnet and no magnetic attraction was observed.

In order to promote the homogeneity of the co-precipitation process inside the hydrogel, we tested two lower concentrations of the $FeCl_3/FeCl_2$ precursor solutions, namely, 0.5/0.25M and 0.1/0.05M and kept the pH at 11.7. After immersion of the iron-loaded hydrogels in ammonia solution, the resulting

Mag$_{0.25}$-TzOA-0 and **Mag$_{0.05}$-TzOA-0** magnetic hydrogels turned more homogeneous, while maintaining consistency (Table 4, entries 3 and 4, respectively).

The optimized recipe for the preparation of the magnetic hydrogels used in this study is shown in Scheme 5: **TzOA-0** dried xerogels were immersed in 0.5/0.25M and 0.1/0.05M solutions, to yield **Fe$_{0.05}$-TzOA-0** and **Fe$_{0.25}$-TzOA-0** hydrogels, respectively, for 5 days until maximum swelling. These were subsequently immersed in $NH_4(OH)$ 0.5 M solution (pH = 11.7) for 2 days to obtain the magnetic hydrogels **Mag$_{0.05}$-TzOA-0** and **Mag$_{0.25}$-TzOA-0**, which were then washed in water until no excess Fe_3O_4 nanoparticles leaked from the hydrogel.

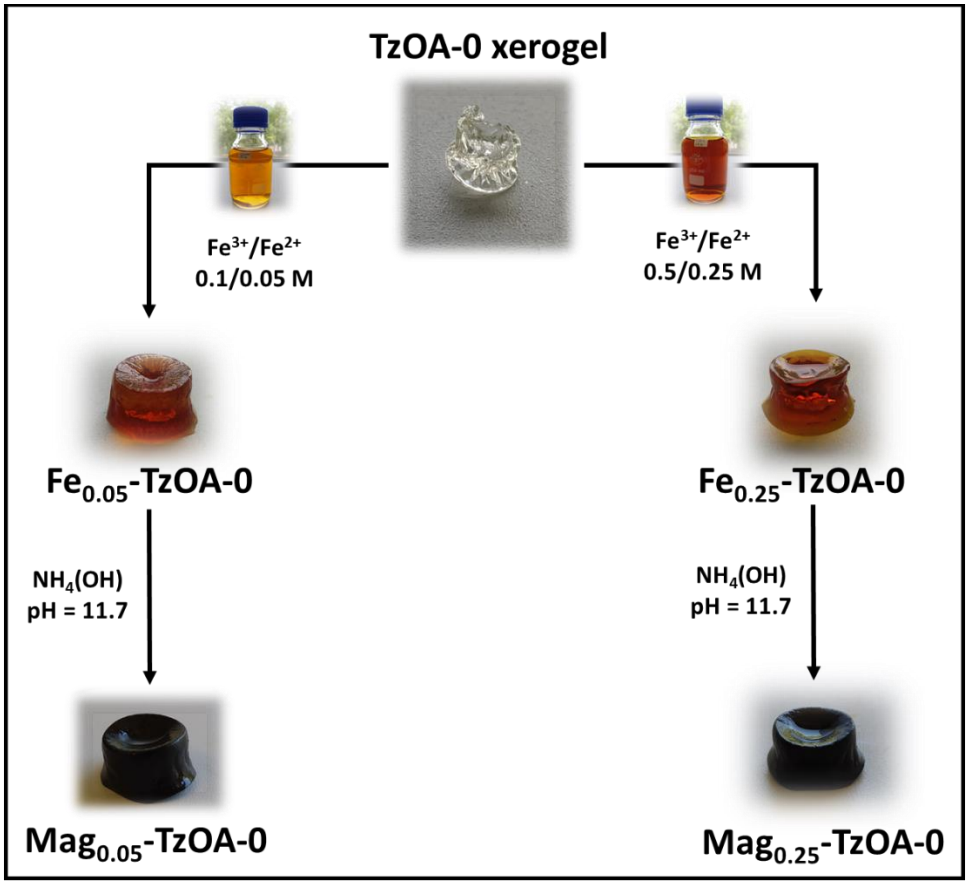

Scheme 5. Synthesis of **Fe-TzOA-0** and **Mag-TzOA-0** hydrogels.

Importantly, the remaining NPs did not leak out of the hydrogel during and after washings and remained embedded in the polymer network, thus permitting **Mag-TzOA-0** hydrogels to be strongly attracted to a static Nd magnet, whereas

their homologues **Fe-TzOA-0** and **TzOA-0** showed no attraction whatsoever (Figure 40).

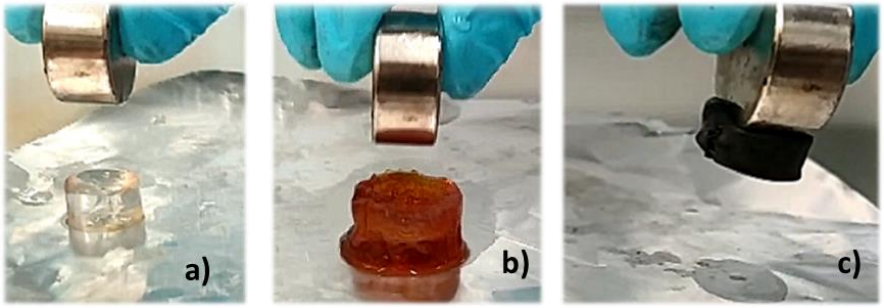

Figure 40. Interaction of DAT-based hydrogels towards Nd Magnet: a) **TzOA-0** b) **Fe-TzOA-0** and d) **Mag-TzOA-0**.

- **Characterization**

The hydrogel formulations **TzOA-0, $Fe_{0.05}$-TzOA-0, $Fe_{0.25}$-TzOA-0, $Mag_{0.05}$-TzOA-0** and **$Mag_{0.25}$-TzOA-0** were further characterized by swelling degree, SEM, TGA, FT-IR, mechanical tests, SQUID (superconducting quantum interference device) magnetometry, powder X-ray diffraction (PXRD), transmission electron microscopy (TEM) and energy dispersive X-ray spectroscopy (EDX).

- **Swelling studies**

The swelling studies were performed in different solvent media according to the hydrogel species: the SD of both **TzOA-0** and **Mag-TzOA-0** hydrogels was performed in neutral aqueous media, whereas the SD of **Fe-TzOA-0** precursors was tested in $FeCl_3$/$FeCl_2$ aqueous solutions at two increasing concentrations, namely 0.1/0.05M and 0.5/0.25M.

Figure 41 shows the SD values for the hydrogels. An interesting trend is observed: **TzOA-0** hydrogels show SD ~ 10, **$Fe_{0.05}$-TzOA-0** hydrogels increase to SD ~ 30 and **$Mag_{0.05}$-TzOA-0** hydrogels decrease back to SD ~ 15 (Figure 41a-b).

The explanation of this trend is shown Figure 41c-e: in **TzOA-0** hydrogels, DATs self-associate through H-bonding, resulting in hydrophobic aggregates. These microdomains restrain water uptake in the hydrogel and thus the SD values for these materials are low (Figure 41c).

When the hydrogels are immersed in the iron solutions, the DATs will coordinate the metal centers, as typically occurs in aminotriazine-metal complexes.[59–62] Coordination of the DATs to Fe, however, comes at the expense of disrupting the DAT-DAT H-bonding network and so the swelling capacity in the **$Fe_{0.05}$-TzOA-0** precursors increases (Figure 41c).

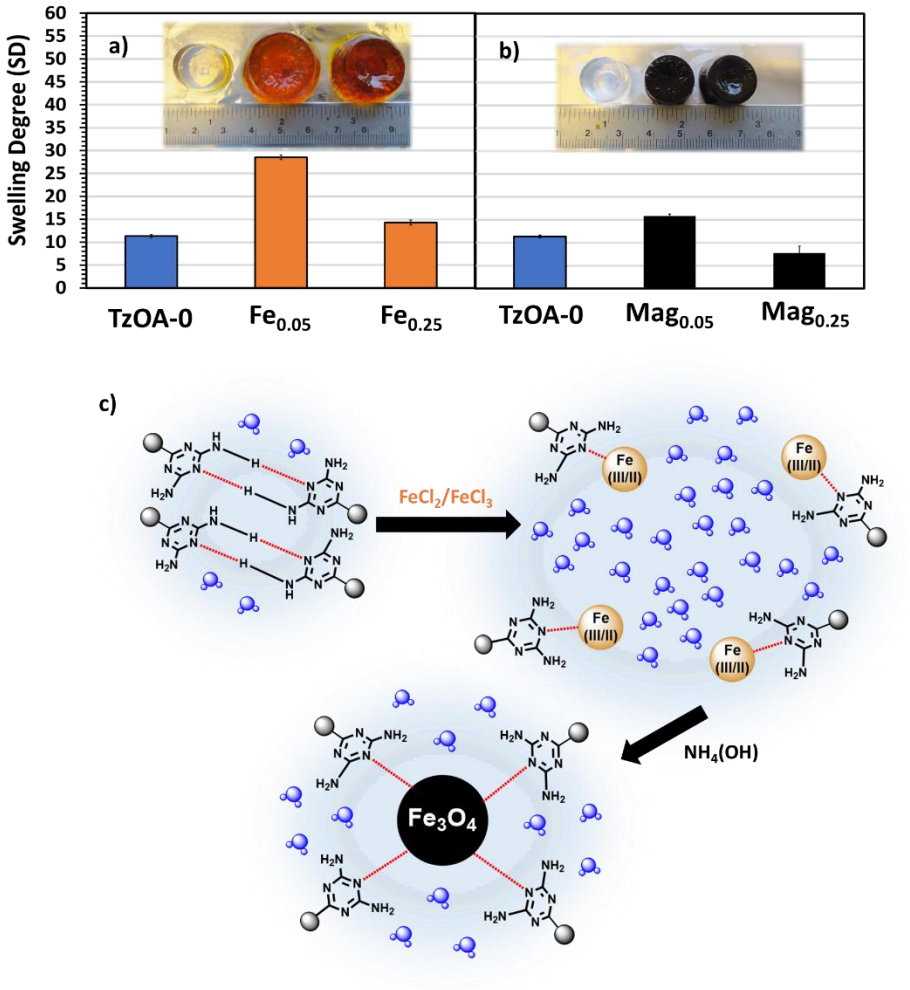

Figure 41. Swelling degree (SD) studies for hydrogels a) **TzOA-0** and **Fe-TzOA-0** b) **TzOA-0** and **Mag-TzOA-0** and c) swelling mechanism.

In **$Mag_{0.05}$-TzOA-0** hydrogels, SPIONs are fully formed inside the network. Unlike atom-sized iron chloride molecules, SPIONs are Fe_3O_4 nanoparticles ranging 10-100 nm in diameter,[63] and so multiple coordination sites between the SPIONs and DATs can occur. In this scenario, the SPIONs act as crosslinking joints, and this decreases the swelling capacity of the hydrogels (Figure 41c).

For higher iron ion concentrations, the following trend is observed: **$Fe_{0.25}$-TzOA-0** show SD ~ 15 and **$Mag_{0.25}$-TzOA-0** show SD ~ 7.5 (Figure 41a-b). The trend is similar as observed for lower iron concentrations, however, is less pronounced. When the solutions in which the hydrogels are immersed become too concentrated, as occurs in the case of **$Fe_{0.25}$-TzOA-0** hydrogels, their capacity of swelling in water is notably decreased, and so does the SD values.

Finally, increasing the SPION concentration in the hydrogel, as in **$Mag_{0.25}$-TzOA-0**, will increase the crosslinking density on the network and so the SD values drop.

- **Scanning Electron Microscopy**

The porous internal structure of the DAT-based hydrogels was investigated using SEM imaging.

TzOA-0 hydrogels showed mean pore sizes of 95.2 ± 23.2 µm, **$Fe_{0.05}$-TzOA-0** hydrogels increase to 815.9 ± 89.3 µm and **$Mag_{0.05}$-TzOA-0** hydrogels decrease back to 365.6 ± 57.5 µm (Figure 42a).

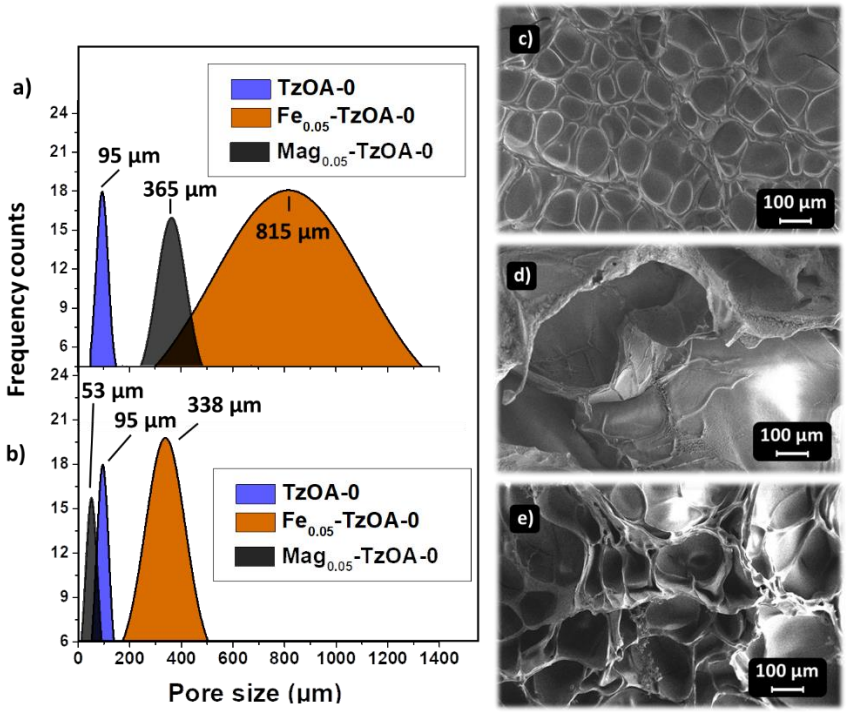

Figure 42. Pore size distributions a) **TzOA-0**, **$Fe_{0.05}$-TzOA-0** and **$Mag_{0.05}$-TzOA-0** hydrogels and b) **TzOA-0**, **$Fe_{0.25}$-TzOA-0** and **$Mag_{0.25}$-TzOA-0** hydrogels. SEM images for c) **TzOA-0** d) **$Fe_{0.05}$-TzOA-0** and e) **$Mag_{0.05}$-TzOA-0** hydrogels.

This up-and-down trend is in accordance with the swelling studies: coordination to Fe ions, as in **$Fe_{0.05}$-TzOA-0** hydrogels, disrupts the DAT-DAT H-bond network and increases the pore sizes. On the contrary, SPIONs in **$Mag_{0.05}$-TzOA-0** hydrogels increase the crosslinking degree and thus mean pore sizes decrease.

$Fe_{0.25}$-TzOA-0 and **$Mag_{0.25}$-TzOA-0** hydrogels show pore sizes of 338 ± 77 µm and 53.3 ± 23.1 µm, respectively (Figure 42b), following the same trend as observed in the SD studies. Digital SEM images of the internal structure of the hydrogels are shown in Fig. 42c-e and Fig. 43.

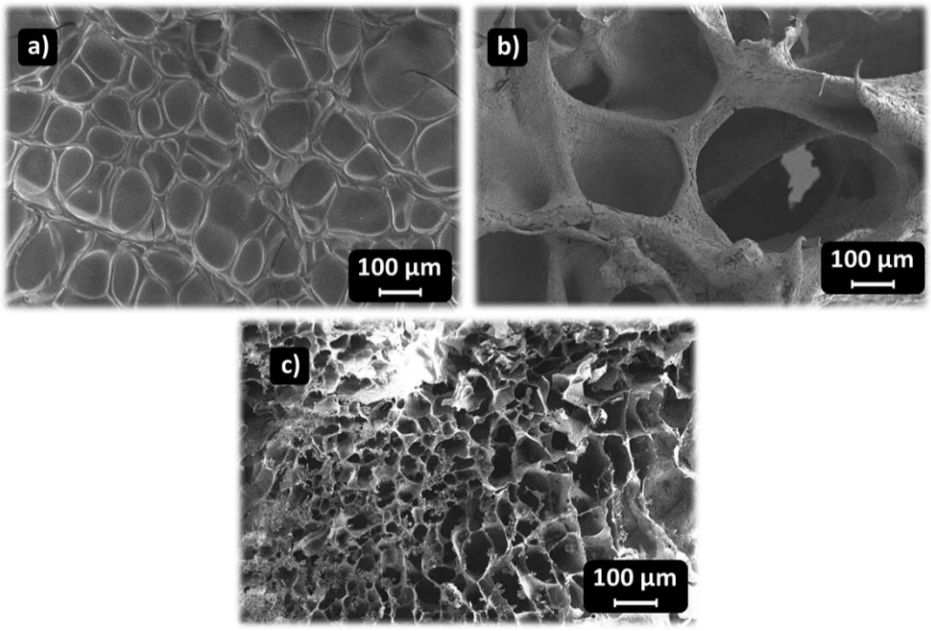

Figure 43. Digital SEM images of DAT-based hydrogels a) **TzOA-0** b) **$Fe_{0.25}$-TzOA-0** c) **$Mag_{0.25}$-TzOA-0**

- **Thermogravimetric Analysis**

TGA afforded useful information about the chemical and physical interactions occurring inside the hydrogels.

Under N_2 atmosphere, the thermal decomposition of **TzOA-0** hydrogels shows a single weight loss at 394ºC, corresponding to the hydrogel polymer backbone (Figure 44, bold blue).[43]

$Fe_{0.05}$-TzOA-0 hydrogels show instead two differentiated weight losses at 257ºC and 650-750ºC (Figure 44, bold orange): the latter provides evidence of a new chemical interaction, which is absent in the **TzOA-0** hydrogels, and this

is attributed to the DAT-Fe bond. The loss at 257ºC corresponds to the polymer backbone and reveals a notable weakening of the polymer scaffold with respect to the **TzOA-0** hydrogels.

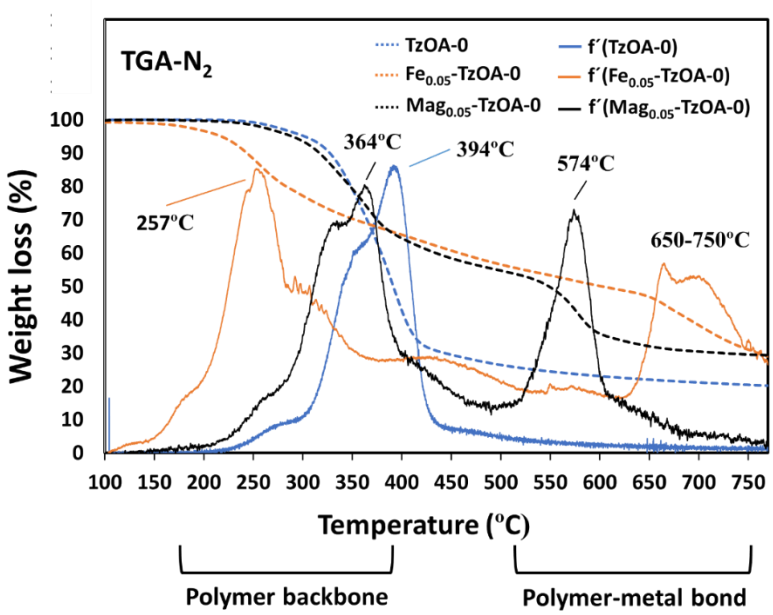

Figure 44. TGA (dashed curves) and TGA derivatives (bold curves) of DAT-based hydrogels carried out under N_2 atmosphere.

$Mag_{0.05}$-TzOA-0 hydrogels show a new loss absent in the **TzOA-0** hydrogels at 574ºC, which corresponds to the DAT-SPION bond (Figure 44, bold black). This loss occurs at significantly lower temperatures than for **$Fe_{0.05}$-TzOA-0** precursors, which points that DAT-SPION bonds are weaker than DAT-Fe bonds. On the contrary, the polymer backbone loss in **$Mag_{0.05}$-TzOA-0** hydrogels occurs at 364ºC, which is higher than in **$Fe_{0.05}$-TzOA-0** precursors.

These observations suggests that formation of the DAT-metal bonds occurs at the expense of weakening the polymer scaffold, which in the DAT hydrogels is sustained through the DAT-DAT H-bond physical network that is responsible for the hydrogel compactness and mechanical strength. It follows that, in **$Fe_{0.05}$-TzOA-0** hydrogels, DAT-Fe bonds are stronger but the DAT-DAT H-bond network is disrupted, whereas in **$Mag_{0.05}$-TzOA-0** hydrogels the DAT-SPION bonds are weaker but the H-bond network is partially consistent.

Further, at high iron precursor concentrations both in **$Fe_{0.25}$-TzOA-0** and **$Mag_{0.25}$-TzOA-0** hydrogels the intensity of the losses for DAT-metal bonds increases drastically, which evidences the increase in the concentrations of Fe

ions and SPIONs for these hydrogels (Figure 45a, bold orange and black, respectively).

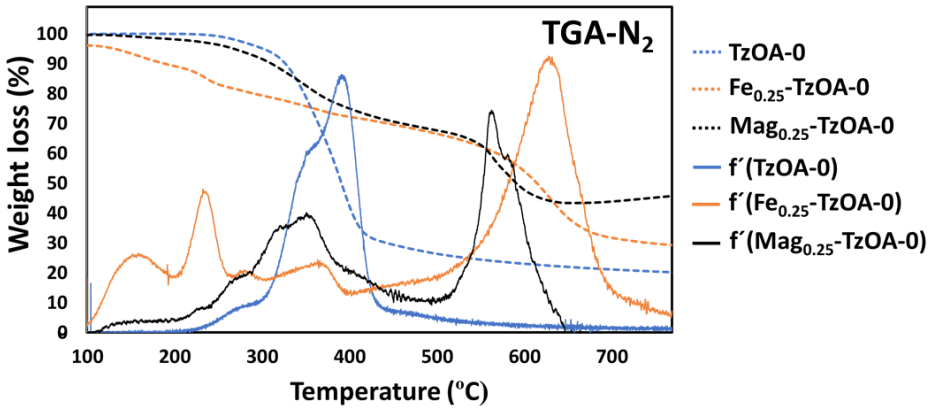

Figure 45. TGA (dashed curves) and TGA derivatives (bold curves) for **TzOA-0**, **$Fe_{0.25}$-TzOA-0** and **$Mag_{0.25}$-TzOA-0** hydrogels under N_2 atmosphere

Finally, in an attempt to quantify the content of SPIONs embedded in the hydrogel, TGA curves of the hydrogels were also carried out in O_2 atmosphere conditions (Figure 46).

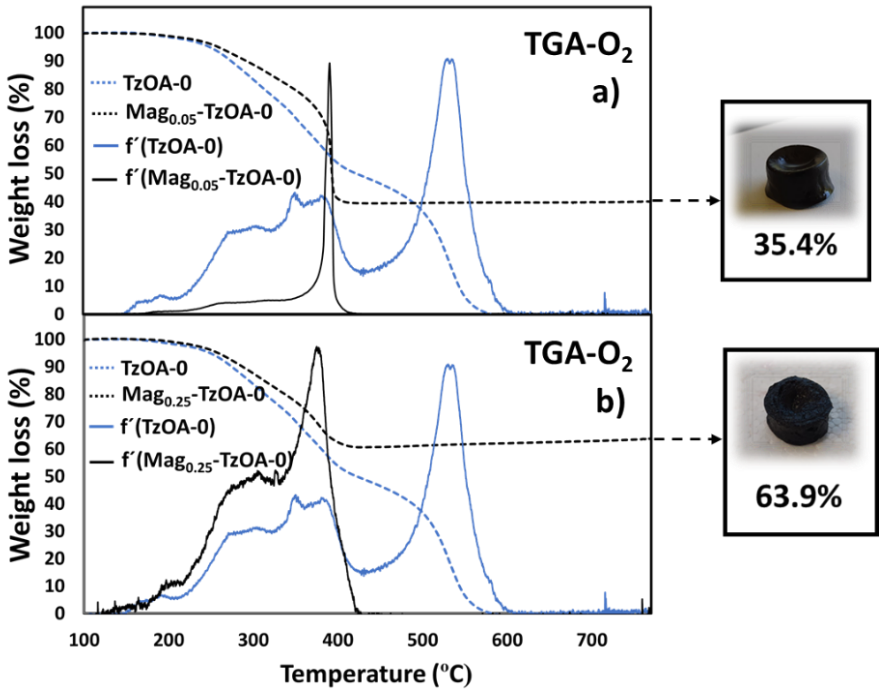

Figure 46. TGA (dashed curves) and TGA derivatives (bold curves) for a) **TzOA-0** and **$Mag_{0.05}$-TzOA-0** hydrogels and b) **TzOA-0** and **$Mag_{0.25}$-TzOA-0** hydrogels under O_2 atmosphere.

Under oxygen atmosphere, all the organic content of the hydrogel decomposes, whereas magnetite nanoparticles (Fe_3O_4) fully oxidate to hematite species (Fe_2O_3), according to the equation: $2Fe_3O_4 + 1/2O_2 \rightleftharpoons 3Fe_2O_3$.[64]

The TGA curves reveal a 35% and 64% hematite mass percent remaining for **$Mag_{0.05}$-TzOA-0** and **$Mag_{0.25}$-TzOA-0** hydrogels, respectively. These values account for 34% and 62% SPION weight content in the former and latter.

- **Infrared spectroscopy**

Further characterization of the hydrogels was carried out with IR spectroscopy; for the sake of comparison, all spectra of the hydrogel species were overlaid with the spectra of the VDAT monomer alone.

The vibrational bands of the VDAT monomer are shown in Figure 47a: ν(NH) at 3310 and 3142 cm^{-1}, δ(N-H) at 1640 cm^{-1}, $\nu(CN)_{ring}$ at 1511-1424 cm^{-1} and the out-of-plane C-H bends of the vinyl group at 958 and 830 cm^{-1}.[65–68]

The IR spectrum of the **TzOA-0** hydrogels reveals the disappearance of the vinyl bands of the VDAT and the presence of the (C-H)-O and the C-O vibrations of the OEGMA moiety,[69] confirming thus the structure of the hydrogel (Figure 47b). Further, intermolecular H-bonds between DATs in the **TzOA-0** hydrogel are effectively illustrated in the blueshift and broadening of the ν(N-H) bands and the shifts in the δ(NH) and $\nu(CN)_{ring}$ bands.[51] These observations suggest that DATs in the hydrogel coordinate *via* complementary H-bonds between the endocyclic ring N atoms and the exocyclic -NH_2 groups, as it is well known to occur in DAT associations (Figure 47e).[70,71]

In the spectrum of the **$Fe_{0.05}$-TzOA-0** hydrogels, two marked changes are observed (Figure 47c): first, the ring CN vibration bands disappear. Secondly, the ν(N-H) and δ(NH) bands shift to 3367-3219 cm^{-1} and 1610 cm^{-1}, respectively. The first observation indicates a strong variation in the electron density of the *s*-triazine ring, which suggests coordination between the ring and the acceptor metal center, as it is observed between complexes of melamine (2,4,6-triamino-1,3,5-triazine) and Ag salts.[61,62] The shifts observed in the NH bands further point electron delocalization of the -NH_2 towards the s-triazine upon coordination to the metal (Figure 47f). This DAT-Fe ion coordination mode correlates with the results observed for the TGA in the high temperature range, which suggested formation of a stable polymer-metal bond.

For higher Fe concentrations, **$Fe_{0.25}$-TzOA-0** hydrogels revealed sharper changes in the N-H stretching and N-H bending bands (Figure 48a), thus suggesting more effective coordination.

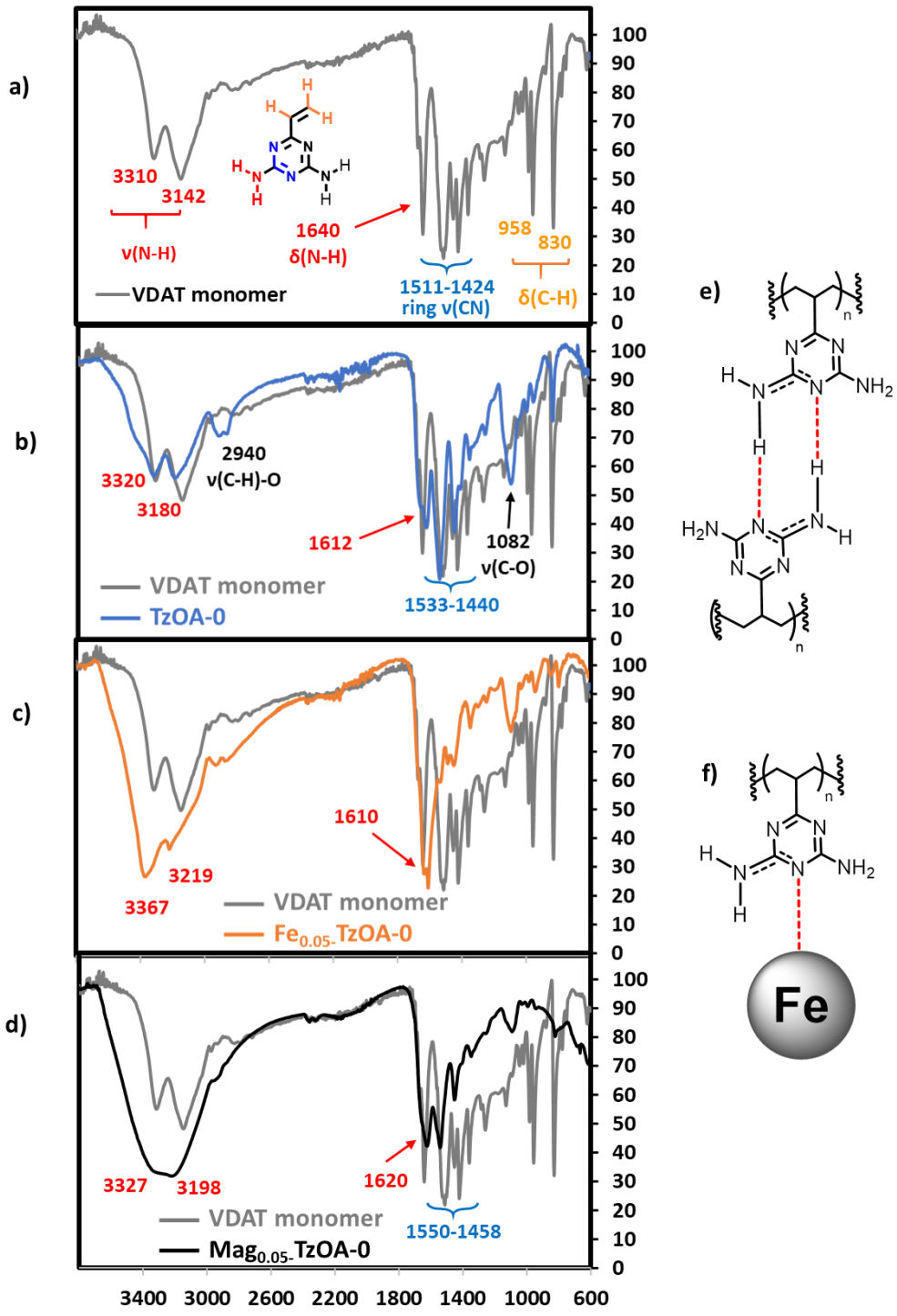

Figure 47. IR spectra of a) VDAT monomer b) TzOA-0 hydrogel c) $Fe_{0.05}$-TzOA-0 hydrogel d) $Mag_{0.05}$-TzOA-0 hydrogel. Coordination modes between e) DAT-DAT and f) DAT-Fe atom. All spectra are overlaid with the VDAT monomer.

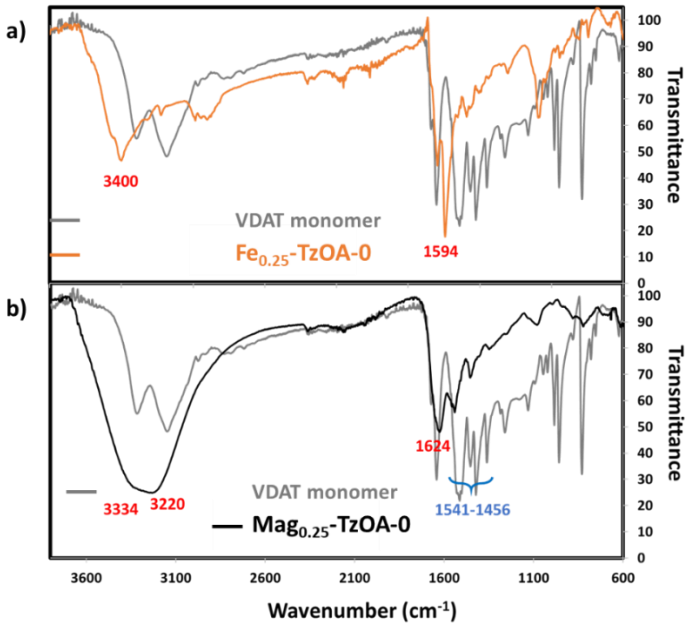

Figure 48. IR spectra of a) **$Fe_{0.25}$-TzOA-0** hydrogel b) **$Mag_{0.25}$-TzOA-0** hydrogel. All spectra are overlaid with the VDAT monomer.

$Mag_{0.05}$-TzOA-0 and **$Mag_{0.25}$-TzOA-0** hydrogels (Figure 47d and Figure 48b, respectively) show a partial disappearance of the ring CN distortion bands with respect to the VDAT monomer and **TzOA-0** hydrogel, which points a weaker N-Fe coordination bond between the s-triazine and the SPIONs (Figure 47f), in accordance with the TGA results. As explained previously, it is expected that DATs display less affinity to coordinate SPIONs as for iron chloride atoms, due to the marked size differences between the two iron species.

- **Mechanical properties**

The physically-crosslinked **TzOA-0** hydrogels prepared in this work presented remarkable mechanical properties. Despite the absence of chemical crosslinking, the hydrogels resisted to cuts and heavy loads (Figure 49). This is attributed to the DAT-DAT physical H-bond network, which not only provides the hydrogels with hydrophobic reservoirs, but also suppress the hydrogel swelling and considerably increase mechanical strengths as well.[72]

The influence of the DAT-DAT H-bond network on the mechanical strengths of the hydrogels is reflected in the stress-strain curves (Figure 50). **TzOA-0** hydrogels compress down to 70% initial height under the experimented conditions, whereas upon introduction of SPIONs, both **$Mag_{0.05}$-TzOA-0** and **$Mag_{0.25}$-TzOA-0** hydrogels compressed down to 80% initial height.

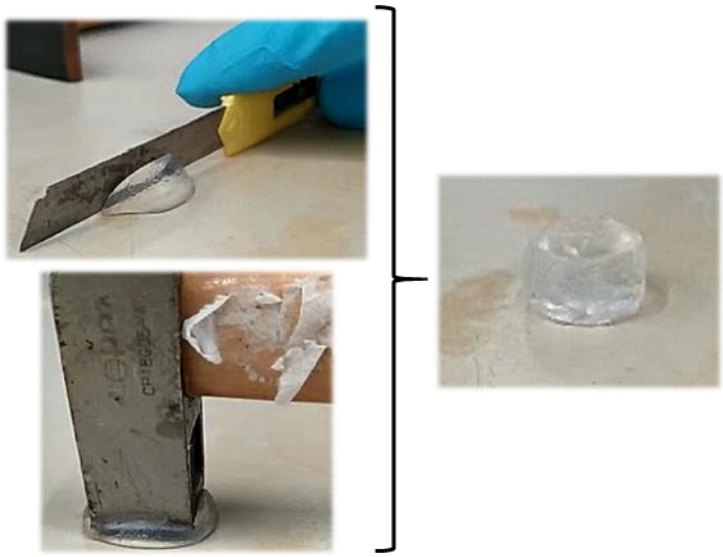

Figure 49. Recovery of physically-crosslinked TzOA-0 hydrogels after performing cuts and stress loads.

This increase in the ability to elongate of the magnetic hydrogels is attributed to the disruption of the DAT-DAT H-bond stiffened network that occurs when DATs coordinate the SPIONs.

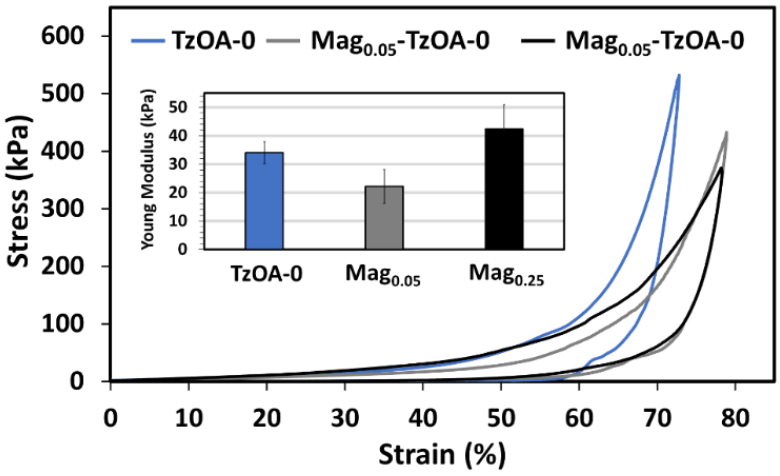

Figure 50. Compression stress-strain curves for DAT-based hydrogels and Young modulus (inset).

Young moduli values recorded for TzOA-0, $Mag_{0.05}$-TzOA-0 and $Mag_{0.25}$-TzOA-0 hydrogels were 34 kPa, 23 kPa and 42 kPa, respectively (Figure 50 inset). These results are in accordance with the trends observed in the SD and SEM studies:

- At low NP concentrations, DAT-SPION coordination brings about disruption of DAT-DAT H-bond network and consequently the rigidity of the magnetic hydrogel drops.

- Conversely, at higher NP concentrations SPIONs behave as crosslinking joints and the stiffness is increased.

A similar trend in the Young moduli values was observed for **TzOAM-6**, **$G_{0.1}$-TzOAM-6** and **$G_{0.5}$-TzOAM-6** hydrogels.[52,73]

➢ **SQUID magnetometry**

The specific magnetization as a function of the magnetic field (H) was measured for the different DAT-based hydrogels (Figure 51, blue).

In the absence of superparamagnetic iron oxide nanoparticles (SPIONs), it is clearly observed that no magnetic response is observed when the H field is applied (Figure 51, blue), whereas a magnetic hysteresis loop of increasing intensity appears for **Mag-TzOA-0** gels as the SPION content in the hydrogels increases (Figure 51 grey and black).

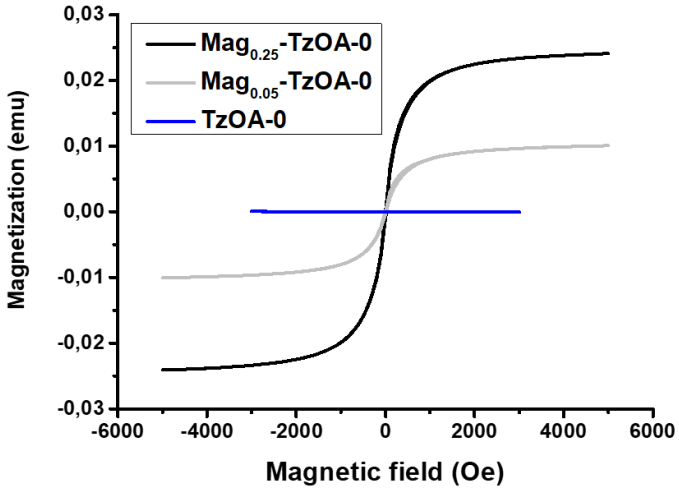

Figure 51. Magnetic hysteresis loop of DAT-based hydrogels.

The magnetic loops from both magnetic hydrogels display a typical S-shaped curve, which implies that SPIONs differ in sizes within a specific range.[74] In addition, the superparamagnetic behavior and the absence of coercitivity of the **Mag-TzOA-0** hydrogels suggest that the SPIONs arrange in single domains throughout the polymer network, showing no signs of aggregation.[46,75]

➢ Power X-ray Diffraction (PXRD)

PXRD provided the crystal structure and sizes of the embedded SPIONs in the DAT-based hydrogels.

The TzOA-0 hydrogel spectrum showed intense broad bands at low 2θ values, indicating the typical polymer amorphous structure (Figure 52, blue).[76]

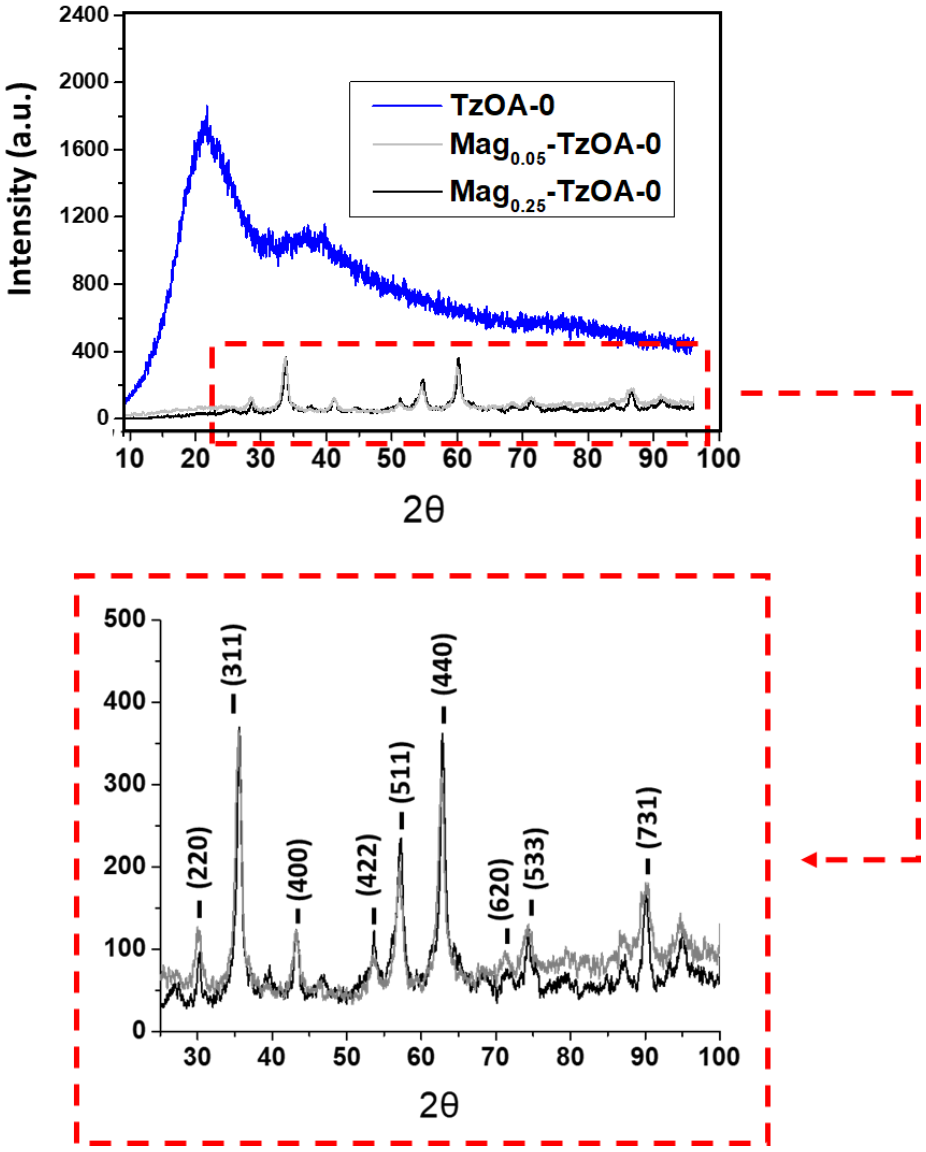

Figure 52. PXRD patterns for DAT-based hydrogels.

For Mag-TzOA-0 hydrogels, the peaks at 2θ = 30.37, 35.60, 43.15, 53.69, 57.33, 62.69, 71.49, 74.30 and 90.18 were attributed to the crystal planes (220), (311), (400), (422), (511), (440), (620), (533) and (731) of the Fe_3O_4

NPs, which are in agreement with the cubic spinel structure of magnetite (JCPDS # 01-111) (Figure 52 inset, grey and black).

The well-defined X-ray diffraction patterns indicate formation of highly crystalline iron oxide NPs, which are seemingly favored by the *prior* formation of DAT-Fe complexes; these operate as nucleation sites for the ordered formation of crystalline SPIONs and avoid overgrowth and aggregation.

Further, the average crystal sizes of the NPs embedded in the hydrogels determined by Scherrer´s formula[77] were 8.07 and 10.5 nm for **Mag$_{0.05}$-TzOA-0** and **Mag$_{0.25}$-TzOA-0** hydrogels, respectively, with an interplanar distance at the (311) crystal face of 2.53 Å, thus confirming that the NP were in the size range of SPIONs reported elsewhere.[63]

- **Transmission Electron Microscopy (TEM)**

TEM images provided useful information about the size, polydispersity and distribution of the SPIONs within the hydrogel network.

Figure 53a-b shows that SPIONs in both **Mag$_{0.05}$-TzOA-0** and **Mag$_{0.25}$-TzOA-0** hydrogels were well dispersed throughout the hydrogel network, evidencing no signs of NP aggregation.[46,75]

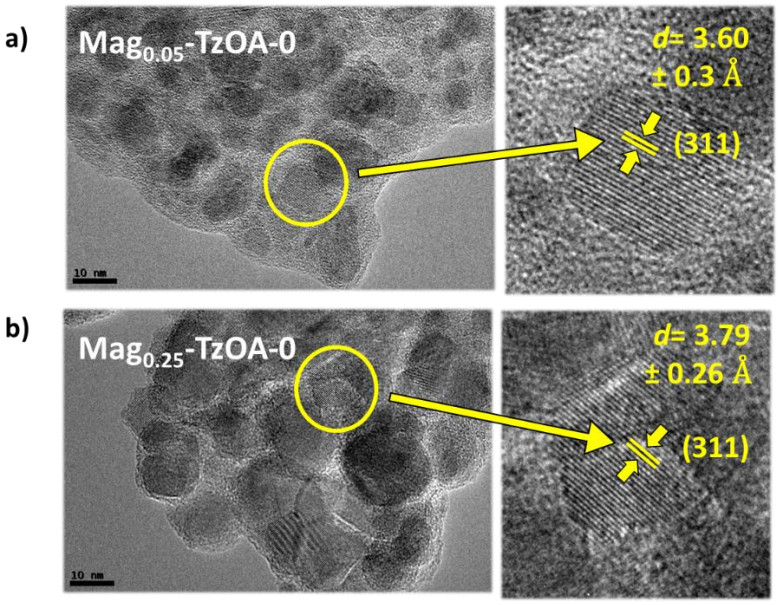

Figure 53. TEM morphologies (left) and single Fe_3O_4 crystals (right) for a) **Mag$_{0.05}$-TzOA-0** hydrogels and b) **Mag$_{0.25}$-TzOA-0** hydrogels.

This is likely a consequence of the DAT-Fe complexes that fixate iron ions during NP formation and avoid unrestrained spreading and overgrowth.

Zooming-in in Figure 53a-b shows clear TEM images of a single Fe_3O_4 crystal for both **Mag$_{0.05}$-TzOA-0** and **Mag$_{0.25}$-TzOA-0** hydrogels, which display a clean lattice pattern with an interplanar distance of 3.6 and 3.8 Å, respectively, at the (311) reflection, showing only a slight deviation from the PXRD results.

The TEM size distributions of the SPIONs embedded in the hydrogels were confirmed as 8.99 ± 2.55 and 17.2 ± 4.36 nm for **Mag$_{0.05}$-TzOA-0** and **Mag$_{0.25}$-TzOA-0** hydrogels, respectively (Figure 54), which shows great resemblance with the crystal sizes observed in the X-ray diffraction studies.

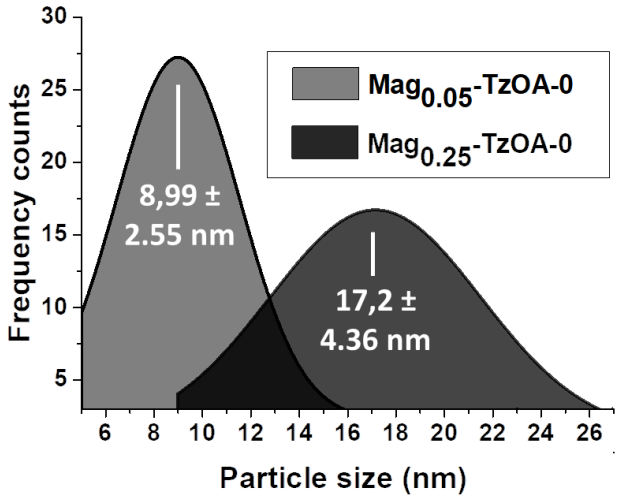

Figure 54. TEM size nanoparticle distribution.

- **Energy Dispersive X-Ray spectroscopy (EDX)**

The homogeneous distribution of the SPIONs was further visualized with EDX spectroscopy, which here is shown for the representative **Fe$_{0.25}$-TzOA-0** and **Mag$_{0.25}$-TzOA-0** series (Figure 55).

For further clarity, carbon and oxygen atoms were omitted from the mappings. In both spectra, iron and nitrogen elements (red and blue, respectively) clearly appeared homogeneously distributed throughout the sample, showing no signs of NP aggregation.

Finally, the presence of chlorine (green) from iron chloride precursor solutions is abundantly present in the **Fe$_{0.25}$-TzOA-0** hydrogels (Figure 55a) evidencing proper uptake of iron chloride species by the DAT moieties, whereas

barely no chloride remains in the **Mag$_{0.25}$-TzOA-0** hydrogels (Figure 55b), which points out efficient yield of the co-precipitation process.

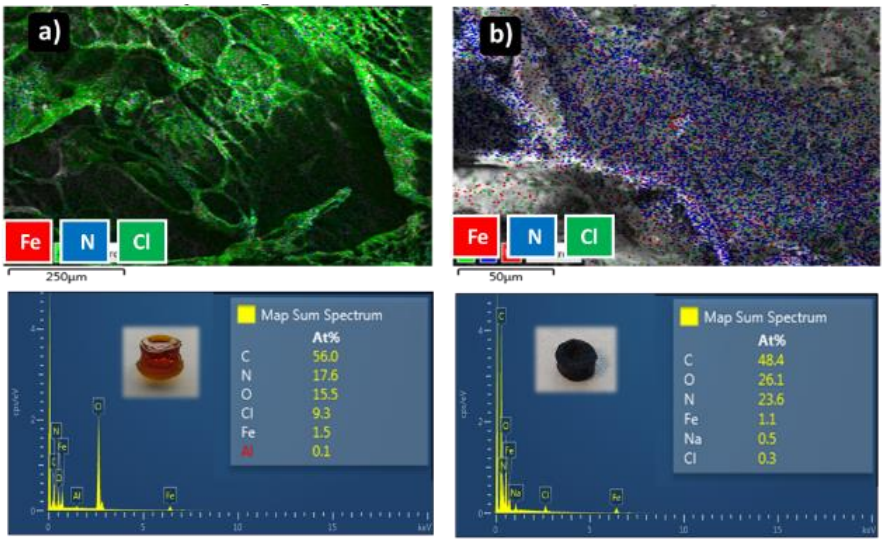

Figure 55. EDX spectroscopy. Electron images (up) and Map sum spectrum (down) for a) **Fe$_{0.25}$-TzOA-0** and b) **Mag$_{0.25}$-TzOA-0** hydrogels.

3.3. References

[1] M. Srinivasan, M. Rajabi, S. A. Mousa, *Nanomaterials* 2015, *5*, 1690–1703.

[2] J. Jeevanandam, A. Barhoum, Y. S. Chan, A. Dufresne, M. K. Danquah, *Beilstein J. Nanotechnol.* 2018, *9*, 1050–1074.

[3] N. Anzar, R. Hasan, M. Tyagi, N. Yadav, J. Narang, *Sensors Int.* 2020, *1*, 100003.

[4] L. A. Kolahalam, I. V. Kasi Viswanath, B. S. Diwakar, B. Govindh, V. Reddy, Y. L. N. Murthy, *Mater. Today Proc.* 2019, *18*, 2182–2190.

[5] A. C. Ferrari, J. C. Meyer, V. Scardaci, C. Casiraghi, M. Lazzeri, F. Mauri, S. Piscanec, D. Jiang, K. S. Novoselov, S. Roth, et al., *Phys. Rev. Lett.* 2006, *97*, 187401.

[6] A. K. Geim, *Science (80-.).* 2009, *324*, 1530–1535.

[7] M. I. Katsnelson, *Mater. Today* 2007, *10*, 20–27.

[8] C. Lee, X. Wei, J. W. Kysar, J. Hone, *Science.* 2008, *321*, 385–388.

[9] R. R. Nair, P. Blake, A. N. Grigorenko, K. S. Novoselov, T. J. Booth, T. Stauber, N. M. R. Peres, A. K. Geim, *Science.* 2008, *320*, 1308.

[10] N. Venkatesh, *Biomed. J. Sci. Tech. Res.* 2018, *4*, 3765–3775.

[11] D. Kim, S. Jon, *Inorganica Chim. Acta* 2012, *393*, 154–164.

[12] H. C. Huang, S. Barua, G. Sharma, S. K. Dey, K. Rege, *J. Control. Release* 2011, *155*, 344–357.

[13] L. Cheng, K. Yang, Y. Li, X. Zeng, M. Shao, S. T. Lee, Z. Liu, *Biomaterials* 2012, *33*, 2215–2222.

[14] A. H. Lu, W. Schmidt, N. Matoussevitch, H. Bönnemann, B. Spliethoff, B. Tesche, E. Bill, W. Kiefer, F. Schüth, *Angew. Chemie - Int. Ed.* 2004, *43*, 4303–4306.

[15] A. K. Gupta, M. Gupta, *Biomaterials* 2005, *26*, 3995–4021.

[16] S. Mornet, S. Vasseur, F. Grasset, P. Veverka, G. Goglio, A. Demourgues, J. Portier, E. Pollert, E. Duguet, *Prog. Solid State Chem.* 2006, *34*, 237–247.

[17] D. W. Elliott, W. X. Zhang, *Environ. Sci. Technol.* 2001, *35*, 4922–4926.

[18] S. Ayyappan, S. Mahadevan, P. Chandramohan, M. P. Srinivasan, J. Philip, B. Raj, *J. Phys. Chem. C* 2010, *114*, 6334–6341.

[19] G. Gnanaprakash, S. Ayyappan, T. Jayakumar, J. Philip, B. Raj, *Nanotechnology* 2006, *17*, 5851–5857.

[20] Y. Y. Lin, H. W. Kao, J. J. Li, J. J. Hwang, Y. L. Tseng, W. J. Lin, M. H. Lin, G. Ting, H. E. Wang, *PLoS One* 2013, *8*, 1–10.

[21] J. Kousalová, T. Etrych, *Physiol. Res.* 2018, *67*, 305–317.

[22] Y. Wang, L. Li, N. Shao, Z. Hu, H. Chen, L. Xu, C. Wang, Y. Cheng, J. Xiao, *Acta Biomater.* 2015, *17*, 115–124.

[23] L. L. Palmese, R. K. Thapa, M. O. Sullivan, K. L. Kiick, *Curr. Opin. Chem. Eng.* 2019, *24*, 143–157.

[24] S. Goenka, V. Sant, S. Sant, *J. Control. Release* 2014, *173*, 75–88.

[25] A. K. Gaharwar, N. A. Peppas, A. Khademhosseini, *Biotechnol. Bioeng.* 2014, *111*, 441–453.

[26] C. Cha, S. R. Shin, N. Annabi, M. R. Dokmeci, A. Khademhosseini, *ACS Nano* 2013, *7*, 2891–2897.

[27] S. R. Shin, S. M. Jung, M. Zalabany, K. Kim, P. Zorlutuna, S. B. Kim, M. Nikkhah, M. Khabiry, M. Azize, J. Kong, et al., *ACS Nano* 2013, *7*, 2369–2380.

[28] P. C. Ma, N. A. Siddiqui, G. Marom, J. K. Kim, *Compos. Part A Appl. Sci. Manuf.* 2010, *41*, 1345–1367.

[29] S. Das, F. Irin, L. Ma, S. K. Bhattacharia, R. C. Hedden, M. J. Green, *ACS Appl. Mater. Interfaces* 2013, *5*, 8633–8640.

[30] A. Servant, V. Leon, D. Jasim, L. Methven, P. Limousin, E. V. Fernandez-Pacheco, M. Prato, K. Kostarelos, *Adv. Healthc. Mater.* 2014, *3*, 1334–1343.

[31] J. M. González-Domínguez, E. Vázquez, R. Rauti, S. Merino, C. Martín, L. Ballerini, M. Prato, *Sci. Rep.* 2017, *7*, 10942.

[32] P. Schexnailder, G. Schmidt, *Colloid Polym. Sci.* 2009, *287*, 1–11.

[33] Y. Li, G. Huang, X. Zhang, B. Li, Y. Chen, T. Lu, T. J. Lu, F. Xu, *Adv.*

Funct. Mater. 2013, *23*, 660–672.

[34] A. Tampieri, E. Landi, F. Valentini, M. Sandri, T. D'Alessandro, V. Dediu, M. Marcacci, *Nanotechnology* 2011, *22*, 015104.

[35] S. Kondaveeti, A. T. S. Semeano, D. R. Cornejo, H. Ulrich, D. F. S. Petri, *Colloids Surfaces B Biointerfaces* 2018, *167*, 415–424.

[36] H. Zhang, A. Patel, A. K. Gaharwar, S. M. Mihaila, G. Iviglia, S. Mukundan, H. Bae, H. Yang, A. Khademhosseini, *Biomacromolecules* 2013, *14*, 1299–1310.

[37] A. M. Rodríguez, A. B. Muñoz-García, O. Crescenzi, E. Vázquez, M. Pavone, *Phys. Chem. Chem. Phys.* 2016, *18*, 22203–22209.

[38] V. León, A. M. Rodríguez, P. Prieto, M. Prato, E. Vázquez, in *ACS Nano*, 2014, pp. 563–571.

[39] J. M. González-Domínguez, V. León, M. I. Lucío, M. Prato, E. Vázquez, *Nat. Protoc.* 2018, *13*, 495–506.

[40] N. Wang, Y. Han, Y. Liu, T. Bai, H. Gao, P. Zhang, W. Wang, W. Liu, *J. Hazard. Mater.* 2012, *213–214*, 258–264.

[41] V. León, J. M. González-Domínguez, J. L. G. Fierro, M. Prato, E. Vázquez, *Nanoscale* 2016, *8*, 14548–14555.

[42] M. S. Dresselhaus, A. Jorio, M. Hofmann, G. Dresselhaus, *Nano Lett.* 2010, *10*, 751–758.

[43] K. R. Paton, E. Varrla, C. Backes, R. J. Smith, U. Khan, A. O'Neill, C. Boland, M. Lotya, O. M. Istrate, P. King, et al., *Nat. Mater.* 2014, *13*, 624–630.

[44] C. Fu, N. M. Ravindra, *Bioinspired, Biomim. Nanobiomaterials* 2012, *1*, 229–244.

[45] Y. Chen-Sheng, C. Fong-Yu, S. Dar-Bin, W. Chao-Liang, *Method for Preparation of Water-Soluble and Dispersed Ion Oxide Nanoparticles and Application Thereof*, 2005, Cheng-Sheng, Y. Fong-Yu, C. Dar-Bin, S. Chao-Liang, W. USA. Application No. US 2005/0271593 A1.

[46] H. U. Worm, P. J. Ryan, S. K. Banerjee, *Earth Planet. Sci. Lett.* 1991, *102*, 71–78.

[47] C. Martín, A. Martín-Pacheco, A. Naranjo, A. Criado, S. Merino, E. Díez-Barra, M. A. Herrero, E. Vázquez, *Nanoscale* 2019, 4822–4830.

[48] D. Guérin, J. C. Vuillemard, M. Subirade, *J. Food Prot.* **2003**, *66*, 2076–2084.

[49] H. Asanuma, T. Ban, S. Gotoh, T. Hishiya, M. Komiyama, *Macromolecules* **1998**, *31*, 371–377.

[50] J. Zhang, N. Wang, W. Liu, X. Zhao, W. Lu, *Soft Matter* **2013**, *9*, 6331.

[51] Y. Honda, K. Kurihara, T. Kunitake, *Chem. Lett.* **1991**, *20*, 681–684.

[52] J. Leganés, A. Sánchez-Migallón, S. Merino, E. Vázquez, *Nanoscale* **2020**, *12*, 7072–7081.

[53] M. Wang, C. Yan, L. M, in *Compos. Their Prop.*, **2012**.

[54] D. G. Papageorgiou, I. A. Kinloch, R. J. Young, *Prog. Mater. Sci.* **2017**, *90*, 75–127.

[55] J. M. González-Domínguez, C. Martín, Ó. J. Durá, S. Merino, E. Vázquez, *ACS Appl. Mater. Interfaces* **2018**, *10*, 1987–1995.

[56] Y. Wang, B. Li, F. Xu, Z. Han, D. Wei, D. Jia, Y. Zhou, *Biomacromolecules* **2018**, *19*, 3351–3360.

[57] B. Li, Y. Li, G. Huang, T. Lu, F. Xu, Y. Chen, T. J. Lu, X. Zhang, *Adv. Funct. Mater.* **2012**, *23*, 660–672.

[58] N. R. Nagireddy, M. M. Yallapu, V. Kokkarachedu, R. Sakey, V. Kanikireddy, J. P. Alias, M. R. Konduru, *J. Polym. Res.* **2011**, *18*, 2285–2294.

[59] R. D. Pike, B. D. Borne, J. T. Maeyer, A. L. Rheingold, *Inorg. Chem.* **2002**, *41*, 631–633.

[60] T. J. Mooibroek, P. Gamez, *Inorganica Chim. Acta* **2007**, *360*, 381–404.

[61] P. Bairi, B. Roy, A. K. Nandi, *J. Mater. Chem.* **2011**, *21*, 11747–11749.

[62] A. Baraka, H. Hatem, M. S. El-Geundi, H. Tantawy, K. Karaghiosoff, M. Gobara, A. Elbeih, M. Shoaib, M. A. Elsayed, M. M. Kotb, *J. Solid State Chem.* **2019**, *274*, 168–175.

[63] Wahajuddin, S. Arora, *Int. J. Nanomedicine* **2012**, *7*, 3445–3471.

[64] E. R. Monazam, R. W. Breault, R. Siriwardane, *Ind. Eng. Chem. Res.* **2014**, *53*, 13320–13328.

[65] N. E. Mircescu, M. Oltean, V. Chis, N. Leopold, *Vib. Spectrosc.* **2012**,

62, 165–171.

[66] E. Valiey, M. G. Dekamin, Z. Alirezvani, *Int. J. Biol. Macromol.* 2019, *129*, 407–421.

[67] Z. Alirezvani, M. G. Dekamin, F. Davoodi, E. Valiey, *ChemistrySelect* 2018, *3*, 10450–10463.

[68] B. C. Smith, *Infrared Spectral Interpretation A Systematic Approach*, CRC Press, Boca Raton (Florida), 1998.

[69] N. S. Vrandečić, M. Erceg, M. Jakić, I. Klarić, *Thermochim. Acta* 2010, *498*, 71–80.

[70] K. E. Maly, C. Dauphin, J. D. Wuest, *J. Mater. Chem.* 2006, *16*, 4695.

[71] G. M. Whitesides, J. P. Mathias, C. T. Seto, *Science,* 1991, *254*, 1312–1319.

[72] L. Tang, W. Liu, G. Liu, *Adv. Mater.* 2010, *22*, 2652–2656.

[73] J. Leganés Bayón, A. M. Sánchez-Migallón, Á. Díaz-Ortiz, C. A. Castillo, I. Ballesteros-Yáñez, S. Merino, E. Vázquez, *Chem. - A Eur. J.* 2020, *26*, 17069–17080.

[74] M. B. Stearns, Y. Cheng, M. R. Parker, M. B. Stearns, Y. Chenga, *J. Appl. Phys.* 1994, *75*, 6894.

[75] C. Binns, M. J. Maher, *New J. Phys.* 2002, *4*, 85.1-85.15.

[76] E. M. Abdelrazek, A. M. Abdelghany, S. I. Badr, M. A. Morsi, *J. Mater. Res. Technol.* 2018, *7*, 419–431.

[77] A. L. Patterson, *Phys. Rev.* 1939, *56*, 978–98

Chapter 4

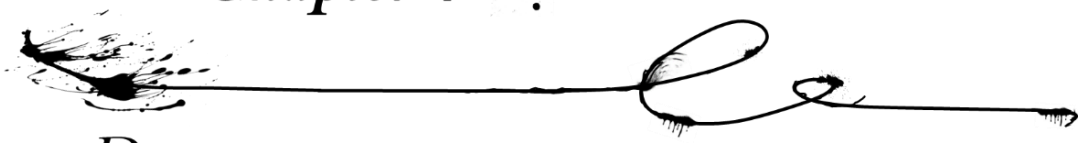

Diaminotriazine Hybrid Hydrogels: Smart Hydrophobic Drug Delivery

4.1. Introduction

4.1.1. Hybrid hydrogels for smart drug delivery

Hybrid hydrogels display a wide array of novel properties that make them suitable for biomedical applications (Figure 1). In particular, their stimuli-responsiveness allows them to respond to specific external stimuli, which are determined by the nature of the nanomaterials embedded in the hydrogel network.[1] This makes hybrid hydrogels particularly appealing materials for stimuli-responsive drug delivery, also coined smart drug delivery.

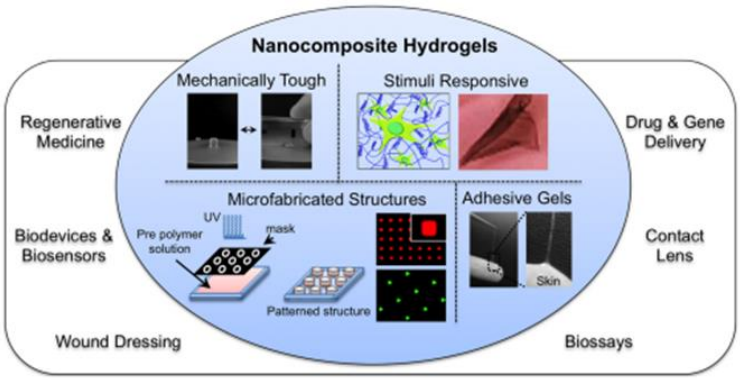

Figure 1. Biomedical applications of hybrid hydrogels.

The presence of NPs not only enhances the delivery performance of the hydrogels but also allows the transport of hydrophobic drugs, or is responsible of multistimuli-response systems, among others. In the next section, several stimuli-responsive hybrid hydrogel systems are discussed.

4.1.1.1. Electro-responsive hydrogels

Hydrogels responsive to electric fields acting as implanted systems have been found to enhance the transdermal release of drug when implanted in the skin upon application of electrical stimulation. When this is applied, electro-responsive hydrogels de-swell or bend and trigger a response.[2]

The drug release mediated by electrical stimulus occurs though several mechanisms, such as migration of the charge towards the opposite charged electrode or hydrogel contraction. Nevertheless, several setbacks typically occur with these systems, namely:

- Slow response times.
- Non-linear drug release.
- Gel fatigue, which typically arises as the electric stimulus is induced.[3,4]

In order to overcome these setbacks, incorporation of different carbon-based nanoparticles, such as multi-walled carbon nanotubes (MWCNTs) and graphene, improves both the mechanical and electrical properties of the nanocomposites.

In this manner, MWCNTs have been used to increase the electrical sensitivity of hydrogels as implantable devices for drug release. For example, polymethacrylic acid (PMAA)/MWCNT hydrogel hybrids significantly increased the response of the hydrogel towards the applied electric field and allowed *in vitro* delivery of sucrose under application of short low-voltage cycles.[5]

Graphene is also an appealing carbon-based nanofiller for electro-responsive hybrid hydrogels due to its high electron mobility and thermal conductivity. In this manner, incorporation of graphene into an electro-responsive PMAA hydrogel 1) reduced the resistive heating of the hydrogel that typically results after electrical stimulation and 2) allowed on-off *in vivo* drug release under short cycles of low voltage (Figure 2).[6]

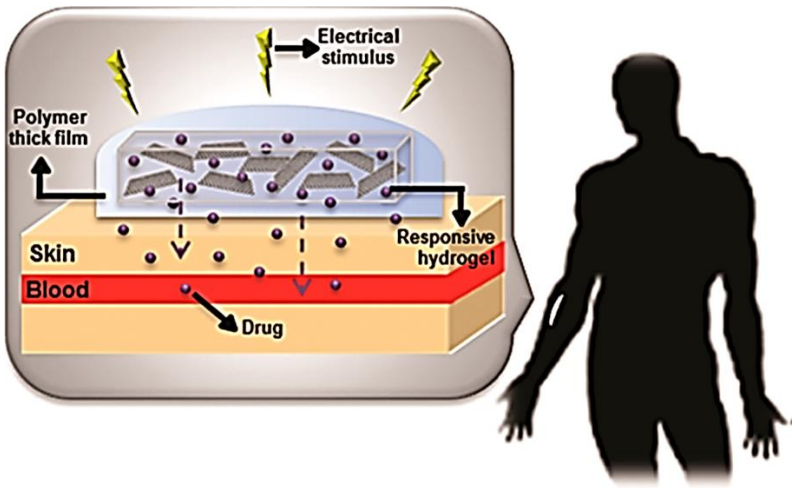

Figure 2. Electro-responsive graphene-based hydrogel as skin patch for transdermal drug delivery.

4.1.1.2. Magnetically-responsive hydrogels

Magnetic hydrogels are hybrid hydrogels that acquire magnetic responsiveness as a consequence of introducing micro- and/or nanomagnetic particles (Fe_2O_3, Fe_3O_4, $CoFe_2O_4$) inside the hydrogels that can quickly respond to an external magnetic field (EMF).[7]

For example, incorporating superparamagnetic iron oxide nanoparticles (SPIONs) into a polyvinyl alcohol (PVA)-based hydrogel allowed fine-tuning drug release by switching the duration time of the EMF. In the absence of the EMF, the particle´s magnetic moments are randomly-oriented and the drug release profile displays a diffusion mode. When the magnetic field is applied, the magnetic moments align and the particles aggregate together, leading to a drastic reduction in the porosity of the hydrogel which hampered the drug release. As a result, the composites displayed on/off switch release patterns (Figure 3).

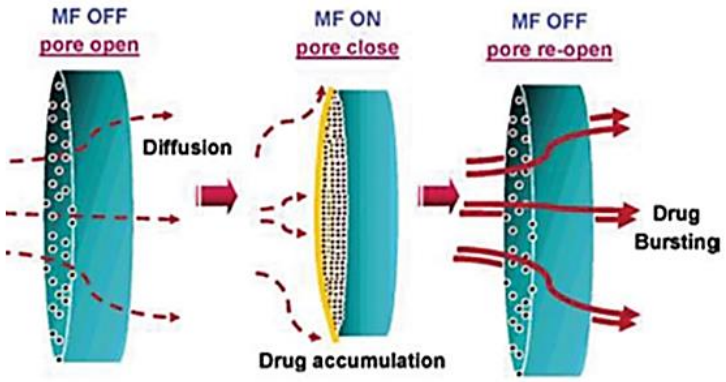

Figure 3. On/off switch mechanism for the release of drug from PVA hydrogel containing SPIONs.

In another example, upon application of an EMF, SPION-embedded alginate hydrogels undergo a large deformation of over 70% in volume change and induced release of various drugs, such as plasmid DNA, mitoxantrone and chemokine in a pulsed manner (Figure 4). Moreover, mesenchymal stem cells were also delivered following this methodology.[8]

Metal nanoparticles may also be remotely heated when subjected to alternating magnetic fields (AMF). Following this principle, combination of SPIONs in a thermo-responsive poly(*N*-isopropylacrylamide) (PNIPAAm) hydrogel and application of an AMF leads to magnetic-induced volumetric

changes in the hydrogel in order to achieve remotely controlled pulsatile release of drugs.[9].

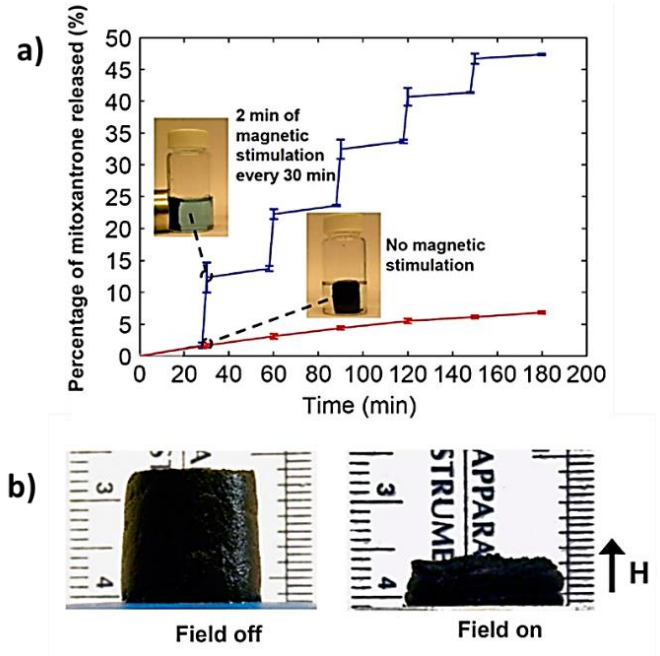

Figure 4. Alginate ferrogels a) Drug release and b) Volume deformation upon application of the magnetic field.

4.1.1.3. Light-responsive hydrogels

Light is a fast and accurate stimulus which may be obtained in available ways and so it is a very attractive impulse to fabricate light-responsive materials. In this manner, incorporation of nanoparticles responsive to electromagnetic impulses into polymer hydrogels may render active hybrid hydrogels able to delivery drugs upon application of a light stimulus.

For example, loading core-shell lanthanide doped upconverting nanoparticles (UCNPs) into polyacrylamide-poly(ethylene glycol) (PAAm-*co*-PEG) hydrogels functionalized with photo-responsive groups was used to convert near-infrared light (NIR) into UV light. Upon irradiation with 980 nm light, photodegradation of the crosslinked network led to release of therapeutic agent (Figure 5).[10]

Gold nanoparticles also absorb visible to NIR light, which may be harnessed to generate local heat and trigger a response. Silica-gold nanoparticles were

incorporated onto PNIPAAm-*co*-PAAm hydrogels and this allowed local heating generated by the nanoparticles after light stimulation.

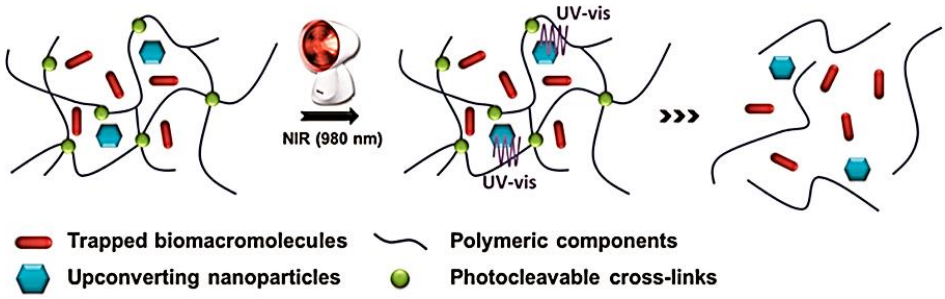

Figure 5. NIR-light-triggered degradation of photo-responsive hydrogel generated by up-conversion of UV light of the lanthanide nanoparticles embedded in the hydrogel.

This heat generation was used to cause both tissue necrosis as well as to deliver appropriate chemotherapeutic agents after volumetric change.[11] Alternatively, carbon-based nanoparticles may also be used for the preparation of light-responsive hybrid hydrogels. Taking advantage of their strong optical absorbance in the NIR region, CNTs have been used to enhance the photothermal conversion effect in hydrogels by combining them with thermo-responsive polymer PNIPAAm.[12]

4.1.1.4. Microwave-responsive hydrogels

Microwaves (MW) are electromagnetic waves with frequencies ranging between 300 MHz and 300 GHz. This low-energy radiation may be used as external stimulus for remote drug delivery, due to their ability to penetrate deeply into living tissue. In this sense, MW radiation has already proved useful for transdermal drug transport and skin permeation enhancer.[13–15]

A few examples have been reported concerning microwave-responsive soft scaffolds.[16–18] For example, Wang *et al*. reported an injectable hydrogel with MW susceptibility that effectively converted MW radiation into localized heat due to the presence of confined ions inside the hydrogel. The simultaneous local hyperthermia effect and doxorubicin (DOX) release rendered these hydrogels potential candidates for tumor ablation therapy upon MW irradiation (Figure 6).[17]

Further, soft, electrically-conductive networks can be used to build MW-sensitive drug reservoirs. Polyaniline/poly(*N*-isopropylacrylamide) (PANI/

PNIPAAm) water-swollen copolymers converted electromagnetic radiation into heat, which was used to induce a sol-gel transition and thus allow tris(2,2'-bipyridine)ruthenium(II) ion (RBPY) release.[18]

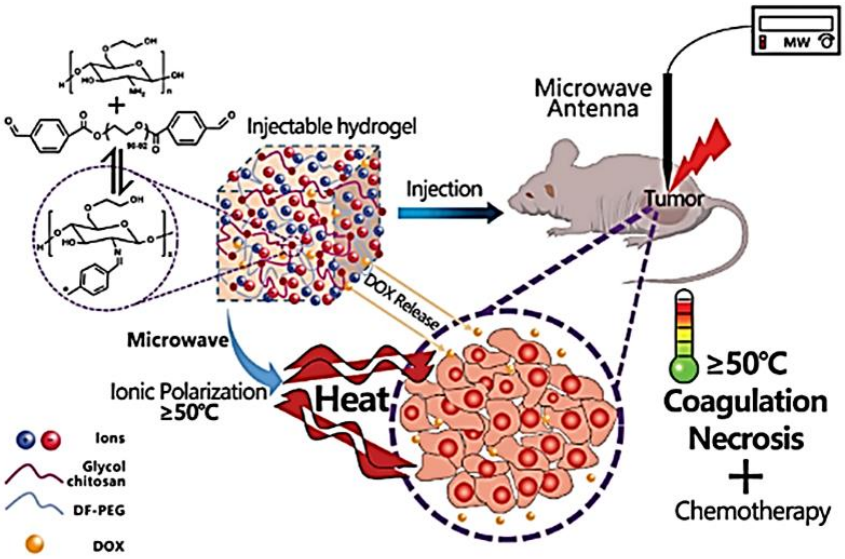

Figure 6. Schematic illustration of microwave ablation therapy from the chitosan-based injectable ionic hydrogel.

All these examples, however, are narrowed to the 2,45 GHz frequencies within the industrial, scientific and medical (ISM) broadbands of the microwaves. However, MW frequencies of 915 MHz could prove beneficial for clinical uses. For instance, MW of 915 MHz have less heating power and their penetration depth is larger (6–8 cm) than MW of 2.45 GHz (2 cm).[19] Thus, researching into soft scaffolds responsive to 915 MHz is desirable, for example, as a means to achieve remote delivery as well as to target deeper organs.

4.1.1.5. Multi-responsive hydrogels

By designing hybrid materials that can deliver cargo in response of multiple stimuli, faster responding systems may be prepared in comparison with materials responsive to a single stimulus, as well additional functionalities and applicability to these systems. Multi-responsive systems have caught the attention in cancer therapy. Since cancer tissues display higher temperature and lower pH values than healthy tissues, multi-stimuli responsive systems such as pH-and temperature-responsive systems are particularly useful to deliver drugs at tumor sites.

For example, incorporating Au nanoparticles conjugated with bovine serum albumin (BSA) into a nanogel and functionalizing with N-end cysteine peptide tumor-homing peptide arginylglycylaspartic acid (iRGD) allowed tracking and identification of the nanogel *in vitro*, due to red fluorescence emission of the gold nanoclusters. Additionally, the pH- and thermo-responsive PNIPAAm-*co*-PAA nanogel allowed delivery of DOX specifically to the tumor site with controlled release profiles.[20]

In a different example that illustrates the versatility of multifunctional systems, Ag-Au bimetallic core-shell nanoparticles were introduced into nanogels for simultaneous optical temperature sensing, targeted tumor and combined chemical and photothermal treatment, while hyaluronic acid chains were introduced as targeting ligands. This way, the fluorescence intensity of the Ag-Au core can be used for imaging and to trigger the release of anticancer drug under local temperature increase of target zones induced by NIR irradiation (Figure 7).[21]

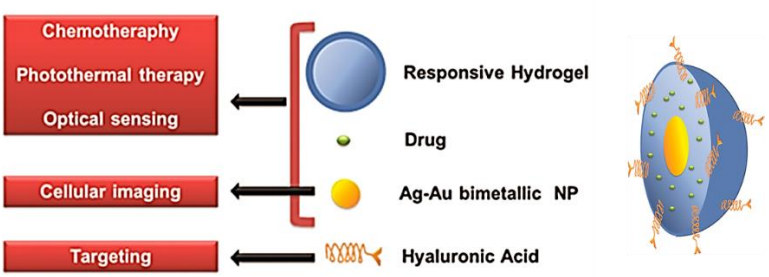

Figure 7. Multifunctional core-shell nanogel for targeted cancer cell delivery.

In a distinctive example, Lv. *et al*[22] proposed selective release of one encapsulated molecule in response to pH and another in response to chemical reduction from a hydrogel reservoir (Figure 8).

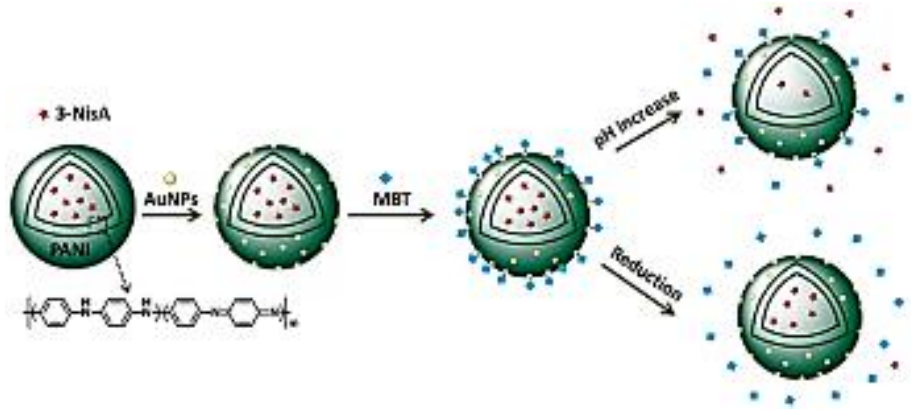

Figure 8. Synthesis of dual delivery containers and selective release of payloads upon pH change or reduction.

First, PANI, a pH- and redox-sensitive polymer, was used to create nanocontainers that encapsulated the first molecule of interest, 3-(nitrosalicylic acid) (3-(NisA)). The nanocontainers were then decorated with gold nanoparticles that allowed loading of the second molecule, 2-(mercaptobenzothiazole) (MBT). When the pH stimulus was applied, the first molecule was released whereas the second molecule loaded onto the gold nanoparticles was released only upon increasing the concentration of the reducing agent. The work is meant to apply the system for anti-corrosion applications, however, the multi-stimuli character of the hydrogel could be applied equally for drug delivery applications.

4.1.2. Hybrid hydrogels for smart hydrophobic drug delivery

Nowadays, the smart delivery of hydrophobic drugs from hydrogels under external stimuli is still a present flaw. The examples in literature rely on pH stimuli to trigger the drugs from these reservoirs,[23–26] while more complex physical stimuli remain unexplored.

Only recently, a few more complex stimuli were investigated: in response to electrical stimulation, the release of curcumin (CUR), a model hydrophobic drug, was triggered from poly(3,4-ethylenedioxythio-phene) (PEDOT)-alginate (Alg) electro-responsive hydrogels.[27] In the absence of stimulus, CUR was slowly released from the PEDOT/Alg hydrogels but was enhanced in response to electrical stimulation by applying a negative voltage (Figure 9). This system could be conceived as a drug delivery implant where the release of the drug can be regulated through the application of an electrical stimulus.

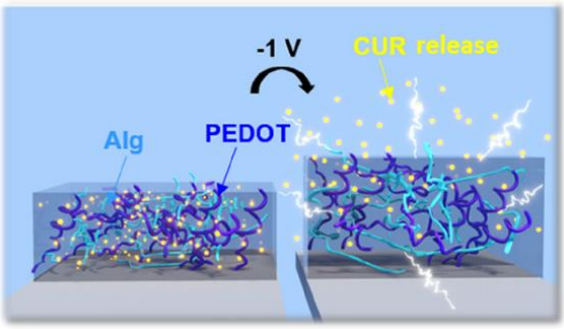

Figure 9 Electrically-stimulated curcumin release from PEDOT/Alg hybrid hydrogels.

In another example, ultrasound exposure was applied to hydrophobically-modified poly(vinyl alcohol) (PVA) hydrogels in order to trigger ON-OFF release

of Nile red (NR) and Ibuprofen (IBU), two poor water-soluble compounds (Figure 10).[28]

Figure 10. Ultrasound-controlled hydrophobic drug delivery from PVA-modified hydrogels.

The drugs were loaded inside silicone oil droplets, which were then dispersed within the PVA chains. Upon application of the ultrasounds, mechanical alterations on the hydrogels were shown to be the main cause of controlled drug delivery.

Therefore, there is a present urge to design smart hydrogels which circumvent the two main setbacks in hydrophobic drug delivery:

- They must incorporate efficiently hydrophobic drugs within the hydrophilic network, which is usually incompatible with this kind of drugs.

- They must deliver these hydrophobic drugs on-demand under external stimuli, since these compounds tend to be entrapped within the network and are not easily released by simple diffusion.

4.2. Results and discussion

In the work carried out so far, despite the DAT hydrogels considerably enhanced the drug loadings for poor water-soluble drugs, these were strongly retained and thus drug release was inefficient. Thus, in the previous chapter we prepared DAT hybrid hydrogels which were conferred with stimuli-responsiveness properties due to the presence of their embedded nanomaterials.

In this chapter, we tested the capacity of these hybrid hydrogels to deliver a hydrophobic model drug under external stimuli, in an attempt to uncage these entrapped compounds from the DAT hydrogels.

4.2.1. Graphene hybrid hydrogels. Smart hydrophobic delivery.

For the smart delivery of graphene-based hydrogels, the following materials were studied:

- **TzOA-M-6** hydrogels, which do not contain graphene
- **G-TzOA-M-6** hydrogels, which contained 0.1 % w/w (**$G_{0.1}$-TzOA-M-6**) and 0.5 % w/w (**$G_{0.5}$-TzOA-M-6)** graphene contents (Figure 11).

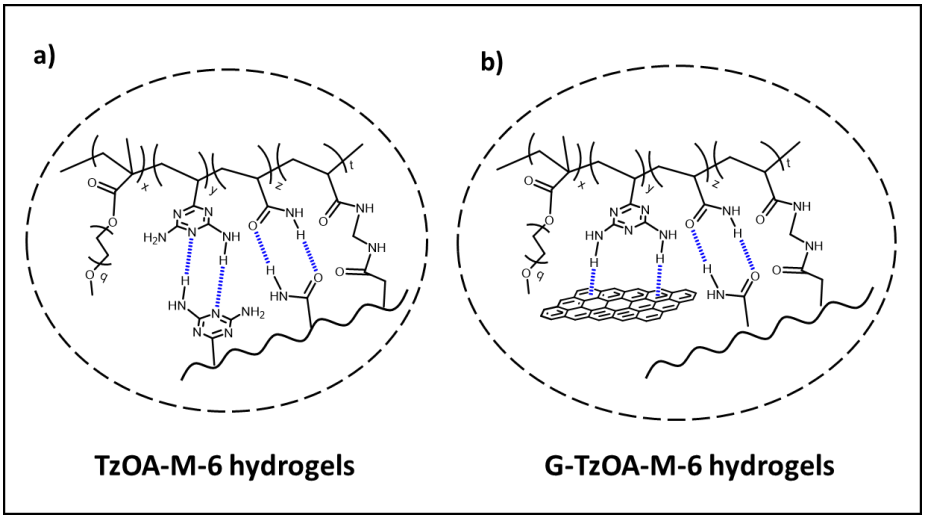

Figure 11. Proposed structure of the graphene hybrid hydrogels a) **TzOA-M-6** hydrogels and b) **G-TzOA-M-6** hydrogels.

Here, both the drug loadings and *in vitro* drug release experiments were carried out using imipramine (**IMI**) as a model hydrophobic drug. The compound **IMI** (a tricyclic antidepressant) has three bulky rings in its structure (Figure 12)

and it was shown to interact favorably with the DAT matrix of the hydrogel. UV/VIS spectrophotometry was used for drug quantification. Absorbance readings focused on the absorbance maxima of **IMI** at λ = 251 nm, followed by interpolation in calibration curves.

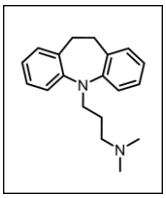

Figure 12. Structure of imipramine (**IMI**).

4.2.1.1. Drug loadings

For drug loading calculations, hydrogels were loaded with a solution of **IMI** in PBS (Phosphate-buffered saline) (pH = 7.4) until maximum swelling had occurred. The drug loading was then calculated by an indirect method (Equation 1):

$$Drug\ loading\ (\%) = \left(\frac{m_0 - m_u}{m_0}\right) \mathrm{x}\ 100$$

Equation 1. Formula for drug loading calculation.

Where m_0 is the total initial mass present in the loading medium and m_u is the mass of the unloaded drug remaining after the hydrogel had incorporated the drug.

Figure 13 shows the drug loadings for **TzOA-M-6** and **G-TzOA-M-6** hydrogels. Interestingly, it is observed that the loadings increase mildly with the graphene content.

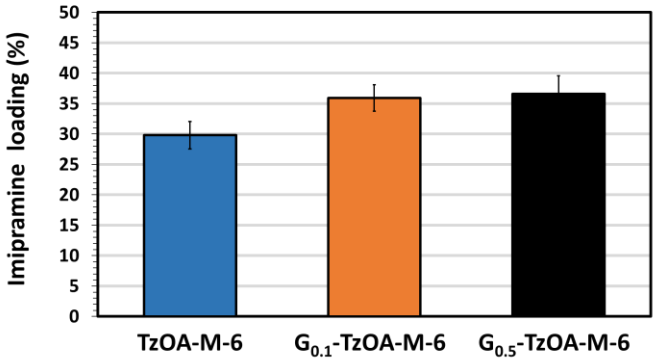

Figure 13. IMI drug loadings for **TzOA-M-6** and **G-TzOA-M-6** hydrogels.

Since **IMI** is able to stablish π-π interactions with other sp^2 carbon structures such as graphene,[29,30] it is likely that an increase in graphene contents consequently leads to higher drug incorporation.

4.2.1.2. Diffusion-mediated drug release

The drug release studies were carried out by immersion of drug-loaded hydrogels in PBS media and placing the vessels in an orbital mixer and shaker. At defined time intervals, aliquots were withdrawn and taken to UV/VIS analysis for quantification.

The release profiles show that after 24h, around 60% of the loaded payload is released from the **TzOA-M-6** hydrogels. In the case of **G-TzOA-M-6** hydrogels, 80% payload is released after that same time (Figure 14). This implies a distinct effect exerted by graphene in the release of **IMI**.

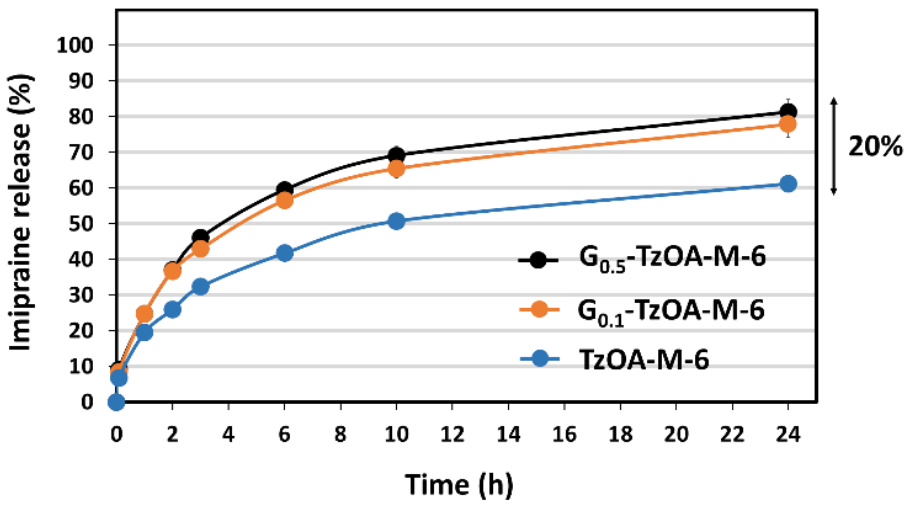

Figure 14. IMI drug release profiles of **TzOA-M-6** and **G-TzOA-M-6** hydrogels in PBS medium.

In **TzOA-M-6** hydrogels, the drug is trapped inside hydrophobic DAT domains through strong π-π interactions and this paces down the release (Figure 15a).

In **G-TzOA-M-6** hydrogels, however, favorable π-π stackings and graphene-NH_2 interactions between DATs and graphene[31] disrupt these domains and **IMI** is uncaged, thus increasing the release (Figure 15b). This

finding marked the positive influence of graphene as an enhancer of the release of hydrophobic drug from a DAT reservoir.

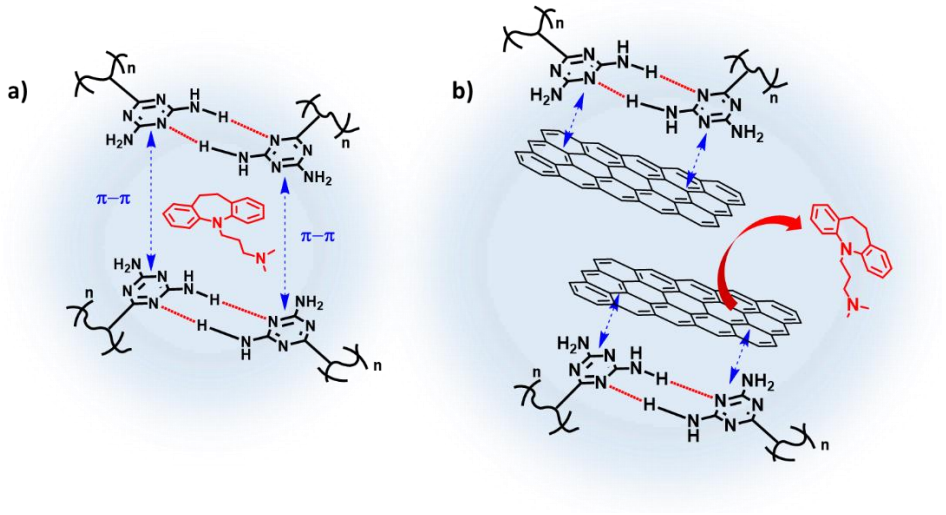

Figure 15. Release mechanism of IMI in PBS medium from a) TzOA-M-6 and b) G-TzOA-M-6 hydrogels.

4.2.1.3. pH-triggered drug release

DAT-based hydrogels are pH-sensitive under acidic medium, being pKa of VDAT = 5.15.[32] By immersing both TzOA-M-6 and G-TzOA-M-6 hydrogels in Simulated Gastric Fluid (SGF, pH =1.2) the release of IMI in response to the pH was evaluated (Figure 16). In comparison with PBS medium (Figure 15), both TzOA-M-6 and G-TzOA-M-6 hydrogels released 10% higher rates in SGF.

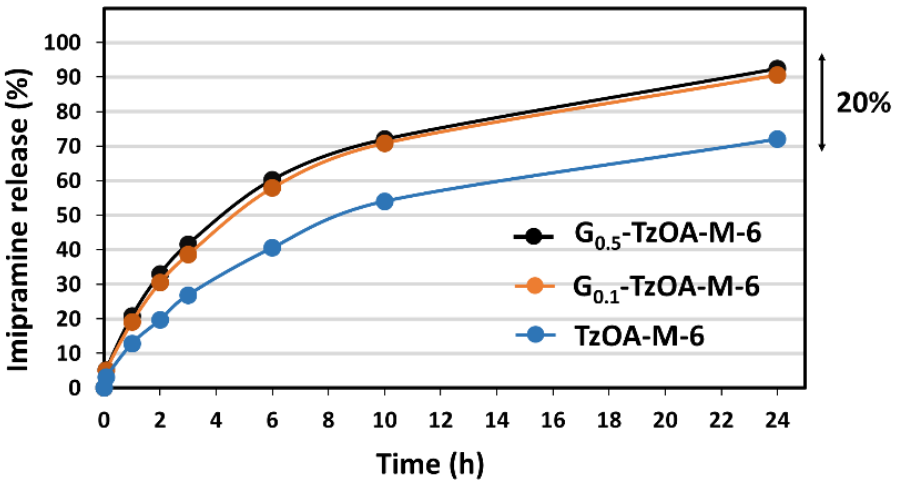

Figure 16. IMI drug release profiles of TzOA-M-6 and G-TzOA-M-6 hydrogels in SGF medium.

This 10% increase is attributed to the pH-stimulus: upon protonation in SGF medium, DATs repel each other and bring about the disruption of the DAT hydrophobic domains, which were responsible of trapping the drug. Thus, the release of **IMI** is enhanced (Figure 17).

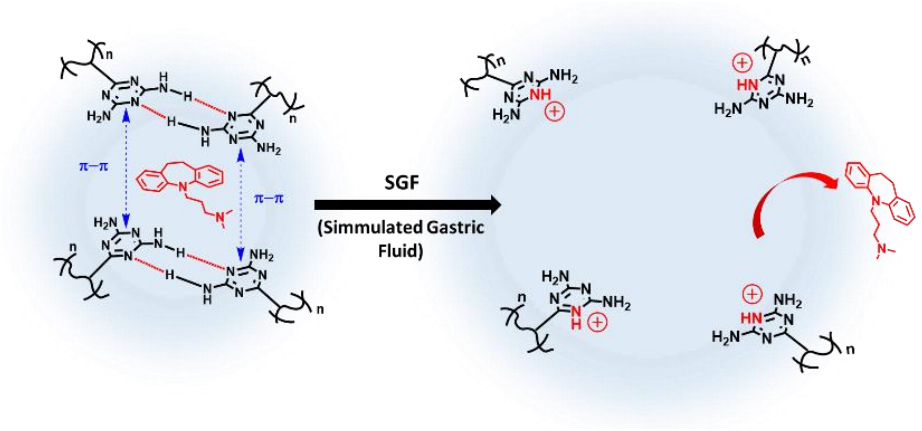

Figure 17. Release mechanism of **IMI** in SGF medium from **TzOA-M-6** hydrogels.

The combined effect of both graphene and pH stimulus on the release rates is summarized in Figure 18: **$G_{0.5}$-TzOA-M-6** hydrogels immersed in SGF medium release 30% higher payloads than **TzOA-M-6** hydrogels immersed in neutral medium.

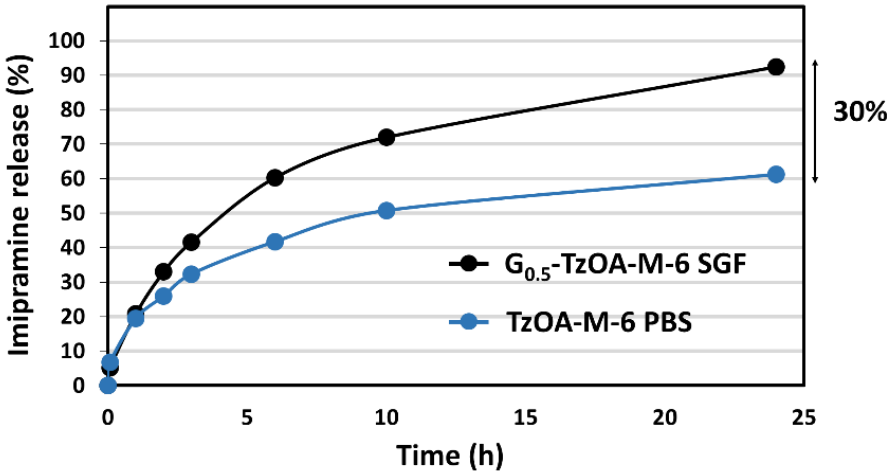

Figure 18. Combined effect of graphene and pH stimulus**. IMI** release from **$G_{0.5}$-TzOA-M-6** hydrogels in SGF medium *vs* **TzOA-M-6** hydrogels in PBS medium.

Thus, the contribution of both factors to the disruption of the DAT hydrophobic domains further enhances the release of drug from the hydrogel.[31]

4.2.1.4. Microwave-triggered drug release

The microwave (MW) radiation are electromagnetic waves with frequencies ranging between 300 MHz and 300 GHz. This low-energy radiation may be used as external stimulus for remote drug delivery.

Polymer and hydrogel systems have been observed to respond to MW irradiation.[16,17] In addition, the incorporation of carbonaceous fillers in the network of polymer composites enhances the absorption of these MW.[33,34] Graphene, in particular, has proven to be an excellent microwave absorber due to its large π-conjugated structure, high dielectric loss and low density.[35]

The majority of microwave systems operate at 2.45 GHz (12.2 cm). We wished to apply our hydrogels for biomedical applications, thus, for this reason, we used a MW device specifically designed by our research group (in collaboration with Sairem Ibérica S.L.), that operates at 915 MHz (33.3 cm). This microwave frequency has less heating power and its penetration depth of around 6–8 cm and could be useful for the delivery of drugs from hydrogels in transdermal applications.[19] This study was carried out with **TzOA-M-6** and **$G_{0.5}$-TzOA-M-6** hydrogels.

a) Microwave fixation conditions

The interaction between MW radiation and any biomaterial with high aqueous content tends to generate heat. This overheating of the scaffold may compromise its applicability in the biomedical field, particularly if the scaffold surpasses physiological body temperatures, i.e., 36–38 ºC, which could damage nearby tissue.

Thus, in order to study the effect of the increase of temperature of the materials after MW exposure, we first irradiated **TzOA-M-6** hydrogels with several conditions of MW irradiation.

Figure 19 shows the 915 MHz MW waveguide that was used in our experiments. The hydrogels were immersed in PBS buffer and the vessel was then sealed inside the waveguide, where the samples were irradiated.

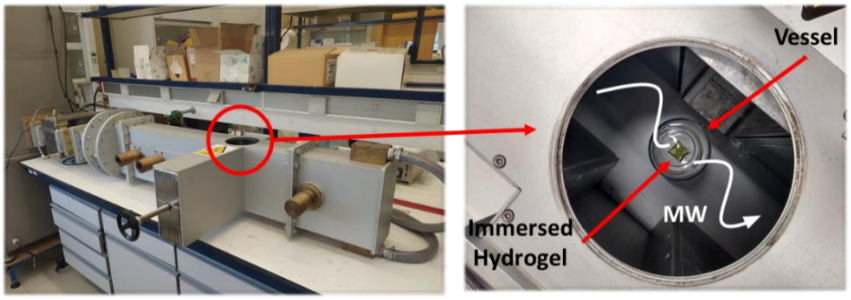

Figure 19. Microwave 915 MHz waveguide.

The TzOA-M-6 hydrogels were irradiated at a fixed frequency of v = 915 MHz and at different incident powers (P_{inc}), namely, P_{inc} = 1 kW, 2 kW and 3 kW. The hydrogels were irradiated for a total of 2 min and the temperature of the materials was recorded every 10 s (Figure 20a). This graph shows the temperature of the materials rises significantly as the P_{inc} increases.

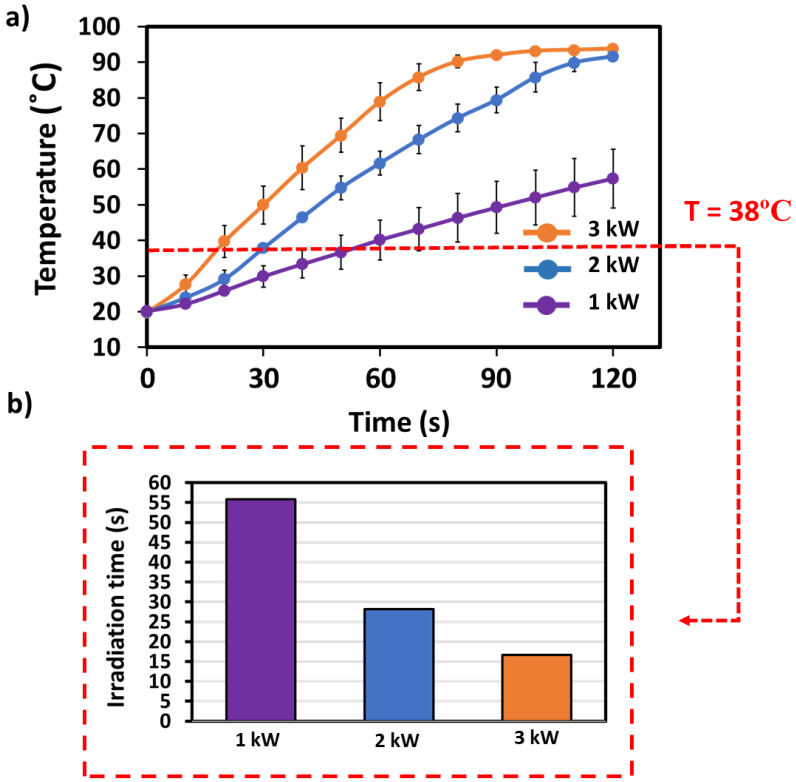

Figure 20. MW irradiation for TzOA-M-6 hydrogels) a) at different incident powers (b) irradiation times before reaching T = 38°C

After two minutes, hydrogels irradiated at P_{inc} = 1 kW reached almost 60 °C, whereas hydrogels irradiated at P_{inc} = 2 kW and 3 kW reached temperatures

over 90 ºC. Interpolation at T = 38 ºC in Figure 20a shows the time required before **TzOA-M-6** hydrogels reached this temperature at each P_{inc} (Figure 20b). The irradiation times (t_{ir}) observed were, approximately, t_{ir} = 15 s, 30 s and 60 s, for P_{inc} = 3 kW, 2 kW and 1 kW, respectively.

Further, since the hydrogels are immsersed in PBS medium, both hydrogel and solvent increased their temperature after MW irradiation. In an attempt to dismiss the heating effect of solvent, the buffer in the absence of the hydrogels was also irradiated following the same conditions (Figure 21).

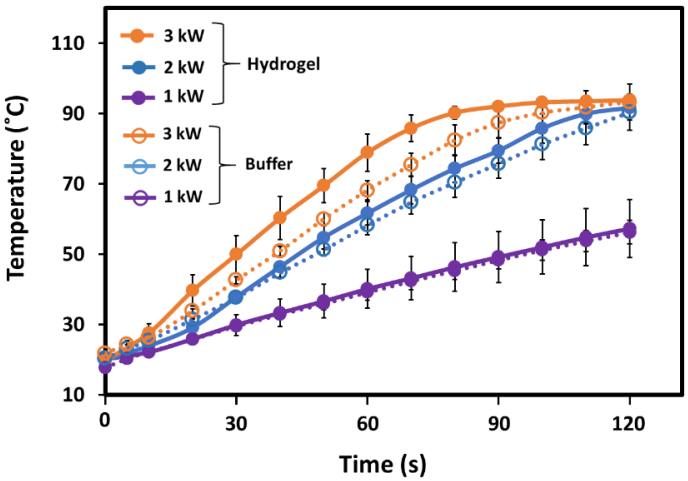

Figure 21. Temperature-rise under MW irradiation of **TzOA-M-6** hydrogels (bold) and free PBS buffered media (dashed).

At P_{inc} = 1–2 kW, similar temperature profiles of free buffer and hydrogel were recorded, whereas at P_{inc} = 3 kW, this difference increased markedly. Thus, for P_{inc} = 1–2 kW, any heat transfer mechanisms other than MW-induced temperature increase, such as convection or conduction between the hydrogel and the solvent, were ruled out.

Further, it was observed during the irradiation experiments at P_{inc} = 3 kW that the hydrogels showed signs of structural damage inside the network. In light of the results observed, the MW chosen irradiation conditions (T < 38 ºC) were:

- P_{inc} = 1 kW for t_{ir} = 60 s
- P_{inc} = 2 kW for t_{ir} = 30 s

Once the conditions were chosen, they were preliminary tested to release **IMI** model drug from **TzOA-M-6** hydrogels. The drug-loaded hydrogels were

immsersed in PBS buffer and irradiated for four cycles, corresponding to the first 3 h of the experiment, and compared with the control reference, which released the drug by simple difussion (Figure 22).

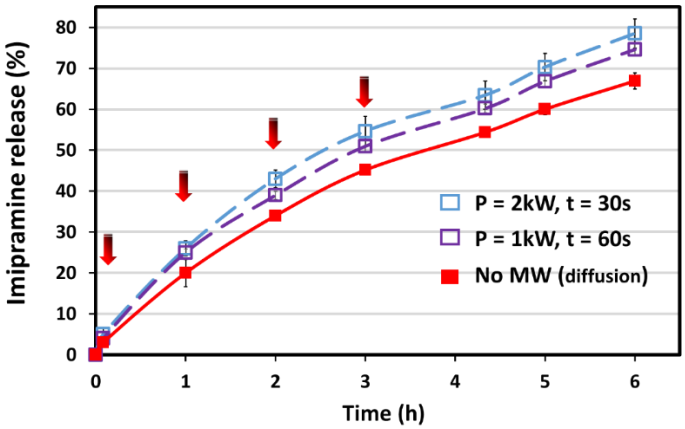

Figure 22. MW-mediated drug release. Red arrows depict each cycle of MW irradiation.

The results showed that MW stimulus slightly enhanced the release of **IMI** from the hydrogels with respect to controls and this improvement increased from P_{inc} = 1 → 2 kW. By the 6th hour, hydrogels irradiated at P_{inc} = 2 kW released 10% higher payloads than control hydrogels. We thus selected the final optmized conditions: P_{inc} = 2 kW for t_{ir} = 30 s in further MW delivery experiments.

These experiments demonstrated the potential of the 915 MHz microwaves in triggering drug release from a delivery reservoir while avoiding overheating of the material, which until now had not been reported.

b) Microwave-triggered drug release

Encouraged by these results, we selected these MW irradiation conditions for *in vitro* drug release experiments of extended 24 h period. In these experiments, both **TzOA-M-6** and **$G_{0.5}$-TzOA-M-6** hydrogels were tested. The MW-stimulated drug delivery studies were performed by immersing the hydrogels in PBS and irradiating them with P_{inc} = 2 kW/t_{ir} = 30 s and for 4 cycles.

The experiments revealed that both **TzOA-M-6** and **$G_{0.5}$-TzOA-M-6** hydrogels slightly increased the release of **IMI** drug when exposed to irradiation with respect to their control counterparts (Figure 23, dashed blue and dashed green *vs* bold blue and bold green, respectively). After 24h, however, the release of irradiated samples and controls levelled off.

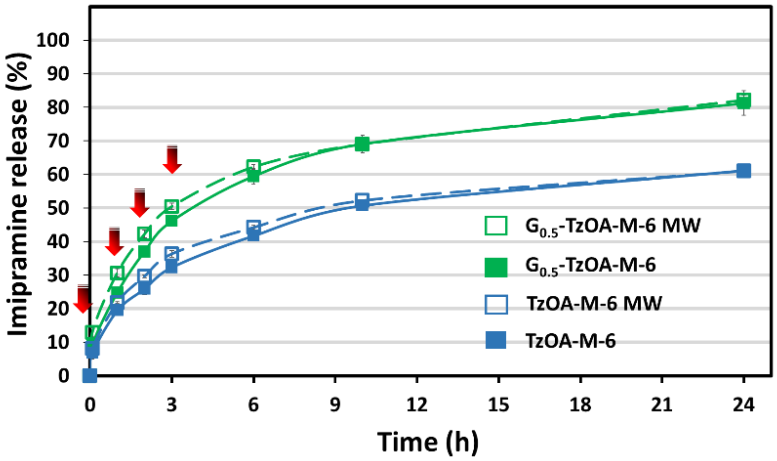

Figure 23. MW-mediated drug release for 24h in PBS medium. Red arrows depict each cycle of MW irradiation.

The same experiment was similarly carried out in SGF buffer, with the aim to evaluate two simultaneous stimuli, namely, pH and MW irradiation. As was observed in PBS medium (Figure 23) both **TzOA-M-6** and **G-TzOA-M-6** hydrogels under MW irradiation and in SGF medium increased the release of **IMI** with respect to their control counterparts (

Figure 24 dashed red and dashed black versus bold red and bold black, respectively).

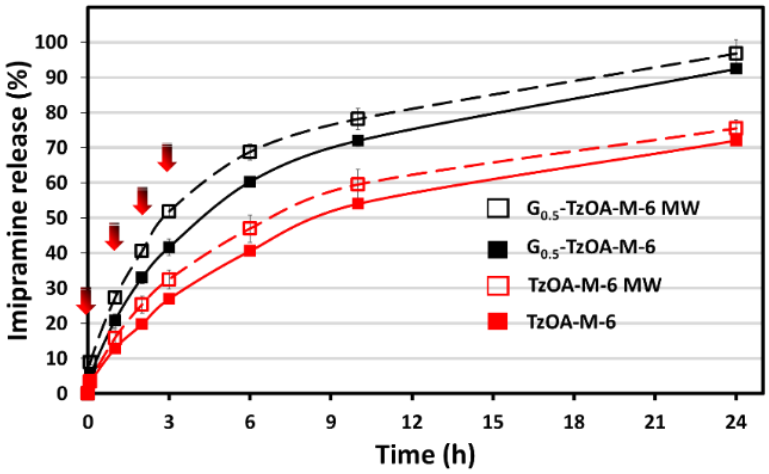

Figure 24. MW-mediated drug release for 24h in SGF medium. Red arrows depict each cycle of MW irradiation.

However, the overall release rates as well as the difference between irradiated and control hydrogels are more pronounced under acidic pH conditions. The enhancement in the drug release rates due to MW irradiation seemed, however, similar for both **TzOA-M-6** and **$G_{0.5}$-TzOA-M-6** hydrogels. This implies that graphene does not enhance the release of drug through MW absorption mechanisms.

c) Mechanism of smart delivery

In light of the results shown in Figure 23 and Figure 24, we proposed that the improvement in the drug release triggered by MW irradiation is based on the interactions between the DAT moieties and the microwave.

In acidic medium, the DAT moieties are now protonated and behave as strong dipoles[36,37] that will interact with the microwaves to a greater extent than in neutral PBS medium. This stronger dipole oscillation could then trigger the drug more in SGF medium (Figure 25).

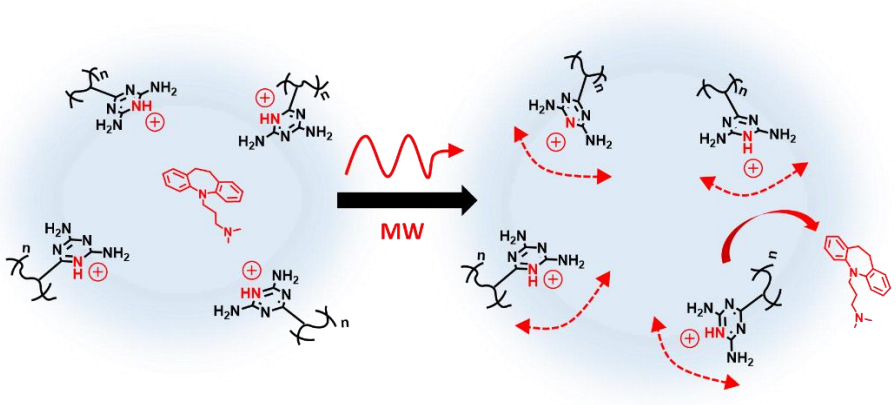

Figure 25- Proposed mechanism of the MW-induced drug release from DAT hydrogels in SGF medium. The dashed curves represent DAT dipolar oscillation.

d) Microwave-induced temperature increase

Paralel to the release experiments, a probe was placed inside the hydrogels in order to meassure their temperature during irradiation. Figure 26 records the temperature increase of both **TzOA-M-6** and **$G_{0.5}$-TzOA-M-6** hydrogels in PBS and SGF media under MW exposure. The results shows that only **$G_{0.5}$-TzOA-M-6** hydrogels in PBS medium stay below $T^a < 38^o$ during all four irradiation cycles (Figure 26, green curve).

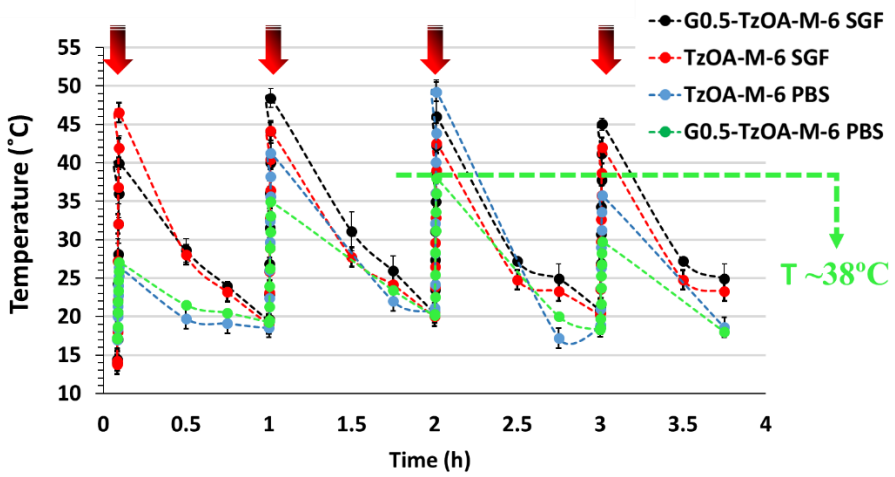

Figure 26. Temperature increasement under MW irradiation for **TzOA-M-6** and **$G_{0.5}$-TzOA-M-6** hydrogels in PBS and SGF media. Red arrows depict each cycle of MW irradiation.

The **TzOA-M-6** hydrogels in both PBS and SGF media and the **$G_{0.5}$-TzOA-M-6** hydrogels in SGF medium all reach up to 50ºC (Figure 26, blue, red and black graphs, respectively). In SGF medium, both H_2O and charged DAT^+ dipoles contribute to MW absorption, leading to generation of heat and temperature increase. Even in PBS medium, the sole contribution of H_2O to the MW absorption generates overheating of the scaffold.

It is noteworthy that graphene embedded inside the hydrogels contributes to MW absorption, due to the π-conjugated of structure of the nanomaterial. For this reason, the graphene hydrogels (**$G_{0.5}$-TzOA-M-6**) in PBS medium, where the DATs are not protonated, reached only 38ºC. Since graphene hybrids avoid overheating of the scaffold, these novel materials could be harnessed for future transdermal applications.

4.2.1.5. *In vitro* cell viability

Once the drug delivery capacities of the DAT-based hydrogels were tested, we wished to evaluate the potential of these materials as possible candidates for biomedical applications.

For this purpose, **TzOA-M-6** and **$G_{0.5}$-TzOA-M-6** hydrogels swollen and lyophilized in both PBS and SGF buffers were used to support the growth of SH-SY5Y cells, a human neuroblastoma cell line (see Figure 27)

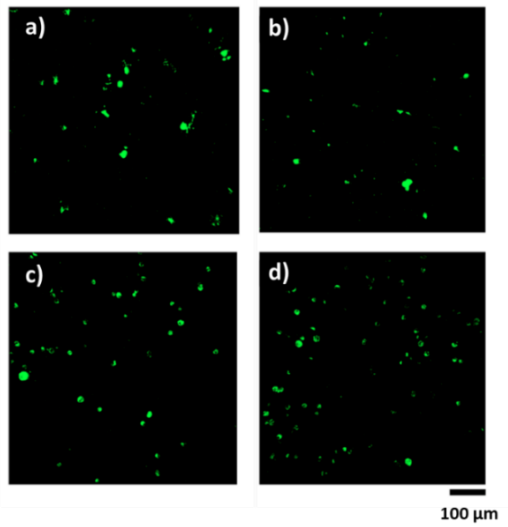

Figure 27. Fluorescence confocal images of SH-SY5Y cell growth in the hydrogels a) **TzOA-M-6** in PBS, b) **$G_{0.5}$-TzOA-M-6 in** PBS, c) **TzOA-M-6** in SGF, d) **$G_{0.5}$-TzOA-M-6** in SGF.

Under our experimental conditions, lyophilized **TzOA-M-6** hydrogels previously swollen in SGF medium significantly presented more living cells that those previously swollen in PBS medium. This is consistent with the pore size distribution of the hydrogels: **TzOA-M-6** in SGF medium present pore sizes of 61.5 µm, whereas **TzOA-M-6** in PBS medium present pores of 14.5 µm.

Furthermore, according to previous research,[38,39] the presence of graphene inside the hydrogel facilitated cell adhesion (Figure 28).

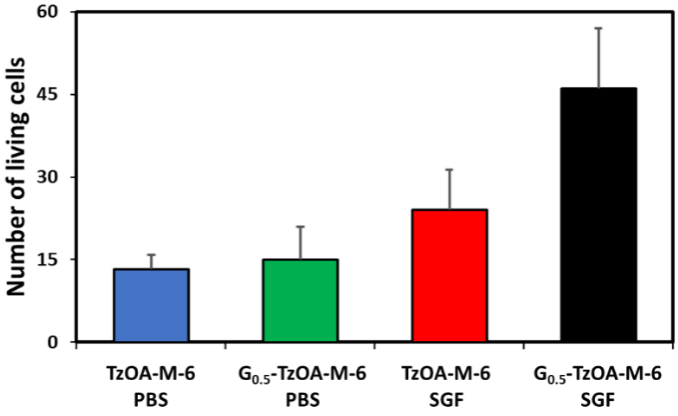

Figure 28. Cell viability studies. Living cells were stained using Calcein-AM.

There was a significant increase in the number of living cells when graphene is incorporated both for PBS and SGF lyophilized hydrogels, particularly for **$G_{0.5}$-**

TzOA-M-6 hydrogels lyophilized in SGF medium; these show the highest number of living cells in comparison to **TzOA-M-6** swollen in PBS.

4.2.2. Magnetite hybrid hydrogels. Smart hydrophobic delivery

For the smart delivery of magnetite-based hydrogels, the materials prepared with the blending method and the *in situ* co-precipitation method were tested to release a hydrophobic drug under the influence of a magnetic field.

As a model hydrophobic drug, we chose Rhodamine 101 (**RHO**) as a representative 8-ring model compound (Figure 29), since it showed the highest drug loading values in DAT hydrogels, and the slowest release mediated by diffusion.

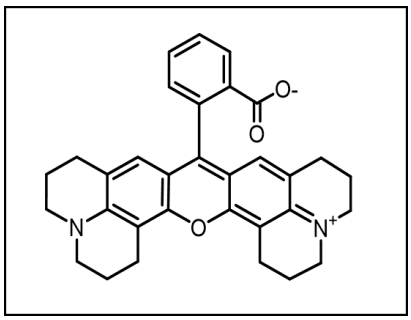

Figure 29. Structure of rhodamine 101 (**RHO**).

4.2.2.1. Blending method

For this method, the magnetic hydrogels **Mag-TzOA-P-1** were studied, alongside their pristine counterpart hydrogels, **TzOA-P-1,** which do not contain SPIONs (Figure 30). In these studies, however, the **Mag_2-TzOA-P-1** hydrogels (2 mg/ml SPION/DMSO) were excluded, since they were too weakly attracted by the Nd magnet, and only **Mag_4-TzOA-P-1** hydrogels (4 mg/ml SPION/DMSO) were tested.

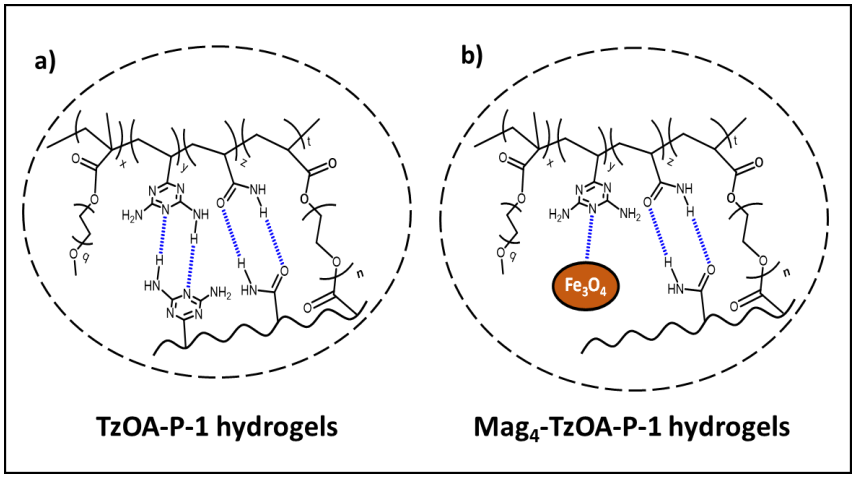

Figure 30. Structure of the hydrogels prepared by the blending method a) TzOA-P-1 hydrogels b) Mag-TzOA-P-1 hydrogels

a) Drug loadings

The drug loadings were obtained by immersion of the hydrogels in an aqueous solution of RHO drug followed by quantification with ¡Error! No se encuentra el origen de la referencia.. Due to the violet color of this rhodamine sub-species, the hydrogels took on an intense pink coloration upon incorporation of the fluorophore (Figure 31).

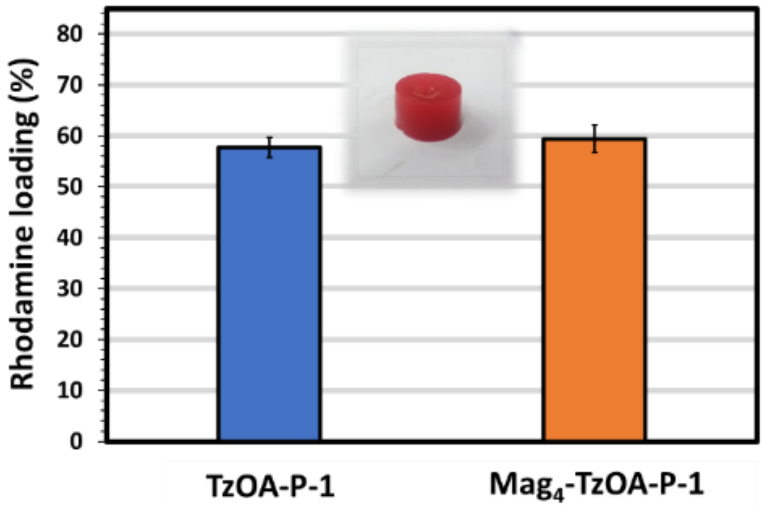

Figure 31. Blending method. Rhodamine drug laodings for TZOA-P-1 and Mag_4-TZOA-P-1 hydrogels

High drug loading values between 57-59% were recorded for both **TzOA-P-1** and **Mag$_4$-TzOA-P-1** hydrogels. These results point favorable polymer-drug interactions between the DATs and the **RHO** drug, in accordance with the theoretical calculations in chapter 2.

b) Magnetic-triggered drug release

The magnetic-triggered drug release studies were carried out by stimulating the hydrogels with a neodymium (Nd) magnet. The hydrogels were immersed in water and the stimulation was performed by moving the magnet underneath the vessels in a circular fashion (Figure 32). The release of the control hydrogels was instead measured by stirring in the absence of the magnet.

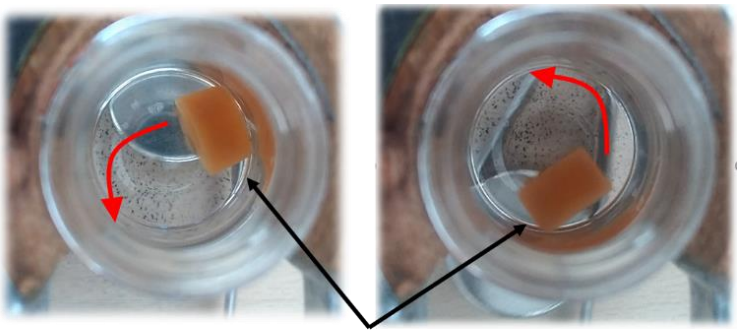

Figure 32. Blending method. Magnetic-stimulated rhodamine release with a static Nd magnet performing circled-fashioned movements.

Figure 33 shows the release curves for the **TzOA-P-1** and **Mag$_4$-TzOA-P-1** hydrogels triggered by the external magnetic field (EMF). In the presence of the magnetic stimulus, the release of **RHO** from **Mag$_4$-TzOA-P-1** hydrogels mildly increases (~2%) with respect to the same hydrogels in the absence of magnetic field (Figure 33 dashed *vs* bold orange curves, respectively). This small difference is attributed to the low magnetic response of the hydrogels towards the static magnet, which is likely a consequence of the blending method used to prepare the **Mag$_4$-TzOA-P-1** hydrogels.

In addition, **Mag$_4$-TzOA-P-1** controls release 4% higher payloads than **TzOA-P-1** hydrogels. (Figure 33 bold orange *vs* blue). It was observed in Chapter 3 that **Mag-TzOA-P-1** hydrogels showed bigger pore sizes than **TzOA-P-1** hydrogels and this explains the small enhancement observed.

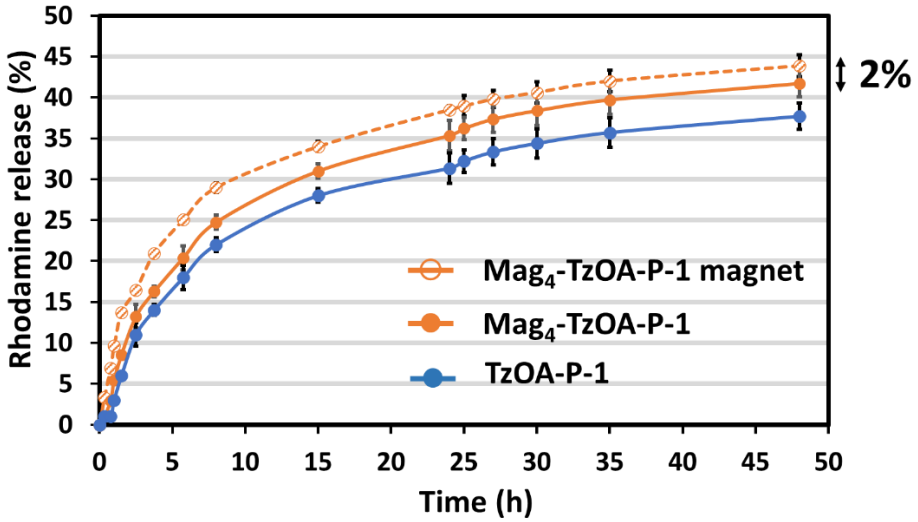

Figure 33. Blending method. Magnetic-triggered rhodamine release from TzOA-P-1 and Mag_4-TzOA-P-1 hydrogels.

4.2.2.2. *In situ* co-precipitation method

For this method, the TzOA-0 physically-crosslinked hydrogels and their magnetic counterparts Mag-TzOA-0 ($Mag_{0.05}$-TzOA-0 and $Mag_{0.25}$-TzOA-0) were studied (Figure 34). The latter were prepared from 0.1M/0.05M and 0.5M/0.25M $FeCl_3/FeCl_2$ precursor solutions, respectively.

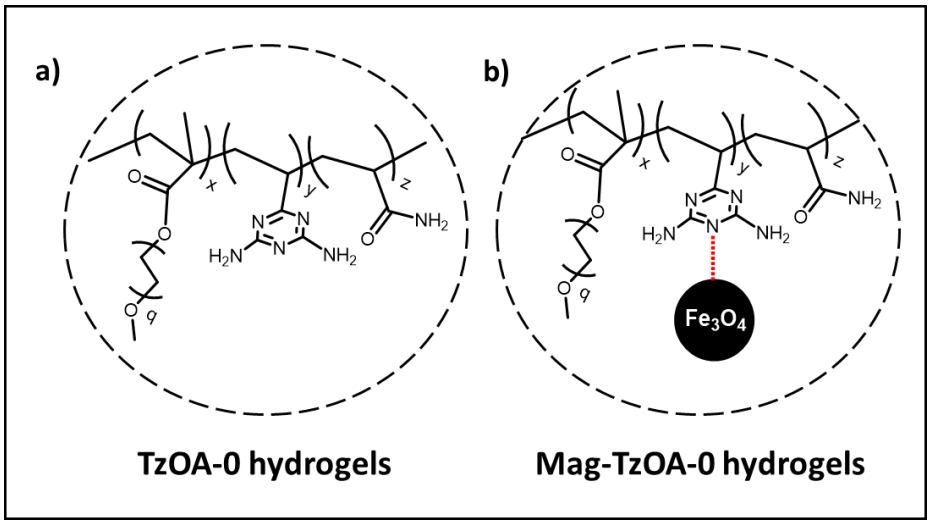

Figure 34. *In situ* co-precipitation method a) TzOA-0 hydrogels b) Mag-TzOA-0 hydrogels.

a) Drug loadings

The drug loading experiments were carried out similar to the drug loadings for the blending method, using **RHO** as model hydrophobic drug. Upon loading of the fluorophore, **TzOA-0** hydrogels took on the typical characteristic pink coloration, whereas the **Mag-TzOA-0** hydrogels preserved a black appearance (Figure 35).

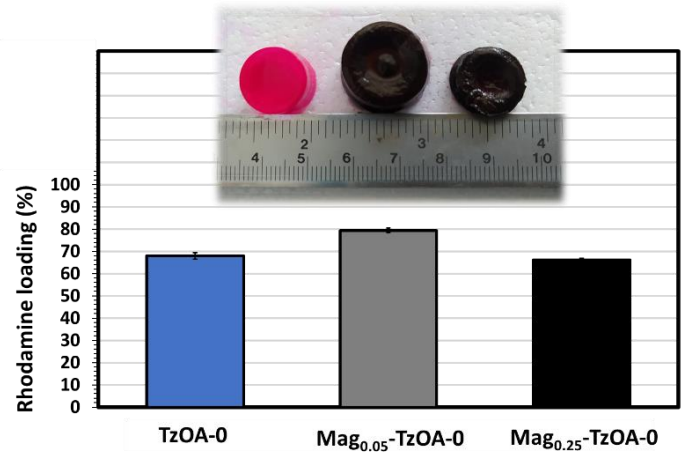

Figure 35. *In situ* co-precipitation method. Rhodamine drug loadings for **TzOA-0**, **$Mag_{0.05}$-TzOA-0** and **$Mag_{0.25}$-TzOA-0** hydrogels

The drug loadings resulted in high values in the range between 66-80%; in ascending order, a 66%, 68% and 80% drug loadings were recorded for **$Mag_{0.25}$-TzOA-0**, **TzOA-0**, and **$Mag_{0.05}$-TzOA-0** hydrogels, which are in accordance with their increasing pore sizes, namely, 53 µm, 95 µm, and 365 µm, respectively.

b) Magnetic-triggered drug release

The drug release tests were carried out similar to the blending method. The hydrogels were immersed in water and the stimulation was performed by moving a Nd magnet underneath the vessels in a circular fashion as shown in Figure 36.

Figure 37 shows the magnetic-triggered release from the hydrogels prepared with the *in situ* co-precipitation method. The magnetic-triggered release of drug was observed to improve as the concentration of superparamagnetic iron oxide nanoparticles (SPIONs) in the hydrogels increased.

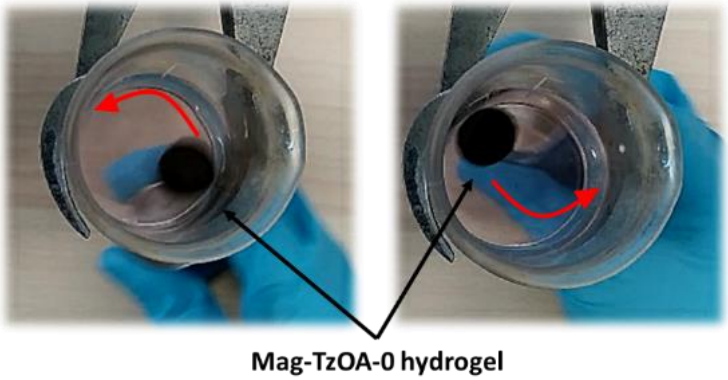

Figure 36. *In situ* co-precipitation method. Magnetic-stimulated rhodamine release with a static Nd magnet performing circled-fashioned movements.

This way, **$Mag_{0.05}$-TzOA-0** and **$Mag_{0.25}$-TzOA-0** hydrogels release 7.7% and 11.5% higher payloads than their respective control counterparts (Figure 37 dashed red and dashed black *vs* bold red and bold black, respectively). This indicates that the release rates may be modulated by tuning the SPION concentration in the hydrogels. Notably, all hydrogels in the absence of the EMF release no more than 30% payloads through simple diffusion, which suggests that the remaining cargo is strongly trapped within the hydrogel mesh due to strong hydrophobic confinements between the rhodamine and the DAT matrix.

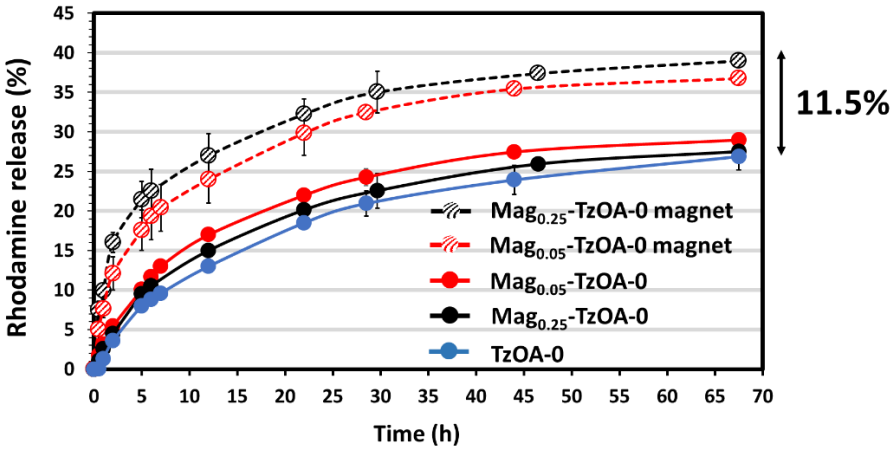

Figure 37. *In situ* co-precipitation method. Magnetic-triggered rhodamine release from **TzOA-0**, **$Mag_{0.05}$-TzOA-0** and **$Mag_{0.25}$-TzOA-0** hydrogels.

Since the drug release performance of the hydrogels prepared with the *in situ* co-precipitation method was higher than those prepared by the blending method, the **TzOA-0**, **$Mag_{0.05}$-TzOA-0** and **$Mag_{0.25}$-TzOA-0** series were tested as possible candidates for magnetic-triggered **on-demand delivery**. This

delivery mode permits the release of a cargo only under the effect of the magnetic field, while minimizing the release by simple diffusion.

For these experiments, the release of RHO was measured *per* cycles instead of a time-dependent profile. Each cycle was carried out stimulating the Mag-TzOA-0 hydrogels by moving the magnet in circular fashions for 15 min while the controls and TzOA-0 hydrogels were stirred for the same amount of time in the absence of the EMF (Figure 38); this way, by limiting the release times to short pulses of 15 min, the time-dependent diffusion was considerable decreased.

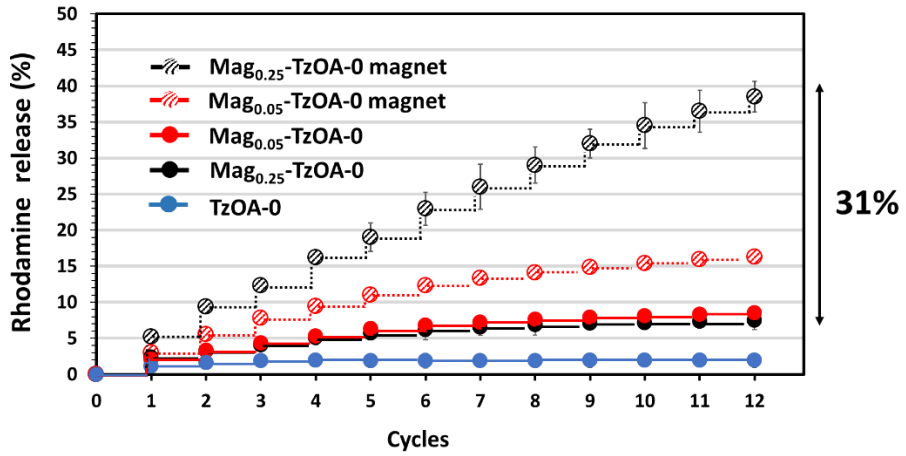

Figure 38. *In situ* co-precipitation method. Pulsatile rhodamine release from TzOA-0, $Mag_{0.05}$-TzOA-0 and $Mag_{0.25}$-TzOA-0 hydrogels.

$Mag_{0.05}$-TzOA-0 and $Mag_{0.25}$-TzOA-0 hydrogels were observed to release 7.8% and 31% higher payloads than their respective controls (Figure 38 dashed red and dashed black *vs* bold red and bold black, respectively).

Further, magnetic-triggered $Mag_{0.05}$-TzOA-0 hydrogels showed pulsatile release only for the first 6 cycles until they reached a plateau (dashed red), whereas magnetic-triggered $Mag_{0.25}$-TzOA-0 hydrogels succeeded maintaining a pulsatile pattern for the entire 12 cycles, thus achieving on-demand drug delivery (dashed black).

In the absence of the EMF, however, all the hydrogels displayed plateau-like release which did not surpass 10% (red, black and blue bold curves).

c) Mechanism of smart delivery

The results observed in Figure 38 reveal that the release rates are largely dependent on the SPION concentration embedded in the hydrogels. Following these observations, a mechanism for the magnetic-triggered release of **RHO** from the **Mag-TzOA-0** hydrogels was proposed, which is based on the double role of the diaminotriazines:

- On the one hand, DATs form coordinative bonds with SPIONs *via s*-triazine N-Fe atoms, so that the nanoparticles are chemically bonded to the polymer network.

- On the other hand, DATs arrange into hydrophobic "pockets", which entrap the **RHO** drug *via* π-π stacking and *CH*-π non-covalent interactions (Figure 39a).

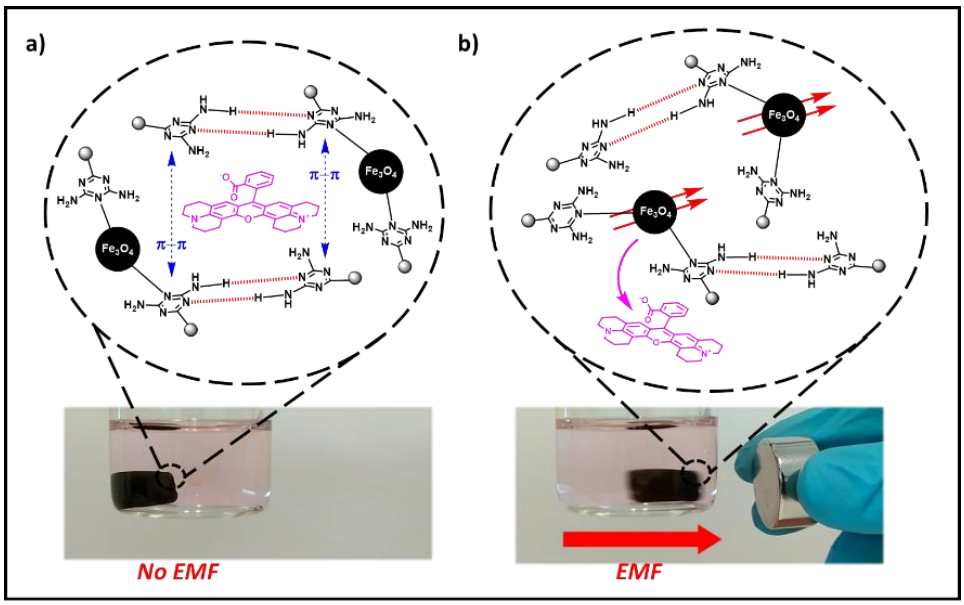

Figure 39. Proposed mechanism for magnetic-triggered drug release of rhodamine from **Mag-TzOA-0** hydrogels a) in the absence of EMF and b) in the presence of EMF.

When magnetic hydrogels come in close contact with the magnet, the SPIONs are attracted by the EMF and pull the covalently bonded polymer scaffold along with them. Rhodamine, however, is not covalently bound to the scaffold and during this strong pull the drug is released from its hydrophobic confinement and expelled from the network, thus increasing the release (Figure 39b).

When the SPION concentration increases, from **Mag$_{0.05}$-TzOA-0** to **Mag$_{0.25}$-TzOA-0** hydrogels, more SPIONs will be coordinated to DATs groups and the response of the hydrogels to the EMF will be stronger, thus expelling **RHO** to a higher extent.

d) *In vitro* cell viability

To characterize the biomedical potential of these materials, **TzOA-0**, **Mag$_{0.05}$-TzOA-0** and **Mag$_{0.25}$-TzOA-0** hydrogels were used to support the growth of SH-SY5Y cells, a human neuroblastoma cell line. Representative images of each experiment are presented in Figure 40a-c.

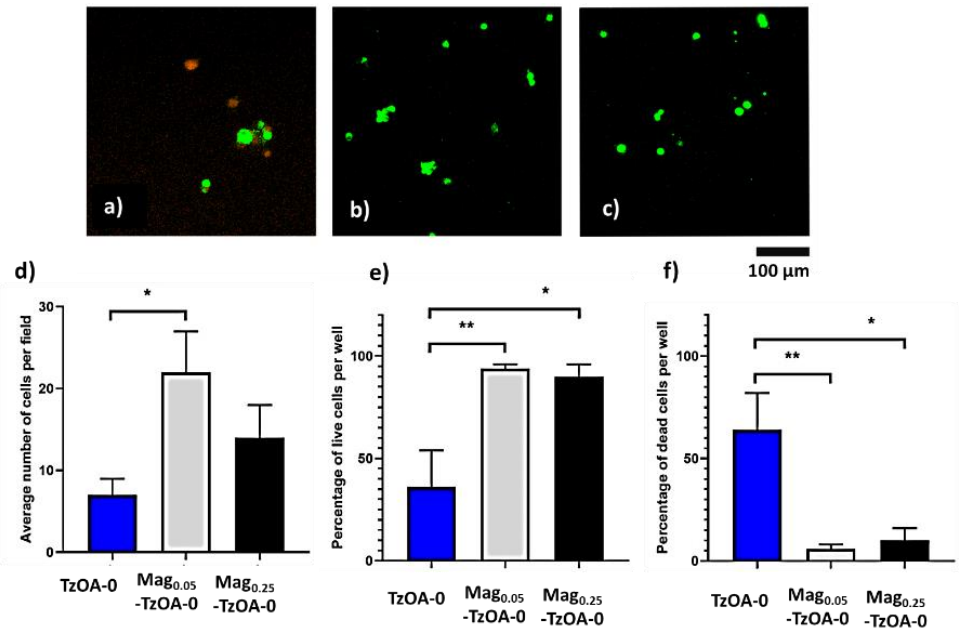

Figure 40. Fluorescence confocal images of SH-SY5Y cell growth in the hydrogels a) **TzOA-0** b) **Mag$_{0.05}$-TzOA-0** and c) **Mag$_{0.25}$-TzOA-0** hydrogels. *In vitro* cell viability studies: d) average number of cells per field e) percentage of living cells per well and f) percentage of dead cells per well, taking **TzOA-0** hydrogels as reference.

Under our experimental conditions, **Mag$_{0.05}$-TzOA-0** hydrogels significantly presented more cells per field than **TzOA-0** hydrogels (Figure 40d, p=0.02). In addition, there was a significant increase in the number of living cells in **Mag$_{0.05}$-TzOA-0** (p=0.01) and **Mag$_{0.25}$-TzOA-0** (p=0.021) compared to **TzOA-0** hydrogels, which increased by an average of 2.5-fold compared to the latter (Figure 40e).

For this same reason, there was a significant decrease in the number of dead cells in **$Mag_{0.05}$-TzOA-0** ($p=0.014$) and **$Mag_{0.25}$-TzOA-0** ($p=0.021$) compared to **TzOA-0** hydrogels, which is reduced around 8 times on average (Figure 40f).

Finally, although all tested hydrogels allowed cell growth on their surface, those that include SPIONs in their composition presented living cells not only on their surface but also inside these structures. These allowed SH-SY5Y cells to settle deeper inside the **Mag-TzOA-0** hydrogels and configure a three-dimensional culture, thus proving these hydrogels favorable biocompatible scaffolds

.

4.3. References

[1] A. K. Gaharwar, N. A. Peppas, A. Khademhosseini, *Biotechnol. Bioeng.* **2014**, *111*, 441–53.

[2] S. Murdan, *J. Control. Release* **2003**, *92*, 1–17.

[3] K. Sutani, I. Kaetsu, K. Uchida, *Radiat. Phys. Chem.* **2001**, *61*, 49–54.

[4] Y. Yang, J. B. F. N. Engberts, *Colloids Surfaces A Physicochem. Eng. Asp.* **2000**, *169*, 85–94.

[5] A. Servant, L. Methven, R. P. Williams, K. Kostarelos, *Adv. Healthc. Mater.* **2013**, *2*, 806–811.

[6] A. Servant, V. León, D. Jasim, L. Methven, P. Limousin, E. V. Fernández-Pacheco, M. Prato, K. Kostarelos, *Adv. Healthc. Mater.* **2014**, *3*, 1334–1343.

[7] Y. Li, G. Huang, X. Zhang, B. Li, Y. Chen, T. Lu, T. J. Lu, F. Xu, *Adv. Funct. Mater.* **2013**, *23*, 660–672.

[8] N. Huebsch, J. Kim, X. Zhao, K. Lee, C. A. Cezar, K. Bouhadir, D. J. Mooney, *Proc. Natl. Acad. Sci.* **2010**, *108*, 67–72.

[9] S. Campbell, D. Maitland, T. Hoare, *ACS Macro Lett.* **2015**, *4*, 312–316.

[10] B. Yan, J. C. Boyer, D. Habault, N. R. Branda, Y. Zhao, *J. Am. Chem. Soc.* **2012**, *134*, 16558–16561.

[11] L. E. Strong, S. N. Dahotre, J. L. West, *J. Control. Release* **2014**, *178*, 63–68.

[12] Z. Cheng, R. Chai, P. Ma, Y. Dai, X. Kang, H. Lian, Z. Hou, C. Li, J. Lin, *Langmuir* **2013**, *29*, 9573–9580.

[13] T. W. Wong, *J. Control. Release* **2014**, *193*, 257–269.

[14] T. W. Wong, A. Nor Khaizan, *Pharm. Res.* **2013**, *30*, 90–103.

[15] N. R. Khan, T. W. Wong, *Expert Opin. Drug Deliv.* **2016**, *13*, 1209–1219.

[16] Y. Haque, E.; Kikuchi, T.; Kanemitsu, K.; Tsuda, *Chem. Pharm. Bull.* **1986**, *34*, 430–433.

[17] J. Wang, D. Wang, H. Yan, L. Tao, Y. Wei, Y. Li, X. Wang, W. Zhao, Y. Zhang, L. Zhao, et al., *J. Mater. Chem. B* **2017**, *5*, 4110–4120.

[18] R. E. Rivero, M. A. Molina, C. R. Rivarola, C. A. Barbero, *Sensors Actuators, B Chem.* 2014, *190*, 270–278.

[19] K. A. Simo, V. B. Tsirline, D. Sindram, M. T. McMillan, K. J. Thompson, R. Z. Swan, I. H. McKillop, J. B. Martinie, D. A. Iannitti, *Hpb* 2013, *15*, 991–996.

[20] S. Su, H. Wang, X. Liu, Y. Wu, G. Nie, *Biomaterials* 2013, *34*, 3523–3533.

[21] W. Wu, J. Shen, P. Banerjee, S. Zhou, *Biomaterials* 2010, *31*, 7555–7566.

[22] L. P. Lv, K. Landfester, D. Crespy, *Chem. Mater.* 2014, *26*, 3351–3353.

[23] S. Wang, R. Attah, J. Li, Y. Chen, R. Chen, *ACS Biomater. Sci. Eng.* 2018, *4*, 4236–4243.

[24] L. Wang, X. Shi, J. Zhang, Y. Zhu, J. Wang, *RSC Adv.* 2018, *8*, 31581–31587.

[25] S. Feng, S. Wang, Y. Lv, L. He, Q. Li, T. Zhang, *Polym. Int.* 2019, *68*, 494–502.

[26] X. Gao, Z. Yu, B. Liu, J. Yang, X. Yang, Y. Yu, *Eur. Polym. J.* 2020, *133*, 109779.

[27] A. Puiggalí-Jou, E. Cazorla, G. Ruano, I. Babeli, M. P. Ginebra, J. Garciá-Torres, C. Alemán, *ACS Biomater. Sci. Eng.* 2020, *6*, 6228–6240.

[28] G. Li, Y. Wang, S. Wang, J. Jiang, 2018, *1700483*, 1–6.

[29] V. Georgakilas, J. N. Tiwari, K. C. Kemp, J. A. Perman, A. B. Bourlinos, K. S. Kim, R. Zboril, *Chem. Rev.* 2016, *116*, 5464–5519.

[30] R. Cavalli, M. Soster, M. Argenziano, *Ther. Deliv.* 2016, *7*, 117–138.

[31] J. Leganés, A. Sánchez-Migallón, S. Merino, E. Vázquez, *Nanoscale* 2020, *12*, 7072–7081.

[32] L. Tang, W. Liu, G. Liu, *Adv. Mater.* 2010, *22*, 2652–2656.

[33] F. Qin, C. Brosseau, *J. Appl. Phys.* 2012, *111*, 061301.

[34] Y. Wang, Y. Du, P. Xu, R. Qiang, X. Han, *Polym. Chem.* 2017, *9*, 29.

[35] J. Zhu, F. Liu, N. Mahmood, Y. Hou, *Graphene-Based Polymer Nanocomposites in Electronics*, 2015.

[36] A. J. Bur, *Polym. Chem.* **1985**, *26*, 963–977.

[37] Z. Ahmad, in *Dielectr. Mater. IntechOpen*, **2012**, pp. 3–26.

[38] C. Martín, S. Merino, J. M. González-Domínguez, R. Rauti, L. Ballerini, M. Prato, E. Vázquez, *Sci. Rep.* **2017**, *7*, 10942.

[39] X. Shi, H. Chang, S. Chen, C. Lai, A. Khademhosseini, H. Wu, *Adv. Funct. Mater.* **2012**, *22*, 751–759.

Chapter 5

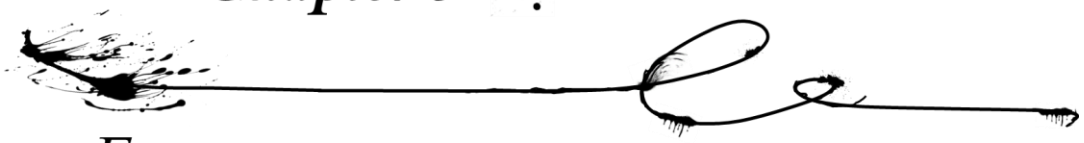

Efficient Synthesis of Light-degradable Hydrogels: Multicomponent Reactions

5.1. Introduction

The work described in this chapter was carried out in a short doctoral stay and focuses on the line of research performed in the Dynamic Biomaterials group at the Institute of New Materials (INM), located in Saarbrücken, Germany.

5.1.1. Photo-responsive groups

Light is one of the most attractive stimuli when it comes to the activation of smart hydrogels, because it can be attained remotely with spatial and temporal precision.[1] Light responsiveness in polymer and hydrogel materials is typically achieved with photo-responsive groups (PRGs), which induce a chemical modification that results in the removal of a molecule triggered by light.

Amongst the most common PRGs is the ortho-nitrobenzyl (*o*-NB) group, which is one of the most useful photolabile compound for the fabrication of photoresponsive hydrogel systems for biomedical applications due to its biocompatibility. Even after photodegradation, the *o*-NB by-products are innocuous to fragile biomacromolecules such proteins, DNAs and RNAs.[5]

The *o*-NB group absorbs light in the UV range (320−410 nm) and results in the cleavage of an *ortho* leaving group.[1,2] This phenomenon starts with the homolytic cleavage of the N=O π bond, which creates a diradical excited species **II** (Scheme 1).

This diradical then abstracts a proton from the benzylic carbon and forms the intermediate **III**, which, following resonance of the π-electrons, leads to cleavage of the leaving group.

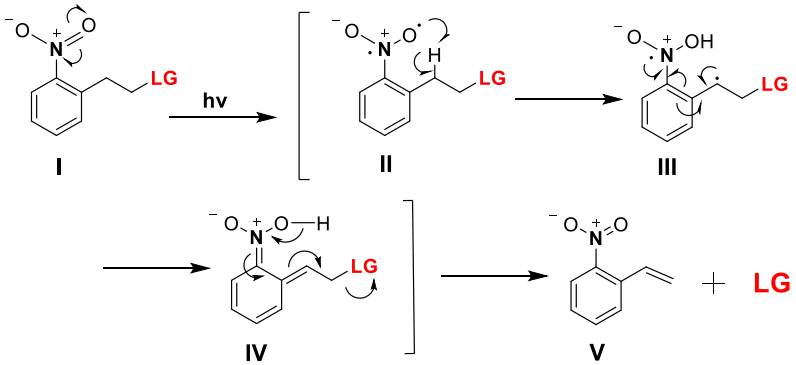

Scheme 1. Mechanism for the photocleavage of the ortho-nitrobenzyl (*o*-NB) photolabile group.

As a consequence of the interaction between the PRG and light, a chemical bond is broken and this can be harnessed, for example, for the preparation of hydrogels that degrade upon light exposure.

5.1.2. Photo-degradable hydrogels

Photo-responsive and photo-degradable hydrogels have proven optimal for biological applications, such as cell migration, cellular function[3] or controlled release of therapeutics.[4] These hydrogels typically consist of a polymeric network and a photoreactive moiety, such as the *o*-NB group.

Many strategies have been developed over the years for the incorporation of the photoactive group into the hydrogel network. The most straightforward method to achieve this is through chemical functionalization of the hydrogel with the PRG group, which then can undergo photocleavage. For example, Kros and coworkers built a photodegradable, covalently crosslinked hydrogel from dextran (DEX) and dithiolated poly(ethyleneglycol) (DSPEG) by means of crosslinking *via* conjugated addition (Figure 1a).[6]

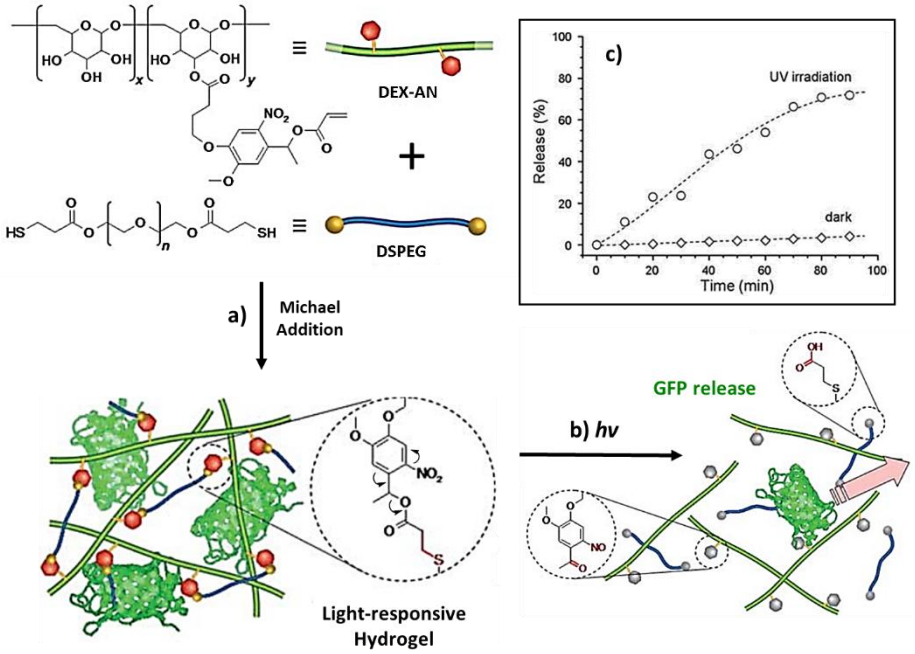

Figure 1. *o*-NB light responsive hydrogel a) *in situ* crosslinking *via* Michael addition b) and c) GFP release during light-triggered degradation.

The hydrogel was rendered light-sensitive by introduction of a non-toxic *o*-NB moiety with two chemical termini: one end was used to bind the *o*-NB group to DEX polymer *via* esterification and afford an acrylate-o-nitrobenzyl-functionalized dextran (DEX-AN). The second end, herein the remaining acrylate end, was used to crosslink the polymer DEX-AN with the DSPEG crosslinker *via* thiol conjugation, in order to obtain an *in situ* photodegradable hydrogel. Upon irradiation, the hydrogel was decomposed due to the cleavage of the photolabile moiety, which triggered the release of the Green Fluorescent Protein (GFP) entrapped in the polymer network (Figure 1b). After 90 min of UV exposure, around 70% GFP was released from the hydrogel, whereas less than 5% release was observed in the absence of UV light irradiation (Figure 1c).

Despite their versatility, the preparation of these photodegradable hydrogels requires high synthetic effort. First, the PRG must be chemically tailored with two different reactive handles, one for selective conjugation to the polymer chain and another for conjugation to the crosslinking agent (Scheme 2a).

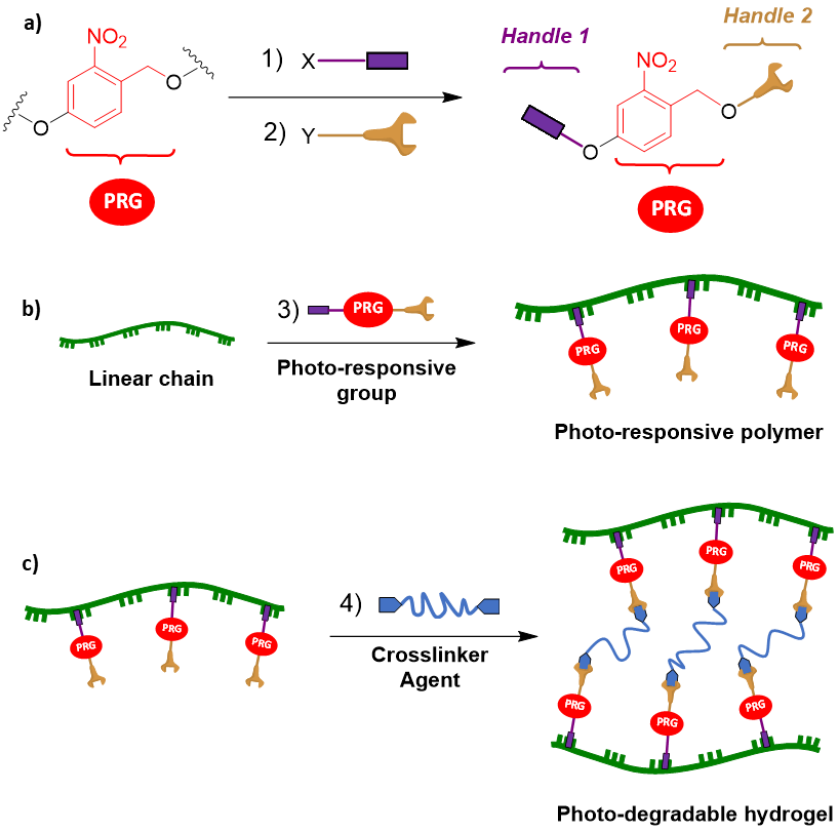

Scheme 2. Stepwise synthesis of a) the photo responsive group (PRG) b) the photo-responsive polymer c) the photo-degradable hydrogel.

Further, the modified PRG must be anchored into the polymer backbone to obtain the photo-responsive polymer (Scheme 2b). Finally, the polymer is crosslinked in order to fabricate the light-degradable hydrogel (Scheme 2c).[7] Overall, these multistep reactions often afford low yields.[1,4] In addition, chemical modification of the PRGs may change the light absorption properties of the molecule, compromising the efficiency of the light-triggered degradation.[7]

5.1.3. The Passerini Multicomponent Reaction

The Passerini multicomponent reaction (MCR) is an optimal solution to overcome this synthetic effort, since it can incorporate both a PRG and a crosslink-able group in a one-pot procedure under mild conditions and high compatibility with various functional groups.[8,9] The reaction involves a carboxylic acid group, an aldehyde group and an isocyanide to form an α-acyloxyamide. This way, upon suitable modification of the PRG with an aldehyde functional group and the crosslink-able end with an isocyanide handle, both elements can be incorporated into a polymer backbone containing a carboxylic acid functionality. As a result, photo-responsive polymers are rapidly synthesized in a *one*-pot process (Scheme 3).[10,11]

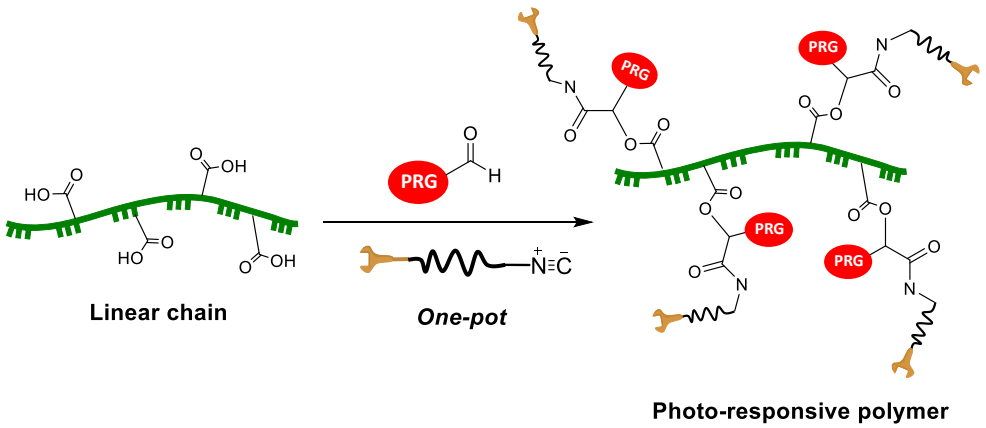

Scheme 3. Passerini Multicomponent Reaction (MCR) for the synthesis of photo-responsive polymers in a *one*-pot process.

Light-degradable hydrogels can then be synthesized *via* straightforward conjugated addition or *click* reaction by mixing the photo-responsive polymer with an appropriate crosslinker agent.

For example, Forsythe and coworkers[7] applied the Passerini reaction to first prepare a library of photolabile 4-armPEG polymers containing a click-able

azide group and a o-NB chromophore responsive to UV–visible light (Scheme 4a).

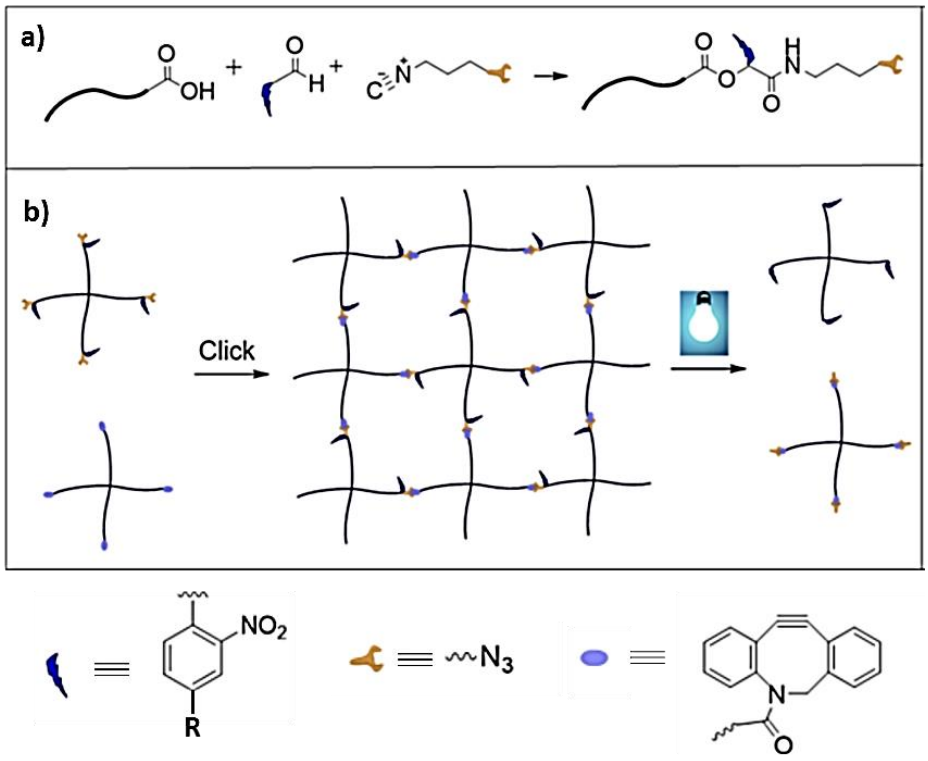

Scheme 4. a) Synthesis of photo-responsible polymers with the Passerini MCR b) Synthesis of light-degradable hydrogels *via* click-reaction.

The polymers were then subsequently crosslinked *via* strain promoted azide–alkyne cycloaddition (SPAAC) in order to fabricate photodegradable hydrogels (Scheme 4b), which were used for selective cell release upon light-triggered degradation.

Despite the number of advantages of the *o*-NB as PRG, the light absorption range of this moiety can damage nearby cells due to prolonged UV exposure. This interval may be further red-shifted towards the IR region by incorporating phenyl donor groups, such as in the photoresponsive group *p*-methoxynitrobiphenyl (PMNB) and *p*-dialkylaminonitrobiphenyl (ANBP) (Figure 2).

These groups increase the probability of the 2-photon excitation phenomenon, which implies the simultaneous absorption of two photons of half the energy. In consequence, the absorption range of the chromophore is

displaced from the UV/VIS region (320–410 nm) to Near Infrared (NIR) region (740 nm), and this not only decreases the phototoxicity of cells exposed to the radiation, but also increases the penetration depth of the wave.[12,13]

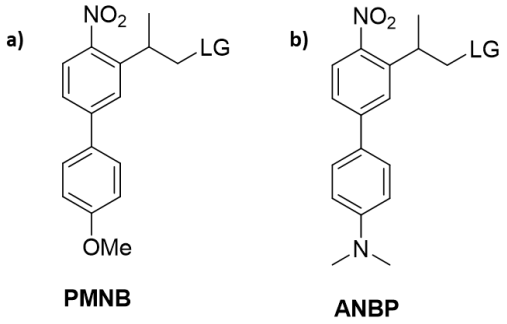

Figure 2. a) *p*-methoxynitrobiphenyl (PMNB) and b) *p*-dimethylaminonitrobiphenyl (ANBP).

In order to prepare light-degradable hydrogels, thus, there is an urge to fabricate light-responsible polymers that gather the following conditions:

- They must require a straightforward synthetic route
- They have to include a photolabile unit
- A crosslink-able end
- An absorption range in the visible-NIR region, which is more desirable for biomedical applications

5.2. Results and Discussion

The purpose of this work, which was carried out during a doctoral stay, is to fabricate a light-degradable hydrogel containing the NIR-responsive group *p*-methoxynitrobiphenyl (PMNB) using the Passerini multicomponent reaction (MCR) procedure, as a means to simplify their synthetic pathways previously reported in the group.[14] This is envisaged by a two-step procedure (Scheme 5):

1) Synthesis of a light-responsive polymer *via* the Passerini MCR between a PMNB-based aldehyde, an azido-terminated isocyanide and 4-arm-polyethyleneglycol (PEG) carboxylic acid.

2) Crosslinking of the polymer *via* copper-free click reaction to obtain the light-responsive hydrogel.

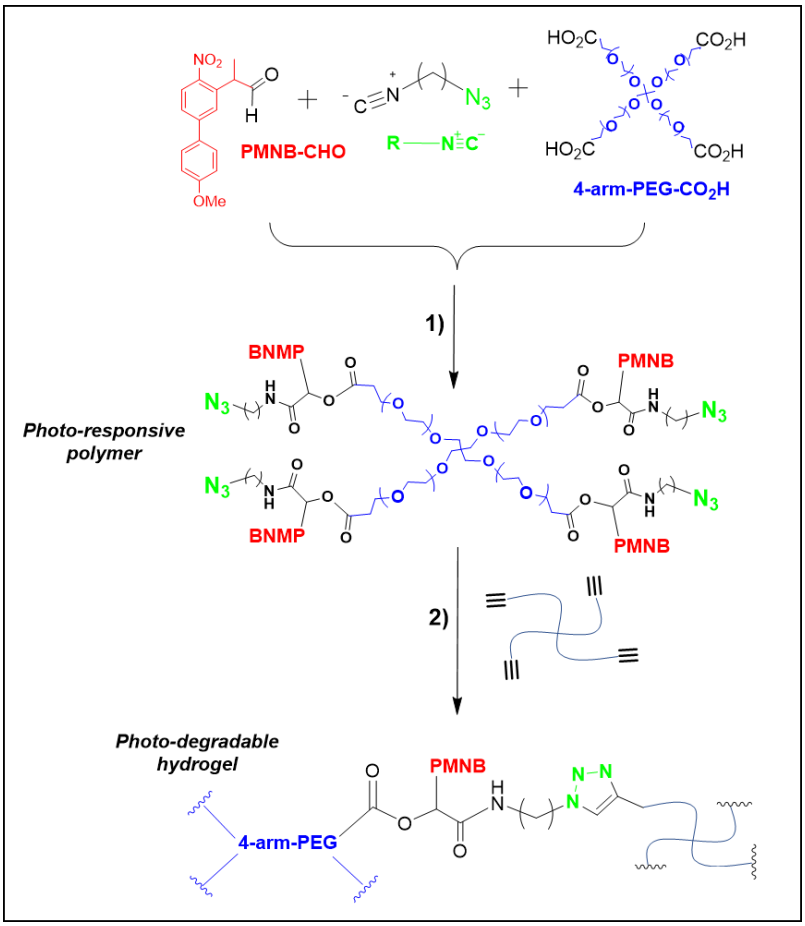

Scheme 5. Passerini one-pot Multicomponent Reaction (MCR) for the synthesis of PMNB-based light-responsive hydrogels.

In order to test the Passerini MCR for the synthesis of the light-responsive polymers and hydrogels, the preparation of their respective monomers was first envisaged.

The obtention of the PMNB-CHO aldehyde was attempted from mild oxidation of the PMNB-OH chromophore, previously synthesized in the group (Figure 3a).[14] Further, the isocyanides were obtained in several steps from the corresponding amines, which where commercially available (Figure 3b). Finally, 4-arm-PEG-CO_2H (10 kDa) was chosen as the carboxylic acid counterpart (Figure 3c).

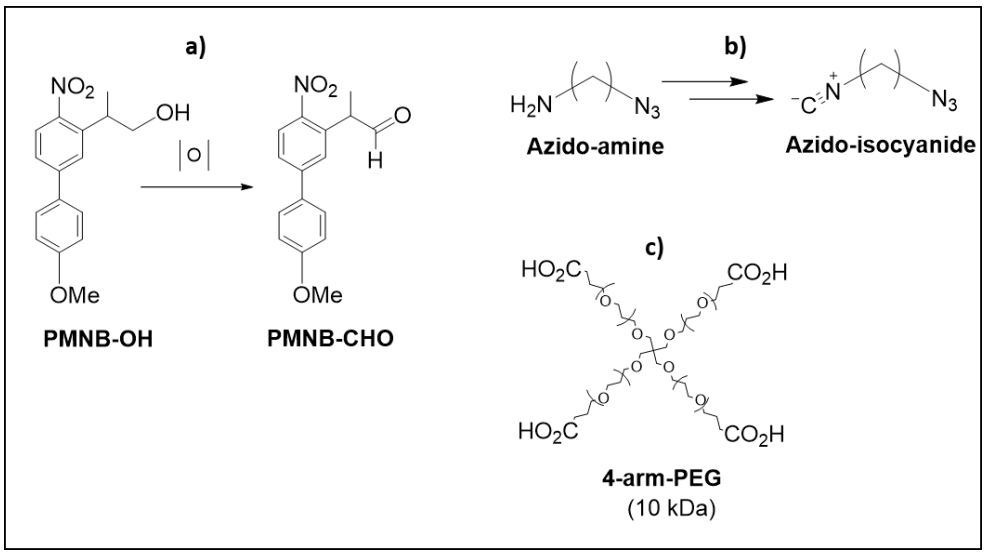

Figure 3. Synthesis of the monomers required for the Passerini MCR: a) the aldehyde b) the isocyanide and c) the carboxylic acid.

5.2.1. Aldehyde synthesis

Two different methodologies for the oxidation of PMNB-OH to PMNB-CHO were attempted: Dess-Martin oxidation and Ley-Griffith oxidation.

5.2.1.1. Dess-Martin oxidation

The Dess-Martin oxidation of PMNB-OH (**17**) to PMNB-CHO (**18**) was attempted following a patented protocol.[15] In this reaction, the chromophore **17** is suspended in dry dichloromethane (DCM) and mixed with the Dess-Martin periodinane (DMP) (Scheme 6). The advantage of this methodology is that it

requires only mild conditions, avoids the use of toxic chromium reagents and is very selective.

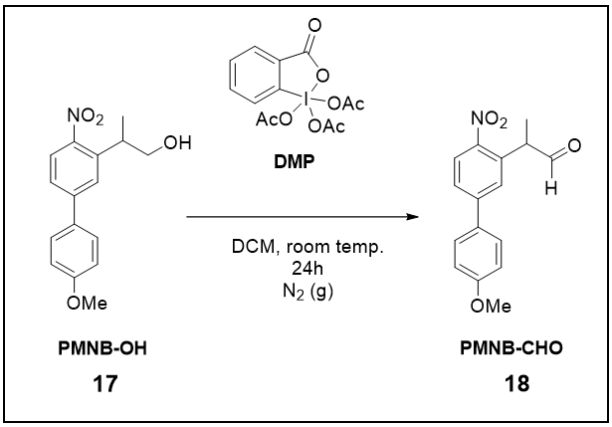

Scheme 6. Synthesis of **PMNB-CHO (18)** *via* Dess-Martin oxidation.

The reaction mechanism occurs through the selective complexation of the hydroxyl group of **17** to the iodine atom of DMP, which allows the alcohol to rapidly perform ligand exchange and form the intermediate **19**. The acetate then acts as a base to deprotonate the H from the alcohol to afford the aldehyde **18** (Scheme 7).

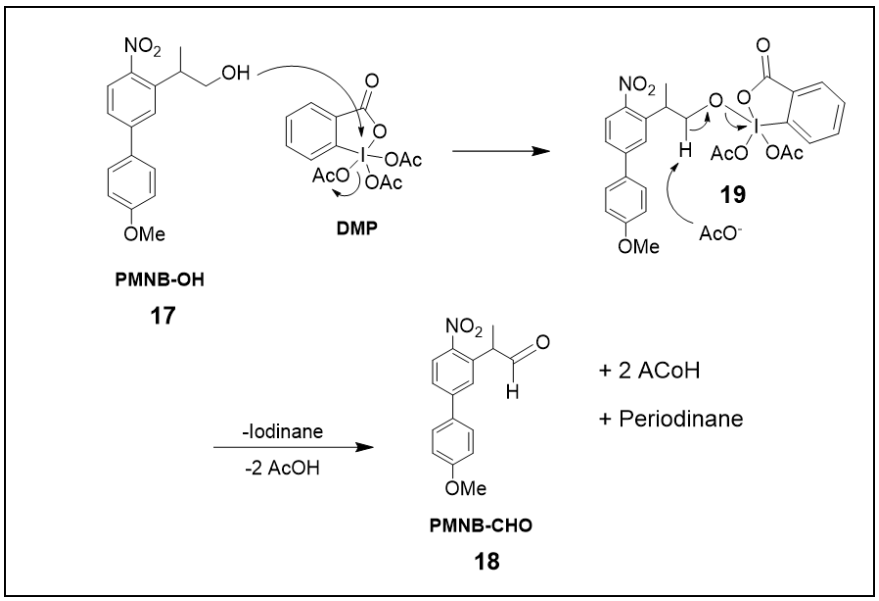

Scheme 7. Reaction mechanism for the synthesis of **PMNB-CHO (18)** *via* Dess-Martin oxidation.

While carrying out the reaction, however, complications were met during work-up due to the formation of an emulsion, which resulted in a contaminated crude, as can be seen in the ^{1}H-NMR spectrum (Figure 4). Nevertheless, the presence of the aldehyde proton provided evidence of the successful formation of **18** (Figure 4, blue square).

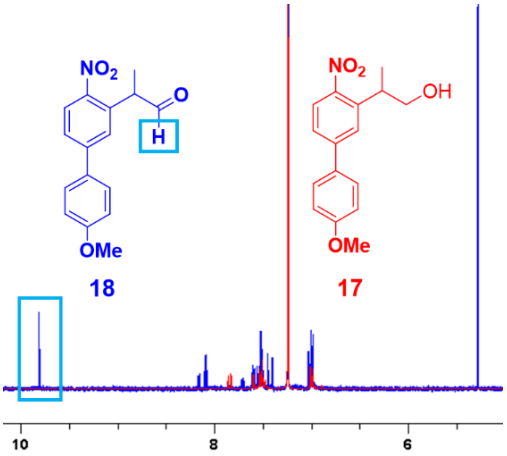

Figure 4. ^{1}H-NMR (DMSO-d_6, 400 MHz) spectrum of reaction crude after work-up.

The purification of aldehyde **18** was attempted with both column chromatography and high-performance liquid chromatography (HPLC). Several experimental conditions for analytical HPLC techniques were tested in order to increase the separation in retention times, Δt_R, between compounds **17** and **18.** These conditions are summarized in Table 1. The best condition was finally tested in a preparative HPLC to purify the reaction crude (Table 1, entry 5).

Table 1. Conditions for purification of **18** with analytical HPLC

Entry[a]	Composition Mobile Phase	HPLC run time (min)	Δt_R between 17-18 (min)
1	80:20 → 5:95	40	0.9
2	90:10 → 5:95	40	0.9
3	90:10 → 5:95	50	1
4	95:5 → 5:95	60	1
5	50:50 → 5:95	60	2.7

[a]Mobile phase: MeCN: H_2O

However, the separation was unsuccessful, which was confirmed by ^{1}H-NMR analysis of both fractions.

5.2.1.2. Ley-Griffith oxidation

In light of the fruitless results with the Dess-Martin reaction, a brief attempt to obtain chromophore **18** from **17** was carried out with the Ley-Griffith oxidation, also based on a patented protocol (Scheme 8).[16] This reaction is based on the oxidant agent tetrapropylammonium perruthenate (TPAP), which is a very mild oxidizing agent. Additionally, TPAP is used in combination with the co-oxidant *N*-methylmorpholine *N*-oxide (NMO) in stoichiometric amounts.

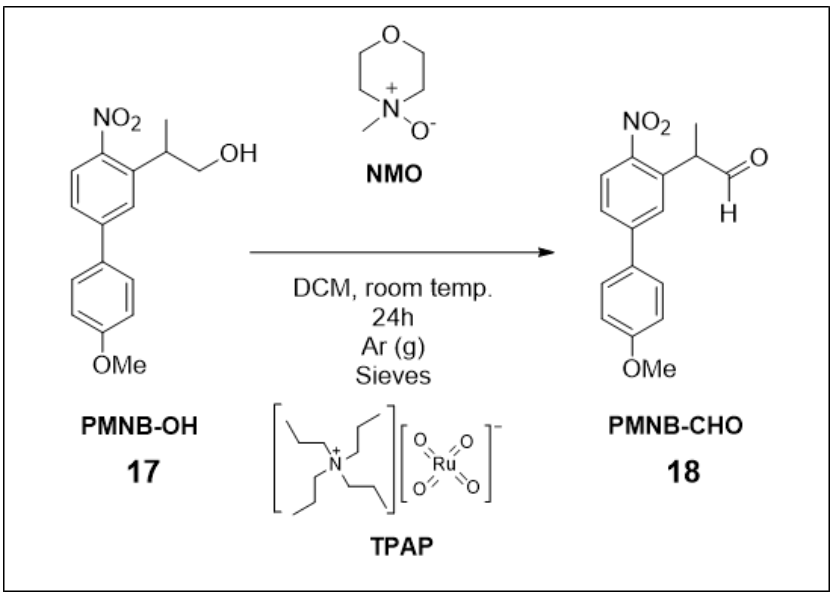

Scheme 8. Synthesis of **PMNB-CHO (18)** *via* Ley-Griffith oxidation.

The reaction mechanism occurs though complexation of alcohol **17** to the rhutenium species TPAP to form the intermediate **20**, which rapidly converts to the aldehyde **18** and generates a Ru (V) species. At this point, NMO reoxidises the ruthenium catalyst back to TPAP and regenerates the catalytic cycle, thus sustaining catalysis (Scheme 9). Since water is produced, it must be taken up by molecular sieves, othwerwise overoxidation of **17** to the carboxylic acid may occur.

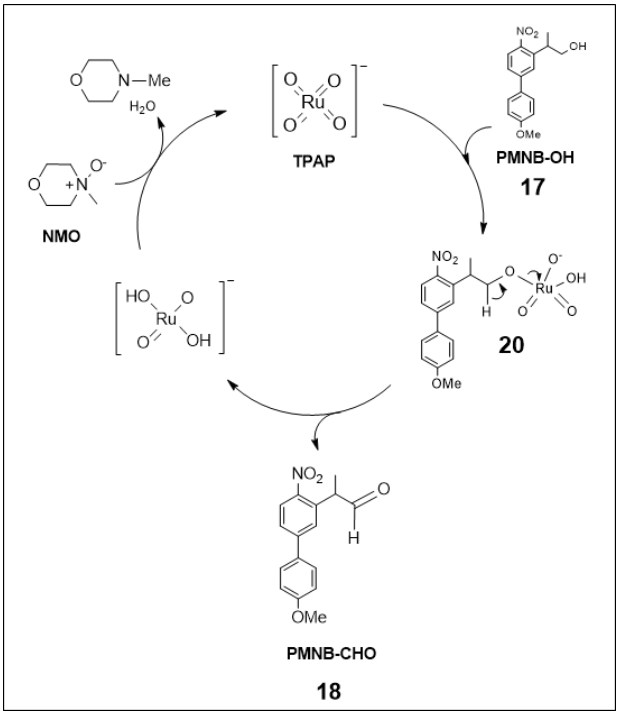

Scheme 9. Reaction mechanism for the synthesis of **PMNB-CHO (18)** *via* Ley-Griffith oxidation.

Due to the shortage of **17**, we could only carry out one attempt following the conditions described in the patent. Moreover, the molecular sieves were removed using a silica pad. Unlike with the Dess-Martin oxidation, very little amount of **18** could be observed in the reaction crude, as shown for the aldehyde signal of the ^{1}H-NMR spectrum (Figure 5, blue square).

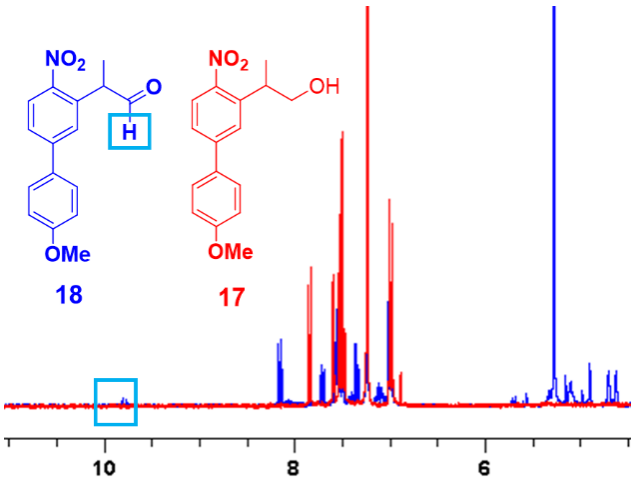

Figure 5. ^{1}H-NMR (DMSO-d_6, 400 MHz) spectrum of reaction crude after work-up.

So far, since every attempt for the synthesis of **18** was unsuccessful and the compound **17** species is known to be a light-sensitive moiety[14], we considered that this starting material had suffered chemical alterations, perhaps by the incidence of light or simply by decomposition.

In order to confirm our suspicions, we performed Quadrupole Time Of Flight (QTOF)-Mass spectrum of compound **17** coupled to HPLC. The latter revealed four peaks, which suggested that the starting material **17** had decomposed (Figure 6a). Of the peaks 1-4, only peak 3 displayed the $[M + H]^+$ mass peak of **17** in the coupled mass spectrum (Figure 6b).

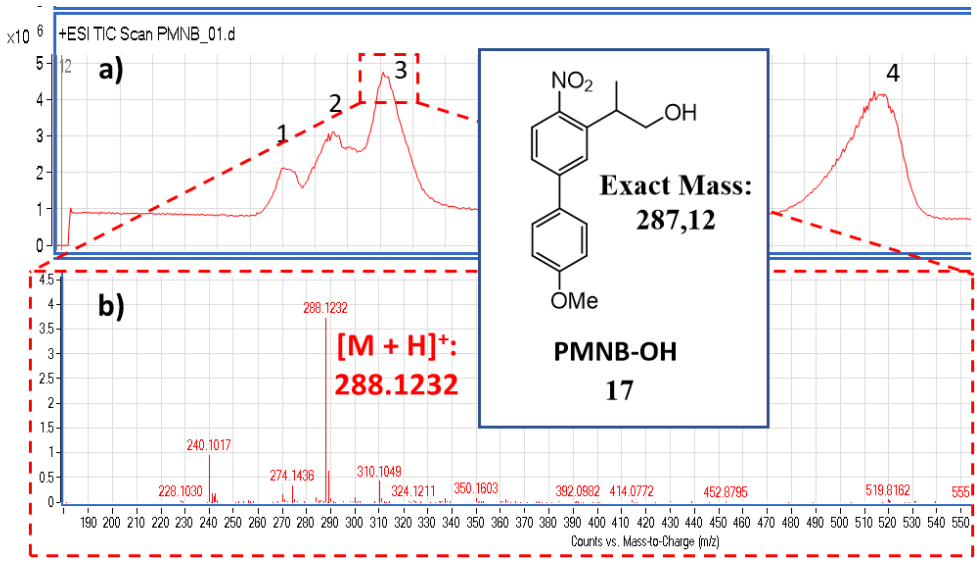

Figure 6. Characterization of **17** a) HPLC and b) QTOF-Mass spectrum of the peak 3.

We thus confirmed that the starting material **17** was a mixture of PMNB-OH as well as other subspecies and that must have decomposed while handling the reactant.

5.2.2. Isocyanide synthesis

The synthesis of the isocyanides followed a two-step procedure: formylation of the commercially available amine, followed by dehydration of the formamide group. Three different amines were chosen as starting materials (Figure 7).

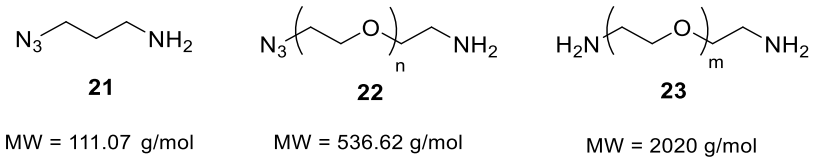

Figure 7. Commercially available amines used for the synthesis of the isocyanide linkers.

5.2.2.1. Formylation

In this first step, formylation of the comercial amines was carried out using ethyl formate, following literature references (Scheme 10).[17–19] The ethyl formate was used in excess, both as a reactant and as a solvent and the reaction was performed under reflux. The reaction takes place straightforwardly, with excellent yields and appeared reproducible for every amine used.

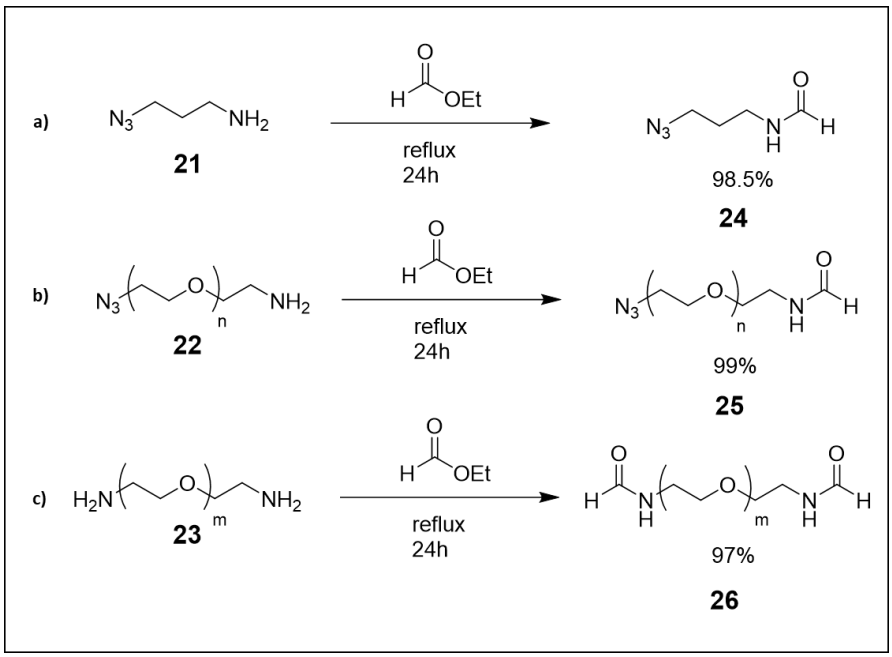

Scheme 10. Synthesis of formamides **24**, **25** and **26**.

It is noteworthy to mention that each resulting formamide differed widely in their macroscopy appearance. This way, short-chain formamide **24** turned a colorless liquid, whereas long-chain formamides **25** and **26** turned brownish viscous liquids and solids, respectively.

The evolution of the reaction was studied with ^{1}H-NMR and it was observed that after 24h, the amines had been quantitatively formylated into their corresponding formamides. The ^{1}H-NMR of the formamide **24** clearly showed two signals, absent for the corresponding amine **21**, corresponding to the aldehyde and amide protons (Figure 8) (See experimental section for the characterization of formamides **25** and **26**).

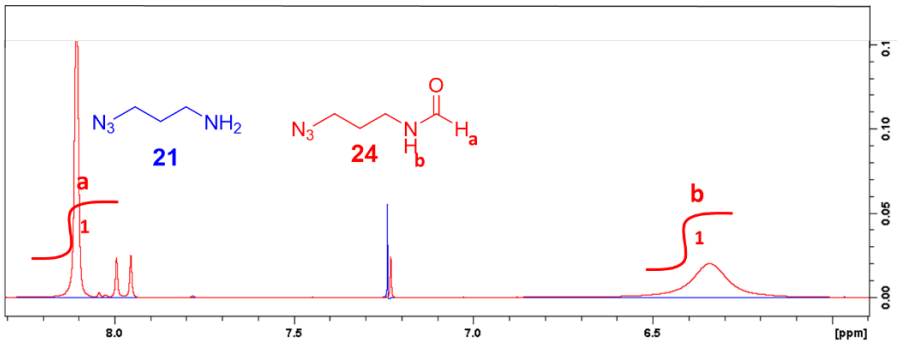

Figure 8. Overlaid ^{1}H NMR spectra of compounds **21** and **24**.

The successful formylation of **21** was also confirmed with FT-IR spectroscopy: the C=O stretching band, absent for the starting material, appeared at 1665 cm^{-1}, evidencing the presence of formamide group (Figure 9). Further, significant alterations in the region 3000-3500 cm^{-1} were observed, corresponding to the N-H stretching bands.

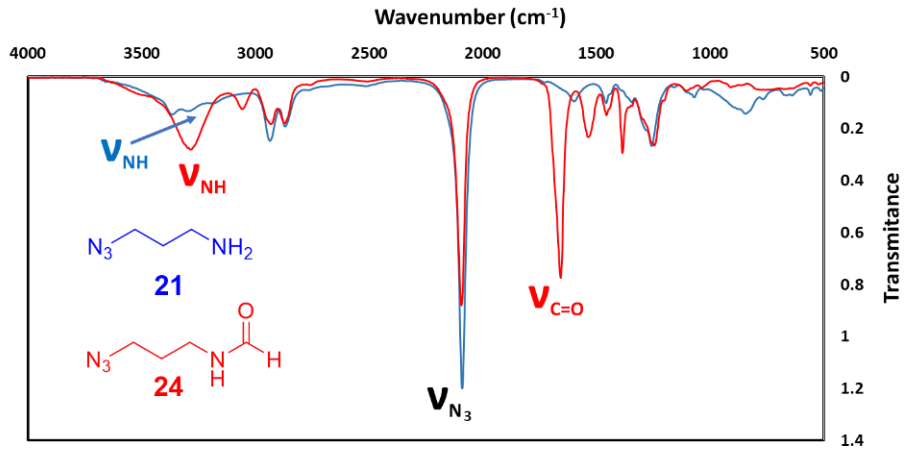

Figure 9. Overlaid FT-IR spectra of compounds **21** and **24**.

Finally, mass spectrometry confirmed the mass peak corresponding to the ion $[M + K]^{+}$ of the compound **24**. The peak at $[M^{+}] = 101$ reveals the presence of **24** after loss of the formyl fragment (Figure 10).

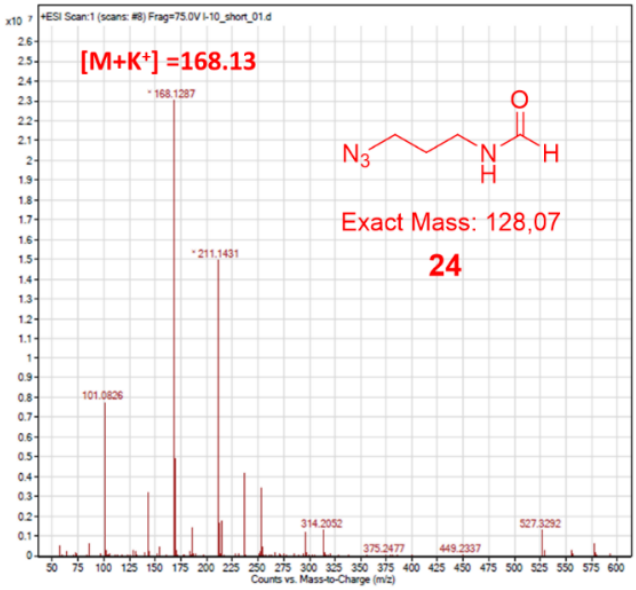

Figure 10. Mass spectrum of compound 24.

5.2.2.2. Amide dehydration

The synthesis of isocyanides was carried out by dropwise addition of dehydrating agent phosphorous oxychloride ($POCl_3$) to the corresponding formamide in the presence of triethylamine (NEt_3), following literature protocols (Scheme 11).[17–19]

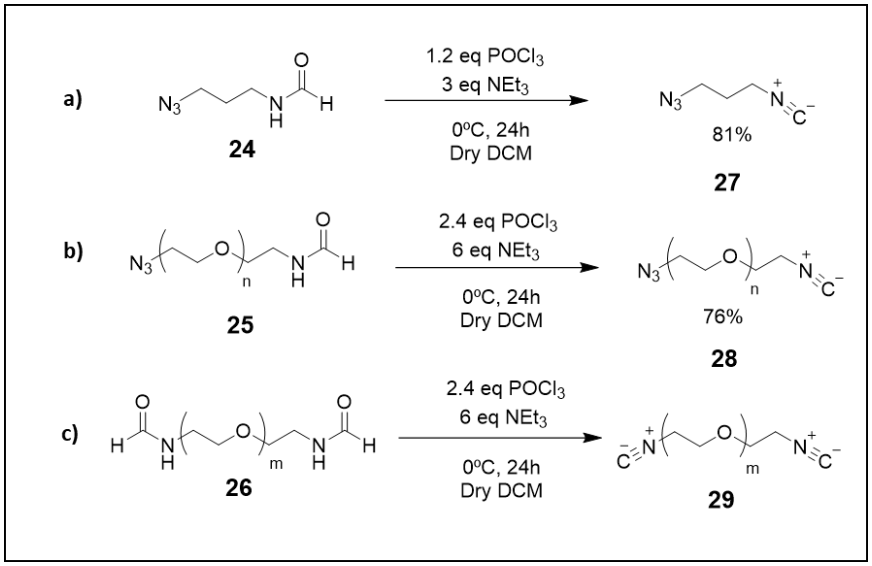

Scheme 11. Synthesis of isocyanides 27, 28 and 29.

Scheme 12 shows the reaction mechanism for the formation of isocyanide **27**, which occurs through dehydration of the corresponding formamide **24**.

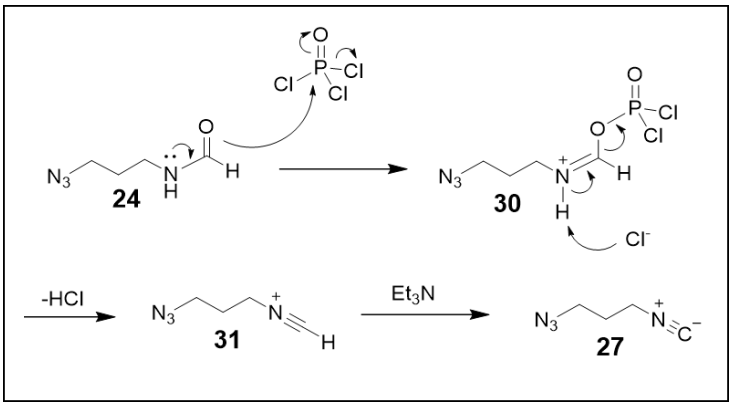

Scheme 12. Reaction mechanism for the synthesis of isocyanide **27** *via* formamide dehydration.

The carbonyl group of **24** carries out nucleophilic attack at the electrophilic phosphorous of $POCl_3$ and generates intermediate **30**. Loss of hydrochloric acid (HCl) and the phosphorous good leaving group leads to the protonated isocyanide **31** that would rapidly generate the isocyanide **27** upon deprotonation with Et_3N.

The short-chain isocyanide **27** was synthesized after 24h with excellent yields (81%). After work-up, **27** was obtained as a light-brown liquid which had a strong foul odor, typically characteristic of the isocyanide compounds. ^{1}H-NMR of the reaction crude revealed that the aldehyde and amide protons of **24** (signals e and d, depicted in red) are no longer present, thus evidencing the dehydration of the amide group (Figure 11).

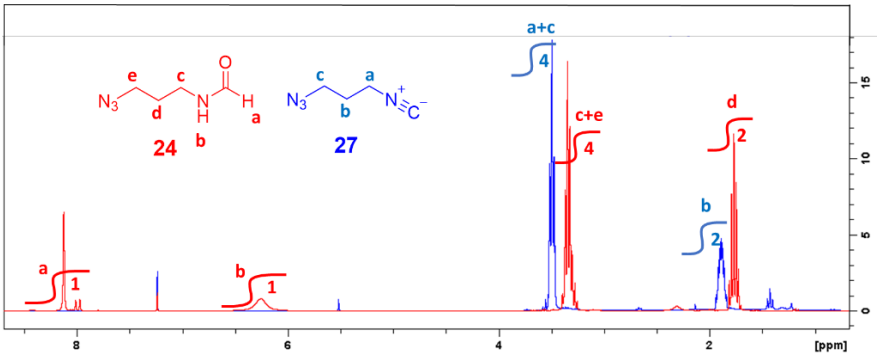

Figure 11. Overlaid ^{1}H-NMR spectra of compounds **24** and **27**.

FT-IR spectroscopy also confirms the disappearance of both the C=O and N-H stretchings of the formamide group, and reveals the new NC stretching band in the vicinity of the N_3 vibration (Figure 12). Finally, the mass spectrum of **27** reveals the $[M+K]^+$ ion (Figure 13).

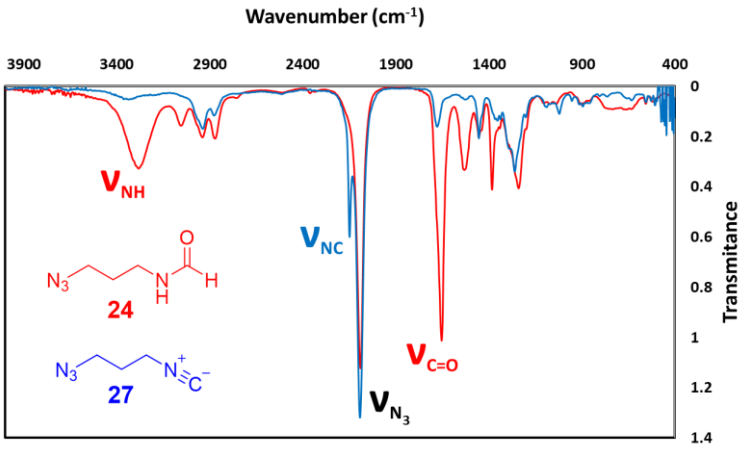

Figure 12. Overlaid FT-IR spectra of compounds **24** and **27**.

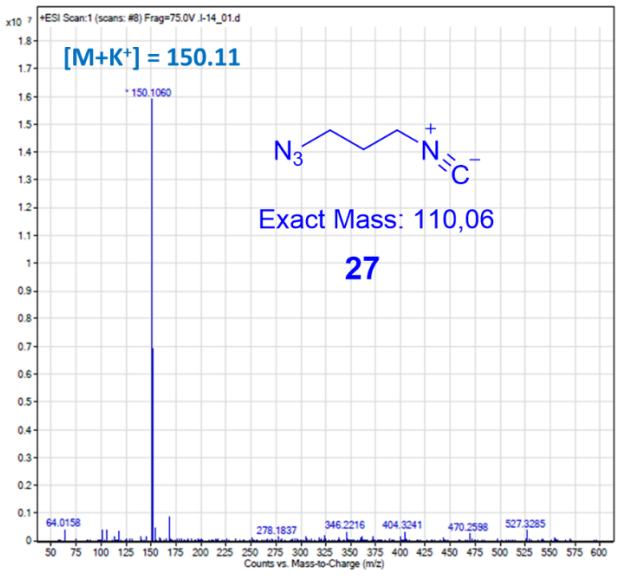

Figure 13. Mass spectrum of compound **27**.

For the syntheses of isocyanides **28** and **29,** it was observed experimentally that increasing the $POCl_3$: NEt_3 ratios from 1.2: 3 → 2.4: 6 resulted in better yields. The synthesis of the bi-isocyanide **29**, however, was met with complications during work-up: a slurry emulsion was formed during extraction which resulted in the formation of brownish gel (Figure 14).

Figure 14. Formation of gel upon isolation of isocyanide **29.**

This could be attributed to a self-polymerization of **29**, which is able to form a crosslinked network and incorporate water due to the hydrophilic oligoethylene glycol chains. The characterization of the isocyanides **28** and **29** are shown in the experimental section.

5.2.3. The Passerini Multicomponent Reaction

We then proceeded to carry out the Passerini multicomponent reaction (MCR) for the formation of light-responsive polymers and hydrogels. Two different syntheses were performed in order to validate the scope of the synthetic method:

1) Synthesis of polymers *via* Passerini MCR (one-step)
2) Synthesis of hydrogels
    - *via* Passerini MCR (one-step)
    - *via* Passerini MCR + click reaction (two-steps)

5.2.3.1. Polymer synthesis

We first attempted the one-step Passerini MCR for the synthesis of light-responsive polymers containing a photolabile group. Initially, this group was meant to be the chromophore **17** (PMNB-CHO), however, since this compound was not able to be synthesized, commercially available aldehydes **32a-b** were instead used to fulfill the synthetic purpose.

The MCR was carried out by mixing the corresponding aldehyde with the carboxylic acid 4-arm-PEG-CO_2H **33** (10 kDa) and the isocyanide **27** in organic solvent in a 10:1:10 ratio, respectively, which points excess of both the

aldehyde and the isocyanide. The mixture was left to stir for 24h at room temperature and the resulting polymers **34a-b** were obtained (Scheme 13).

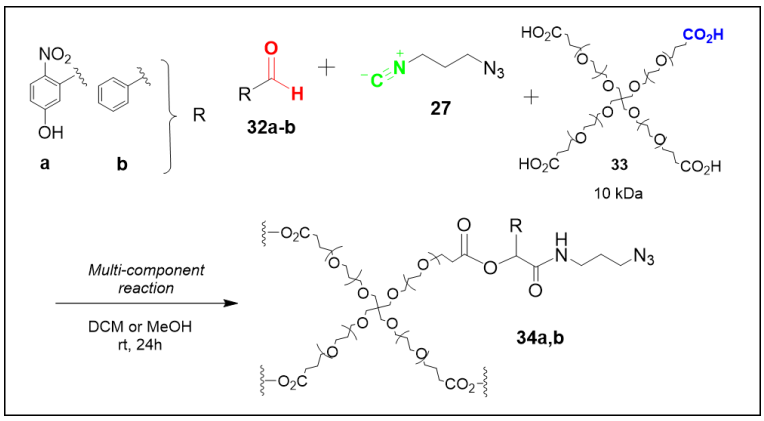

Scheme 13. Syntheses of polymers **34a-b** *via* Passerini MCR.

The reaction mechanism of the Passerini MCR proceeds first by protonation of the aldehyde **32** by the carboxylic acid followed by nucleophilic addition of the isocyanide **27** to give the nitrilium ion **35**. Attack of carboxylate gives intermediate **36**, which undergoes acyl group transfer and amide tautomerization and gives the desired polymer **34** (Scheme 14).

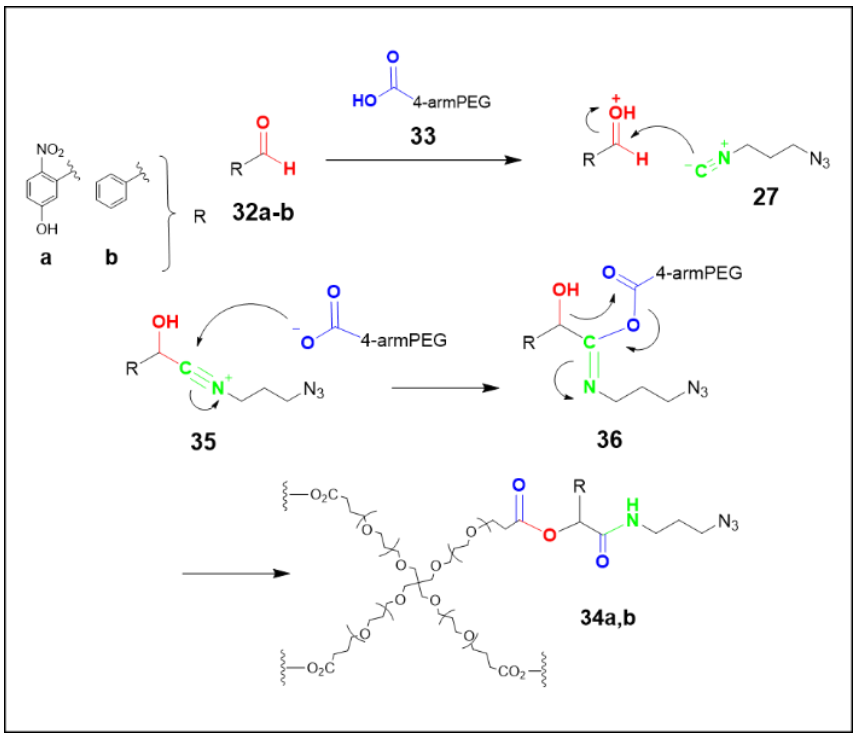

Scheme 14. Reaction mechanism for the synthesis of polymers **34a-b** *via* Passerini MCR.

For the nitroaldehyde **32a**, the reaction was carried out in MeOH (**¡Error! La autoreferencia al marcador no es válida.**, entry 1) whereas for benzaldehyde **32b** it was performed in DCM (**¡Error! La autoreferencia al marcador no es válida.**, entry 2) due the difference in solubilities between both aldehydes.

Table 2. Syntheses of polymers **34a-b** *via* Passerini MCR.

Entry[a]	R	Substrate	Product	Solvent	Purification
1	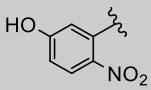	**32a**	**34a**	MeOH	Precipitation
2		**32b**	**34b**	DCM	Dialysis

[a]T = room temp, t = 24h, vol solvent = 1 ml, 4-arm-PEG-CO_2H content = 5%, monomer ratio **32: 33: 27 =** 10: 1: 10

In fact, these differences in solubility also determined the treatments used to isolate the resulting polymers **34a** and **34b** from their corresponding unreacted monomers.

For the isolation of **34a**, a precipitation technique was used. This was carried out by pouring the reaction crude into cold ether, where the polymer is insoluble and precipitates, whereas the reactants remain in solution. The precipitate is then centrifuged and the supernatant removed, along with the unreacted monomers in solution. The compound is then redissolved in a minimum amount of methanol (MeOH) and the process is repeated. After centrifugation and drying overnight, the polymer **34a** was obtained (Figure 15).

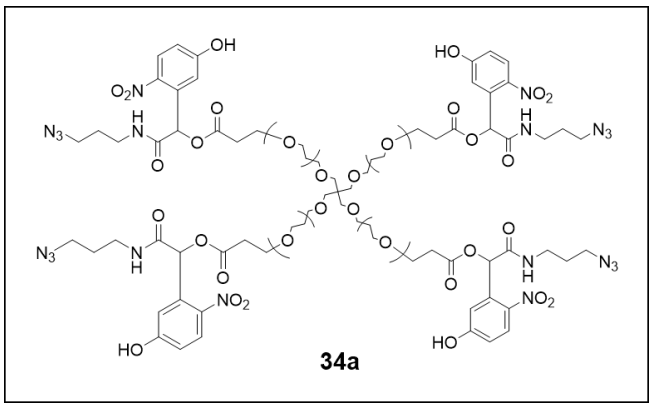

Figure 15. Structure of MCR polymer **34a**.

For the isolation of the polymer **34b**, a dialysis method was followed. The mixture is placed inside a dialysis membrane of 3kDa cutoff weight, through which the polymer is unable to fit whereas the reactants are filtered. The membrane was then dialyzed three times: in acetone, in acetone: water 50: 50 and finally in water in order to freeze-dry the solution and afford the isolated polymer **34b** (Figure 16).

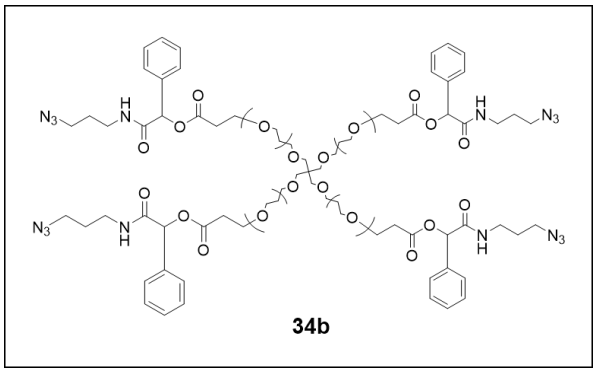

Figure 16. Structure of MCR polymer **34b**.

The characterization of **34a-b** was difficult to ascertain using ^{1}H-NMR and so FT-IR spectra instead proved more useful. Figure 17 shows the overlaid spectra of isocyanide **27** and its corresponding MCR polymer **34a.**

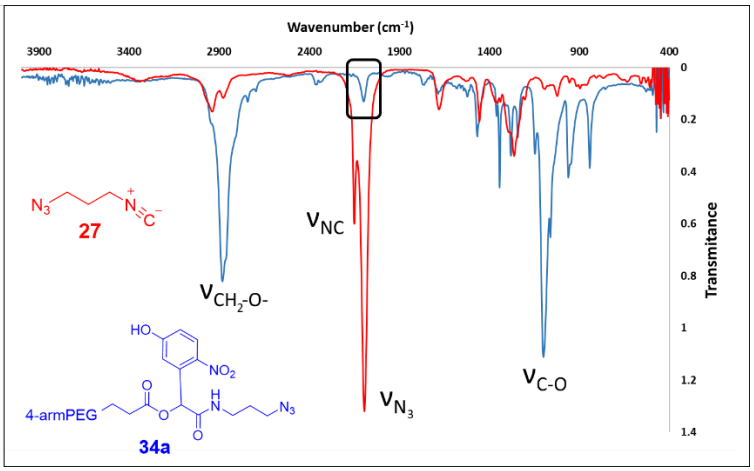

Figure 17. Overlaid FT-IR spectra of compounds **27** and **34a.**

It is observed that the spectrum of the polymer preserves the N_3 band whereas the NC vibration disappears, thus confirming the incorporation of **27** into the polymer backbone. The presence of the PEG backbone of **33** in the

polymer **34a** is further confirmed with the intense C-O and -CH_2-O- stretching vibrations. The FT-IR spectra of **34b** is shown in the experimental section.

Finally, in order to aim for the Passerini *in situ* polymer synthesis under biocompatible conditions, the possibility to perform the MCR reaction in water instead of an organic solvent was considered. Thus, a solubility test in water between the isocyanides **27-29** was performed (Figure 18).

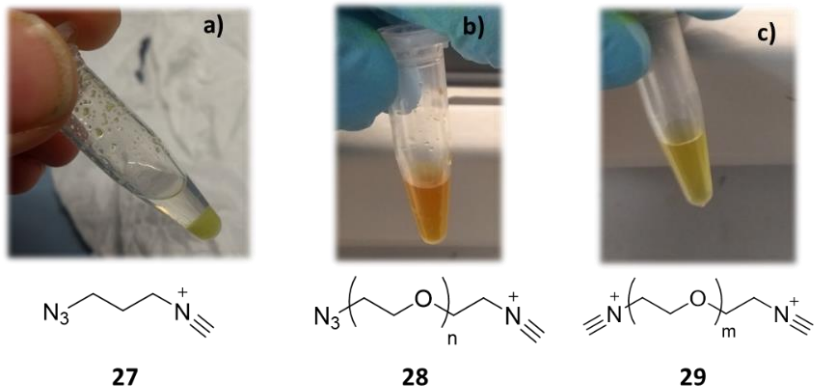

Figure 18. Water solubility tests for isocyanides a) **27** b) **28** and c) **29.**

The results showed that the short-chain isocyanide **27** is insoluble in water, whereas PEG-based isocyanides **28** and **29** were both water-soluble. This allowed expanding the scope of the Passerini MCR method to aqueous media for future *in vivo* applications.

5.2.3.2. Hydrogel synthesis

We next focused in the fabrication of hydrogels. In the first approach, we attempted the straightforward synthesis of hydrogels *via* the Passerini MCR in a one-step procedure.

Commercially available PEG-dialdehyde **37** (2 kDa) and 4-arm PEG-CO_2H **33** were used as the aldehyde and carboxylic acid counterparts, respectively; here, the dialdehyde **37** acts as the crosslinker agent. Further, compound **27** was chosen as the isocyanide moiety.

The carboxylic acid **33** is first dissolved in DCM, followed by addition of **37** and **27**, after which the solution adopts a brownish color. The mixture is then left to stir at room temperature for 5 days until gelation of **38** is observed (Scheme 15).

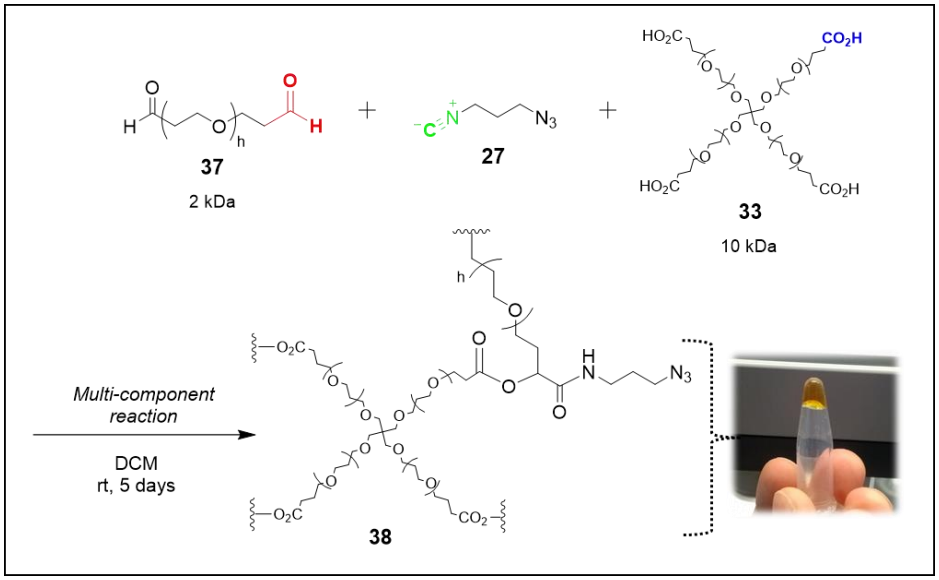

Scheme 15. Synthesis of hydrogel **38** *via* Passerini MCR.

The first attempt for the synthesis of **38** used water as a solvent and with a mass polymer content of 4-arm-PEG-CO_2H of 5% w/w with respect to the total mass of solvent. The monomer ratio for **37: 33: 27** (aldehyde: carboxylic acid: isocyanide) was kept at 1: 2: 2.8, respectively, which points stoichiometric conditions for **37** and **33** and slight excess of **27**. Under these conditions, however, no gelation occurred due to the insolubility of **27** in water (Table 3, entry 1).

Table 3. Synthesis of hydrogel **38** *via* Passerini MCR.

Entry[a]	Solvent	Monomer ratio 37: 33: 27	4-arm-PEG-CO_2H content (%)	Observations
1	Water	1: 2: 2.8	5	**27** insoluble in water
2	DCM	1: 2: 2.8	5	No gelation
3	DCM	1: 2: 2.8	20	No gelation
4	DCM	1: 2: 5.4	20	Gelation of **38**

[a]T = room temp, t = 5 days, vol solvent = 1 ml

The following experiments were thus performed in DCM, both at 5% 4-arm-PEG-CO_2H content (Table 3, entry 2) and at 20% 4-arm-PEG-CO_2H content (Table 3, entry 3), in order to increase the mass ratio of polymer relative to solvent and facilitate gelation. However, none of the experiments afforded the desired hydrogel.

We next decided to increase the excess of isocyanide **27**, increasing the **37: 33: 27** (aldehyde: carboxylic acid: isocyanide) monomer ratio from 1: 2: 2,8 → 1: 2: 5,4 (Table 3, entry 4). The mixture appeared a viscous substance for the first 48h, until it formed a gel after 5 days (Figure 19).

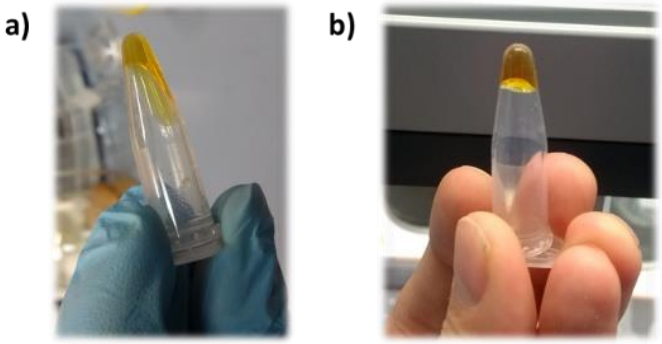

Figure 19. Gelation of **38** a) after 2 days b) after 5 days.

In a second approach, we attempted to synthesize light-responsive hydrogels by means of crosslinking between the polymer **34a** and a suitable alkyne *via* copper-free click chemistry.

Such reaction was performed in PBS medium, by simply mixing the MCR polymer and the dibenzocycloctyne (DBCO) alkyne **39** (20 kDa), which rapidly undergoes click reaction *via* strain-promoted 1,3-dipolar cycloaddition with the azide group of **34a** (Scheme 16).

Immediately after mixing the components, **40** was formed, indicating the effectiveness of the click reaction (Table 4, entry 1). In order to adapt the synthesis of this hydrogel for conditions *in vivo* in the presence of cells, we tried to increase the gelation times of the hydrogel. Upon decreasing the polymer content down to 10% → 2.5% w/w, the hydrogel fully formed after 5 h (Table 4, entry 2). Finally, we attempted to pour water into the Eppendorf vial inside which **40** was synthesized and the gel was observed to incorporate the solvent, thus confirming its capacity to swell in water.

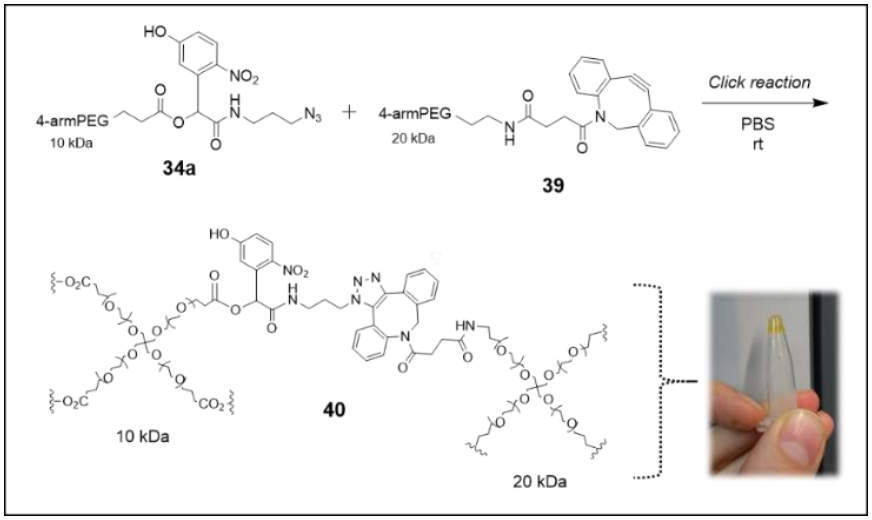

Scheme 16. Strain-promoted click reaction for the synthesis of hydrogel **40.**

Table 4. Synthesis of **40** *via* click reaction.

Entry[a]	4-arm-PEG-DBCO content (%)	Gelation time of 40
1	10%	1-5 s
2	2.5%	~ 5 h

[a]T = room temp, volume = 1 ml PBS, monomer ratio **34a: 39** = 1: 1

The results observed in this study pointed that the Passerini MCR was a straightforward and useful methodology for the fabrication of smart hydrogels responsive to light stimuli. However, by substitution of the light responsive chromophore with another chemical functionality, the scope of this procedure may expand to the fabrication of a wide variety of stimuli-responsive polymers and hydrogels synthesized in a facile *one-pot* process.

5.3. References

[1] P. Schmittinger, *Chlorine Princ. Ind. Pract.* 2007, *324*, 11–17.

[2] C. A. DeForest, K. S. Anseth, *Nat. Chem.* 2011, *3*, 925–931.

[3] J. You, A. Haque, D. S. Shin, K. J. Son, C. Siltanen, A. Revzin, *Adv. Funct. Mater.* 2015, *25*, 4650–4656.

[4] D. R. Griffin, J. L. Schlosser, S. F. Lam, T. H. Nguyen, H. D. Maynard, A. M. Kasko, *Biomacromolecules* 2013, *14*, 1199–1207.

[5] I. Tomatsu, K. Peng, A. Kros, *Adv. Drug Deliv. Rev.* 2011, *63*, 1257–1266.

[6] K. Peng, I. Tomatsu, B. Van Den Broek, C. Cui, A. V. Korobko, J. Van Noort, A. H. Meijer, H. P. Spaink, A. Kros, *Soft Matter* 2011, *7*, 4881–4887.

[7] V. X. Truong, F. Li, J. S. Forsythe, *ACS Appl. Mater. Interfaces* 2017, *9*, 32441–32445.

[8] A. Dömling, W. Wang, K. Wang, *Chem. Rev.* 2012, *112*, 3083–3135.

[9] W. A. Velema, B. L. Feringa, *Angew. Chem.* 2014, *126*, 8826–8830.

[10] L. Li, A. Lv, X. X. Deng, F. S. Du, Z. C. Li, *Chem. Commun.* 2013, *49*, 8549–8551.

[11] X. X. Deng, L. Li, Z. L. Li, A. Lv, F. S. Du, Z. C. Li, *ACS Macro Lett.* 2012, *1*, 1300–1303.

[12] A. Specht, F. Bolze, L. Donato, C. Herbivo, S. Charon, D. Warther, S. Gug, J. F. Nicoud, M. Goeldner, *Photochem. Photobiol. Sci.* 2012, *11*, 578–586.

[13] S. Piant, F. Bolze, A. Specht, *Opt. Mater. Express* 2016, *6*, 1679.

[14] A. Farrukh, J. I. Paez, A. del Campo, *Adv. Funct. Mater.* 2019, *29*, 1–11.

[15] *Novel Benzamide Derivatives as Modulators of the Follicle Stimulating Hormone*, 2008, Bonnet, B., Campo, B., Raveglia, I.Ricaboni, M. USA. Application. No. WO 2008/117175 A2.

[16] *Indole Antagonists of P2Y1 Receptor Useful in the Treatment of Thrombotic Conditions*, n.d., LAM, Patrick, CLARK, Charles G. USA. Application. No. WO 2008/048981 A2.

[17] V. X. Truong, F. Li, J. S. Forsythe, *ACS Appl. Mater. Interfaces* 2017, *9*, 32441–32445.

[18] S. Brauch, M. Henze, B. Osswald, K. Naumann, L. A. Wessjohann, S. S. Van Berkel, B. Westermann, *Org. Biomol. Chem.* 2012, *10*, 958–965.

[19] A. V. Gulevich, L. S. Koroleva, O. V. Morozova, V. N. Bakhvalova, V. N. Silnikov, V. G. Nenajdenko, *Beilstein J. Org. Chem.* 2011, *7*, 1135–1140.

Chapter 6

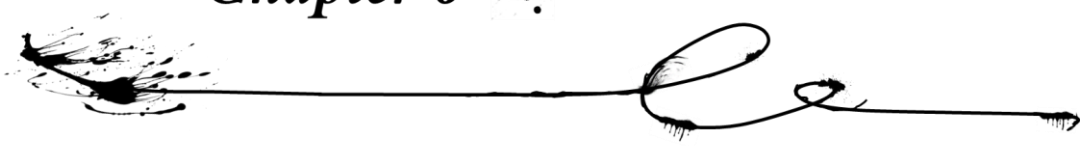

Experimental Section

6.1. Materials

All reagents were purchased from chemical companies as reagent-grade materials and used as received.

Sigma-Aldrich: Oligo(ethylene glycol) methyl ether methacrylate (OEGMA, M_n = 950), acrylamide (AM), *N,N'*-methylenebis(acrylamide) (MBA), potassium peroxydisulfate (KPS), metronidazole (MZ), ibuprofen (IB), epichlorohydrin, sodium disulfide, melamine, iron chloride (II) 98% anhydrous, phosphate buffered saline (PBS, pH = 7.4), Dess-Martin periodinane (DMP), *N*-methylmorpholine (NMO), tetrapropylammonium perruthenate (TPAP), 1-azido-3-aminopropane, poly(ethylene glycol) (PEG) diamine (M_n = 2000), phosphorus oxychloride ($POCl_3$), triethylamine (NEt_3), sodium thiosulfate, potassium carbonate, ethyl formate, benzaldehyde, O-(2-Aminoethyl)-O'-(2-azidoethyl)nonaethyleneglycol (M_w = 536.62) and 5-hydroxy-2-nitrobenzaldehyde.

TCI chemicals: Benzocaine (BZ), naproxen (NX), imipramine (IMI) hydrochloride, retinoic acid (RA) and 2,4-diamino-6-[2-(2-methyl-1-imidazolyl)ethyl]-1,3,5-triazine.

Fluka: Rhodamine 101 (RHO).

Panreac: Ammonia solution (30%).

Across: Iron chloride (III) 98% anhydrous.

JenKem technologies: 4-arm-PEG-CO_2H (M_n = 10 kDa), PEG-dialdehyde (M_n = 2 kDa) and 4-arm-PEG-DBCO (M_n = 20 kDa).

AimanGZ: Neodymium magnets (N35 grade, 4250 G).

Bay Carbon Inc: Graphite powder (SP-1 reference).

Simulated Gastric Fluid (SGF, pH = 1.2) was prepared from a 0.063M solution of HCl.

6.2. Monomer syntheses and characterization

^{1}H-NMR and ^{13}C-NMR spectra were measured at 298K in a Bruker Advanced Neo 400 (400 MHz).

ESI-MS spectra were recorded using a QTos Ultima 3.

HPLC analysis and purification of the compounds was performed with a HPLC JASCO 4000 (Japan) equipped with a diode array UV-Vis detector and fraction collector.

FT-IR spectra were measured in a IRAffinity-1S Shimadzu spectrophotometer.

UV/VIS Spectra were recorded with a Varian Cary 4000 UV/VIS spectrometer.

6.2.1. Triazine synthesis

6-vinyl-2,4-diamino-1,3,5-triazine, 4

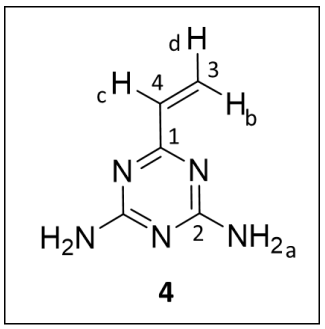

4

The synthesis of VDAT was carried out according a patented procedure.[1] In a typical procedure, 2,4 diamino-6-[2-(2-methyl-1-imidazolyl)ethyl]-1,3,5-triazine **5** (0.17 mol, 37.5 g) was suspended in 75 mL deionized water with stirring. Epichlorohydrin **6** (0.17 mol, 13.4 ml) and sodium disulfide ($1.7x10^{-3}$ mol, 400 mg) were added and the mixture was heated under reflux for 3h. The crude product was filtered off and washed with 250 mL of cold water. The product was filtered under vacuum and dried in a desiccator to give a pure colorless solid (12.3 g, 54%).

^{1}H-NMR (DMSO-d_6, 400 MHz): 6.67 ppm (s, 4H, Ha), 6.4 ppm (dd, ^{1}H, *J* = 17.3 Hz, 1H, Hb), 6.3 ppm (dd, ^{1}H, *J* = 17.3 Hz, 1H, Hc) 5.62 ppm (dd, ^{1}H, *J* = 10.1 Hz, 1H, Hd).
^{13}C-NMR (DMSO-d_6, 400 MHz): 170 ppm (C1), 167.2 ppm (C2), 136.7 ppm (C3), 123.8 ppm (C4).
IR (cm^{-1}): 3310, 3142,1640,1511,1424, 958, 830.

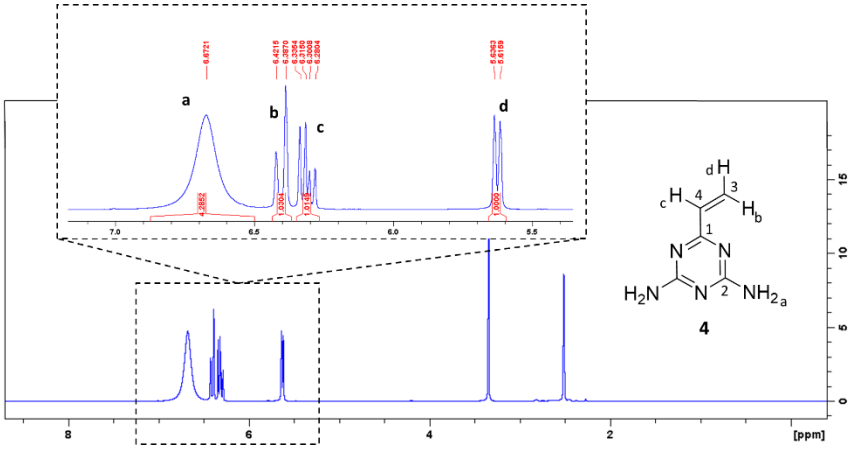

Figure S1. ^{1}H-NMR (DMSO-d_6, 400 MHz) of the VDAT monomer **4**.

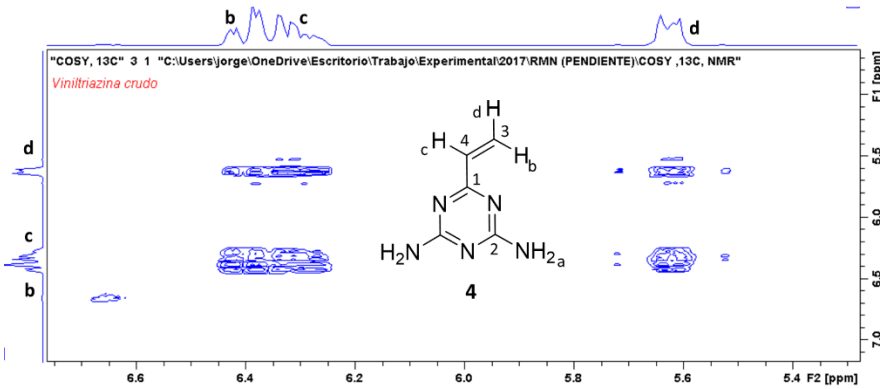

Figure S2. ^{1}H -NMR COSY (DMSO-d_6, 400 MHz) of the VDAT monomer **4**.

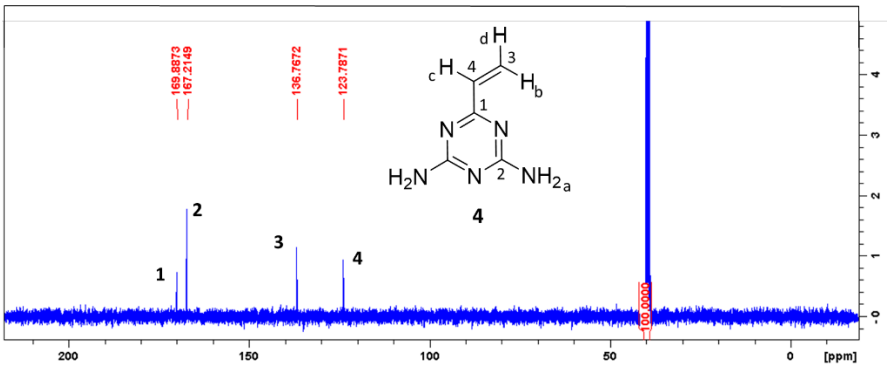

Figure S3. ^{13}C-NMR (DMSO-d_6, 400 MHz) of the VDAT monomer **4**.

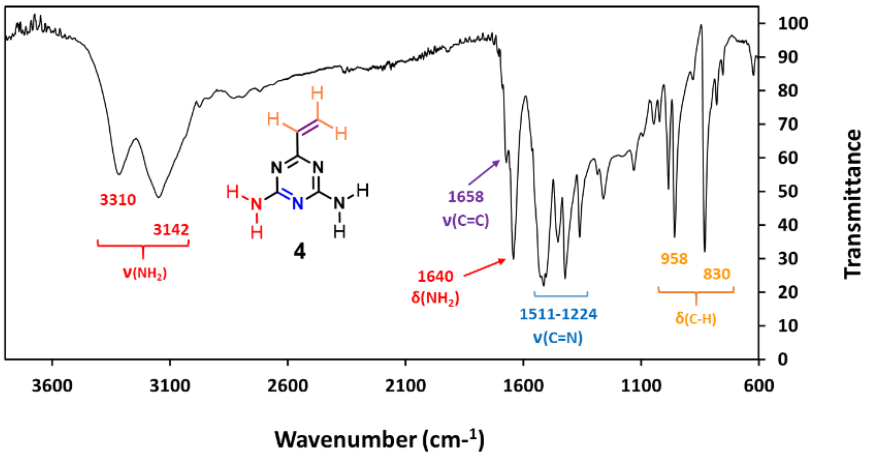

Figure S4. FT-IR characterization of VDAT monomer **4**.

2,4-bis(N-allylamino)-6-chloro-1,3,5-triazine, 12

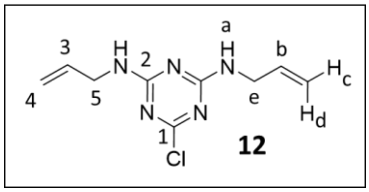

To a 50 ml solution under stirring and in an ice bath, a solution of cyanuric chloride **3** (4.99 mmol, 0.92 g) in 10 ml THF is added. Then, allylamine **11** (16 mmol, 1.2 ml) is added dropwise, followed by DIPEA (10.33, 1.8 ml). The reaction is left to stir at room temperature for 24h. THF is then evaporated, yielding a pale yellow solid. 50 ml water are added and the whitish solid is washed under vacuum. The process is repeated 3 times and the washed solid is dried in a dissicator for 24h. A pure solid is obtained (0.92 g, 82%).

^{1}H-NMR (DMSO-d_6, 400 MHz): 6.37 ppm (s, 2H, Ha); 5.85 ppm (ddt, *J* = 5, 10, 15.5 Hz, 2H, Hb); 5.14 ppm (dd, *J* = 1.5, 17 Hz, 2H, Hc); 5.05 ppm (dd, *J* = 1, 10 Hz, 2H, Hd); 3.85 ppm (m, 4H, He).
^{13}C-NMR (DMSO-d_6, 400 MHz): 168 ppm, (C1); 164.5 ppm (C2); 134.5 ppm (C3); 114.7 ppm (C4); 42.3 ppm (C5).

2,4,6-tris(N-allylamino)-1,3,5-triazine, 13

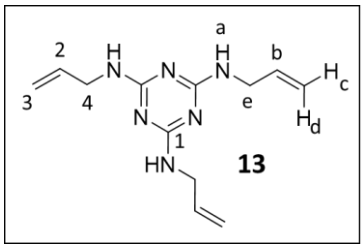

To 100 ml THF, cyanuric chloride **3** (50.4 mmol, 9.3 g) is added under ice. Allylamine **11** (300 mmol, 20 ml) is then added dropwise, followed by diisopropylethylenediamine (DIPEA) (91.8 mmol, 16 ml). The dispersion is then stirred and left for 96h at room temperature. The solvent is evaporated and 100 ml water are added, followed by formation of an orange

dispersion, which is neutralized with HCl cc. The precipitate is filtered, washed with water and dried in dissicator for 48h. A pure solid is obtained (9.2 g, 84%).

^{1}H-NMR (DMSO-d_6, 400 MHz): 6.65 ppm (m, 3H, Ha); 5.84 ppm (ddt, *J* = 5.5, 11, 15.5 Hz, 3H, Hb); 5.10 ppm (dd, *J* = 1.5, 17, 3H, Hc); 4.99 ppm (dd, *J* = 1, 10, 3H, Hd); 3.81 ppm (t, *J* = 5.5 Hz, 6H, He).
^{13}C-NMR (DMSO-d_6, 400 MHz): 165.7 ppm (C1); 136.5 ppm (C2); 114.5 ppm (C3); 42.3 ppm (C4).

6-(4-vinylphenyl)-2,4-diamino-1,3,5-triazine, 15

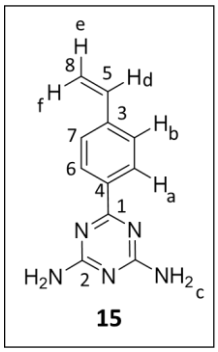

15

In a 25 mL two-necked flask, KOH (1.5 mmol, 99 mg) and methanol (6 mL) were placed. To a methanolic solution (6 ml) of KOH (1.5 mmol, 99 mg) in a 25 ml two-necked flask, cyanoguanidine **1** (7.5 mmol, 630.5 mg) was added under stirring. 4-cyanostyrene **14** (7.5 mmol, 1.017 g) is then added and the mixture is heated at 53 °C during 72 h. The crude is washed with cold ethanol (3 x 5 mL), filtered off and a white pure solid is obtained (1,13 g ,71%).

^{1}H-RMN (DMSO-d_6, 500 MHz): 8.23 ppm (d, *J* = 8.3 Hz, 2H, Ha), 7.56 ppm (d, *J* = 8.3 Hz, 2H, Hb), 6.75-6.82 ppm (m, 5H, Hc and Hd), 5.93 ppm (d, *J* = 18.1 Hz, 1H, He), 5.35 ppm (d, *J* = 11.2 Hz, 1H, Hf).
^{13}C-RMN (500 MHz, DMSO): 169.8 ppm (C1), 167.4 ppm (C2), 139.6 ppm (C3), 136.6 ppm (C4), 136.2 ppm (C5), 128.0 ppm (C6), 125.9 ppm (C7), 115.7 ppm (C8).

6.2.2. Aldehyde synthesis

p-methoxynitrobiphenyl aldehyde, 18

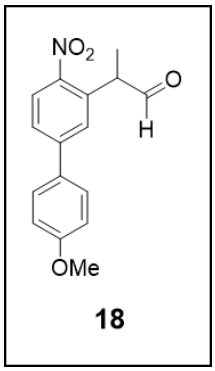

18

Via **Dess-Martin Oxidation:** To a solution of PMNB-OH **17** (10 mg, 0.035 mmol) in dry DCM (1 ml) was added Dess-Martin periodinane (DMP) (14.8 mg, 0.035 mmol, 1 eq) in 1 ml DCM. The resulting mixture was stirred overnight. The reaction was then diluted in DCM and washed with saturated sodium thiosulfate (2 ml) and then with sodium bicarbonate (2 ml). The organic layers were collected and dried over sodium sulfate, filtered and evaporated to dryness. The crude

was then purified either by column chromatography (Hex: AcOEt / 90: 10) or preparative HPLC (50B-95B 60 min 360 nm). TLC (Hex: AcOEt / 75: 25) R_f = 0.65.

Via **Ley-Griffith oxidation:** PMNB-OH **17** (10 mg, 0.035 mmol) and *N*-methylmorpholine *N*-oxide (NMO) (5.31 mg, 0.0525 mmol, 1.5 eq) were dissolved in dry DCM (2 ml) and transferred to a purged flask with molecular sieves (20 mg). Tetrapropylammonium perruthenate (TPAP) (0.003 mmol, 0.09 eq) in dry DCM (1 ml) is added and left to stir overnight. The crude was filtered through a silica pad, evaporated and purified by column chromatography (Hex/AcOEt 90:10). TLC (Hex/AcOEt 75:25) R_f = 0.65.

6.2.3. Isocyanide synthesis

6.2.3.1. Amine formylation

General procedure: the corresponding amine was dissolved in ethylformate (6 ml) and the solution was heated to reflux (54ºC). After 24h, the solution was concentrated under reduced pressure to give a pure product which was used directly in the next step.

_N_-(3-azidopropyl)formamide, 24

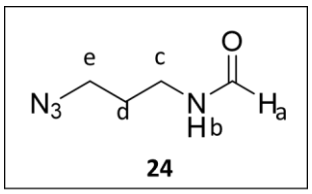

24

Prepared from 1-azido-3-aminopropane **21** (1.29 g, 12.9 mmol). The formamide **24** was obtained as a colorless liquid (1.63 g, 99%).

^{1}H-NMR ($CDCl_3$, 400 MHz): 8.01 ppm (m, 1H, Ha), 6.26 ppm (m, 1H, Hb), 3.35 ppm (m, 4H, Hc and He), 1.77 ppm (q, *J* = 6.56 Hz, 2H, Hd).
IR (cm^{-1}): 3280, 2091, 1655.
QTOF$^+$: [M+K+H]/Z= 168.13.

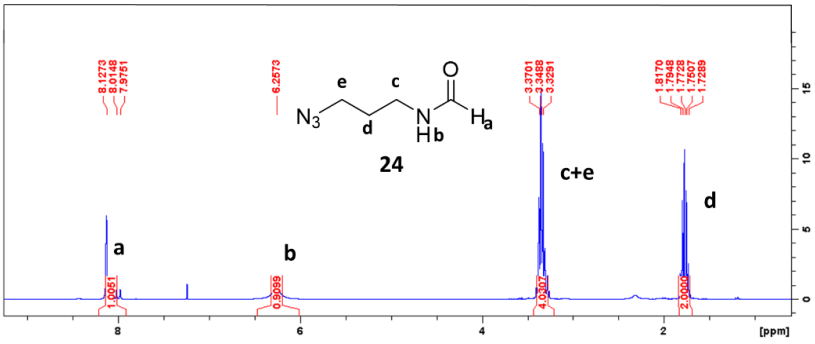

Figure S5. ^{1}H-NMR ($CDCl_3$, 400 MHz) spectrum of formamide **24**.

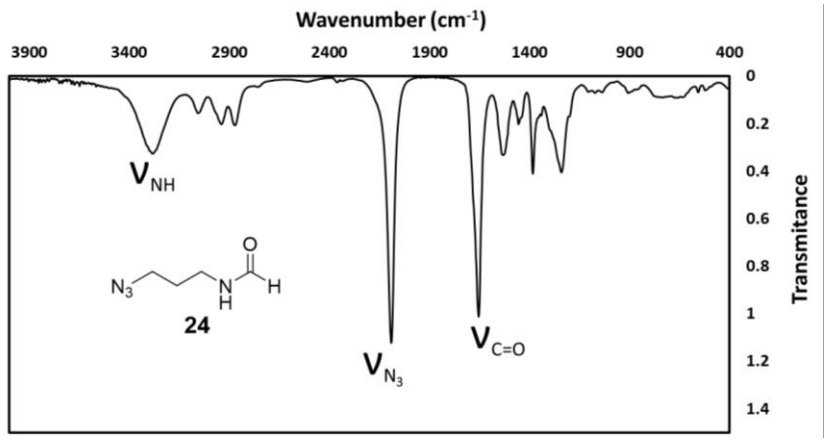

Figure S6. IR spectrum of formamide **24**.

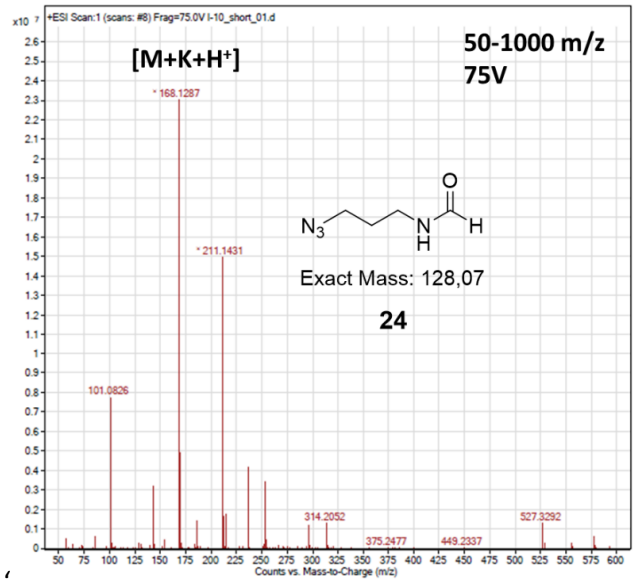

Figure S7. Mass-QTOF spectrum of formamide **24**.

Azido-PEG formamide, 25

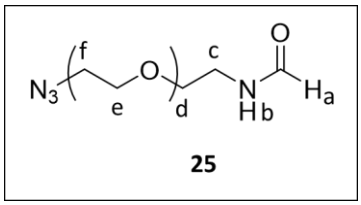

Prepared from O-(2-Aminoethyl)-O′-(2-azidoethyl)nonaethylene glycol **22** (0.585 g, 1.11 mmol). The formamide **25** was obtained as a brownish oil (0.61 g, 99%).

^{1}H-NMR ($CDCl_3$, 400 MHz): 8.01 ppm (m, 1H, Ha), 6.80 ppm (s,1H, Hb), 3.60 ppm (m, 37H, Hd, He and Hf), 3.44 ppm (m, 2H, Hc).
IR (cm^{-1}): 2866, 2100, 1674, 1092.
QTOF$^+$: [M+H]/Z= 555.33.

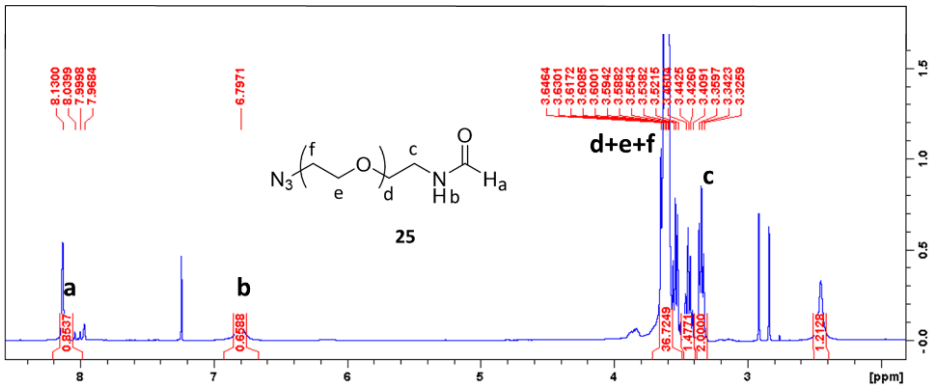

Figure S8. ^{1}H-NMR ($CDCl_3$, 400 MHz) spectrum of formamide **25.**

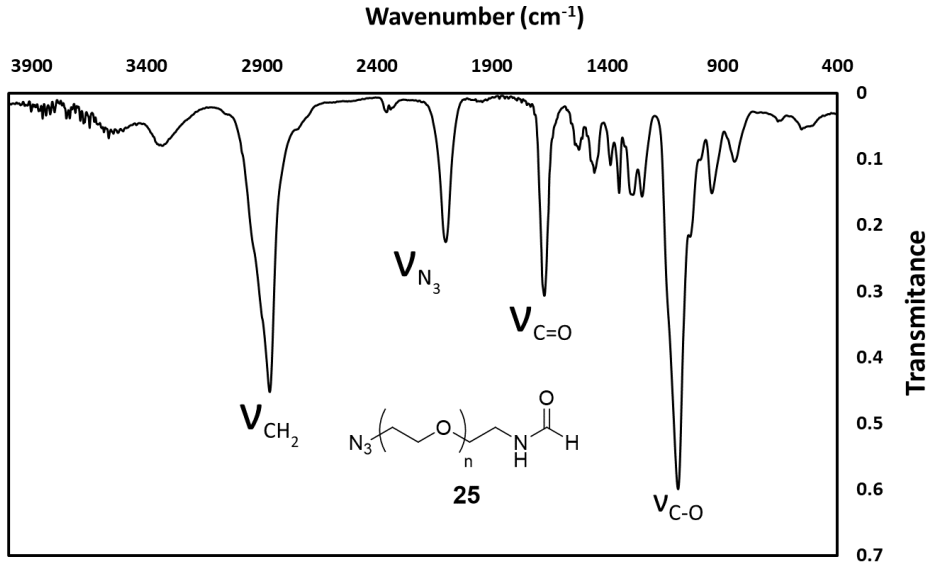

Figure S9. IR spectrum of formamide **25.**

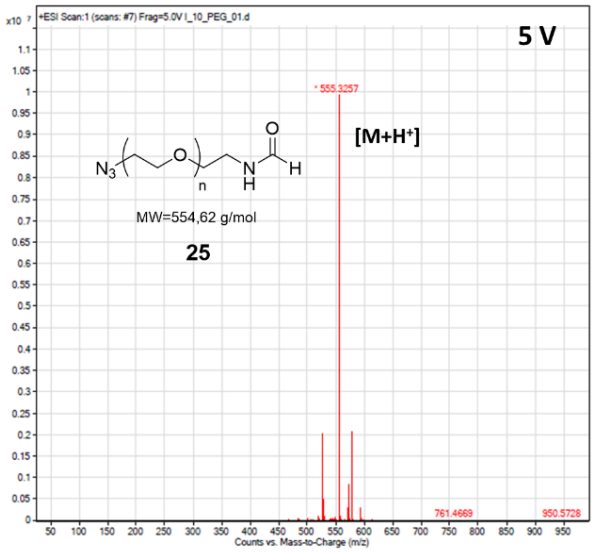

Figure S10. Mass-QTOF spectrum of formamide **25**.

PEG diformamide, 26

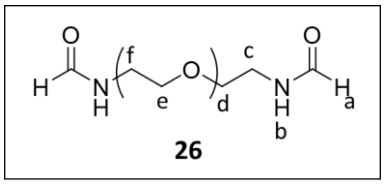

Prepared from PEG diamine **23** (0.64 g, 0.32 mmol). The formamide **26** was obtained as a pale-brown solid (0.64 g, 97%).

^{1}H-NMR ($CDCl_3$, 400 MHz): 8.06 ppm (m, 2H, Ha), 6.63 ppm (s, 2H, Hb), 3.44 ppm (m, 207H, Hc, Hd, He and Hf).
IR (cm^{-1}): 2872, 1676, 1092.
QTOF$^+$: [M]/3: 720.77, [M]/2: 1050.13.

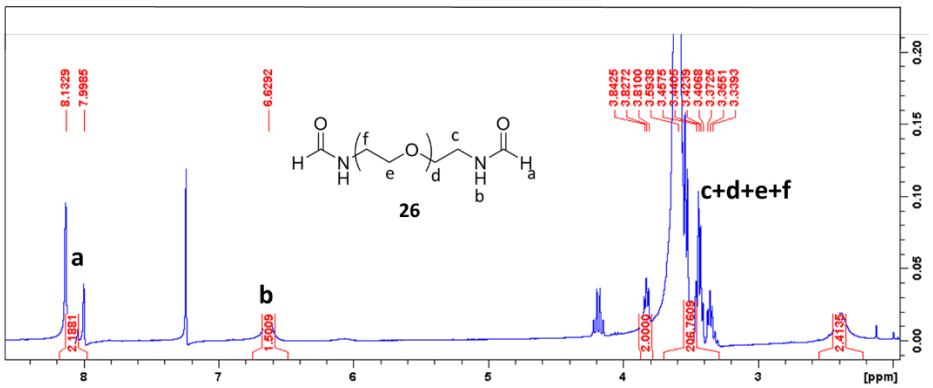

Figure S11. ^{1}H-NMR ($CDCl_3$, 400 MHz) spectrum of formamide **26.**

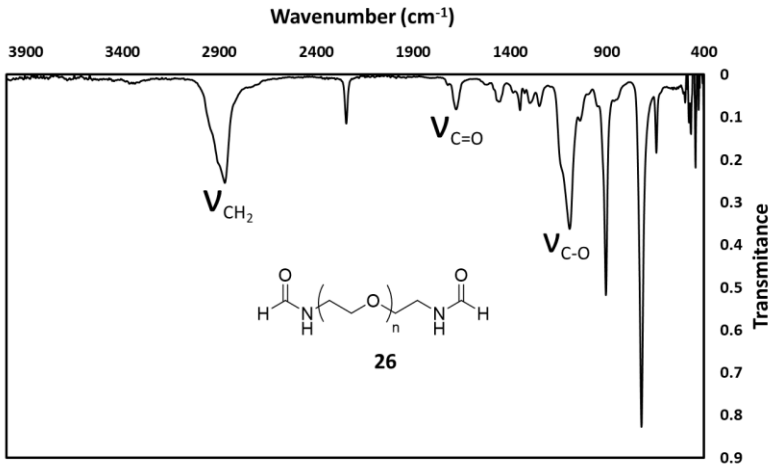

Figure S12. IR spectrum of formamide 26.

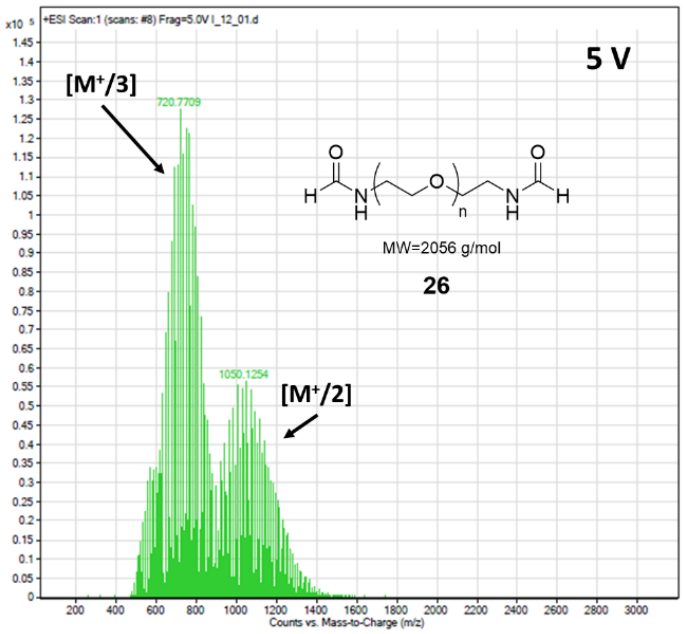

Figure S13. Mass-QTOF spectrum of formamide 26.

6.2.3.2. Amide dehydration

General procedure: the corresponding formamide was placed under nitrogen atmosphere and dissolved in dry dichloromethane. Triethylamine was added and the reaction mixture was cooled in an ice bath. Phosphorus oxychloride was then added dropwise and the reaction mixture was warmed to room temperature and left to stir overnight. The reaction was then poured over

a potassium carbonate solution under an ice bath. The resulting suspension was stirred for 2-3h and the organic layer was separated. The aqueous phase was extracted with ethyl acetate, the combined organic layers dried over K_2CO_3 and the organic solvent evaporated *in vacuo*.

N-(3-azidopropyl)isocyanide, 27

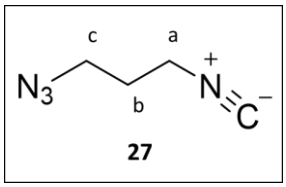

Prepared from *N*-(3-azidopropyl)formamide **24** (0.81 g, 6.34 mmol) in dry dichloromethane (12 ml). Triethylamine (2.65 ml, 19.02 mmol, 3 eq) was added, followed by phosphorus oxychloride ($POCl_3$) (7.1 ml, 7.61 mmol, 1.2 eq) as explained above. After addition of $POCl_3$ the colorless solution turns yellow until next day, where the resulting solution is brown. The reaction was then poured over a potassium carbonate solution (30 ml, 0.2 gr/ml), separated and extracted with ethyl acetate (2x 30 ml). The isocyanide **27** was obtained as a brown liquid with strong foul odor (0.57 g, 81%).

^{1}H-NMR ($CDCl_3$, 400 MHz): 3.49 ppm (t, *J* = 6.34 Hz, 4H, Ha and Hc), 1.89 ppm (m, 2H, Hb).
IR (cm^{-1}): 2149, 2093.
QTOF$^+$: [M+K]/Z = 150.11.

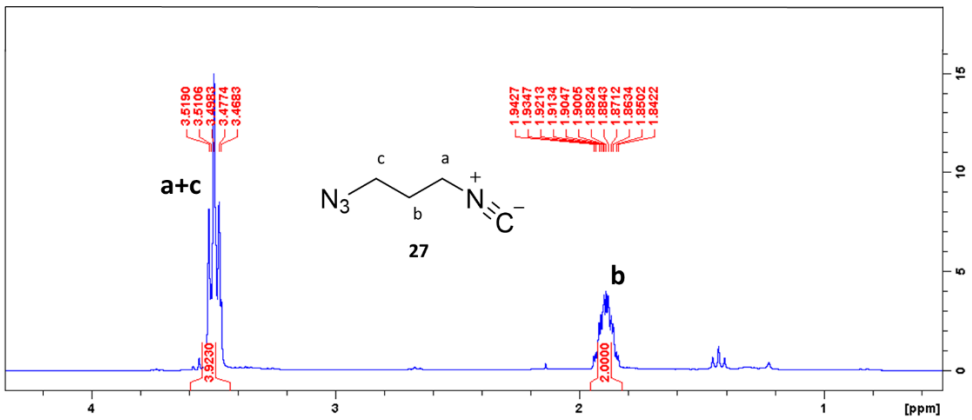

Figure S14. ^{1}H-NMR ($CDCl_3$, 400 MHz) spectrum of isocyanide **27.**

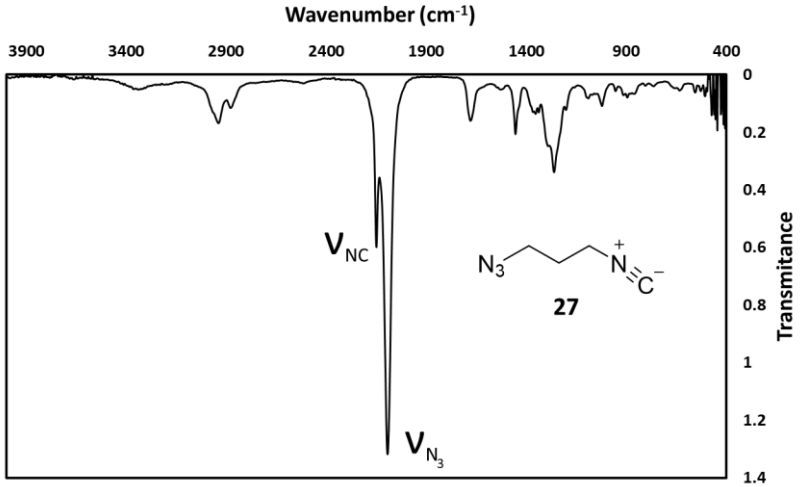

Figure S15. IR spectrum of isocyanide 27.

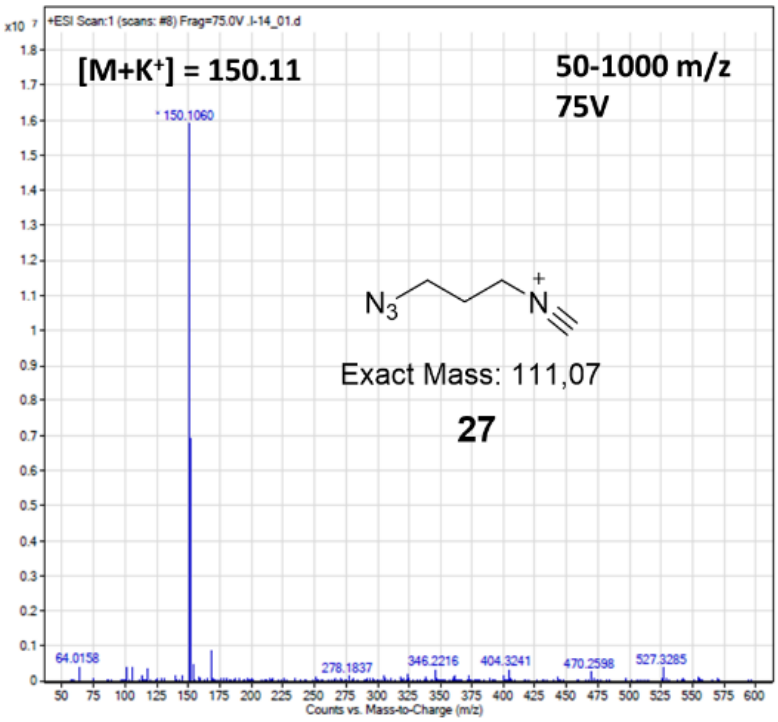

Figure S16. QTOF-Mass spectrum of isocyanide 27.

Azido-PEG isocyanide, 28

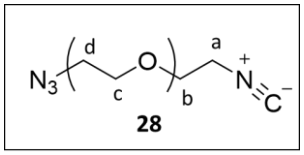

Prepared from azido-PEG formamide **25** (0.45 g, 0.82 mmol) in dry dichloromethane (2 ml). Triethylamine (0.68 ml, 4.92 mmol, 6 eq) was added, followed by phosphorus oxychloride (1.84 ml, 1.97 mmol, 2.4 eq) as explained above. After addition of $POCl_3$ the colorless solution turns yellow until next day, where the resulting solution is brown. The change in color is however slower than for **27**. The reaction was then poured over a potassium carbonate solution (5 ml, 0.2 gr/ml), separated and extracted with ethyl acetate (2x 10 ml). The isocyanide **28** was obtained as a brown oil with mild foul odor (0.33 g, 76 %).

^{1}H-NMR ($CDCl_3$, 400 MHz): 3.60 ppm (m, 40H, Hb, Hc and Hd), 3.35 ppm (t, *J* = 4.96 Hz, 2H, Ha).
IR (cm^{-1}): 2866, 2151, 2100, 1096.
QTOF$^+$: $[M+NH_4^+]/Z$ = 554.34.

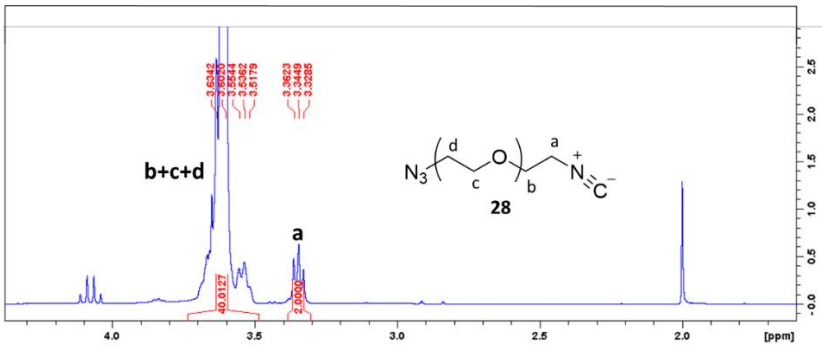

Figure S17. ^{1}H-NMR ($CDCl_3$, 400 MHz) spectrum of isocyanide **28.**

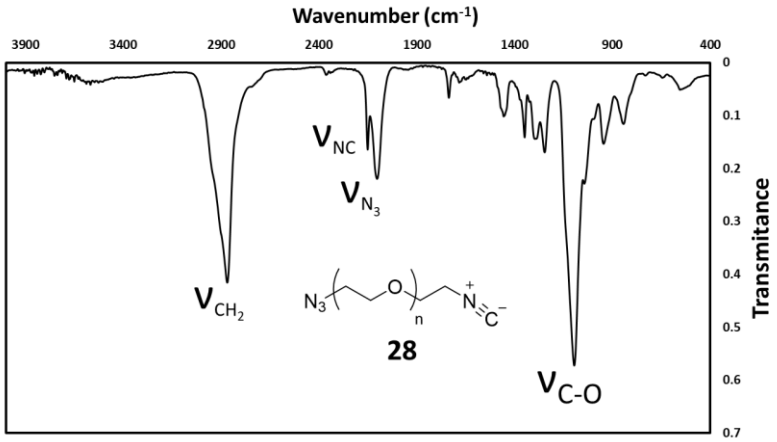

Figure S18. IR spectrum of isocyanide **28.**

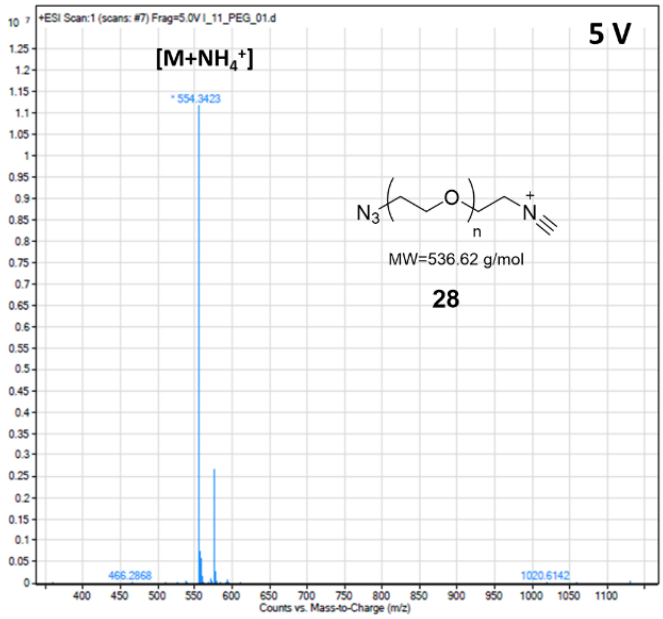

Figure S19. QTOF-Mass spectrum of isocyanide **28.**

PEG di-isocyanide, 29

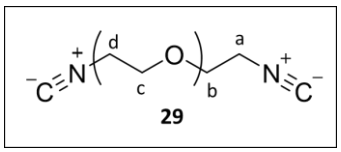

Prepared from PEG diformamide **26** (1.36 g, 0.66 mmol) in dry dichloromethane (12 ml). Triethylamine (0.55 ml, 3.96 mmol, 6 eq) was added, followed by phosphorus oxychloride (1.47 ml, 1.58 mmol, 2.4 eq) as explained above. After addition of $POCl_3$ the colorless solution turns yellow, changing from light orange to dark wine red and finally to a dark brown suspension at the next day. The reaction was then poured over a potassium carbonate solution (60 ml, 0.2 gr/ml) under an ice bath. Immediately after addition, a brown precipitate appears at the bottom of the aqueous phase. The resulting suspension was stirred for 2-3h and the organic layer was separated. The extraction of aqueous phase was problematic since it formed a single phase, especially when extracted with DCM. For this reason, the organic phase was evaporated without extraction. The isocyanide **29** was obtained as a brown solid with mild foul odor.

^{1}H-NMR ($CDCl_3$, 400 MHz): 3.59 ppm (m, 736 H, Hb, Hc and Hd), 3.35 ppm (t, *J* = 4.55 Hz, 4H, Ha).
IR (cm^{-1}): 2883, 2152, 1103.
QTOF$^+$: [M]/3: 749.47, [M]/2: 1049.14.

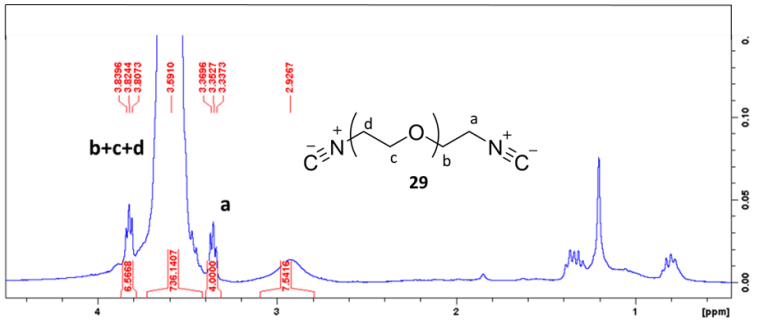

Figure S20. ^{1}H-NMR ($CDCl_3$, 400 MHz) spectrum of isocyanide **29**.

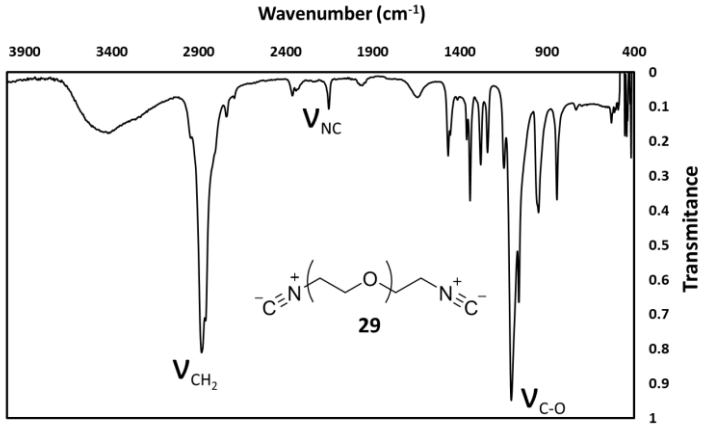

Figure S21. IR spectrum of isocyanide **29**.

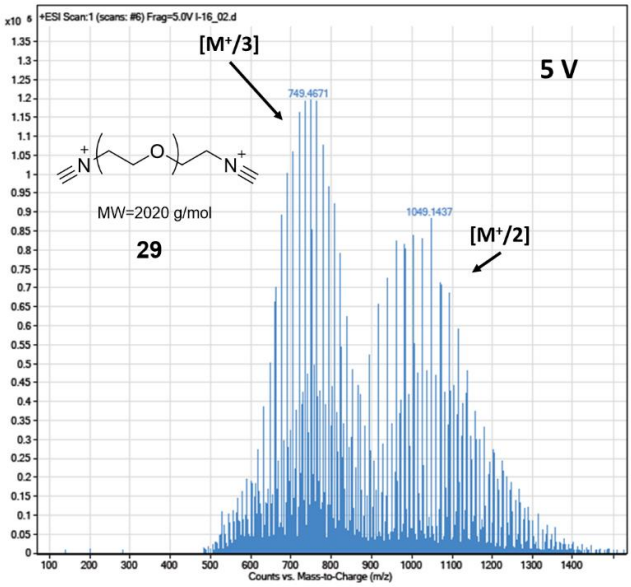

Figure S22. QTOF-Mass spectrum of isocyanide **29**.

6.3. Nanomaterial syntheses and characterization

6.3.1. Synthesis of few-layer graphene

The mechanochemical exfoliation of graphite was performed by following a ball-milling procedure.[2,3] A 30 mg mixture of graphite/melamine (1:3) was ball-milled at 100 rpm for 30 min. The solid was then dispersed and sonicated in 20 ml of ultrapure water; the dispersion was placed in dialysis tubing (Spectrum labs, 6–8 kDa MWCO) and dialyzed against hot water (70 ºC), with the aqueous medium replaced every 2 hours until melamine was no longer detected. The dispersion was then left to stabilize for five days and the aggregated graphite was removed from the dispersion. The graphene aqueous suspension was freeze-dried at -80ºC and 0.05 mbar and the resulting few-layer graphene powders were collected and characterized.

6.3.2. Synthesis of magnetite nanoparticles

Blending method: a 0.2M $FeCl_2$ and 0.1M $FeCl_3$ solution at a 1:4 Fe(II)/Fe(III) ratio in 2M HCl was stirred and then 1g of glycine was added. The solution was alkalinized with NaOH 5M dropwise until pH reached 10, where the SPIONs precipitated. The precipitate was washed several times with DI water and recollected. Further glycine (3g) was added to complete adhesion process and the suspension was sonicated for 30 min. The SPIONs were then washed with ethanol to remove excess glycine and the suspension was centrifuged to obtain the purified nanoparticles.

6.3.3. Characterization

TGA measurements were carried out on a Q50 system from TA instruments at 10 ºC/min under an N_2 atmosphere. The Raman spectra were obtained on an InVia Renishaw microspectrophotometer with a 532 nm point-based laser. The samples were prepared by dropping graphene aqueous dispersions onto silicon oxide surfaces (WRS materials). The resulting spectra were collected by probing different random locations on the sample and applying baseline corrections, noise filtering and normalization. In order to determine the band parameters (widths, normalized intensities and positions) the spectra were fitted with Lorentzian-based bands. Transmission Electron Microscopy (TEM) and High Resolution TEM (HRTEM) were carried out on a Jeol 2100 HRTEM system. The nickel grid was immersed (LC200-Ni Lacey Carbon Grid from Electron Microscopy Sciences) into the graphene aqueous dispersions. SQUID

measurements were carried out in a superconducting quantum interference device (SQUID) from Quantum Design (Ever Cool), with a maximum magnetic field H of +/- 2.5T and a lowest magnetization range of 10^{-6} emu. The magnetic hysteresis loops were carried out at room temperature, from 0 to H_{max}, H_{max} to -H_{max} and -H_{max} to H_{max}.

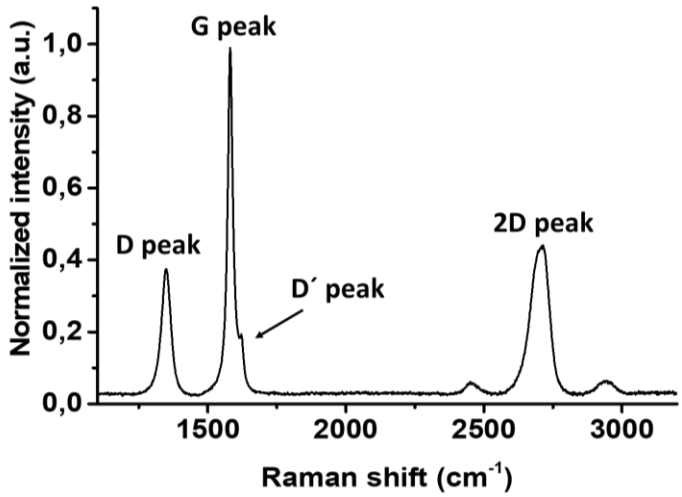

Figure S23. Raman spectrum of few-layer graphene.

Table 1. Elemental analysis of few-layer graphene.

	C (%)	H (%)	O (%)	N (%)
	95.66 ± 0.04	0.51 ± 0.04	3.11 ± 0.08	0.56 ± 0.02

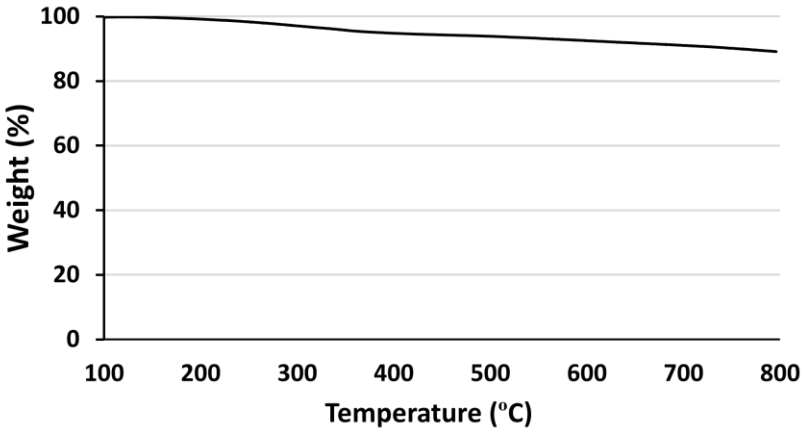

Figure S24. TGA analysis of few-layer graphene.

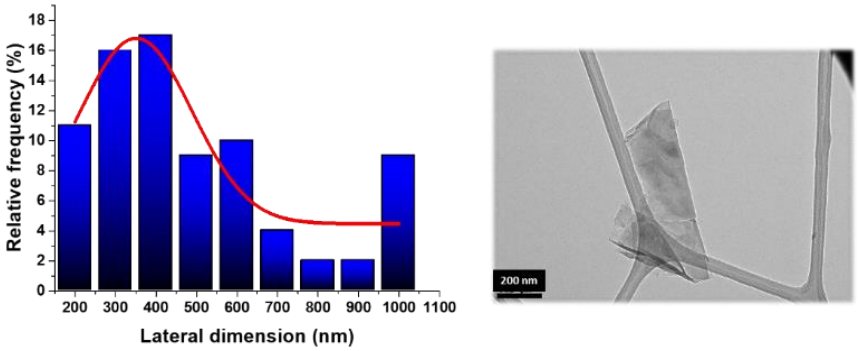

Figure S25. TEM characterization: Lateral size distribution (left) and TEM representative image (right).

6.4. Hydrogel synthesis

6.4.1. *Via* radical polymerization

General procedure: in a typical procedure, the appropriate triazine monomer, oligo(ethylene glycol) methyl ether methacrylate (OEGMA) (135 mg/ml), acrylamide (AAm) (135 mg/ml), chemical crosslinker and potassium peroxydisulfate (KPS) initiator were dissolved in 2 ml DMSO at room temperature. The mixture was then sonicated prior to casting into pre-heated cylindrical silicon molds (1 cm × 0.7 cm) and placed in an oven at 70 ºC for 15 min. The resultant organogels were washed thoroughly in 600 ml deionized water, which was replaced twice a day for 4 days, until all DMSO had been phase-inverted and all unreacted monomer was washed out. The removal of unreacted monomers was monitored by UV/VIS spectroscopy. The fully washed and swollen hydrogels were dried in an oven until all water had been removed and dry xerogels were obtained.

Figure S26. Silicon molds used for the synthesis of the hydrogels.

6.4.1.1. Chemically-crosslinked hydrogels

a) Pristine hydrogels

TzOA-M-6: prepared from 6-vinyl-2,4-diamino-1,3,5-triazine (**4**) (150 mg/ml), crosslinker *N,N´*-methylenebis(acrylamide) (MBA) (2 mg/ml) and KPS (2 mg/ml).
TzOA-P-1: prepared from 6-vinyl-2,4-diamino-1,3,5-triazine (**4**) (150 mg/ml), crosslinker poly(ethylene glycol) diacrylate (PEGDA) (2 mg/ml) and KPS (2 mg/ml).
Tz_1OA-M: prepared from 2,4-bis(N-allylamino)-6-chloro-1,3,5-triazine (**12**) (30 mg/ml), crosslinker MBA (2 mg/ml) and KPS (2 mg/ml).

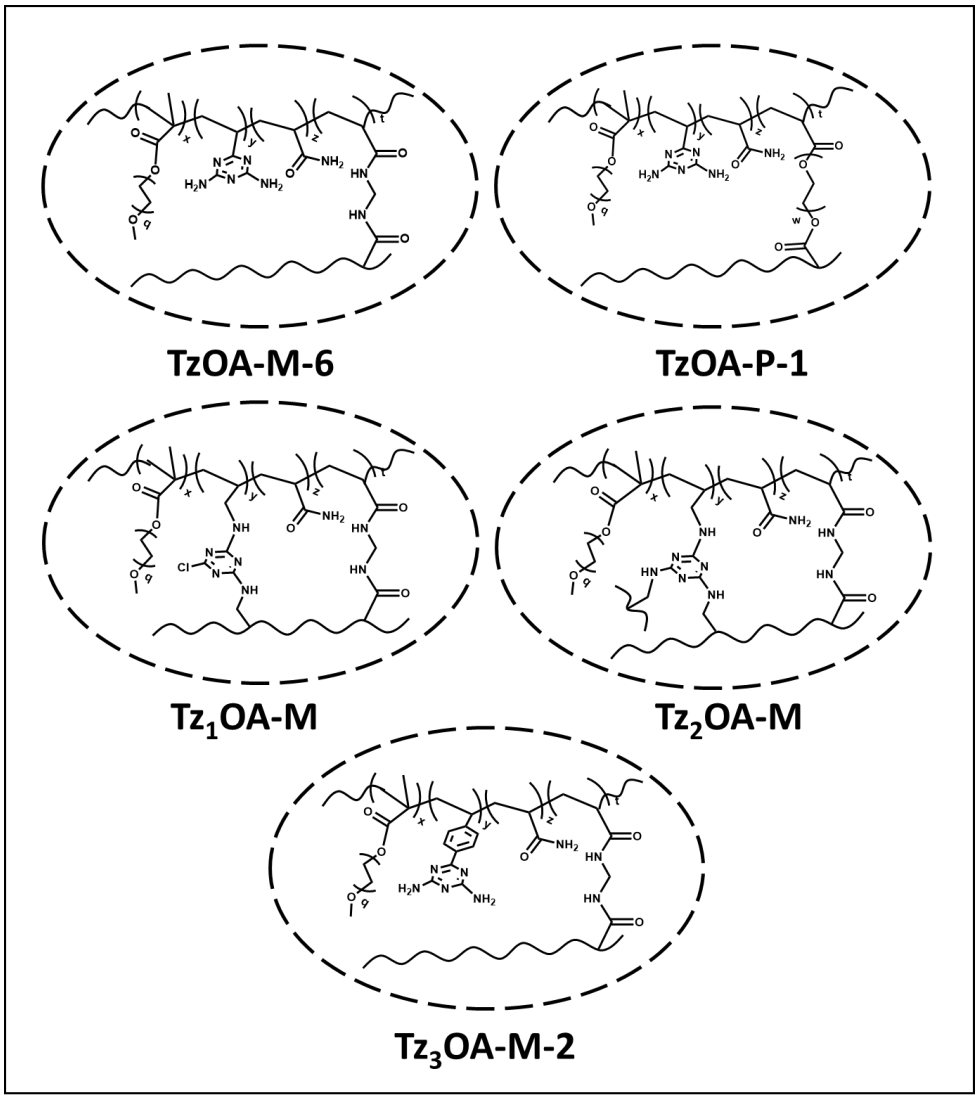

Figure S27. Chemically-crosslinked hydrogels.

Tz_2OA-M: prepared from 2,4,6-tris(N-allylamino)-1,3,5-triazine (**13**) (30 mg/ml), crosslinker MBA (2 mg/ml) and KPS (2 mg/ml).
Tz_3OA-M-2: prepared from 6-(4-vinylphenyl)-2,4-diamino-1,3,5-triazine (**15**) (30 mg/ml), crosslinker MBA (2 mg/ml) and KPS (8 mg/ml). For these hydrogels, the polymerization was carried out for 30 min instead.

b) Graphene hybrid hydrogels

Prepared from 6-vinyl-2,4-diamino-1,3,5-triazine (**4**) (150 mg/ml), crosslinker MBA (2 mg/ml) and KPS (2 mg/ml), dissolved in few-layer graphene (FLG)/DMSO dispersions.

$G_{0.1}$-TzOA-M-6: prepared from 0.42 mg/ml (0.1% w/w content) FLG/DMSO.
$G_{0.5}$-TzOA-M-6: prepared from 2.1 mg/ml (0.5% w/w content) FLG/DMSO.

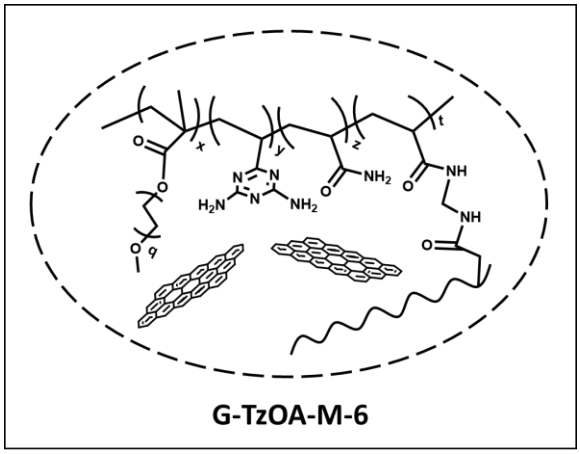

Figure S28. Graphene hybrid hydrogels.

c) Magnetite hybrid hydrogels

Blending method: Prepared from 6-vinyl-2,4-diamino-1,3,5-triazine (**4**) (150 mg/ml), crosslinker PEGDA (2 mg/ml) and KPS (2 mg/ml) dissolved in superparamagnetic iron oxide nanoparticles (SPIONs)/DMSO dispersions.

Mag_2-TzOA-P-1: prepared from 2 mg/ml (SPIONs)/DMSO.
Mag_4-TzOA-P-1: prepared from 4 mg/ml SPION/DMSO.

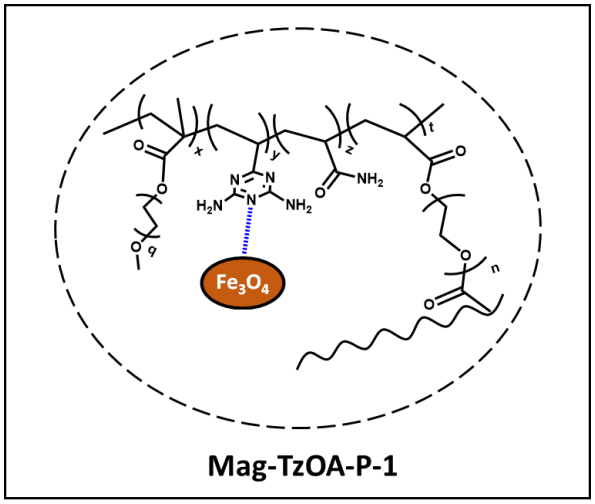

Figure S29. Magnetite hybrid hydrogels (blending method).

6.4.1.2. Physically-crosslinked hydrogels

a) Pristine hydrogels

TzOA-0: prepared from 6-vinyl-2,4-diamino-1,3,5-triazine (**4**) (150 mg/ml) and KPS (2 mg/ml). No crosslinker was added.

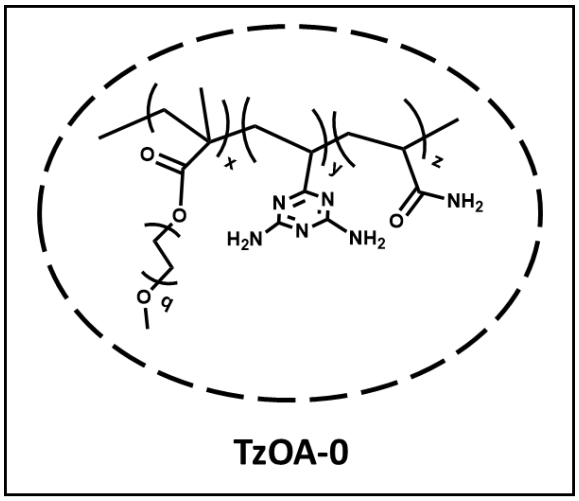

Figure S30. Physically-crosslinked hydrogels.

b) Magnetite hybrid hydrogels

In situ co-precipitation method: the hydrogels were prepared in a two-step procedure. First, fully formed, dried **TzOA-0** xerogel samples were immersed in

7 ml $FeCl_3/FeCl_2$ solutions in a 2:1 molar ratio (0.1M/0.05M and 0.5M/0.25M solutions for **$Fe_{0.05}$-TzOA-0** and **$Fe_{0.25}$-TzOA-0** hydrogels, respectively) for 5 days until maximum swelling. Further, iron-loaded **Fe-TzOA-0** hydrogels were immersed in a 0.5M ammonia solution (pH = 11.7) after which superparamagnetic iron oxide nanoparticles (SPIONs) immediately started *co*-precipitating inside the hydrogels. After 48h, the magnetic hydrogels were washed in water for two days, until no excess of black magnetite precipitates were observed in the rinsing solution. The washed and swollen magnetic hydrogels were then dried until xerogel state for further use.

$Mag_{0.05}$-TzOA-0: prepared from immersing **$Fe_{0.05}$-TzOA-0** hydrogels in ammonia, followed by the rest of the treatments.
$Mag_{0.25}$-TzOA-0: prepared from immersing **$Fe_{0.25}$-TzOA-0** hydrogels in ammonia, followed by the rest of the treatments.

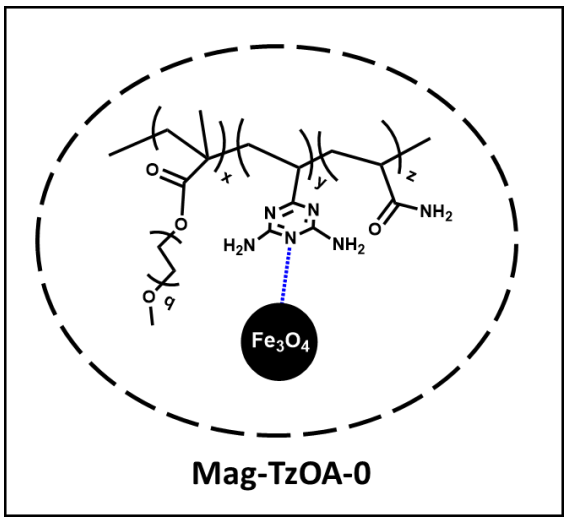

Figure S31. Magnetite hybrid hydrogels (*in situ* co-precipitation method).

6.4.2. *Via* Passerini Multicomponent Reaction

6.4.2.1. Polymer synthesis

***General procedure**: to* carboxylic acid **33** (50 mg, 0.02 mol) dissolved in organic solvent (0.5 ml) was added the appropiate aldehyde **32** (0.2 mmol, 10 eq) dissolved in 0.25 ml under stirring. A solution of isocyanide **27** (0.2 mmol, 10 eq) in 0.25 ml was then added and left to stir overnight (addition of the

isocyanide changes the color to light brown). 4-arm-PEG-CO_2H (**33**) polymer content = 5%.

Passerini MCR polymer 34a

Prepared from 5-hydroxy-2-nitrobenzaldehyde **32a.** The reaction is carried out in MeOH**.** After 24h, the crude is precipitated in 20 ml cold diethyl ether, centrifuged (10ºC, 4000 rpm, 30 min) and left to dry overnight. **34a** is obtained as a pale-yellow solid.

IR (cm^{-1}): 2881, 2094, 1097.

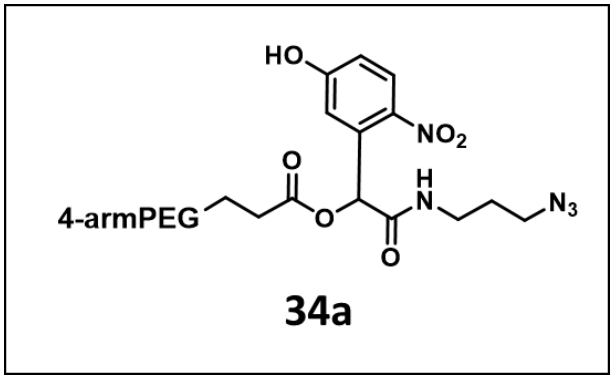

Figure S32. Passerini polymer **34a.**

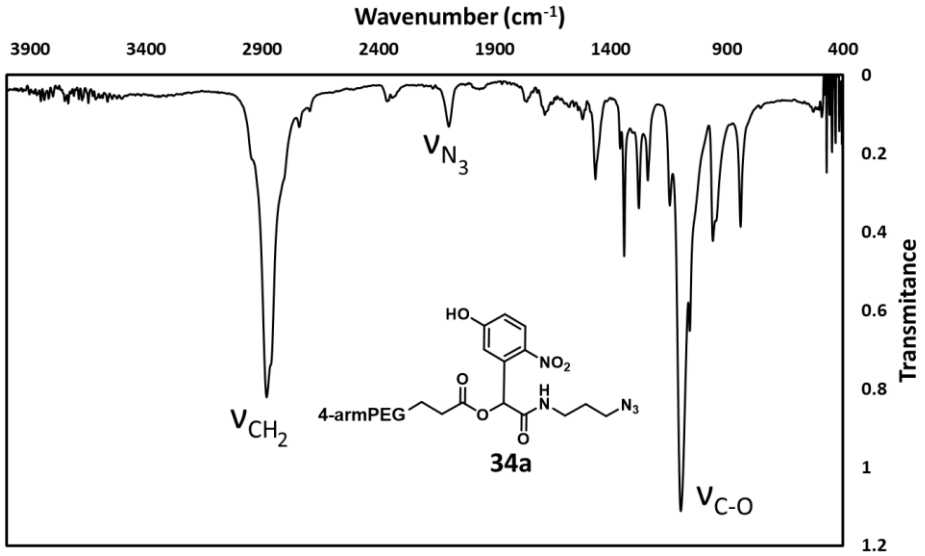

Figure S33. IR spectrum of Passerini polymer **34a.**

Passerini MCR polymer 34b

Prepared from benzaldehyde **32b.** The reaction is carried out in DCM**.** After 24h, the crude is dialyzed in acetone (2x 500 ml), acetone/water (1x 500 ml) and water (2x 500 ml) and freeze-dried all weekend. **34b** is obtained as a pale-yellow solid. FT-IR: ν(CH_2): 2881 cm^{-1} , ν(N_3): 2098 cm^{-1}, ν(C-O): 1095 cm^{-1}.

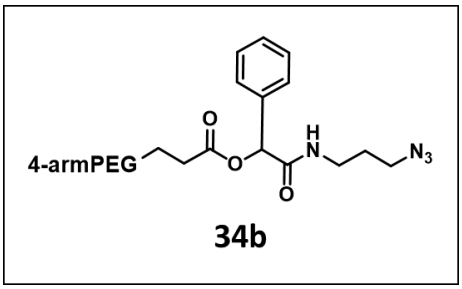

Figure S34. Passerini polymer **34b.**

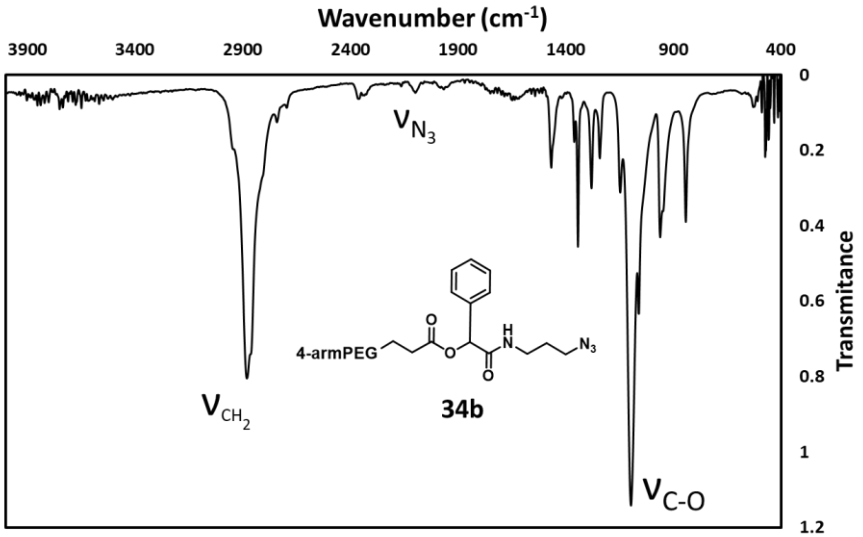

Figure S35. IR spectrum of Passerini polymer **34b.**

6.4.2.2. Hydrogel synthesis

Passerini MCR hydrogel 38

Carboxylic acid **33** (40 mg, 0.016 mmol, 2 eq) is dissolved in DCM (0.1 ml) and PEG-dialdehyde **37** (2kDa) (0.008 mmol, 1 eq) dissolved in 0.05 ml DCM is added. Isocyanide **27** (0.009 mmol, 5.4 eq) dissolved in DCM (0.05 ml) is

finally added and the solution becomes light brown and viscous. The reaction is left in an Eppendorf for 5 days, until gelation is observed. 4-arm-PEG-CO_2H polymer content = 20%.

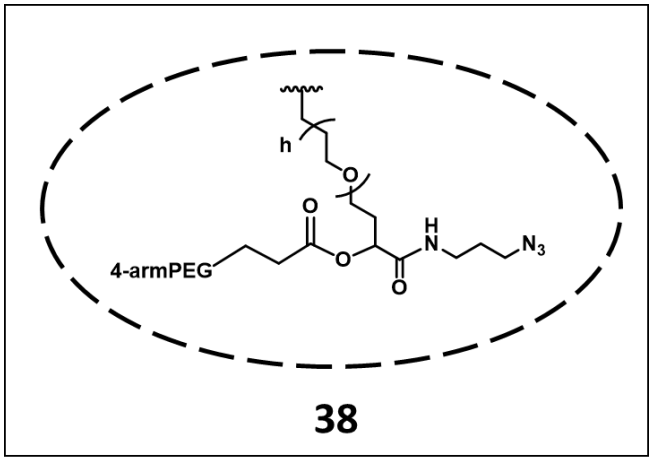

Figure S36. Passerini hydrogel 38.

Passerini MCR hydrogel 40

To a 34a (0.00025 mmol) solution in 25 µl PBS is added 4 arm PEG-DBCO 39 (20 kDa) (0.00025 mmol, 1 eq) in 25 µl PBS. The solution is stirred and slowly after 5 min a viscous solution is observed; full gelation of 40 is observed after 5h. 4 arm PEG-DBCO polymer content = 2.5%.

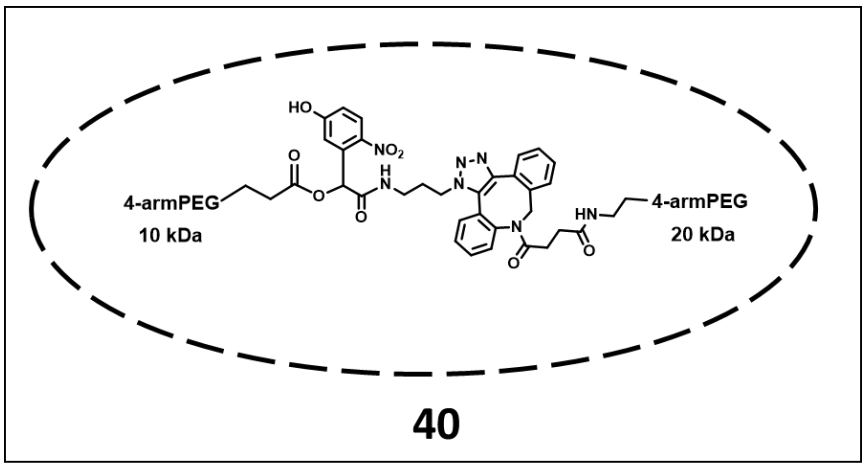

Figure S37. Passerini hydrogel 40.

6.5. Hydrogel characterization

6.5.1. Swelling studies

Swelling studies were performed using a gravimetric method, by immersing dried hydrogel pieces in ultrapure water or SGF medium at room temperature. The samples were initially weighed so that the average initial weights were similar (~7 mg). The weights were recorded at defined time intervals until the hydrogel samples reached a constant weight. Prior to weighing, the samples were placed on filter paper to remove excess water. The swelling degree (SD) was then calculated according to the following equation:

$$SD = \frac{W_t - W_0}{W_0}$$

Where W_0 and W_t are the initial weigh and weight at time t, respectively. Maximum swelling values were calculated by weight subtraction between the hydrogels swollen to their maximum and the corresponding dried xerogels.

For **$Fe_{0.05}$-TzOA-0** and **$Fe_{0.25}$-TzOA-0** hydrogels, the SD values were obtained by weight subtraction between swollen hydrogels in 0.1M/0.05M and 0.5M/0.25M $FeCl_3$/$FeCl_2$ solutions and their corresponding dried xerogels, respectively. Six samples were weighed for each sample.

6.5.2. Scanning Electron Microscopy (SEM)

The samples were prepared by swelling the hydrogels until their maximum swelling state followed by freezing. The samples were then freeze-dried in a Telstar Lyoquest freeze dryer to remove all water from the hydrogel. The porous microstructure of the samples was analyzed by SEM imaging using a Gemini SEM 500 from Zeiss. Freeze-dried samples were placed in a sample-holder and introduced onto the microscope stage for imaging at an accelerating voltage of 2–3 kV. Pore size distributions were obtained by plotting the average pore sizes of several digital images for each sample

6.5.3. Mechanical properties

Compressive and tensile tests were carried out with a Mecmesin Multitest 2.5-i dynamic mechanical analyser. For compressive studies, hydrogel samples (10.7 mm diameter x 6.8 mm height) were uniaxially compressed between two

plates at a rate of 6 mm/min and a cell load of 50 N. Young´s modulus values were recorded in in the strain range between 2-10% relative to the total height of the sample. Fatigue tests were carried out by performing 100 compressive cycles with a rate of 40 mm/min and a 50 N cell load. Tensile test probes were prepared from silicon molds that met the ISO 37 standard. Samples were uniaxially stretched at 60 mm/min with a 50 N cell load until the probe broke. The fracture toughness was calculated from the area under the stress-strain curves. Six samples were measured for each measurement.

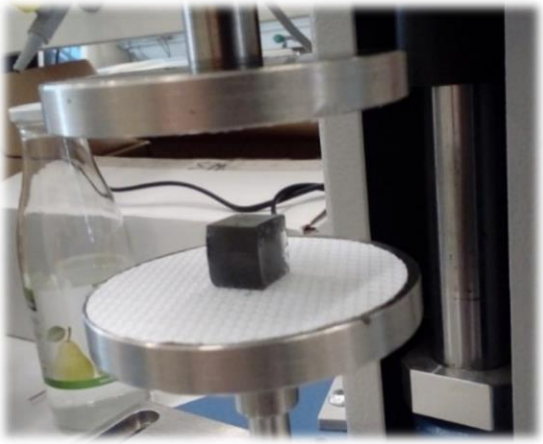

Figure S38. Mechanical compressive tests. Hydrogels are compressed within two plungers and the data is recorded.

6.5.4. Infrared (IR) spectroscopy

Triturated xerogel samples were measured in a FT-IR, IRAffinity-1S Shimadzu spectrophotometer in a 600-4000 cm^{-1} range, and the resulting spectra were normalized. Each sample was measured in duplicate. Polymers were measured either in solid state or dissolved in a concentrated solution in an appropriate solvent.

6.5.5. Thermogravimetric Analysis (TGA)

The fully swollen hydrogels were frozen and lyophilized in a Telstar Lyoquest freeze dryer. The samples were then analyzed on a Q50 system from TA instruments at 10 ºC/min under N_2 or O_2 atmosphere. For density scanning calorimetry (DSC) and mass couplings, a simultaneous DSC-TGA QSeries instrument (SDT Q600) was used, which was coupled to a mass spectrometer for evolved gas analysis (EGA). Each sample was analyzed in triplicate.

6.5.6. Superconducting Quantum Interference Device (SQUID) magnetometry

Swollen hydrogel pieces (5.7 ± 0.9 mg) were analyzed in a superconducting quantum interference device (SQUID) from Quantum Design (Ever Cool), with a maximum magnetic field H of +/- 5T and a lowest magnetization range of 10^{-6} emu. The magnetic hysteresis loops were carried out at room temperature, from 0 to H_{max}, H_{max} to $-H_{max}$ and $-H_{max}$ to H_{max}.

6.5.7. Powder X-Ray Diffraction (PXRD)

Xerogel samples were first grinded to fine grain powders. PXRD data were then recorded on a Philips (Panalytical) model X'Pert MPD diffractometer using Cu KAlpha1 (1.54056 Angstroms) at 40 kV and 40 mA. Diffraction patterns were collected over a range of 0–100° 2θ at a scan rate of 0.01° 2θ min at a scan velocity of 0.004° s^{-1}.

6.5.8. Transmission Electron Microscopy (TEM)

TEM analyses were performed on ethanolic dispersions of fine grinded hydrogel samples previously sonicated for 2 min. Dispersions were then dip-casted on Holey C (EMS) grids until solvent evaporation. The samples were then investigated using a High-Resolution Transmission Electron Microscope (HRTEM) JEOL 2100 at an accelerating voltage of 200 kV. Images were taken with a Gatan Orius (2x2MPi) digital camera under low exposure conditions (low-dose, <5μA) in order to avoid polymer matrix degradation.

6.5.9. Energy Dispersive X-Ray (EDX) spectroscopy

Hydrogel samples were swollen until maximum state followed by freeze-drying. Hydrogels were then sampled by SEM imaging (Gemini SEM 500, Zeiss) with an EDS 80 mm^2 Oxford detector at an accelerating voltage of 10-15 kV. Each sample was measured in triplicate.

6.5.10. Microwave irradiation experiments

All microwave irradiation experiments were carried out using a 915 MHz microwave reactor developed in our group in collaboration with Sairem Ibérica S.L., equipped with a semiconductor generator (5 kW maximum output power,

with a 2.5% reflected power) working with progressive waves. For these experiments, only **TzOA-M-6** and **$G_{0.5}$-TzOA-M-6** hydrogels were studied.

Study of temperature rise with MW exposure

For preliminar temperature studies at different incident powers (P_{inc}), fully swollen **TzOA-M-6** cubic-shaped hydrogels (1.5 cm × 1.5 cm × 1.5 cm approx.) were placed in contact with a Nortech fibre optic thermometer and immersed in 50 mL of PBS in a glass beaker.

The beaker was placed inside a waveguide chamber and the chamber was sealed prior to irradiation. The samples were irradiated at increasing incident powers (P_{inc} = 1 kW, 2 kW and 3 kW) for a total irradiation time (t_{ir}) of t_{ir} = 120s and the temperature was monitored every 10s. Each sample was irradiated in triplicate. The temperature with respect to time at different P_{inc} was then plotted. The t_{ir} at T=38ºC were obtained by interpolation of T = 38ºC on each curve.

For the studies at several cycles, **TzOA-M-6** and **$G_{0.5}$-TzOA-M-6** hydrogels previously loaded with **IMI** drug were immersed in the corresponding buffer (PBS or SGF) and exposed to four MW cycles at P_{inc}= 2 kW for 30s/cycle. Temperatures were this way monitored every 5s. After each cycle the samples were allowed to cool to room temperature (20 ºC) outside the chamber and the process repeated. All measurements were carried out in triplicate.

6.6. In vitro drug delivery studies

6.6.1. Drug loading

For the studies carried out in chapter 2, dried hydrogel samples were immersed in a 0.002M solution of the corresponding drug (**MZ**, **BZ**, **IB**, **NX**, **IMI** and **RHO**) in PBS for 4 days at room temperature until maximum swelling had occurred. For **RA**, hydrogels were introduced in a 0.00017M solution of **RA** in PBS/SDS (0.1M). For the separate studies carried out in chapter 4, hydrogels were loaded in a 0.009M **IMI** solution in PBS or in a 0.0002M **RHO** solution in water. Loaded hydrogels were then briefly washed with 2 mL of PBS buffer (or water for **RHO**) to remove unloaded drug from the surface of the samples, and the washings were collected with the remaining unloaded solution. The drug loading was then calculated by an indirect method:

$$Drug\ loading\ (\%) = \left(\frac{m_0 - m_u}{m_0}\right) * 100$$

Where m_0 is the total initial mass present in the loading medium and m_u is the mass of the unloaded drug remaining after the hydrogel had incorporated the drug. The drug loading was quantified by UV/VIS spectrophotometric analysis at the absorbance maxima according to each drug solution (λ = 222 nm, 230 nm, 251 nm, 285 nm, 320 nm, 353 nm and 575 nm for IB, NX, IMI, BZ, MZ, RA and RHO, respectively). The absorbance values were then interpolated in a calibration curve, according to the Lambert–Beer law. Each measurement was carried out in duplicate.

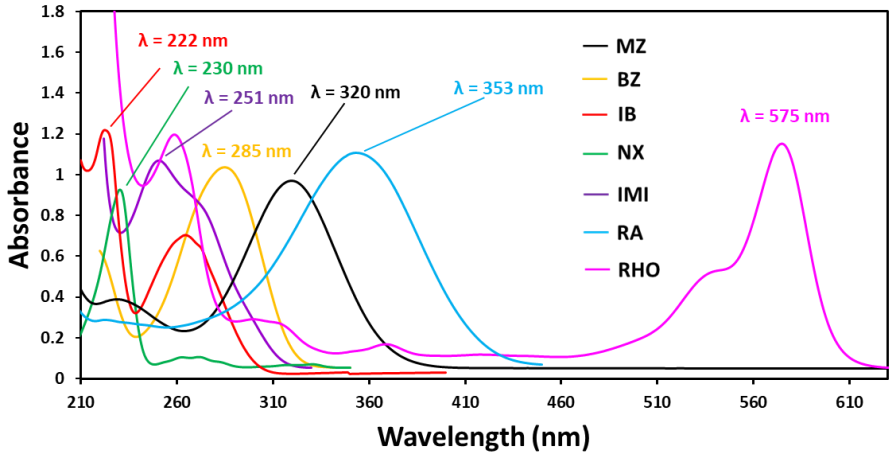

Figure S39. UV/VIS spectra of model commercial drugs in PBS and water (for RHO).

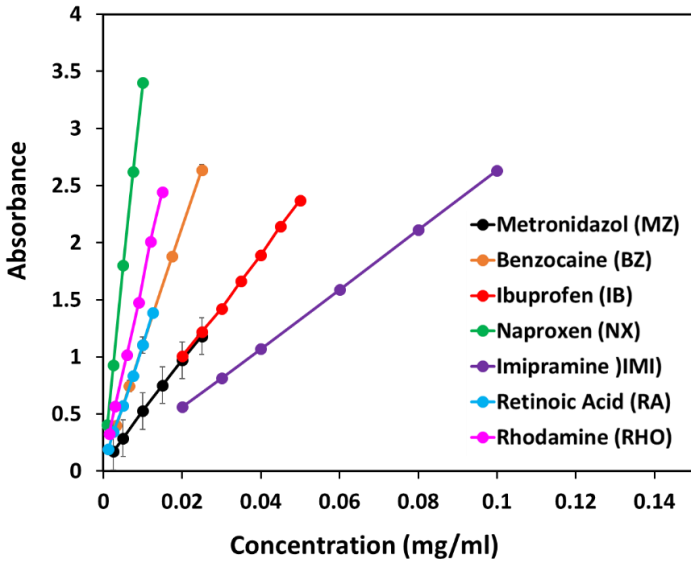

Figure S40. Calibrate curves for the drug solutions in PBS medium or water.

6.6.2. Drug release

6.6.2.1. Pristine hydrogels

For the release of **MZ, BZ, IB, NX** and **IMI** drugs carried out in chapter 2, the drug-loaded hydrogels were immersed in 50 mL of buffered media (PBS or SGF media). For release of **RA** and **RHO** drugs, hydrogels were immersed in 25 ml of PBS/SDS (0.1M) and 20 ml of water, respectively. The samples were placed in an orbital mixer and shaker with a heating platform (ROTATERM 3000435 JP SELECTA) operating at 70 rpm and 37ºC. At defined time intervals, aliquots of 5 mL were stored for further analysis and replaced with the same volume of the fresh corresponding buffer, so that the volume of the release medium remained constant. The aliquots were quantified by UV/VIS spectrophotometric analysis with interpolation in calibration curves following the Lambert–Beer law. Each measurement was carried out in duplicate, and the average release profile was obtained.

6.6.2.2. Graphene hybrid hydrogels

All drug delivery experiments were carried out with **TzOA-M-6**, **$G_{0.1}$-TzOA-M-6** and **$G_{0.5}$-TzOA-M-6** hydrogels.

Difussion-mediated drug release

The hydrogels were first loaded with **IMI** drug as explained in the loading studies. The release experiments were performed in PBS buffer and the UV/VIS readings were performed at λ = 251 nm similar as in the release of pristine hydrogels. Each measurement was carried out in duplicate, and the average release profile was obtained.

pH-triggered drug release

The delivery studies were carried similarly as the diffusion-mediated studies, however, the drug release was carried out in SGF buffer instead.

Microwave-triggered drug release

All microwave irradiation experiments were carried out using a 915 MHz microwave reactor developed in collaboration with Sairem Ibérica S.L., equipped with a semiconductor generator (5 kW maximum output power, with

a 2.5% reflected power) working with progressive waves. For these experiments, only **TzOA-M-6** and **$G_{0.5}$-TzOA-M-6** hydrogels were studied.

The preliminar drug release studies carried out at different P_{inc} were performed by immersing **IMI**-loaded **TzOA-M-6** hydrogels in 50 mL of PBS solution in a glass beaker inside the waveguide chamber. Hydrogels were then exposed to four MW cycles under two different conditions (P_{inc} = 1 kW for t_{ir} = 60s and P_{inc} = 2 kW for t_{ir} = 30s). Each cycle was performed at every hour for a total of 3h. After each cycle, the beaker was removed from the chamber and 5 mL aliquots were withdrawn from the solutions and stored. Inmediately after, 5 mL of fresh PBS buffer were added to maintain a constant volume and the samples were left to cool to rt, after which they were sealed back inside the chamber. After each cycle the final volume of PBS solution was observed to remain constant, therefore any possible evaporation of the solvent after MW exposure was ruled out. Absorbance readings were performed with UV/VIS spectrophotometric analysis at λ = 251 nm. All measurements were performed in duplicate.

For 24h experiments, **IMI**-loaded **TzOA-M-6** and **$G_{0.5}$-TzOA-M-6** hydrogels immersed in the corresponding buffer were subjected to four MW cycles of P_{inc}= 2 kW, t_{ir} = 30s. Each cycle was performed at every hour for a total of 3h and the hydrogels were left to release for 24 h. Following treatments and analysis were performed in a similar manner. Each measurement was carried out in duplicate.

6.6.2.3. Magnetite hybrid hydrogels

For the blending method, **TzOA-P-1** and **Mag_4-TzOA-P-1** hydrogels were studied. For the *in situ* co-precipitation method, **TzOA-0**, **$Mag_{0.05}$-TzOA-0** and **$Mag_{0.25}$-TzOA-0** hydrogels were studied.

Magnetic-triggered drug release

Dried hydrogel samples were loaded with 2 ml of **RHO** aqueous solution (0.0002 M) until all the drug solution was sucked up by the hydrogels. The hydrogels were then immersed in 20 ml water and stimulated by placing a Nd magnet (4250 G, N35 grade) underneath the vessel for 15 minutes performing circled-fashion movements. After stimulation with the magnet, an aliquot (~3.3 ml) was withdrawn from the solution and measured in the UV/VIS spectrophotometer at λ = 575 nm.

For time-dependent experiments, aliquots were measured at approximately t(h) = 0, 0.5, 1, 2, 5, 6, 7, 12, 22, 28.5, 44 and 67.5. After each measurement, the aliquots were poured back to the vessel so that the final volume remained constant.

For cycle-dependent experiments, aliquots were measured after each cycle of magnetic stimulation (1 cycle = 15 min), for cycles 1-12. After each measurement, the aliquots along with the rest of the solution were discarded and 20 fresh ml of water were replaced.

For both blending and *in situ* co-precipitation methods, the release of drug from control hydrogels in the absence of external magnetic field (EMF) was performed similarly as above, however, the solutions along with the immersed hydrogel were stirred in the absence of the external Nd magnet. All measurements were carried out in duplicate.

6.7. Theoretical calculations

The structural and electronic features of the triazine supramolecular moieties and their interactions with rhodamine 101 and metronidazol were characterised by density functional theory (DFT)[4,5] as implemented in the SIESTA (*Spanish Initiative for Electronic Simulations with Thousands of Atoms)* code.[6] We used the Perdew–Burke–Ernzerhof (PBE)[7,8] functional to pre-optimised all calculations with a double- ζ polarised (DZP) basis set, with a kinetic energy cut-off of 450 Ry. The interaction between ionic cores and valence electrons was described by the Troullie–Martins norm-conserving pseudopotentials.[9] Afterwards, we re-optimised all our minima with a methodology that takes into account the van der Waals dispersive forces, both quantitatively and economically, such as the vdW-DF2.[10] All the energies have been corrected with the Counter Poisse correction to take into account the BSSE errors.[11,12] This methodology was used as implemented in the SIESTA code. The supramolecular networks were relaxed using the conjugate gradient method until the forces were below 0.04 eV/Å on all atoms under a Γ-center 3×3×3 k-point mesh grid for all calculations. In all cases, the optimisation of these systems was allowed with an iterative cycle of a variable cell and optimisation procedure, to enable the triazine, rhodamine 101 or metronidazole molecules, to adopt the desired stacking.

6.8. Citotoxicity assays

SH-SY5Y Cell Culture

For **TzOA-M-6** and **$G_{0.5}$-TzOA-M-6** hydrogels, Human neuroblastoma SH-SY5Y cells (Sigma-Aldrich) were maintained in Eagle's Minimum Essential Medium (EMEM), supplemented with 10% decomplemented fetal bovine serum, 2 mM L-glutamine, 1 % antibiotics-antimycotics, in a humidified atmosphere supplied with 5 % CO_2 at 37 °C until confluent. For **TzOA-0**, **$Mag_{0.05}$-TzOA-0** and **$Mag_{0.25}$-TzOA-0** hydrogels, SH-SY5Y cells were maintained in MEM/F12 instead.

Calcein-AM Viability Assay

For **TzOA-M-6** and **$G_{0.5}$-TzOA-M-6** hydrogels, cell viability was assessed using calcein-AM, a nonfluorescent cell permeable derivative of calcein which becomes fluorescent inside living cells. Dried hydrogels were first swollen in PBS or SGF media and then lyophilized. Samples were then cut into homogeneous slices (approximately 25 mm^2 surface area), transferred to separate wells of a 24-well plate and sterilized by UV illumination from both sides for 10 min. A dilution of $2{\cdot}10^6$ cells/mL in complete medium was prepared and 50 µL of this solution were soaked into each hydrogel. After 20 min of incubation at room temperature, following the procedure described by Rödling *et al*,[13] complete medium was added to each well and cells were incubated for 24 h under standard cell culture conditions. The following day, cells were washed with PBS buffer and incubated with 1 µM calcein-AM and 1.5 µM propidium iodide diluted in complete medium for 15 min at 37 °C. After washing once with PBST, cells were maintained in complete medium until each hydrogel was transferred to a glass slide to visualize green fluorescence.

For **TzOA-0**, **$Mag_{0.05}$-TzOA-0** and **$Mag_{0.25}$-TzOA-0** hydrogels, dried hydrogel samples were instead swollen in water and cut similarly into homogeneous slices (approximately 25 mm^2 surface area). Four samples of each hydrogel were transferred to separate wells of a 24-well plate and allowed to dry completely at room temperature. Before cultivation, hydrogels were sterilized by UV illumination for 20 min. A dilution of $4{\cdot}10^6$ cells/mL in complete medium was prepared and 25 µL of this solution were soaked into each hydrogel. The following treatments were similar.

Confocal Microscopy and image analysis measurements

For **TzOA-M-6** and **$G_{0.5}$-TzOA-M-6** hydrogels, images *per* experimental condition were taken by scanning the hydrogels with confocal microscopy using a Zeiss LSM 800 system (Carl Zeiss, Weimar, Germany). Fluorescent images for each condition were taken as duplicates and acquired using the 10× objective with 1 excitation laser at 494 nm for Calcein-AM (X and Y axes = 638,9 μm). Confocal z slices of around 260 μm were used (from 150 μm to 615 μm) with a 15 μm z interval. Cell counting was done by ImageJ (Fiji, NIH Image)[14] by a blind data collection with Cell Counter plugin. A logistic regression model was used to fit number of cells to the presence of graphene and type of hydrogel (PBS or SGF; SPSS, IBM SPSS Statistics, vs. 24).

For **TzOA-0**, **$Mag_{0.05}$-TzOA-0** and **$Mag_{0.25}$-TzOA-0** hydrogels, fluorescent images for each condition were taken as duplicates and acquired using the 10× objective (X and Y axes = 638,9 μm) with one excitation laser at 494 nm for calcein-AM and other excitation laser at 501 nm for propidium iodide. Confocal z slices of around 360 μm were used (from 275 μm to 465 μm) with a 30 μm z interval. Cell counting was done by ImageJ (Fiji, NIH Image) (Rasband, W.S., ImageJ, U. S. National Institutes of Health, Bethesda, Maryland, USA, https://imagej.nih.gov/ij/, 1997-2018.) by a blind data collection with Cell Counter plugin.

Statistical data analysis

SPSS software package (version 24 for Windows) was used to analyze the data statistically, taking $p<0.05$ (95% CI) as the threshold for statistical significance. Quantitative variables were presented as mean ± SEM. Comparisons among hydrogels were conducted with the Kruskal-Wallis procedure for independent samples and the DMS post hoc test

.

6.9. References

[1] N. Sawa, Wakaba-cho, Tadotsu-cho, N. Kagawa-kan, T. Masuda, Kitahirayama-cho, M. K, *Process for Synthesizing 2-Vinyl-4,6-Diamino-s-Triazine*, 1987, Sawa, N., Masuda, T. Japan. Application. No. 85305954.1.

[2] V. León, J. M. González-Domínguez, J. L. G. Fierro, M. Prato, E. Vázquez, *Nanoscale* 2016, *8*, 14548–14555.

[3] J. M. González-Domínguez, V. León, M. I. Lucío, M. Prato, E. Vázquez, *Nat. Protoc.* 2018, *13*, 495–506.

[4] J. Y. Jung, J. H. Park, Y. J. Jeong, K. H. Yang, N. K. Choi, S. H. Kim, W. J. Kim, *Korean J. Physiol. Pharmacol.* 2006, *10*, 289–295.

[5] C. H. Chu, C. W. Leung, *Integr. Equations Oper. Theory* 2001, *40*, 391–402.

[6] J. M. Soler, E. Artacho, J. D. Gale, A. García, J. Junquera, P. Ordejón, D. Sánchez-Portal, *J. Phys. Condens. Matter* 2002, *14*, 2745–2779.

[7] J. P. Perdew, K. Burke, M. Ernzerhof, *Phys. Rev. Lett.* 1996, *77*, 3865–3868.

[8] J. P. Perdew, K. Burke, M. Ernzerhof, 1996, *77*, 3865–3868.

[9] N. Troullier, J. L. Martins, *Phys. Rev. B* 1991, *43*, 1993–2006.

[10] K. Lee, É. D. Murray, L. Kong, B. I. Lundqvist, D. C. Langreth, *Phys. Rev. B - Condens. Matter Mater. Phys.* 2010, *82*, 081101–1.

[11] H. B. Jansen, P. Ros, *Chem. Phys. Lett.* 1969, *3*, 140–143.

[12] B. Liu, A. D. Mclean, *J. Chem. Phys.* 1973, *59*, 4557–4558.

[13] L. Rödling, E. M. Volz, A. Raic, K. Brändle, M. Franzreb, C. Lee-Thedieck, *Adv. Healthc. Mater.* 2018, *7*, 1–14.

[14] W. S. Rasband, *ImageJ, U. S. National Institutes of Health, Bethesda, Maryland, USA, Https://Imagej.Nih.Gov/Ij/, 1997-2018.*

Conclusions

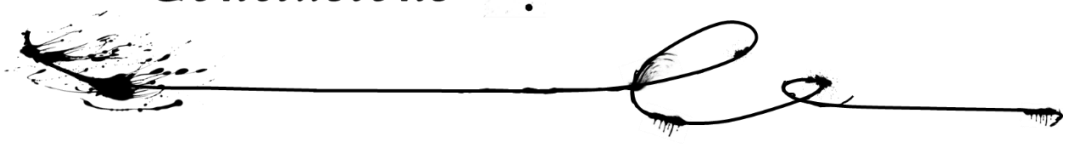

Conclusions

The DAT moiety has proven a suitable building block for the preparation of **hydrophobic hydrogels**. These novel materials have been prepared *via* radical polymerization process in DMSO medium, followed by phase inversion in water to yield the corresponding hydrogels. SEM studies confirmed their porous structure of these materials. In addition, the hydrogels showed a moderate swelling capacity, which allowed them to be mechanically resistant and circumvent the typical brittleness of hydrogels.

Favorable intermolecular H-bond formation between DATs allowed formation of **hydrophobic microdomains** inside the hydrogels, which are responsible for their enhanced capacity to incorporate drugs of poor water solubility. It was observed that higher drug loading values were obtained as the hydrophobicity of the loaded drugs increased.

Density Functional Theory (DFT) calculations predicted stable formation of supramolecular "pockets" between DATs, which act as stabilizing cavities for hydrophobic drugs:

- Via π-π stackings between the drug and the triazines.
- Via CH-π interactions between the drug species and the aliphatic polymer backbone.

The results suggest that these hydrophobic microdomains were more stable inside the polymeric network than in a polymer-free environment.

In the same line with the theoretical modellings, it was also observed that the higher hydrophobic drugs were released in a more sustained manner.

In addition, these hydrogels are **smart materials** since they respond to external stimuli.

The basic nature of the DATs also conferred the hydrogel with **pH-responsiveness.** Under acidic medium, the swelling degree and pore sizes was increased, in consequence, the drug release was enhanced ~10%.

These new hydrogels could find **applications in tissue engineering**, since it was shown that a growth factor, such as retinoic acid, was successfully released in a sustained manner.

Hybrid diaminotriazine-nanocomposite hydrogels have been succesfully prepared and characterized using graphene and iron oxide nanoparticles as nanomaterials.

Graphene was introduced successfully into DAT-based hydrogels and resulted homogeneously distributed throughout the material. It was observed that the graphene embedded inside the network induced a disruption of the DAT hydrophobic domains, presumably due to graphene-DAT favorable interactions. This scenario led to:

- Homogenization of the internal porous structure
- Mechanical properties enhancement
- Increase in the swelling degree
- Improvement in the release of the hydrophobic drug.

A **microwave (MW) radiation** of 915 MHz was used as remote external stimulus. It was observed that exposure of the drug-loaded hydrogels to cycles of MW radiation led to improvement of the drug release rates.

- At low pH values, the release was further enhanced under MW irradiation in a synergistic manner, evidencing the capacity of the hydrogels to respond to several simultaneous stimuli.
- Graphene helped controlling the temperature of the hybrid hydrogels after MW exposure, which is necessary for example for transdermal applications, since this reduces the risk of overheating nearby tissues.

The introduction of **magnetic nanoparticles** inside the DAT-based hydrogels resulted in smart materials that were strongly attracted to a magnet. For their fabrication, it was observed that the *in situ* co-precipitation method resulted in hybrids with both higher magnetic behavior and structural integrity than the blending method.

Favorable DAT-metal interactions were demonstrated between the *s*-triazine N atoms and the iron atoms, which favors the formation of superparamagnetic iron oxide nanoparticles (SPIONs) inside the hydrogels. The formation of DAT-metal bonds occurs at the expense of the disruption of DAT-DAT H-bonds and this resulted in an increase in the swelling capacities and pore sizes of the hydrogels, as well as mechanical loosening of the scaffold.

The embedded SPIONs appeared as crystalline iron oxide nanoparticles, which were in agreement with the cubic spinel structure of magnetite. The crystalline pattern, superparamagnetic behavior and few-nanometer size of the nanoparticles indicated no signs of aggregation inside the hydrogels, as well as homogeneous distribution.

The magnetic hydrogels were evaluated as hydrophobic reservoirs for magnetic-triggered drug delivery. The hybrids showed high drug loadings for rhodamine 101, the highest hydrophobic drug used in this work. In the absence of the magnetic impulse, rhodamine was strongly retained within the DAT network, due to hydrophobic confinement effect. Under the effect of the magnetic field, the drug release was considerably increased, possibly due to the disruption of the hydrophobic entrapment, and allowed these hybrids to achieve *on-demand* drug release. Higher release ratios were observed as the SPION content inside the hydrogels increased, pointing the suitability of these hydrogels for *smart* delivery applications.

The hybrid hydrogels were tested for cell viability with human neuroblastoma cell lines (SH-SY5Y cells). Both the graphene and magnetite hybrids resulted in higher number of living cells grown inside the scaffolds with respect to their nanomaterial-free homologues. The hydrogels thus proved promising candidates for *smart* delivery of hydrophobic drugs under external stimuli in the presence of cells, which points them particularly appealing for tissue engineering applications.

In the work performed in the predoctoral stay, the scope for the synthesis of stimuli-responsive materials was expanded to the fabrication of **light-responsive hydrogels**. The *p*-methoxynitrobenzyl (PMNB) moiety was chosen as the non-toxic photo-labile group.

The Passerini reaction was successfully used for the synthesis of polymers, which were further used *via* biorthogonal click reaction to obtain light-sensitive hydrogels. It was demonstrated that this method could be used for the *in situ* fabrication of light-sensitive materials in the presence of cells.